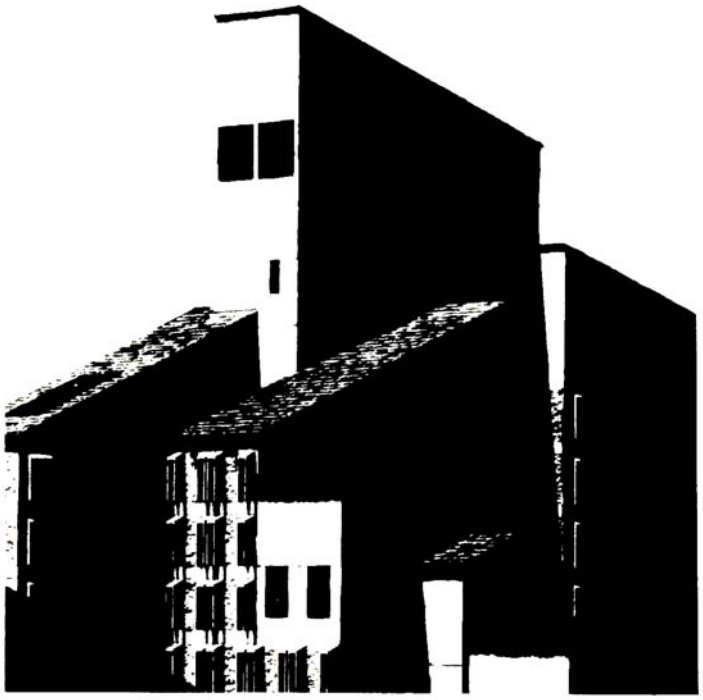

THERMAL RESPONSE OF REINFORCED CONCRETE STRUCTURES IN NUCLEAR POWER PLANTS

Kaspar Willam, Yunping Xi , Keun Lee and Byunhun Kim

SESM No. 02-2009

Department of Civil, Environmental,
and Architectural Engineering

College of Engineering
and Applied Science

University of Colorado at Boulder

TABLE OF CONTENTS

Part I

Part II

Part III

PART I:
HIGH TEMPERATURE PROPERTIES OF CONCRETE AND STEEL

1 Introduction

This is the report for a research project sponsored by Oak Ridge National Laboratory in 2008 – 2009. The objectives of the project were to review and summarize thermal responses of reinforced concrete structures used in nuclear power plants. There are totally three parts of the report. The first part focuses on responses of various materials under high temperatures including concrete and steel, the second part on structural performances, and the third on spalling damage of concrete under high temperatures.

The first part of the report includes several aspects: damage mechanisms of the materials under high temperatures, available experimental results, current code specifications, and prediction models for thermal responses of the materials. The material properties include strength, stiffness, stress-strain relations, transport properties (e.g. thermal conductivity), short-term thermal expansion, long-term thermal creep, shrinkage, and the interactive effects among temperature variation, vapor diffusion, and mechanical loading in concrete. The bond behavior between concrete and steel under high temperatures is also included. This part is listed as the first part of the report, because thermal responses of reinforced concrete structures used in nuclear power plants depend on thermal responses of materials such as concrete and steel under high temperatures.

The second part of the report focuses on the structural responses of reinforced concrete structures under high temperatures, such as beams, columns, and slabs. The second part of the review includes available experimental results, current code specifications, and prediction models for thermal responses of the reinforced concrete structures. In addition, we developed a numerical model for characterizing high temperature responses of reinforced concrete beams. The model prediction was compared with available test data in the literature and with predicted results by a commercial finite element code.

The third part of the report is for spalling damage of concrete under high temperatures, which is a special form of fire damage when the heating rate is very high. The review includes experimental results, damage mechanisms, and theoretical and numerical analysis. A recently developed numerical model and experimental results obtained by the authors were described in detail together with a comprehensive literature review on spalling damage of concrete.

2 Responses of Concrete to High Temperatures

2.1 Damage mechanisms of concrete under high temperatures

There are four types of major damage mechanisms responsible for deterioration of properties of concrete under high temperatures: (1) phase transformations taking place in cement paste; (2) phase transformations taking place in aggregate; (3) thermal incompatibility between the cement paste and aggregate; and (4) spalling of concrete. The first three damage mechanisms will be discussed in this section, and the last mechanism, the spalling of concrete is a complicated topic and will be described in details in another report (UCB-CEAE-SESM-R003-2009). The first three damage mechanisms result in reduced strength and stiffness of concrete, while the last one leads to reduced cross section of structural members and loss of structural integrity.

2.1.1 Phase transformations in cement paste

Major products of hydration reactions of Portland cement are Calcium Silicate Hydrates ($C_3S_2H_3$ or simplified as C-S-H), Calcium Hydroxide (CH), and Ettringite ($C_6A\overline{S}_3H_{32}$). All of the hydration products decompose under high temperatures. The decomposition processes of the hydration products at various temperature ranges are listed in Table 2.1 (Schneider 2002).

Table 2.1 Decomposition of cement paste at various temperature ranges (Schneider 2002)

Temperature range [°C]	Transformation or decomposition reaction	Heat of reaction or transformation [kJ/kg]	Heat of reaction or transformation [MJ/m^3 concrete]	Mass of reaction [kg/m^3 concrete]
30 - 120	Desorption or evaporation of physically adsorbed water	Heat of evaporation of water: 2258	290	130 kg water
30 - 300	gel destruction: 1. stage of dehydration	Heat of hydration: 250	< 20	< 78 kg hardened cement paste
120 - 600	Release of chemically adsorbed or zeolithically bonded water	Heat of evaporation of water: > 2258	> 135	60 kg water
450 - 550	Decomposition of portlandite $Ca(OH)_2 \rightarrow CaO + H_2O$	1000	< 40	< 40 kg CaO
570	Transformation of quartz $\alpha \rightarrow \beta$ SiO_2	5,9	8,8 1,2	1500 kg quartz 200 kg quartz
600 - 700	Decomposition of CSH-phases; formation of β-C_2S	Heat of hydration: 500	< 120	< 240 kg hardened cement paste
600 - 900	only calcite: dissociation of calcite	Heat of decomposition: 1637	2360	1600 kg limestone $CaCO_3$-content approx. 90 %
from 1100 - 1200	Melting of concrete, formation of glassy materials	Melting heat: 500 - 1000	quartzitic: 1575 calcitic: 1125	2100 kg concrete 1500 kg concrete

The chemical reactions for the decomposition processes can be described as following,

Decomposition of C-S-H : $3.4CaO \cdot 2SiO_2 \cdot 3H_2O \rightarrow 3.4CaO \cdot 2SiO_2 + 3H_2O\uparrow$

Decomposition of CH : $Ca(OH)_2 \rightarrow CaO + H_2O\uparrow$

The formation of $CaCO_3$ is due to accelerated carbonation reaction of CH,
$C_a(OH)_2 + CO_2 + H_2O \rightarrow C_aCO_3 + 2H_2O$
Then, $CaCO_3$ decomposes at high temperatures.
Water evaporates under high temperatures.

Associated with the formation of new phases in the chemical reactions are changes in volume as well as in stiffness of cement paste. There are cracks and voids formed in cement paste along with the decomposition of CH, which results in major damage of concrete. Similarly, the stiffnesses of the new products are different from the stiffness of the original phases, which leads to a change in stiffness of concrete when temperature rises.

2.1.2 Phase transformations in aggregates

For normal weight concrete, there are two common aggregate groups: siliceous aggregates such as quartzite, gravel, granite and flint; calcareous aggregates such as limestone, dolomite and anorthosite. It is generally known that siliceous aggregates, especially quartzite, experience phase transformation at approximately T = 570°C from α-quartz to β-quartz. This crystal transformation is reversible and endothermic which involves a heat of transformation of 5.9 kJ/kg of SiO_2. Assuming about 75 percent of the quartzitic aggregate in the concrete participates in the transformation, the heat of transformation is found to be 8.8 MJ/m^3 for quartzitic and about 1.2 MJ/m^3 for calcitic concrete.

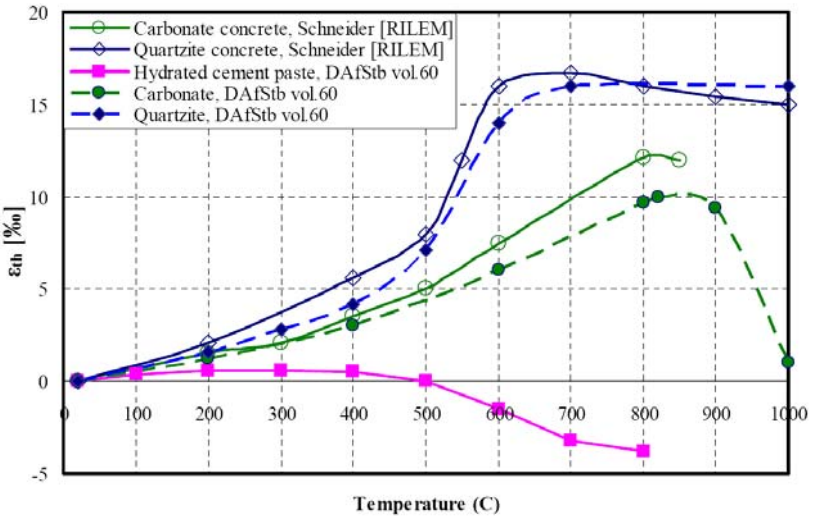

Figure 2.1 Thermal strains for different concretes, aggregates and hydrated cement paste

2.1.3 Thermal incompatibility between cement paste and aggregate

Concrete is a composite material with aggregates as inclusions and cement paste as matrix. The two phases have different thermal and mechanical properties and thus respond differently upon a temperature rise. The aggregates in concrete expand with increasing temperature. Cement paste may expand if the thermal expansion is dominant and may shrink if the moisture loss is dominant. The combined effect of the deformation mechanisms of the two phases depends on many factors such as heating rate, holding period, and composition of the concrete. Figure 2.1 illustrates these effects. The thermal incompatibility between the two phases causes very large mismatch in the deformation between aggregates and cement paste, which results in cracks in the interface transition zone around aggregates. Subsequent heating, drying, and loading may cause coalescence of the cracks to form discrete large cracks leading to spalling of concrete and/or failure of concrete structures.

2.2 Strength of concrete under high temperatures

The compressive strength of concrete at high temperature is largely affected by the following factors: 1) Individual constituent of concrete, 2) Sealing and moisture conditions, 3) Loading level during heating period, 4) Testing under 'hot' or 'cold residual' conditions, 5) Rate of heating or cooling, 6) Duration under an elevated temperature (holding period), 7) Time

maintained in moist conditions after cooling before the strength test is carried out, and 8) Number of thermal cycles (Khoury, 2002). Before discussing thermal responses of concrete under high temperatures, it is important to distinguish several different loading scenarios for strength testing. Three testing methods are commonly used to examine the strength and stiffness of concrete under a high temperature. These testing methods are referred to as stressed tests, unstressed tests, and unstressed residual strength tests (Phan, 1996). The schematic of the three test methods is shown in Figure 2.2.

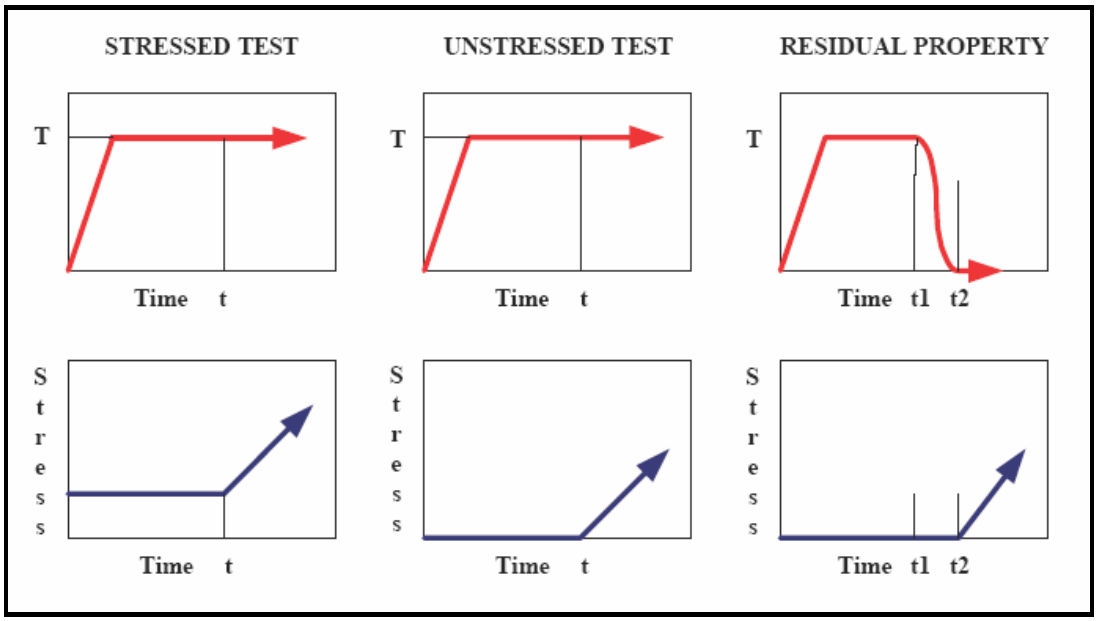

Figure 2.2 Schematic of temperature and loading histories for the three test methods

Stressed test is a test in which a preload, generally in the range of 20 percent to 40 percent of the ultimate compression strength of concrete at room temperature, is applied to the concrete specimen prior to heating, and the load is sustained during the heating period. After the specimen reaches a steady state temperature condition, the stress or the strain is increased to a prescribed loading rate until the specimen fails. The test results of this test are most suitable for representing fire performance of concrete in a column or in the compression zone of beams and slabs where the structural member is suddenly subjected to an overload during fire due to failure of other structural member.

Unstressed test is similar to the stressed test except that the preload level is zero. The concrete is unstressed prior to the final loading. The test results are most suitable for representing the performance of concrete elements with low stress levels under service conditions and loaded under high temperatures.

Unstressed residual strength test is a test in which the specimen is cooled to room temperature after one or several cycles of heating without preloading. The mechanical load is then applied (after the heat treatment) at room temperature under stress or strain control until the specimen

fails. The results of this test are most suitable for assessing the post fire (or residual) properties of concrete.

All three test methods can be used to determine the compressive strength (the maximum stress), the modulus of elasticity, the strain at the maximum stress, and the dissipated mechanical energy as function of temperatures.

In this section, we will focus on the general trends of the test data for concrete under various heating and loading conditions, and with various types of aggregates. The effects of concrete mix design and curing time are not included.

2.2.1 Experimental results on strength of concrete under high temperatures

Abrams (1971) conducted a study of four variables including aggregate types (carbonate dolomite sand and gravel, siliceous, and expanded shale lightweight aggregates), testing methods (unstressed, stressed and unstressed residual experiments), concrete strengths (ranging from 22.8 MPa to 44.8 MPa), and temperatures (from 93˚C to 871˚C). The specimens were 75 mm×150 mm cylinders. Abrams' test data are important because they were used as a main reference in the current ACI design code for concrete under high temperatures.

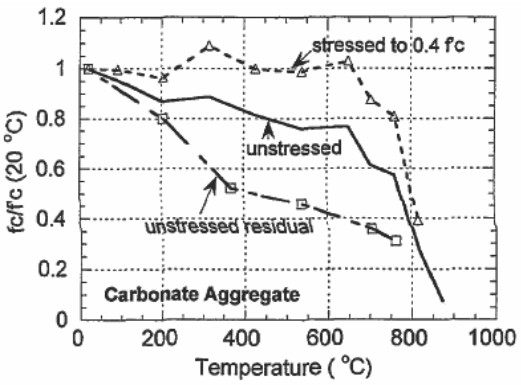

(a) Carbonate aggregate concrete

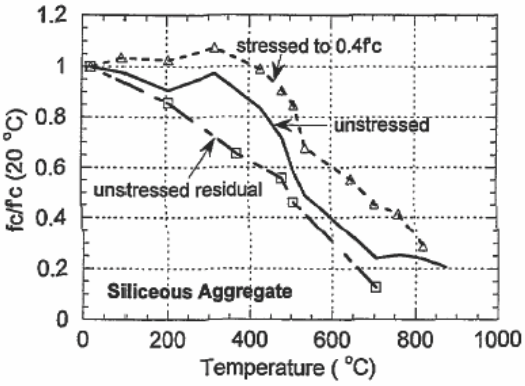

(b) Siliceous aggregate concrete

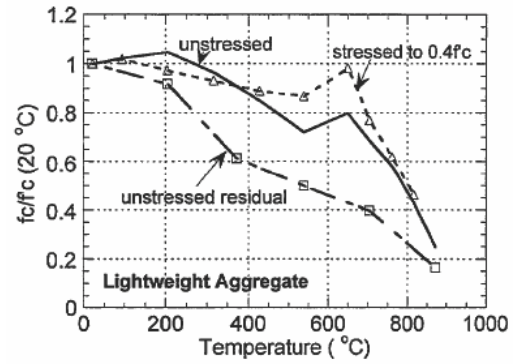

(c) Lightweight aggregate concrete

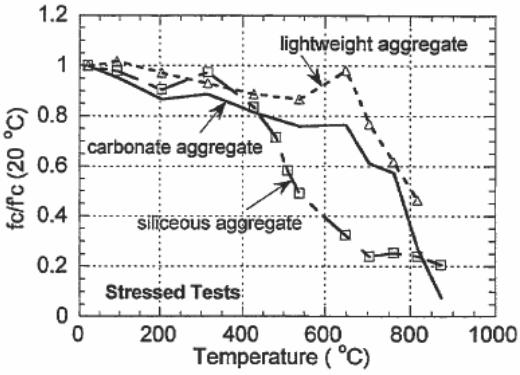

(d) Stressed tests

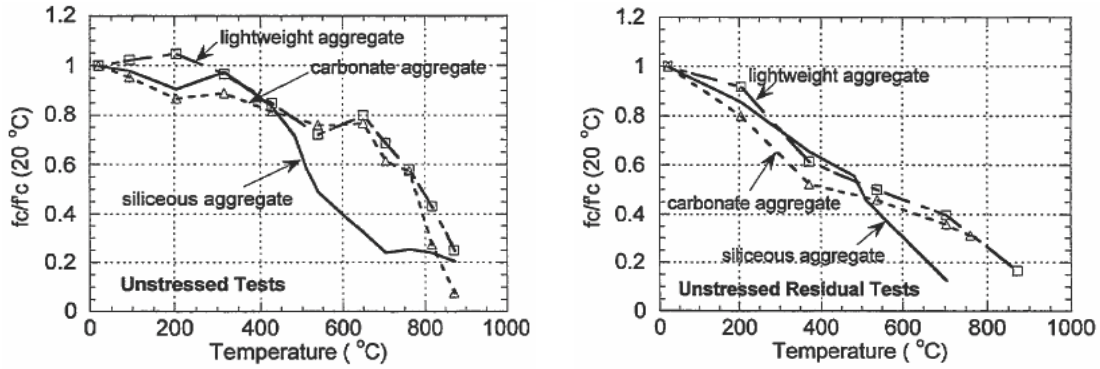

(e) Unstressed tests (f) Unstressed residual tests

Figure 2.3 Hot isothermal test results obtained by Abrams (1971)

Figure 2.3 summarizes the test results. Up to about 480˚C, all three concretes exhibited similar strength loss characteristics under each test condition (stressed, unstressed, and unstressed residual). Above 480˚C, the siliceous aggregate concrete had greater strength loss and retained less strength for all three test conditions. Specimens made of carbonate aggregates and lightweight aggregates behaved about the same over the entire temperature range and retained more than 75 percent of their original strength at temperatures up to 649˚C in unstressed tests. For the siliceous aggregate, the strength was 75 percent of the original strength at 430˚C.

Compressive strengths of specimens with preload (stressed tests) were generally 5 percent to 25 percent higher than those without preload (unstressed tests). This may be due to the possibility that the preload helps to close existing cracks in concrete. This phenomenon will be discussed in more detail later in Section 2.2.4. The unstressed residual specimens had the lowest strength compared with the stressed and unstressed specimens tested at high temperatures. This is because the cooling of concrete actually generates very significant damage in concrete, as shown recently by Lee et al. (2008). The test results of Abrams (1971) indicate that strength recovery took place only in a limited temperature range in the case of the stressed and unstressed experiments.

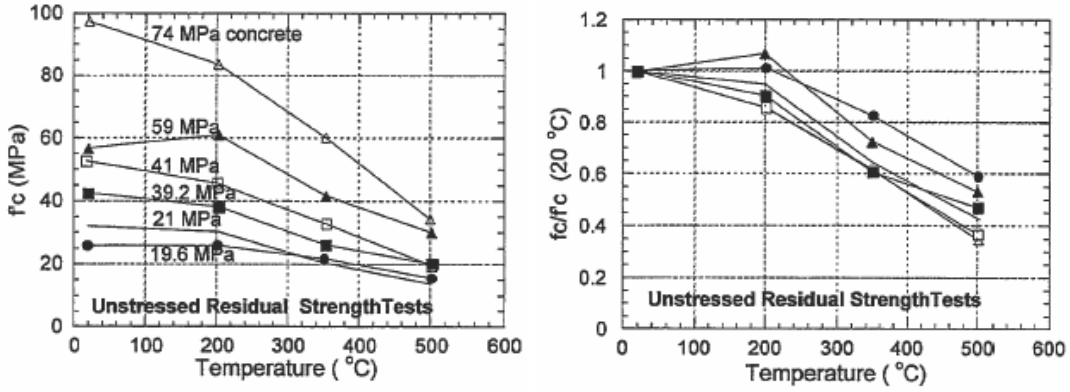

(a) Compressive strength (b) Normalized strength

Figure 2.4 Residual compressive strength obtained by Morita et al. (1992)

Morita et al. (1992) conducted unstressed residual strength tests (see Figure 2.4). The specimens were 100 mm×200 mm cylinders. The heating and cooling rate were 1˚C/min and target temperatures were 200˚C, 350˚C, and 500˚C. The holding time at target temperatures to allow a steady state was 60 min. The test data showed that high strength concrete has higher rate of reduction in residual compressive strength.

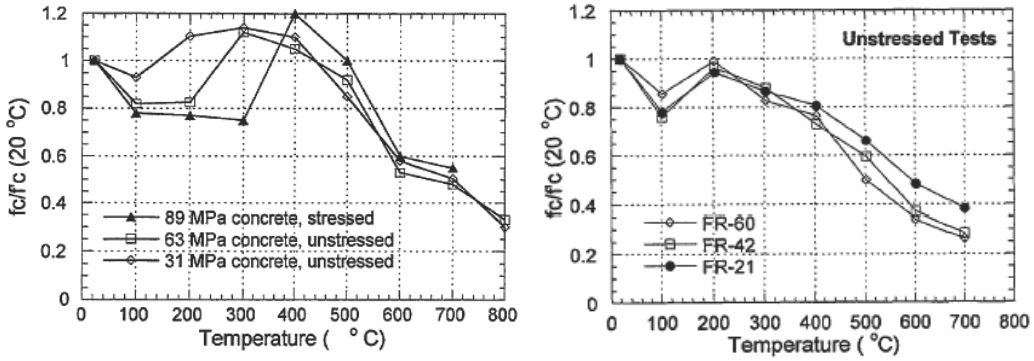

(a) (b)

Figure 2.5 Compressive strength vs. Temperature under hot isothermal conditions by (a) Castillo and Durani, 1990 and (b) Furumura et al. 1995

The effect of elevated temperatures on concrete strength and load-deformation behavior of High Strength Concrete (HSC) and Normal Strength Concrete (NSC) were investigated by Castillo and Durani (1990). Type I Portland cement with natural river sand and crushed limestone were used for preparing the concrete specimens in the form of 51mm×102 mm cylinders. Figure 2.5(a) shows the test results. In the case of the stressed experiment, 40 percent of the ultimate compressive strength at room temperature was applied to the specimens and sustained during the heating period. In the unstressed experiment, when exposed to temperatures in the range of 100°C to 300˚C, HSC showed a 15 percent to 20 percent loss of compressive strength, whereas the NSC showed almost no strength loss in the temperature range. HSC recovered its strength between 300°C and 400˚C, reaching a maximum value of 8 percent to 13 percent above the strength at room temperature. This phenomenon will be discussed in more detail later in Section 2.2.3. At temperature above 400˚C, HSC progressively lost its compressive strength which dropped to about 30 percent of the room temperature strength at 800 ˚C. The trend of NSC was similar to that of HSC.

Furumura et al. (1995) performed unstressed tests and unstressed residual tests on 50 mm×100 mm concrete cylinders using three compressive strength levels: 21 MPa (normal strength concrete FR-21), 42 MPa (intermediate strength concrete FR-42), and 60 MPa (high strength concrete FR-60). The heating rate was 1˚C/min and target temperatures were from 100˚C to 700˚C with an increment of 100˚C. The time at target temperatures to allow a steady state was two hours. The concrete was made from ordinary Portland cement. They observed that, for the unstressed tests, the compressive strength decreased at 100˚C, recovered to room temperature strength at 200˚C and then decreased monotonically with increasing temperature beyond 200˚C (see Figure 2.5(b)). For the unstressed residual tests, the compressive strength

decreased gradually with increasing temperature for the entire temperature range without any recovery.

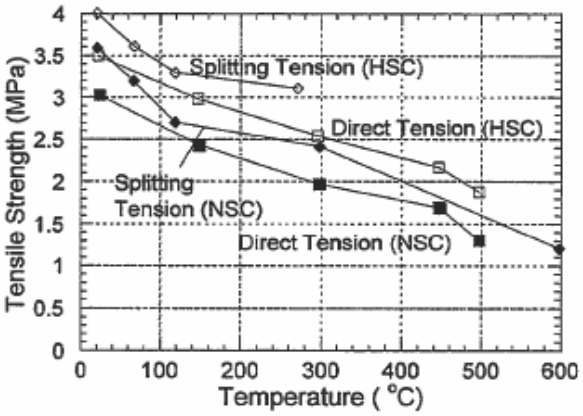

Figure 2.6 Unstressed residual tensile strength obtained by Noumowe et al. (1996)

Noumowe et al (1996) conducted unstressed residual strength tests to compare the performance of HSC exposed to high temperatures with NSC. The specimens were 160 mm×320 mm cylinders and 100 mm×100 mm×400 mm prisms. Normal strength concrete (38.1 MPa) and high strength concrete (61.1 MPa) were used. The prismatic specimens had enlarged ends and were used to measure tensile strength. Calcareous aggregates were used for both concretes. The specimens were heated at a rate of 1˚C/min to target temperatures of 150˚C, 300˚C, 450˚C, 500˚C, and 600˚C, which was maintained for one hour, and then allowed to cool at 1˚C/min to room temperature. Uniaxial compressive tests, splitting tensile tests, and direct tensile tests were performed to obtain residual compressive strength, modulus of elasticity, and residual tensile strength versus temperature relationships. Figure 2.6 shows the residual tensile strength relationship. Residual tensile strengths for NSC and HSC decreased similarly and almost linearly with increase of temperature. Tensile strengths of HSC at all temperatures were 15 percent higher than those of NSC. Also, the tensile strengths measured by splitting tension experiments were higher than those obtained in direct tension.

2.2.2 ACI specifications on the strength of concrete under high temperatures

The current ACI code, ACI/TMS-216 was developed based primarily on the early test data by Abrams (1971), which showed the temperature dependence of the uniaxial concrete compressive strength as shown in Fig. 2.3. Figures 2.7, 2.8, and 2.9 are taken from ACI/TMS-216 on "Fire Resistance" of concretes with three different types of aggregates. The figures illustrate the reduction of compressive strength of $f_c^{'}$ = 3900 psi concrete in the temperature range up to T = 1600°F. The general trends show that axial pre-loading σ_{pre} = 0.4 $f_c^{'}$ leads to higher strength properties when compared to unstressed conditions. Furthermore, residual strength after cooling leads to far greater degradation of strength than hot testing.

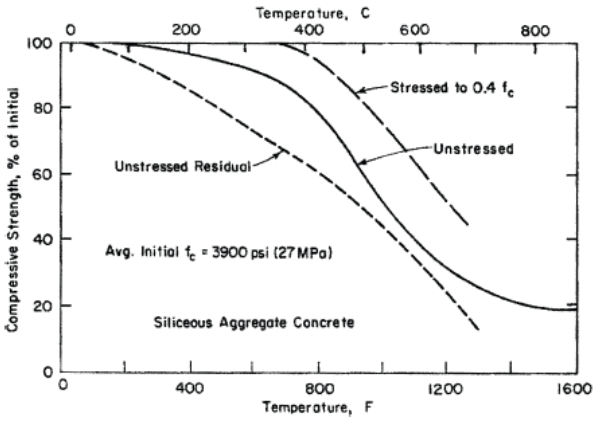

Fig. 2.7 Compressive strength of siliceous aggregate concrete: ACI-216

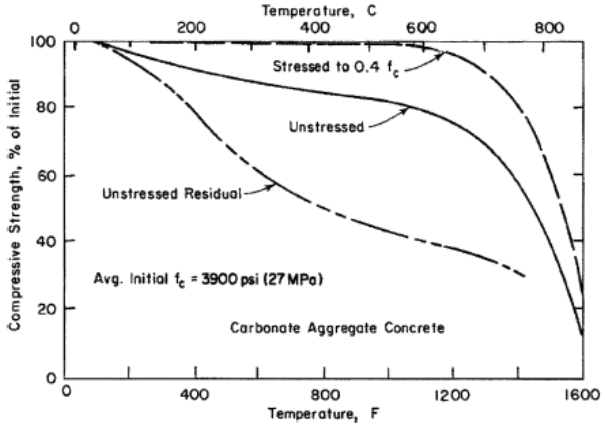

Fig. 2.8 Compressive strength of carbonate aggregate concrete: ACI-216

For nuclear power plants under service condition, some parts of reinforced concrete structures are exposed to constant elevated temperatures of not more than 100 °C. Therefore, it is important to compare the ACI provisions on degradation of concrete strength in the low temperature ranges for various loading and heating conditions and with different aggregates.

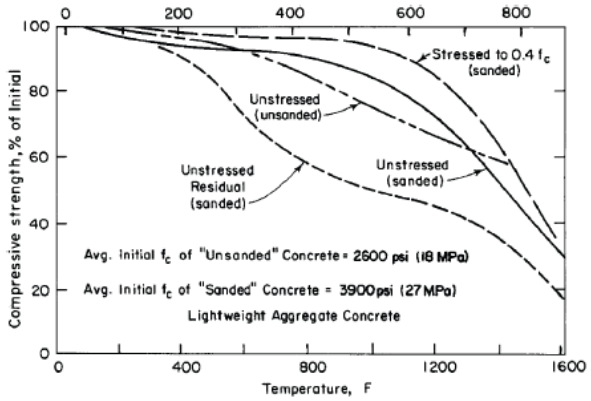

Fig. 2.9 Compressive strength of semi-lightweight concrete: ACI 216

From Figures 2.7, 2.8, and 2.9 it is clear that ACI-216 provisions do not call for degradation of the temperature dependent strength properties when prestressing and hot test conditions (stressed to $0.4 f_c^{'}$) are considered for all three types of aggregates. Whereas the hot strength of siliceous concrete (Figure 2.7) does not decrease up to 200°F = 93°C, the residual strength (unstressed residual cold testing) exhibits less than 5% degradation below the reference unloaded concrete compression strength. Interestingly enough, both hot and residual carbonate aggregate concretes (Figure 2.8) exhibit higher degradation properties than siliceous aggregate concrete up to 200°F = 93°C. However the reduction relative to the reference unloaded concrete compressive strength is still less than about 5%. The main difference between siliceous and carbonate aggregate concrete appears at higher temperatures. For the semi-lightweight concrete, the degradation of the concrete under hot test conditions started at about 100 °C, but the degradation is not significant up to 500 °C. It should be pointed out that caution must be used in the practice, because the properties of lightweight concrete really depend on the type of lightweight aggregate used in the concrete.

2.2.3 The temperature to start the reduction of compressive strength

It has been established that compressive strength of concrete decreases with increasing temperature. However, determination of the temperature at which the reduction of strength should start is not an easy task. This is mainly because test data do not show the simple monotonic decreasing trend for concrete strength as shown in ACI 216, instead, many test data showed that the strength of concrete decreases first, and regains or even exceeds the original strength in the temperature range of 100 to 200 °C, and then decreases with further temperature increase. This phenomenon may be described as a first down, then up, and further down trend (or simply the down-up-down trend) in compressive strength of concrete under high temperatures. There are some explanations on the physical mechanisms responsible for the down-up-down trend, although there is no widely accepted theory validated by systematic experimental studies. The current design codes did not consider such a variation in strength of concrete under high temperature.

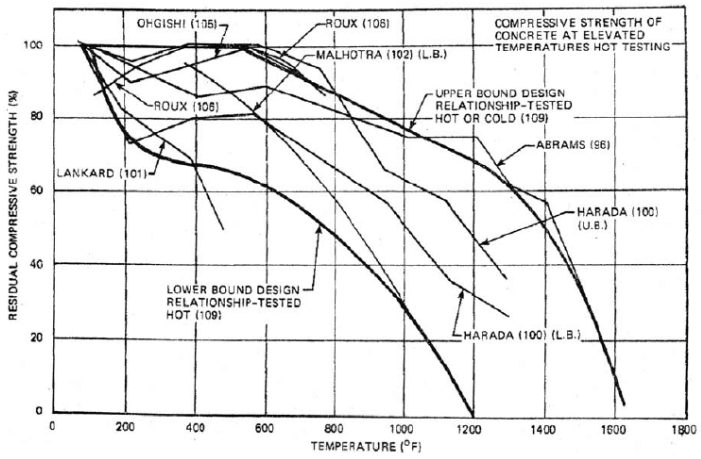

Fig. 2.10 Temperature sensitivity of compressive strength when tested hot (unsealed-unstressed), Freskakis et al. (1979)

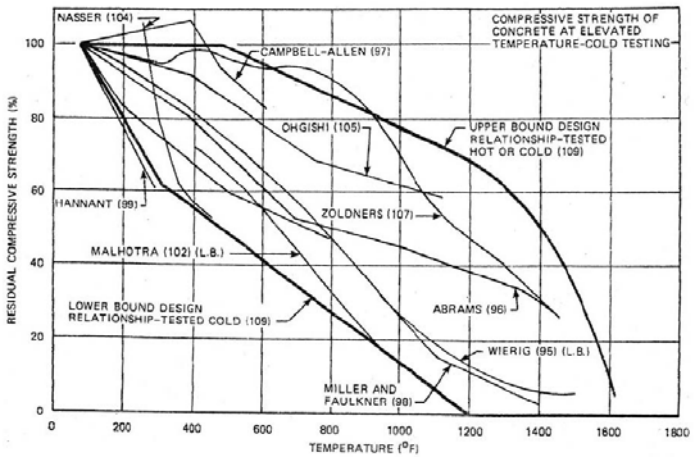

Fig. 2.11 Temperature sensitivity of compressive strength when tested cold (unsealed-unstressed), Freskakis et al. (1979)

Freskakis et al. (1979) as illustrated in Figures 2.10 and 2.11 summarizes early test data from different researchers. They show large scatter of hot and cold (residual test) experiments which resulted from a number of different mix designs and testing conditions. One can see from the figures that some of the curves showed the variation of compressive strength in the low temperature range (the down-up-down trend). One should keep in mind that the tests were performed under unsealed and unstressed conditions, whereas testing of sealed specimens would further reduce the strength values because of internal pore pressures generated by high temperatures.

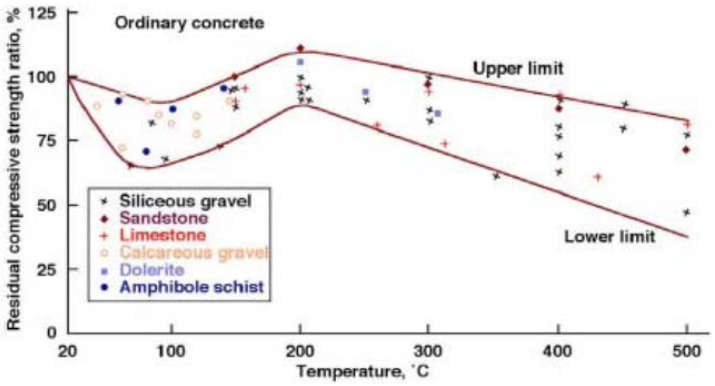

Fig. 2.12 Effect of aggregate on concrete strength materials exposed to high temperatures, Blundell et al (1976)

Blundell, Diamond and Browne (1976) published the early test data (see Figure 2.12), which illustrates more clearly the down-up-down trend of concrete strength in the range of T = 50 ~ 200°C. The compression strength of concrete drops, regains and even exceeds at 200°C the reference strength at room temperature depending on the aggregate and moisture condition. Whereas these variations depend strongly on the aggregate type, they disappear at temperature exposures above 200°C when the strength decreases progressively as expected in oven-dry concrete materials.

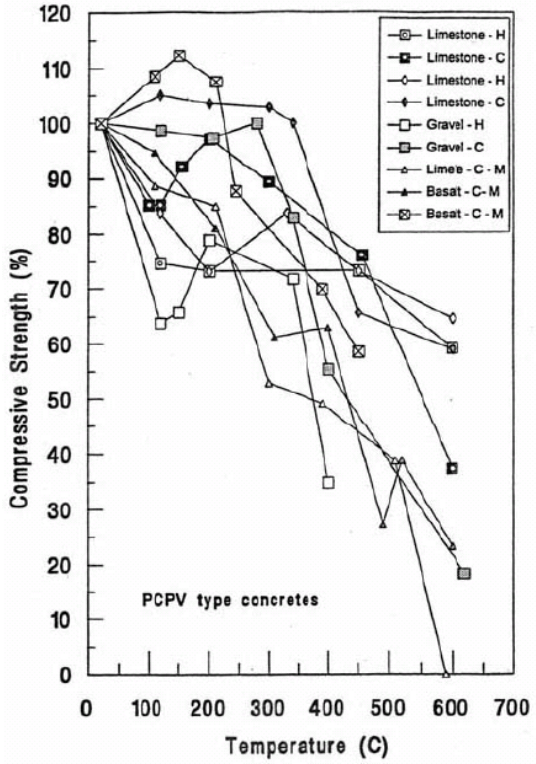

Figure 2.13 Unsealed PCPV concrete specimens tested hot (H) and cold (C), Khoury (1976)

Similar observations to the early test data (Blundell, Diamond and Browne 1976) were made by Khoury (1976) which are reproduced in Figure 2.13. The data demonstrate the strong influence of aggregate type on the temperature sensitivity of strength of pressure vessel concrete when tested hot (H) and cold (C).

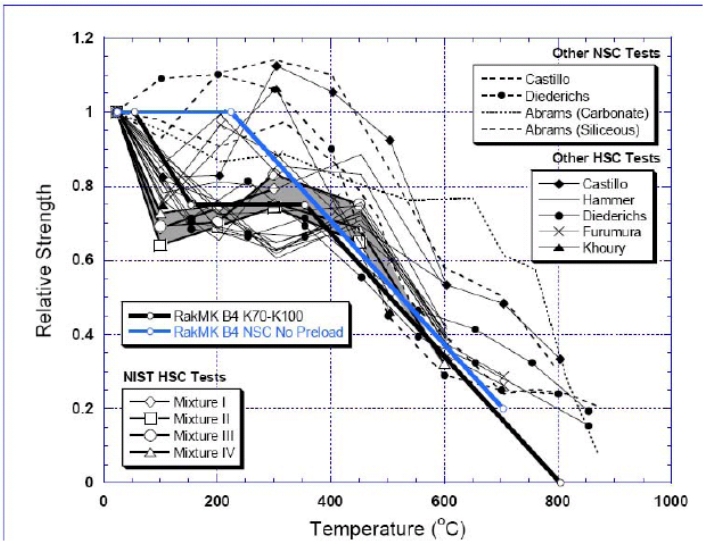

Figure 2.14 Unstressed High Temperature Data of NSC vs HSC, Phan and Carino (2003)

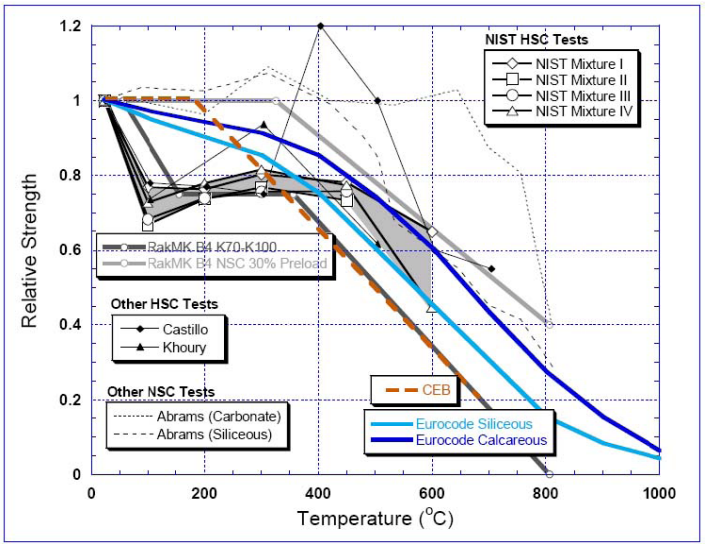

Figure 2.15 Stressed High Temperature Data of NSC vs HSC, Phan and Carino (2003)

Evaluating temperature effects on HPC, Phan and Carino (2003) presented NIST data of a broad experimental program using hot testing with and without preloading. They compared the test results of different HPC mix designs with related design rules. Figures 2.14 and 2.15 compare NSC and HSC test data with the predictions of the Finnish Design Code RakMK B4 which was at that time the only fire code separating temperature limits for HSC and NSC. Whereas there is no degradation of the compressive strength beyond 200˚C in the case of normal strength concrete, both Figures 2.14 and 2.15 illustrate the early reduction of compressive strength of the high strength concrete data at 100˚C down to 72% of the reference strength at room temperature.

On code specifications for the starting temperature for strength reduction, ACI 216 was based on Abrams (1971) test data, and the strength reduction started from very low temperature range depending on loading conditions and aggregate types, as shown in Figures. 2.7, 2.8, and 2.9. Reviewing the provisions for temperature dependent strength values in ASCE Manual No 78 (1992) and Eurocode EN 1992-1-2 (2004) we note that the temperature dependent compressive strength is not reduced for temperatures T≤ 100°C, i.e. $f_{c\,T}^{'}/f_{c}^{'} = 1$. In contrast to normal strength concrete this temperature reduction factor diminishes to $.f_{c\,T}^{'}/f_{c}^{'} = 0{:}75$ for high strength concrete which was discussed by Phan and Carino (2003), and was further examined very recently by Kodur et al. (2008) in the context of fire resistance of high strength concrete.

A very recent study of high temperature compression data was presented by Kodur et al. (2008). Figures 2.16 and 2.17 compare test data on NSC and HSC tested under hot conditions with the predictions of Eurocode EC2 for siliceous and carbonate concretes. Whereas there is no degradation of the compressive strength up 200˚F in the case of normal strength concrete, Fig. 2.17 illustrates the early reduction of compressive strength down to 75% when high strength concrete is tested at 200˚F.

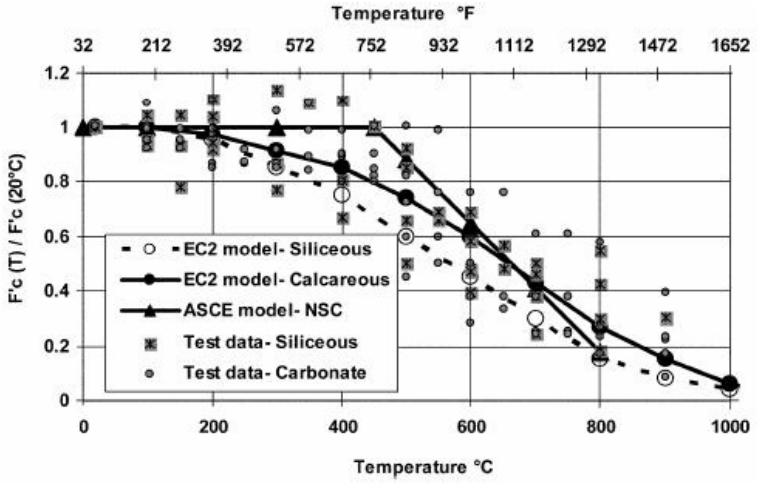

Fig. 2.16 High Temperature Models for NSC Concrete, Kodur et al. (2008)

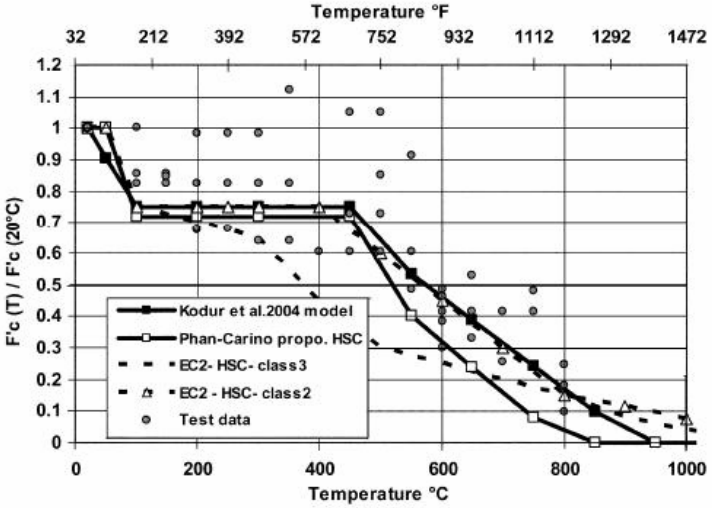

Fig. 2.17 High Temperature Models for HSC Concrete, Kodur et al. (2008)

2.2.4 The effect of pre-loading on strength of concrete under high temperatures

Preloading during heating has positive effects on both compressive strength and modulus elasticity of concrete. Figure 2.18 demonstrates the positive effects (measured in the 'hot' state for unsealed CRT HITECO ultra-high performance concrete). Comparison of Figure 2.18 (a) and (b) shows that the compressive strength and modulus of elasticity of the specimen under sustained loading is larger than those of specimens without the sustained loading. This aspect can be explained from the fact that compressive preloading inhibits crack development - although this explanation has not been fully validated.

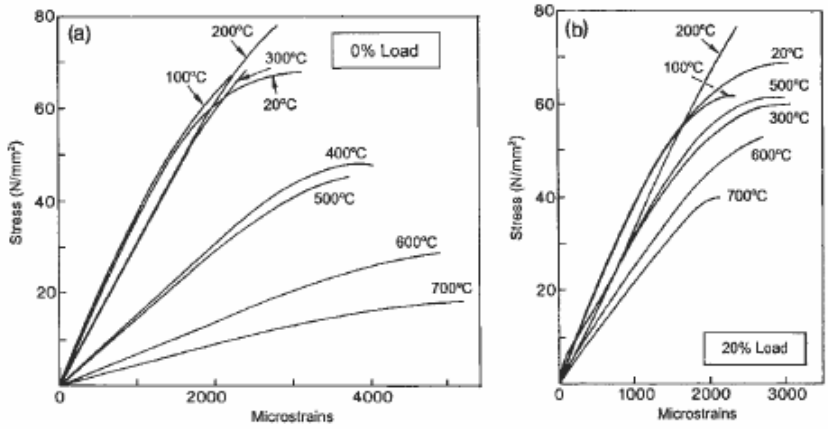

(a) For 0% load (b) For 20% load

Fig. 2.18 The effects of loading and temperature during heating in uniaxial compression of unsealed concrete specimens (Khoury, 2002)

Figure 2.19 (Khoury 2002) shows the positive effect of temperature upon the residual (after cooling) compressive strength and the elastic modulus of unsealed C70 HITECO concrete containing thermally stable Gabbro Finnish aggregate. The specimens were heat cycled at 2˚C/min under 0 percent and 20 percent of preload in compression, respectively. The results are shown in terms of percentage of strength and elastic modulus prior to heating. The figure shows the down-up-down trend of compressive strength as well as the increase of compressive strength with 20% preloading. It also shows the enhancement of stiffness with the 20% preloading.

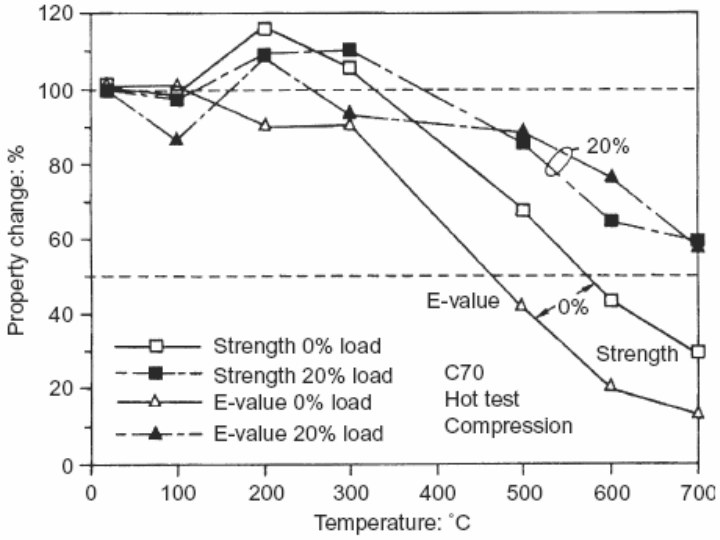

Figure 2.19 Effect of temperature upon the residual (after cooling) compressive strength and elastic modulus of unsealed C70 HITECO Concrete -20 percent load: expressed as a percentage of strength prior to heating (Khoury, 2002)

2.2.5 Prediction of concrete strength under high temperatures

In addition to the code specifications for the reduction of concrete strength under high temperatures, there are several models for prediction of compressive strength of concrete. These models were developed mainly for numerical analysis of thermal responses of concrete structures under high temperatures. The prediction models for complete stress-strain curves of concrete under high temperatures will be discussed later. The parabolic expression of unstressed and residual compressive strength by Bicanic (2004) leads to the strength model below:

$$\frac{f_c^T}{f_c^0} = 1 - 0.016\theta^2, \qquad \theta = \frac{T - T_0}{100}, \qquad 0 \le \theta \le 7.9 \tag{2.1}$$

where f_c^0 is the reference compressive strength at room temperature and the degradation of unstressed and residual compressive strength increases with temperature as shown in Figure 2.20.

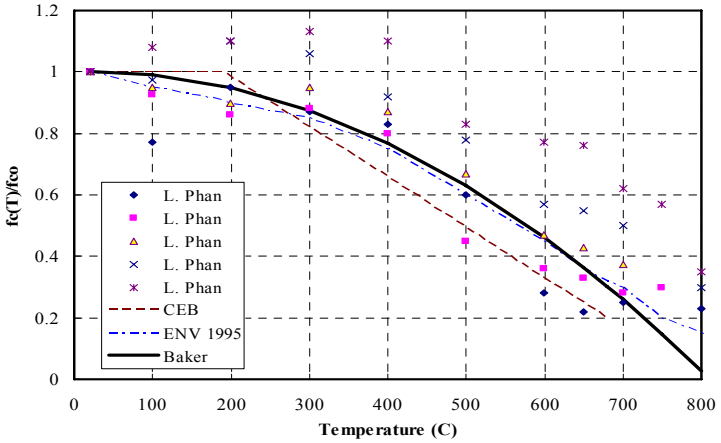

Fig. 2.20 Normalized unstressed residual compressive strength

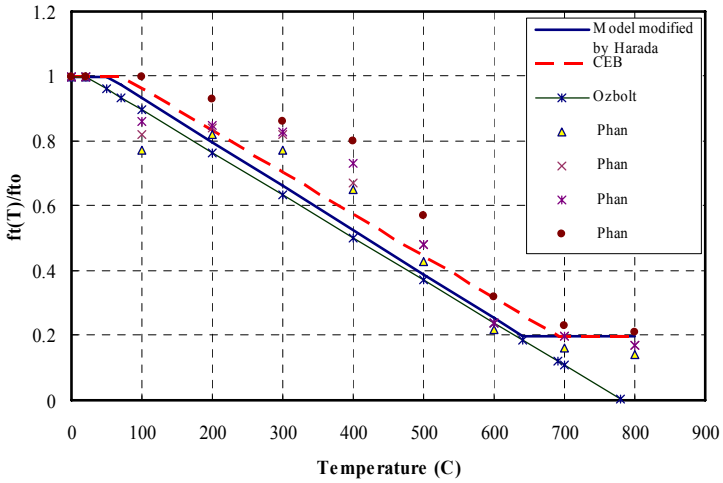

Fig. 2.21 Normalized tensile strength of concrete vs. temperature

The compressive strength-temperature relationship was compared by Phan (1996) with different test data to validate the temperature-dependence of the compressive cylinder strength of NSC. In the uniaxial compression tests, stress free test specimens were first heated up to the target temperature and subsequently loaded mechanically at constant temperature (isothermal hot experiments). The concrete used in the five test programs had a maximum compressive strength f_c^0<50MPa. For comparison the design curve of ENV 1992-1-2 is included in the figure for concrete made of siliceous aggregate.

There are not many test data available for tensile strength of concrete under high temperatures. Based on available test data, a tensile strength model was developed by Harada (Phan, 1996), which is shown in Figure 2.21. It is a linear decrease for the concrete tensile strength with increasing temperature. The rate of heating was assumed to have negligible effect on the reduction of tensile strength at high temperatures.

$$\frac{f_t^T}{f_t^o} = 1, \quad 20^oC < T < 50^oC \tag{2.2}$$

$$\frac{f_t^T}{f_t^o} = 1 - 0.1356\theta, \qquad 0 \le \theta \le 6.4 \tag{2.3}$$

$$\frac{f_t^T}{f_t^o} = 0.2 \quad 640^oC < T < 800^oC \tag{2.4}$$

in which f_t^0 is the reference tensile strength of concrete. f_t^0 can be taken as $f_t^{'}$, which is the tensile strength of concrete at room temperature, $f_t^{'} = 7.5\sqrt{f_c^{'}}$ with $f_c^{'}$ in psi (ACI 318-02).

2.3 Stiffness of concrete under high temperatures

2.3.1 Experimental results on stiffness of concrete under high temperatures

Similar to compressive strength of concrete, stiffness of concrete also decreases with increasing temperature. Castillo and Durani (1990) conducted tests to determine modulu of elasticity of HSC and NSC under hot condition where the modulu decreased by 5 to 10 percent in the temperature range of 100˚C to 300˚C (Figure 2.22). Beyond 300˚C, the elastic modulus decreased at a faster rate with increase in temperature. At 800˚C, the elastic modulu were only 20 to 25 percent of the value at room temperature.

Morita et al. (1992) observed that high strength concrete have higher rate of reduction in modulus of elasticity than normal strength concrete after being exposed to temperatures up to 500˚C where the specimens of 100 mm×200 mm cylinders were tested under unstressed residual conditions (Figure 2.23 (a) and (b)). Noumowe et al (1996) conducted residual modulus of elasticity of NSC and HSC where the modulus remained approximately 10 percent to 25 percent higher than those of NSC for entire temperature range (Figure 2.23(c)). Furumura et al. (1995) performed unstressed residual modulus of elasticity tests using three compressive strength levels.

He observed the modulus of elasticity, in general, decreased gradually with increase of temperature. Figure 2.23(d) shows the test results.

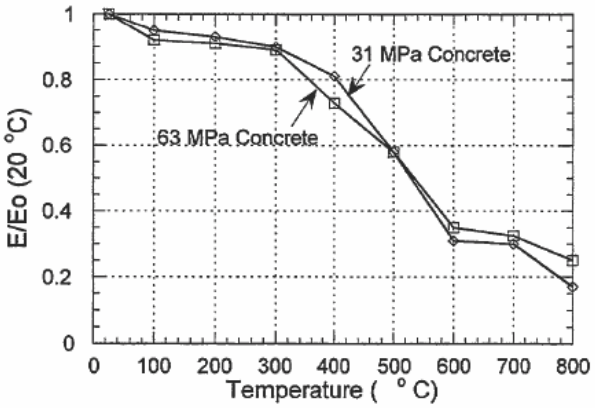

Fig. 2.22 Modulus of Elasticity under hot conditions by Castillo and Durani (1990)

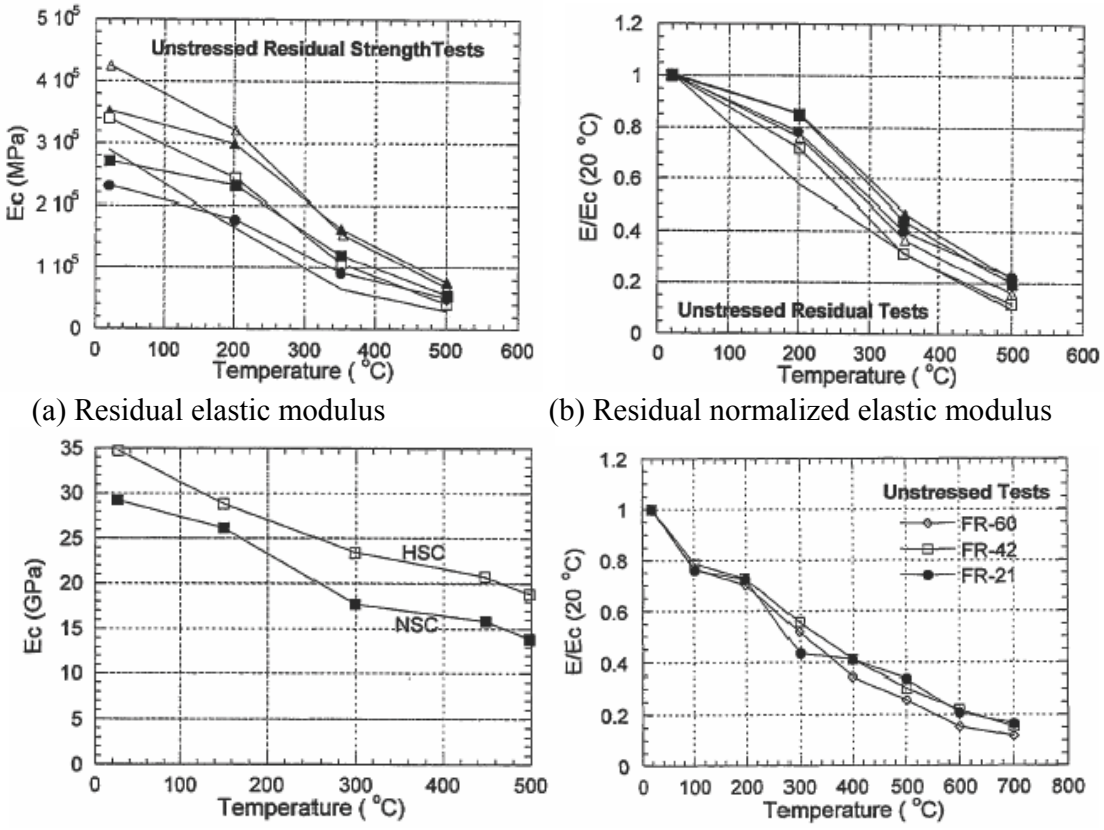

(a) Residual elastic modulus

(b) Residual normalized elastic modulus

(c) Residual elastic moduli for HSC and NSC

(d) Normalized elastic Modulus of HSC and NSC

Fig. 2.23 Hot isothermal test results obtained by (a), (b) Morita et al.,1992 and (c) Noumowe et al., 1996, and (d) Furumura et al., 1995.

Figure 2.24 shows the effect of cooling methods on modulus of elasticity of concrete. The slow cooling means cooling the specimens in a chamber at the rate of 1°C/min. from the targeted

temperatures down to room temperature; the natural cooling means cooling the specimens under room temperature; and the fast cooling stands for cooling of specimens in a water tank. Test data showed that the water cooling (fast cooling) resulted in the largest reduction in the stiffness of concrete. This is due to the fact that there is a steep thermal gradient in the concrete during the fast cooling which causes more damage than the natural and slow cooling methods.

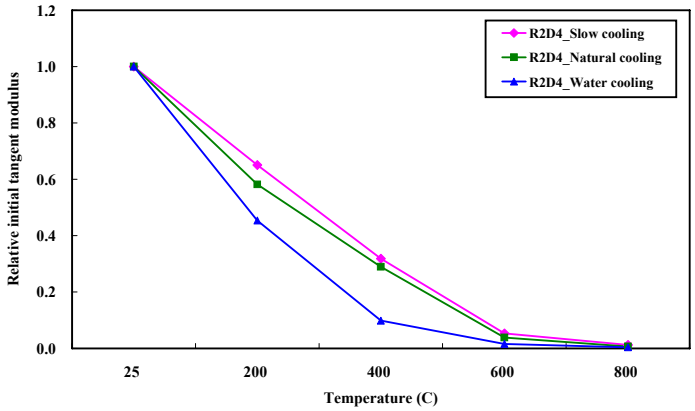

Fig. 2.24 The effect of cooling methods on modulus of elasticity of concrete (Lee et al. 2008)

2.3.2 Prediction of stiffness of concrete under high temperatures

The degradation of the temperature dependent modulus of elasticity under unloaded condition is expressed in terms of a parabolic expression by Bicanic (2004):

$$\frac{E(T)}{E_o} = (1 - 0.1\theta)^2, \quad 0 \le \theta \le 10 \tag{2.5}$$

$$\theta = \frac{T - T_o}{100}$$

in which E_0 and T_0 are reference values for the modulus of elasticity and temperature. The reference value for modulus of elasticity of concrete at room temperature can be calculated using the formula in ACI 318.

$$E_0 = 33\,\gamma_c^{1.5}\sqrt{f_c'} \tag{2.6}$$

in which E_0 is in psi; γ_c is the unit weight of concrete in lb/ft^3 (140 – 150 lb/ft^3 for normal strength concrete); and f_c' is the compressive strength of concrete in psi. Figure 2.25 illustrates the test data by Phan (1996) for the validation of temperature-dependent modulus of elasticity.

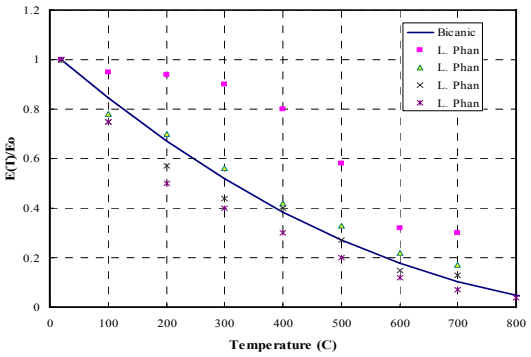

Fig. 2.25 Normalized Young's modulus (hot and unstressed condition)

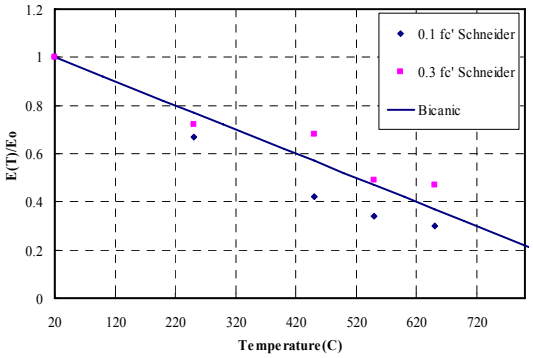

Fig. 2.26 Normalized Young's modulus vs. temperature (stressed condition)

Aggregate type and the amount of preloading (stressed test data) have a strong influence on the modulus of elasticity. Lightweight aggregate concrete exhibits a smaller reduction of the modulus of elasticity than normal strength concrete. In the case of stressed experiments, Figure 2.26 shows that the temperature dependent modulus of elasticity with 30% preloading of concrete strength exhibits linear rather than parabolic degradation with increasing temperature. The linear model in Figure 2.3.4 is expressed as

$$\frac{E(T)}{E_0} = 1 - 0.1\theta, \qquad 0 \le \theta \le 10 \tag{2.7}$$

Most recently, Lee et al. (2009a) developed a multiscale model for predicting the stiffness of concrete under high temperatures. The model takes into account the phase transformations of the constituents in cement paste under various temperature ranges, and the model uses composite mechanics method to calculates the effective modulus of elasticity of concrete including the contributions of all constituent phases.

2.4 Stress-strain relations of concrete under high temperatures

2.4.1 Experimental results on stress-strain relations of concrete under high temperatures

The load-deformation plots for HSC and NSC are shown in Figure 2.27(a) and (b) (Castillo and Durani, 1990). NSC specimens did exhibit ductile failure except for 200˚C. Between 300˚C and 800˚C, the NSC specimens were able to undergo large post-peak strains while the decrease in strength was more gradual. HSC showed brittle failure up to 300˚C, and with further increasing temperature, the HSC specimens began to exhibit a more ductile failure. Furumura (Furumura et al., 1995) obtained stress-strain curves for concretes with different strengths, as shown in Figure 2.28(a) and (b). HSC exhibited steeper slopes than the NSC at temperature up to 300˚C to 400˚C in the unstressed test.

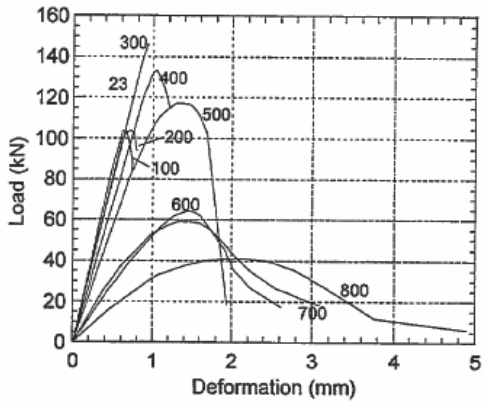

(a) Load-deformation of HST

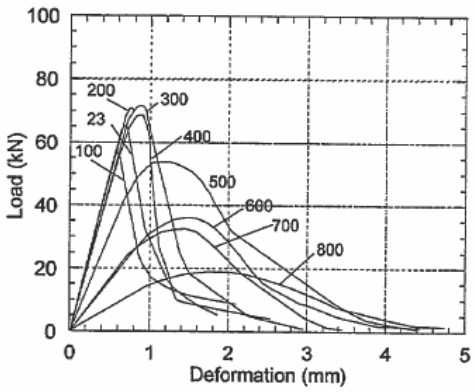

(b) Load-deformation of NSC

Fig. 2.27 Hot isothermal test results obtained by Castillo and Durani (1990)

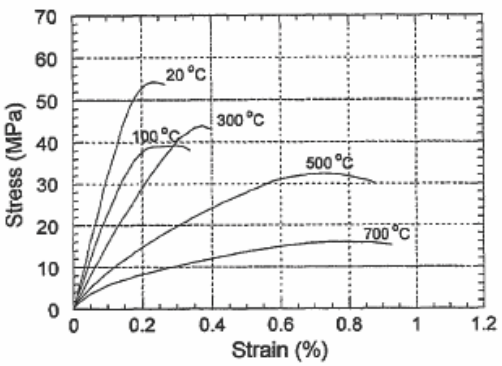

(a) Stress-strain curves (FR-42)

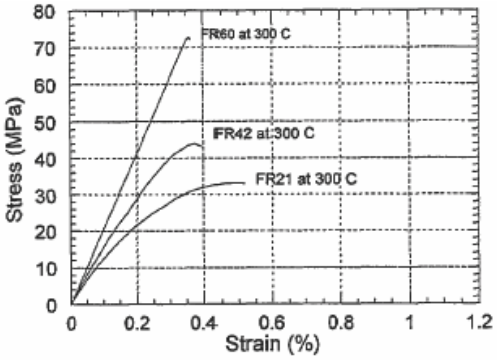

(b) Stress-strain curves at 300˚C

Fig. 2.28 Hot isothermal test results obtained by Furumura et al. (1995)

Figure 2.29 show the effect of cooling methods on stress-strain curve of concrete (Lee et al. 2008). Comparing the test data of normal cooling and fast (water) cooling, one can clearly see that both the peak stress (the strength) and the initial slope (the stiffness) of the curves of fast cooling method are lower than those obtained by normal cooling. Therefore, it can be concluded that fast cooling has adverse effect on both strength and stiffness of the concrete.

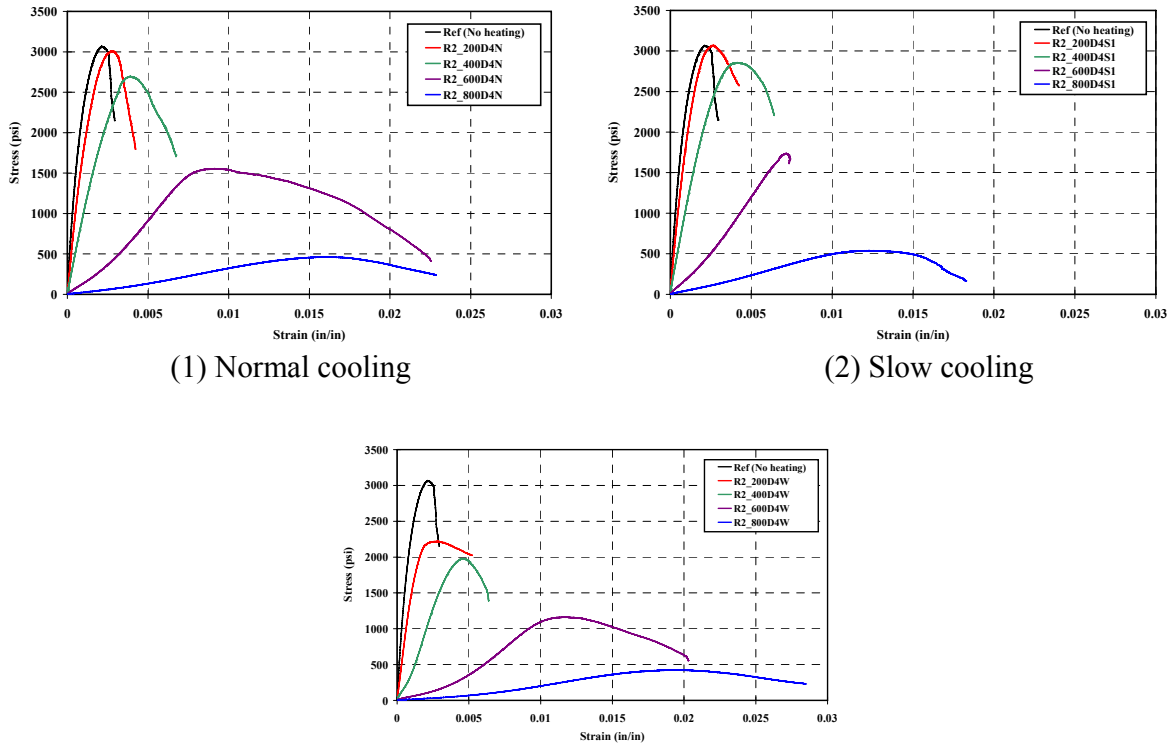

(1) Normal cooling

(2) Slow cooling

(3) Fast (water) cooling

Fig. 2.29 Stress-strain curves of concrete specimens by (1) normal cooling, (2) slow cooling, and (3) fast (water) cooling after heating to 200, 400, 600, and 800 ˚C (Lee et al. 2008).

2.4.2 Prediction of stress-strain relations of concrete under high temperatures

As shown in Figure 2.30 stress-strain relationships of siliceous aggregate concrete at different temperatures were specified in Eurocode (ENV 1992-1-2,1995) illustrating the gradual decrease of strength and stiffness on one hand, and the concomitant increase of ductility at the other hand when elevated temperatures are considered.

Freskakis (1984) examined the behavior of a reinforced concrete section where both the temperature-dependent material properties were used for concrete and steel. Stress-strain relationships for the concrete based on the lower and upper bound relations are presented in Figure 2.31.

The most recent review on stress-strain relations of concrete under high temperatures was by Kodur et al. (2008), in which a table was included in the appendix listing various equations for stress-strain relations of concrete with application for high temperatures. This table is listed in Section 2.9 as Table 2.5.

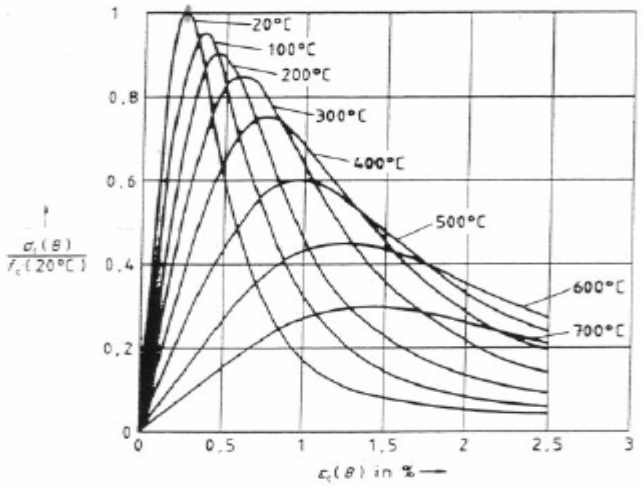

Fig. 2.30 Stress-strain relationships of concrete made of siliceous aggregate at different temperatures, Eurocode (ENV 1992-1-2,1995)

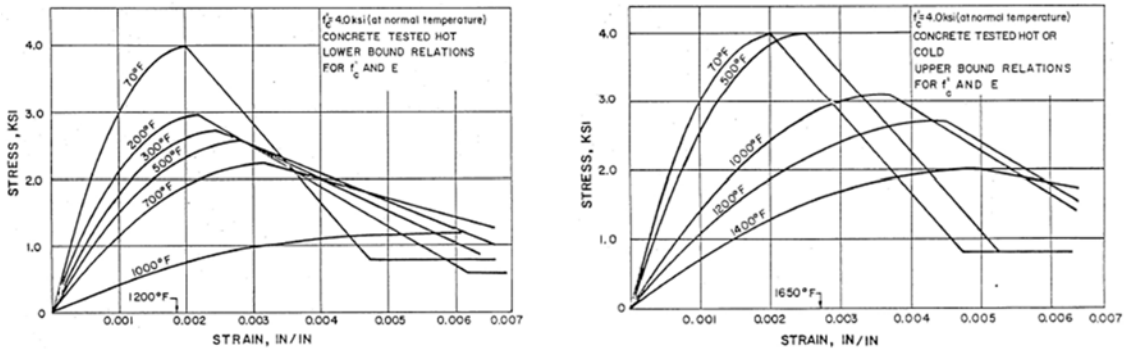

(a) Lower bound (b) Upper bound

Fig. 2.31 Stress-strain relationship for concrete (Freskakis, 1984)

2.5 Thermal expansion of concrete under high temperatures

Free thermal strain of concrete is defined as the strain of concrete induced by heating without loading and drying. Free thermal expansion of concrete is usually measured under a saturated state to avoid the drying effect. In a typical test for thermal expansion of concrete, a concrete specimen is submerged in a water tank and the change in the length of the specimen is measured while the water temperature rises to a target level (see AASHTO TP60-00). Under this special condition, both cement paste and aggregate expand with increasing temperature. However, this is not a valid testing method when the environmental temperature is higher than 100 °C since water starts to evaporate and cannot be used as the testing media. Furthermore, it is not the actual situation for a real concrete structure under service condition or under an accidental condition, where both heating and drying take place at the same time and thus the coupling effect must be taken into account, which will be discussed in detail in Section 2.7.

Thermal expansion of concrete is mainly affected by the type and the amount of aggregate. An average value for the coefficient of thermal expansion of concrete is about 10 millionths per degree Celsius (10 x 10^{-6}/°C or 6 x 10^{-6}/°F), although the value ranges from 6 x 10^{-6}/°C to 13 x 10^{-6}/°C. Table 2.2 shows some experimental results on the coefficient of thermal expansion of concretes made with aggregates of various types. These data were obtained from tests on small concrete specimens in which all factors were kept the same except aggregate type. In each case, the fine aggregate was made of the same material as the coarse aggregate.

Table 2.2 Effect of Aggregate type on thermal Expansion Coefficients

Aggregate type	Coefficient of thermal expansion millionths per °C
Quartz	11.9
Sandstone	11.7
Gravel	10.8
Granite	9.5
Basalt	8.6
Limestone	6.8

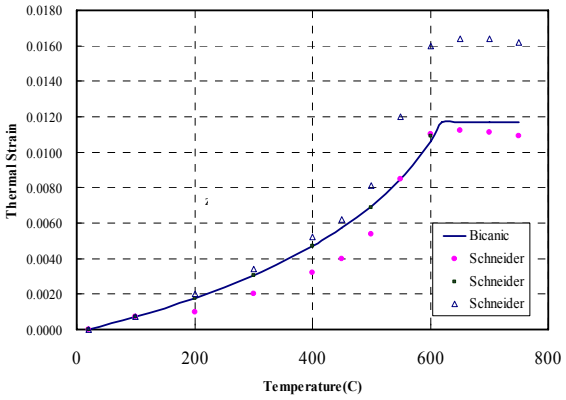

Fig. 2.32 Thermal strain of concrete vs. temperature

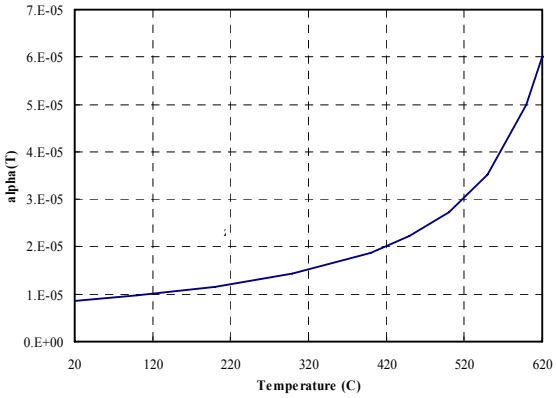

Fig. 2.33 Coefficient of thermal expansion of concrete vs. temperature

Coefficient of thermal expansion of concrete is temperature dependent and its temperature-dependent behavior is highly nonlinear. Assuming all other influential parameters remain constants except temperature, the relationship between thermal strains and temperature is shown in Figure 2.32, which was developed by Nielsen, Pearce and Bicanic (2004). The thermal strain increases with temperature up to T = 620 °C and beyond which it is assumed to remain a constant. The coefficient of thermal expansion corresponding to Figure 2.32 is a function of temperature as illustrated in Figure 2.33. One can see from Figure 2.33 that under low temperature range (e.g. from 20 – 120 °C), the variation of α (coefficient of thermal expansion) is not large, and thus α can be considered as a constant under room temperature.

The expressions below are for the thermal strain and coefficient of thermal expansion shown in Figures 2.32 and 2.33. They consider the temperature dependence of the thermal expansion in an incremental format (thermo-hypo-elasticity):

$$\dot{\varepsilon}_{th} = \alpha(T)\dot{T} \tag{2.8}$$

$$\varepsilon_{th} = -6\times10^{-3}\ln\left[1-\frac{\theta}{7}\right] \tag{2.9}$$

$$\alpha=\frac{6\times10^{-5}}{7-\theta} \quad 0\le\theta\le6, \quad \theta=\frac{T-T_o}{100} \tag{2.10}$$

2.6 Creep and shrinkage of concrete under high temperatures

Nuclear power plants are usually designed for operation in a very long period of time. Therefore, long-term deformation of concrete materials used for nuclear power plant structures under service condition is of significant importance for design professionals and for management agencies. As mentioned earlier, the service condition of nuclear power plant structures are quite complex, which involves elevated temperatures, drying environment, and mechanical loading applied simultaneously. The long-term deformation of concrete under such a combined loading condition is also quite complicated. In this section, we will discuss the response of concrete to each of the individual loading first, and then discuss the coupling effect among the combined loadings.

2.6.1 Creep of concrete under room temperature

Long-term deformation of concrete under loading without drying and heating/cooling can be described by creep and/or relaxation. Creep of concrete is defined as long-term strain of concrete under a constant stress without the effect of drying shrinkage and thermal expansion. It is also called basic creep. Relaxation is defined as long-term variation of stress under a constant strain without drying and heating/cooling. The effect of drying will be discussed in detail later. Creep and relaxation are caused by the same deformation mechanisms in the concrete. The primary mechanism is considered as the activation energy in cement paste. Long-term applied stress overcomes the activation energy limit of the material and triggers breaking of the bond in cement paste and leads to long-term deformation (Bazant and Kaplan 1996). Other creep mechanisms were reviewed in detail by Jennings and Xi (1992). Relaxation test under a constant level of strain is much more difficult to perform than a creep test under a constant level of stress. As a result, creep test data and creep models for concrete are widely available in the literature, while relaxation test data and models for concrete are rarely seen. Under room temperature, the creep strain of concrete can be expressed as

$$\varepsilon(t',t) = J(t',t)\sigma(t') = \frac{\left(1+\phi(t',t)\right)}{E_0}\sigma(t') \tag{2.11}$$

where $\varepsilon(t',t)$ is the total strain at time t due to a constant stress $\sigma(t')$ applied at time t', J(t', t) is creep compliance at time t, whereas t' is age of the concrete at loading, E_0 is the reference

Young's modulus, and $\phi(t',t)$ is called creep coefficient. The physical meaning of the compliance function is the long-term strain of concrete under unit stress, $J(t', t) = \varepsilon(t,t')/\sigma(t')$. In experimental studies, the ratio ε/σ is also called specific creep. The creep coefficient $\phi(t',t)$ ranges from 3 to 5 according to ACI 209. It means that the ultimate creep strain (the creep strain at infinitely long time) is 3 to 5 times of the instantaneous elastic strain.

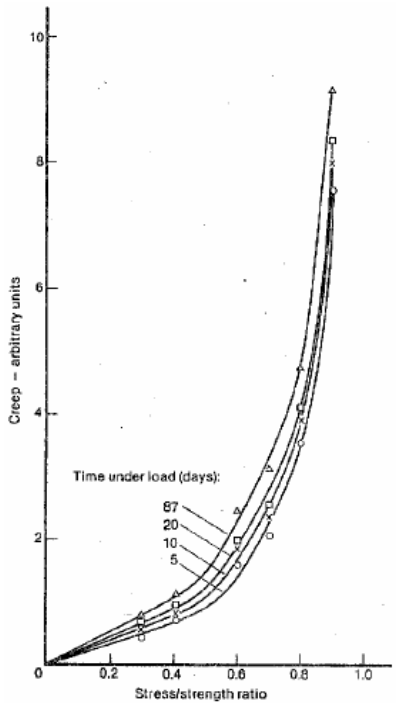

Fig. 2.34 The effect of stress/strength ratio on creep of concrete (Gvozdev 1966)

At low stress levels, the compliance function and the specific creep do not depend on the applied stress level. From Eq. (2.11), it means that the creep of concrete is proportional to the applied stress, and the creep compliance is stress independent. This is shown in Figure 2.34 when stress/strength ratio σ/f_c' is below 0.5 (Gvozdev 1966, also see Neville 1983, Fig. 5.2). Therefore, a creep compliance obtained under a certain stress level can be used for estimating creep of any other stress level, which is very convenient for practical application. In this case, conventional linear viscoelastic models can be used to characterize the creep of concrete. At high stress levels, however, the compliance function and the specific creep become stress dependent. In Figure 2.34, the creep strains do not vary proportionally with the stress/strength ratio. Therefore, a compliance function obtained at a lower stress level cannot be used to characterize the creep at higher stress level. More importantly, the compliance function may become excessively high with increasing time, which may lead to creep rupture at the material level and creep collapse due to excessive creep deformations at the structure level. In this case, conventional linear viscoelastic models cannot be used to characterize the creep of concrete. In Figure 2.34, starting from stress/strength ratio of 0.5, the creep strain increases not in proportion with the stress/strength ratio, which indicates a possible change of deformation mechanism for concrete creep.

Basically, there is a stress limit for "linear" concrete creep. Above the limit, the compliance function is stress dependent, and an excessive long-term creep may occur. In structural design, we want to keep the compliance function stress independent and avoid excessive long-term deformation. That is one of the reasons why the applied stress level is limited to $0.45f_c'$ for prestressed concrete structures according to the ACI 318-05 provision 18.4.2.

2.6.2 Experimental results for creep of concrete under high temperatures

When temperature increases, there are two possible scenarios in the concrete in terms of long-term deformation. The first one is the acceleration of creep, and the compliance function becomes temperature dependent, $J(t', t, T)$. In this case, creep deformations are accelerated by the elevated temperature, or the creep deformation at the reference temperature takes place in a shorter time at an elevated temperature, and there is no change in the underlying creep mechanisms in the material. In terms of activation energy, the elevated temperature accelerates the process of bond breaking and deformation process. This usually happens when the elevated temperature is not very high. In this case, the creep compliance obtained under room temperature can be extended into high temperature range but an accelerated time scale must be used, which can be modeled by the Arrhenius equation (Bazant and Kaplan 1996). The second possible scenario is that the creep mechanism of concrete is changed under the elevated temperature, and the compliance function may become temperature dependent as well as stress dependent. The stress limit for the room temperature is usually reduced under high temperature, which means that excessive creep may occur at a lower stress level. This usually happens at very high temperature. In this case, the compliance obtained under room temperature is not valid under the high temperature. Arrhenius equation is not valid for the acceleration of creep. For both cases, temperature limits must be established in order to avoid excessive creep deformation.

ACI 209 reports (1992, 1997) and Neville (1983) summarized the creep of concrete under elevated temperatures. At 50°C, creep strain is approximately two to three times as great as at 19-24°C. From 50-100°C, creep strain continues to increase with temperature, reaching four to six times that experienced at room temperature. Nasser and Neville (1965) found that the rate of creep at 70 °C increases up to 3.5 times higher than at 23 °C. Figure 2.35 is the creep test data obtained by Arthananari and Yu (1967), in which the specific creeps at four different temperature levels can be compared, 20°C, 40°C, 60°C, and 80°C. One can see that the creep under 80°C is about two times of the creep at 20°C. In this temperature range, there may be no change in the fundamental creep mechanisms. The creep strain is simply accelerated by the elevated temperatures.

Under higher temperatures, however, excessive creep strain may occur indicating the change of creep mechanism. Cruz (1968) investigated the elastic and inelastic properties of concrete exposed to high temperatures up to 650°C for five hours and showed the results in Table 2.3. One can see that the creep at 480°C is about 15 times of the creep at room temperature, and the creep at 650°C is more than 30 times. Similarly, Figure 2.36 shows the creep strains measured under high temperatures by Marechal (1972), in which the creep strain under 480°C is about 15 times of the creep at room temperature. In these cases, the mechanisms of creep strains in the high temperature range are totally different from those under the room temperature. Under such high temperatures, phase transformations take place in cement paste, and cracks develop in

concrete. The measured long-term strains included various time-dependent effects and the creep mechanisms under room temperature is only one of the important deformation mechanisms.

Table 2.3 Creep and stiffness of concrete under various temperatures (Cruz 1968)

Temperature		Number of Tests	Ratio of E at elevated temperature to E at 23°C (75°F)			Ratio of creep as a multiple of creep at 23°C (75°F)
°C	°F		High	Low	Average	
23	75	21	-	-	1.0	1.0
150	300	3	0.87	0.77	0.81	3.3
425	800	4	0.57	0.54	0.56	6.4
480	900	5	0.49	0.42	0.46	14.9
650	1200	5	0.41	0.32	0.36	32.6

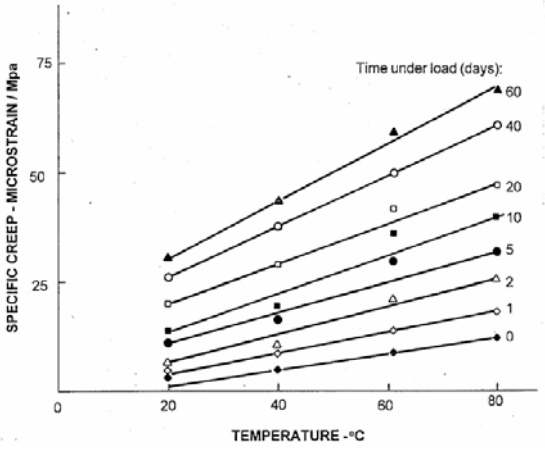

Fig.2.35 Creep test data for concrete under various temperatures (Arthananari and Yu 1967)

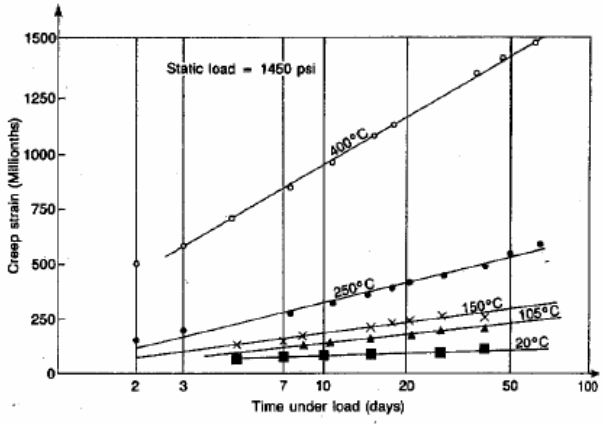

Fig. 2.36 Creep strains of concrete at various temperatures (Marechal, 1972)

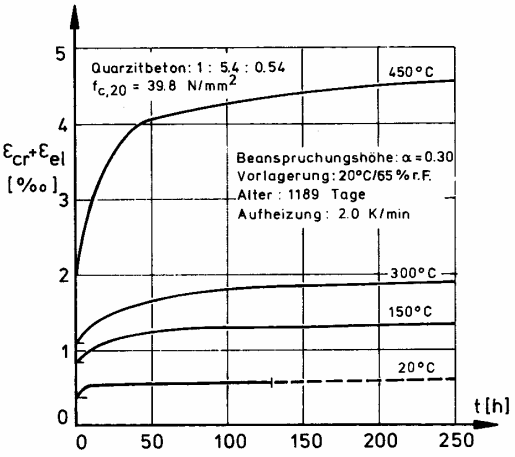

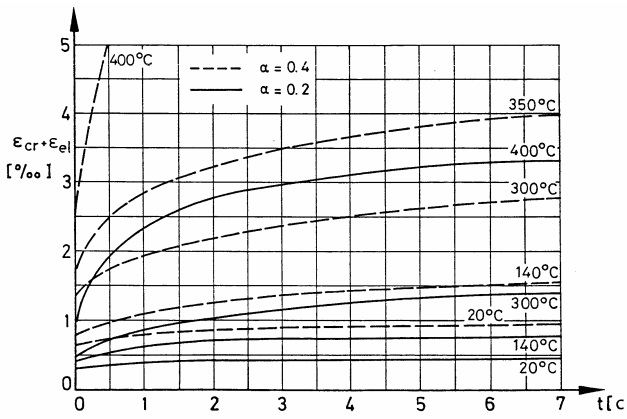

Fig. 2.37 Creep test data for unsealed concrete with quartz aggregate under various temperatures (Schneider 1979)

Fig. 2.38 Influence of loading levels on creep of concrete under various temperatures (Gross 1973)

Figure 2.37 shows the creep vs. time curves for unsealed concrete under various temperatures. Since the specimens were not sealed, there was moisture exchange between the concrete and the environment. So, measured strains were actually due to combined effect of heating, drying, and loading. The creeps under high temperatures were much higher than that under room temperature, similar to other reported test data. Figure 2.38 shows the creep vs. time curves under two different loading levels. One can see that under room temperature (20°C), the increase of loading level from 20% of compressive strength to 40% doubles the creep strain, which means the deformation mechanism may remain the same. However, when the temperature increased to 400°C, the same increase of loading level caused very large increase of creep strains, which is similar to the trend shown in Figure 2.34. The large strain from 40% loading level indicated that the deformation mechanism may be changed: some damage development in the concrete was attributed to the large strain in addition to the conventional creep mechanism of concrete under high temperatures.

2.6.3 Aging of concrete creep properties at different temperatures

Since the compliance function $J(t', t, T)$ depends on age of concrete, it is important to note that elevated temperatures have significant effect on the actual age of concrete, especially for young concrete structures. High temperature accelerates hydration reactions of cement and makes the concrete mature earlier. This effect actually reduces the creep strain of concrete. The general rule is that high temperature increases the maturity of concrete and thus reduces the creep. Therefore, the effect of high temperature on concrete creep is basically two-fold. At one hand, high temperature accelerates the creep, and on the other hand, high temperature reduces concrete creep by improving its maturity. The first effect is usually more significant than the second, and therefore, the creep of concrete under high temperature is usually higher than that under room temperature. At very high temperatures, there is another factor that must be considered, which is the dehydration of cement paste. Dehydration of C-S-H and CH start from 400 °C. Dehydration reduces the strength and stiffness of concrete, and increases the creep of concrete.

Figure 2.39 illustrates the effect of concrete age on the modulus of elasticity at 20°C and 95°C. The thermal creep tests were carried out on the Wylfa concrete for over 12.5 years (Browne and Blundell 1969, Browne and Bamforth, 1975). Whereas there is a significant increase of the elastic properties over the 12.5 year period at room temperature, there are little changes due to ageing of the instantaneous response at 95°C. This is because the concrete under 95°C was matured in a short period time (accelerated curing), and further curing does not increase the maturity and thus no effect on the stiffness of the concrete.

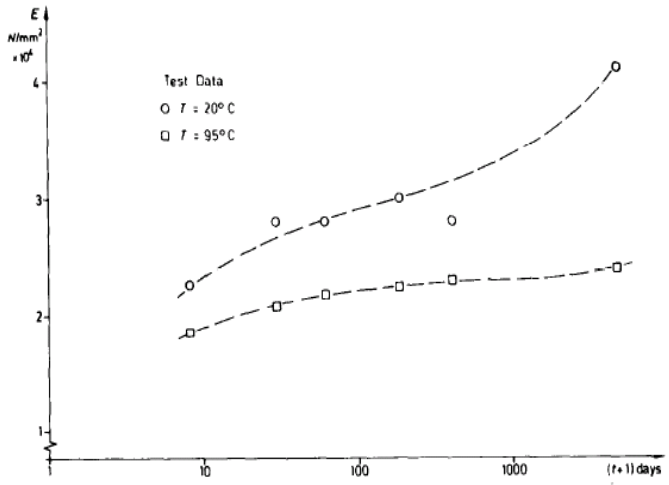

Fig. 2.39 Effect of age on the elastic properties of concrete (Browne and Bamforth 1975)

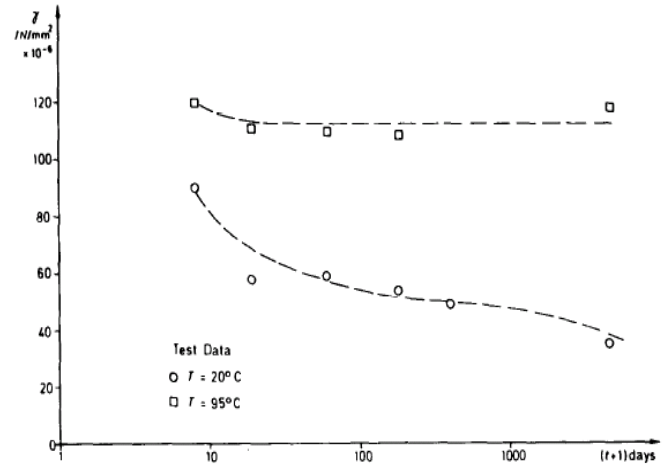

Fig. 2.40 Effect of age on thermal creep after loading for 102 days (Browne and Bamforth 1975)

In analogy, the effect of age at loading is shown in Fig. 2.40 which illustrates the creep response when the load is applied for a duration of 102 days at different loading ages. Whereas the creep deformations diminish significantly at room temperature, there is little change of the creep capacity of concrete matured at elevated temperature of 95°C. This is because, under room temperature, the longer the curing period, the higher the maturity of the concrete, and thus the lower the creep. Figure 2.41 shows the creep deformations of concrete specimens loaded for 102 days after maturing for 12.5 years at room and elevated temperatures. In this case, the aging of concrete was completed after 12.5 year of curing, and thus contributed no effect on the creeps of the concretes. The creep under 95°C is much higher than that under room temperature simply due to the acceleration effect of the elevated temperature.

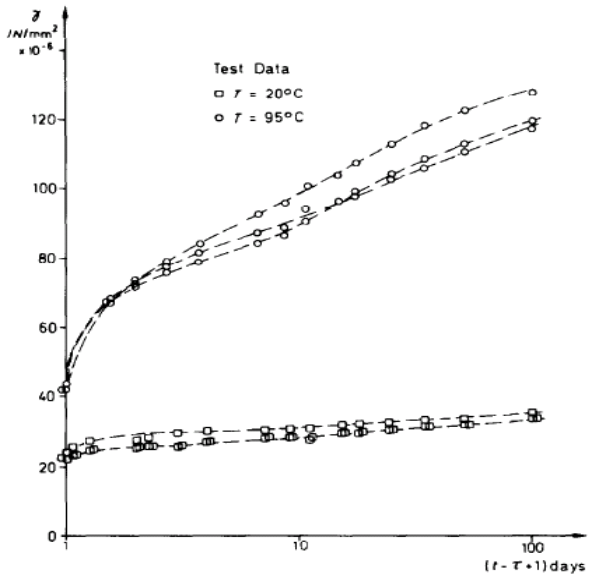

Fig. 2.41 Thermal creep for loading at the age of 12.5 years (Browne and Bamforth 1975)

2.6.4 Modeling creep of concrete under high temperatures

Creep of concrete can be described by two different types of models. The first one is empirical models or phenomenological models that are usually developed based on available test data. There are some constants in the models that need to be validated by test data. The advantage of this type of model is that a specific form of compliance function can be chosen to best fit experimental results, and therefore, it is capable of characterizing conventional creep strain as well as strains resulted from other damage mechanisms. The disadvantage is that since it is based on curve fitting of available test data, there is no confidence when it is used for predicting the strains outside of the range of available test data. The second type of creep models is rate-type models based on viscoelasticity, which are usually for numerical analysis. This type of models is very accurate for characterizing strains due solely to creep mechanism, and not sufficient when the basic deformation mechanisms are changed. The description on the rate-type of creep model is quite lengthy and thus will not be included in this report. Detailed description can be found in the book by Bazant and Kaplan (1996).

The following is an example of empirical models for concrete creep under high temperatures developed by (Schneider 1979). The creep compliance function as defined in Eq. (2.11) was selected as a specific function:

$$J(T,\sigma) = \frac{1}{E}(1+\kappa)+\frac{\Phi}{E} \tag{2.12}$$

in which κ may be chosen as 0 for elastic analysis, and the stiffness of concrete is

$$E = E_0 \cdot f(T) \cdot g(\sigma,T) \tag{2.13}$$

Function f(T) describes the decrease of E with increasing T (heated without compressive load), and function g(s,T) describes the increase of E due to external loads

$$g = 1{,}0 + \frac{\sigma(T)}{f_c(20\ ^\circ C)} \cdot (T - 20)/100 \tag{2.14}$$

The creep function Φ in Eq. (2.12) is

$$\Phi = g\phi + \frac{\sigma(T) \cdot (T - 20)}{f_c(20\,^\circ C) \cdot 100} \tag{2.15}$$

$$\phi = C_1 \tanh \gamma_\omega (T - 20) + C_2 \tanh \gamma_0 (T - T_g) + C_3 \tag{2.16}$$

$$\gamma_\omega = (0.3\,\omega + 2.2)\ 10^{-3} \tag{2.17}$$

ω = the moisture content in the concrete in % by weight. The constants in Eq. (2.16) are listed in Table 2.4.

Table 2.4 Parameters for the empirical creep model

Parameter	Dimension	Quarzite concrete	Limestone concrete	Lightweight concrete
C_1	1	2.6	2.6	2.6
C_2	1	1.4	2.4	3.0
C_3	1	1.4	2.4	3.0
γ_0	$^\circ C^{-1}$	$7.5 \cdot 10^{-3}$	$7.5 \cdot 10^{-3}$	$7.5 \cdot 10^{-3}$
T_g	°C	700	650	600

2.6.5 Shrinkage of concrete under high temperatures

Shrinkage of concrete is defined as long-term strain of concrete due to drying without loading and heating. Shrinkage tests performed under different temperatures will result in different results. Figure 2.42 shows the test data from Schneider (2002). One can see that the shrinkage of concrete at 60°C is actually higher than those at 110°C and 140°C.

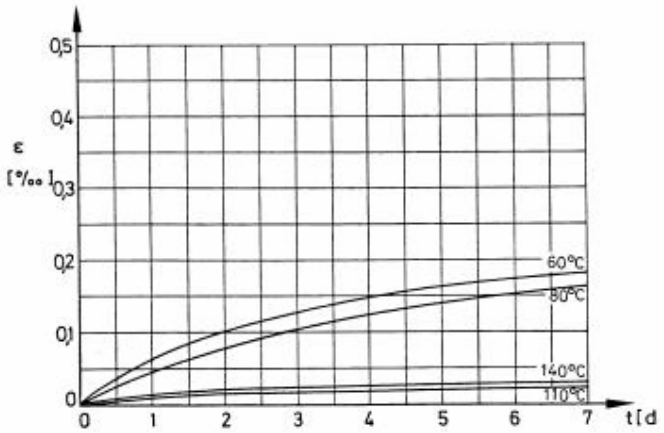

Fig 2.42 Shrinkage of concrete under different temperatures (Schneider 2002)

There are many shrinkage models for concrete under room temperature. Since the shrinkage of concrete is induced by moisture loss, therefore, most of the models are related to diffusion theory of moisture in concrete, which will not be described in this report. For the shrinkage of concrete under high temperature, however, there has been not much research. Shrinkage of concrete is coupled with creep and mechanical loading under elevated temperatures, which will be described in the next section. Some empirical values for shrinkage of concrete were suggested by Schneider (2002):

- limestone concrete: 20-100 °C; e_s = 200 to 300·10^{-6}
- limestone concrete: ~ 80 °C; e_s = 300 to 400·10^{-6}
- quartzite concrete: 20-100 °C; e_s = 200 to 450·10^{-6}
- limestone concrete: ~150 °C; e_s = 500·10^{-6}
- limestone concrete:150-350 °C; e_s = 800·10^{-6}

2.7 The coupling effects among loading, drying, and heating

2.7.1 The interactive effects among U, P, and T

As mentioned in above section, the basic creep of concrete is the long-term strain of concrete under a constant loading without drying and heating/cooling. In reality, mechanical loadings are applied together with drying and heating on concrete structures, especially in nuclear power plant structures. The effect of drying on concrete is drying shrinkage, which is defined as the long-term deformation of concrete under drying without loading and heating. Although there are extensive researches on drying shrinkage of concrete under room temperature, information on drying shrinkage of concrete under high temperature is not systematic. This is because under a fire condition, drying and heating are coupled together and are very difficult to study separately. The coupling effects among loading, drying, and heating, called thermo-hygro-mechanical coupling are very important and should be considered in determining long-term deformation of concrete under high temperatures.

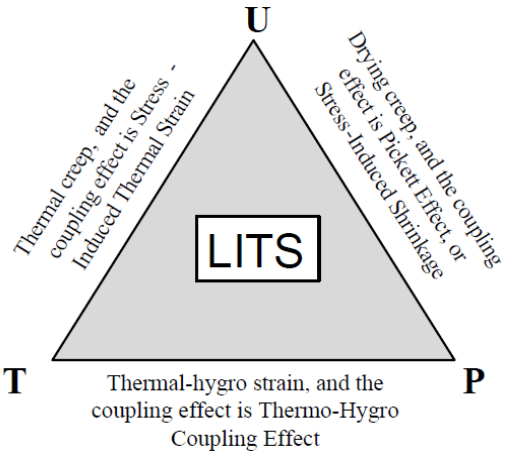

Fig. 2.43 Concrete materials exposed to hygro-thermo-mechanical loading environment.

Figure 2.43 shows the mutual interactive effects in concrete materials exposed to thermo-hygro-mechanical loading environment. In the figure, T represents high temperature; P stands for internal pore pressure in concrete, and P is often replaced by H (humidity) because H = P/Ps where Ps is the saturation vapor pressure; and U is the mechanical part of the deformations. For the effect of a single variable, the deformation of concrete under heating without drying and mechanical loading is called thermal expansion; the deformation of concrete under drying without heating and mechanical loading is drying shrinkage; and the deformation of concrete under sustained mechanical loading without drying and heating is basic creep. Under room temperature, there have been many research efforts on the coupling between any two of the three variables:

U – P (simultaneous loading and drying) – The total deformation is called drying creep.
The coupling effect is due to Pickett effect or stress-induced shrinkage.
U – T (simultaneous loading and heating) – The total deformation is called thermal creep.
The coupling effect is due to stress-induced thermal strain.
T – P (simultaneous heating and drying) – The total strain is called hygro-thermal strain.
The coupling is due to hygro-thermal interaction.

For a structure under fire or under elevated temperature service conditions (e.g. a containment structure), the total deformation of concrete is due to simultaneous actions of all three variables, T – P – U, which is called Loading Induced-Thermal Strain (LITS, see Fig. 2.43). Although there have been extensive research involving two variables at room temperature, there has been no systematic research on the coupling effects under high temperatures.

T – P (heating and drying coupling)

When considering the effect of temperature on structural deformation, the moisture condition of the structure must be taken into account. If a structure is heated without any control on environmental moisture, like a fire scenario, there will be a significant moisture loss from the concrete, and thus, aggregate particles expand due to increased temperature, and cement paste shrinks due to the loss of moisture. The total strain will be a combination of the thermal expansion of concrete and the drying shrinkage of cement paste. On the other hand, if there is an

adequate moisture supply from the environment during heating, there will be no moisture loss from the concrete, and then the total strain will be a combination of the thermal expansion of concrete and the swelling of cement paste.

For a concrete specimen under simultaneous heating and drying, the interactions of $T - P$ during the heating and holding period are different. The heating period is also called the transient period, and the holding period is the period when the interior temperature in concrete has reached the target temperature. During the heating period, the pore relative humidity in capillary pores increases and leads to swelling of concrete; and during the holding period, the pore relative humidity decreases due to the moisture loss and leads to shrinkages of concrete. Both swelling and shrinkage should be combined with the thermal expansion induced by the raising temperature. In addition, there is a coupling effect which will not be discussed in detail in this report (see Lee et al. 2009b)

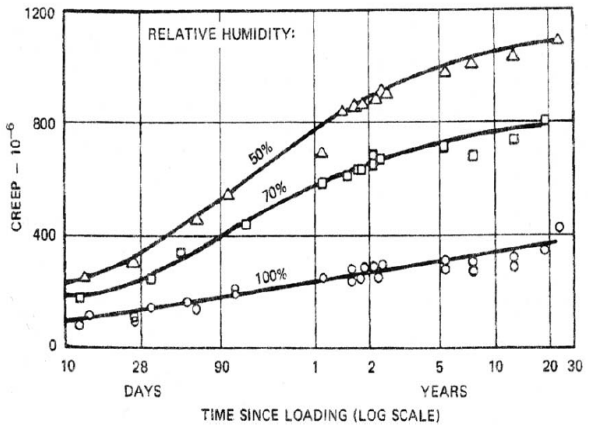

Fig. 2.44 Creep of concrete stored at different relative humidities (Neville 1970)

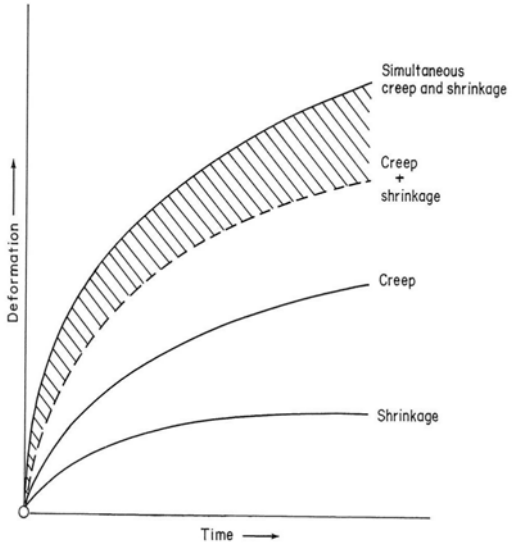

Fig. 2.45 The coupling effect between loading and drying, Pickett effect

U – P (loading and drying coupling)

Drying creep (loading and drying) is usually larger than basic creep (loading only). It is shown in Figure 2.44, where the creep strain at 50% relative humidity is higher than that under 100%. As shown in Figure 2.45, the strain due to simultaneous compression and drying is not the sum of drying shrinkage (drying only) and the basic creep from the compressive load (loading only). The total strain is actually larger than the sum of the two (Bazant 1988; Bazant and Xi 1994). The additional strain from the coupling mechanism is called stress-induced shrinkage or the Pickett effect as shown in the shaded area of Figure 2.45. The drying effect depends on the size of structure and drying rate. For a small structure, for example, the concrete can be dried out quickly and the drying effect will diminish soon. The size effect is controlled by the diffusion process of the moisture.

U – T (loading and heating coupling)

The effect of U – T coupling discussed in previous sections indicates that the loading effect U is accelerated by the temperature effect T, thus the creep at high temperature is higher than the creep at room temperature. But, what really happened in concrete is more complicated. Thermal expansion of concrete is usually measured in a stress free environment, in which concrete expands freely upon an increase of temperature. In a real concrete structure under elevated temperatures, the concrete is loaded when it is heated. When a high temperature and sustained load are applied to a concrete structure simultaneously, the total strain is not merely the sum of the free expansion due to the elevated temperature and the contraction due to the compressive load. There is an additional mechanism that plays an important role, which is similar to the stress-induced shrinkage (due to loading and drying at the same time). As shown in Figure 2.46, the concrete expands freely upon the heating under 0% stress level. As expected, the thermal expansion of concrete increases approximately linearly with increasing temperature. However, when 10% stress (of the strength under room temperature) is applied at the same time, the total strain decreases considerably. When a 30% level of compressive stress is applied, there is no thermal expansion altogether, and instead, the specimen exhibits load induced shrinkage!

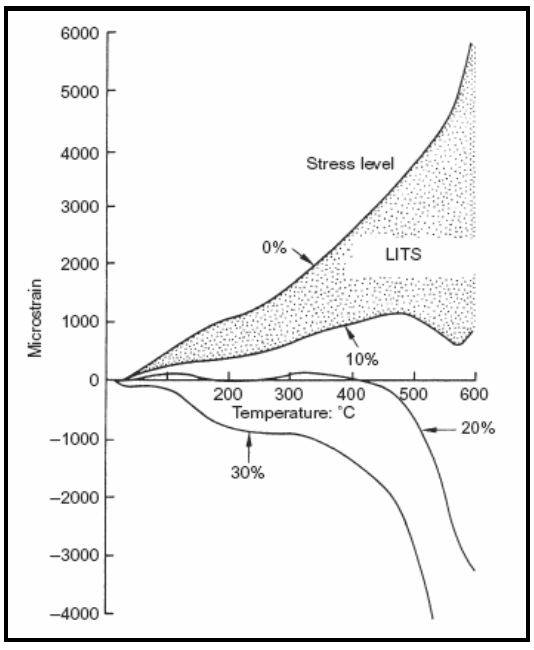

Fig. 2.46 Strain of unsealed concrete measured during heating at 1˚C/min under three uniaxial compressive load levels (percent of strength prior to heating) – excluding the initial elastic strain (Khoury et al. 2002).

The difference between the free thermal expansion and the strain under simultaneous loading and heating (see Figure 2.46, shaded area of 10% stress) is called Load-Induced Thermal Strain (LITS) (Khoury et al. 2002). It is important to note that LITS is not the elastic strain due to the sustained load (which was excluded in the figure), and it increases dramatically with increasing temperature. Under simultaneous loading and heating, the thermal expansion of concrete may be

reduced significantly by LITS. It should be pointed out that LITS is the coupling of the three parameters T – P – U.

In summary, both the movement of moisture and thermal energy during heating accelerate the creep of concrete. The actual deformation mechanisms of concrete under simultaneous heating, drying, and mechanical loadings are very complex (Khoury and Majorana 2001). During heating and drying (the transient period), the effects of drying and heating depend on the size of the structural member. The time dependent effects diminish much faster in smaller concrete members than in massive concrete structures. In short, the long-term creep and shrinkage deformations play a critical role in the service load performance of concrete structures under elevated temperatures.

2.7.2 Modeling the coupling effects

In order to characterize the various coupling effects as we described earlier, it is necessary to separate (decompose) the coupling effects and develop models to estimate each one of them individually. However, decomposition of total strain of concrete due to combined thermal and mechanical loadings is a complicated issue, mainly because the definitions of the terminologies used in the literature are not consistent among researchers. In this report, we will restrict to the definitions and explanations given by Khoury (1985a & 2002). When the temperature and sustained mechanical load are applied to the specimen simultaneously, the total thermo-mechanical strain will be observed. The decomposition of the total strain can be considered experimentally or numerically to estimate the effect of combined thermal and mechanical action or the influence of each strain component of the total strain. The total strain decomposes into the following components:

Total strain = FTS(Free Thermal Strain) – LITS(Load Induced Thermal Strain)

The definition for each terminology is as follows.

FTS (Free thermal strain) - FTS is a function of temperature and time. It includes drying shrinkage (due to moisture loss) and expansive strains. As one can see, FTS is not the free thermal expansion we discussed earlier, because it includes drying shrinkage.

Load induced thermal strain (LITS) - LITS is the strain that develops when concrete is heated for the first time under load. LITS is composed of transient creep, basic creep, and the elastic strain that occurs during the heating process. The term ‘basic creep’ is used cautiously here, because this strain strictly occurs when concrete is loaded at constant temperature and after all internal reactions have been completed (Khoury 1985b).

LITS = Transient Creep + Basic Creep + Elastic strain (during the heating process)

Transient creep is classified as transitional thermal creep and drying creep in case of unsealed specimen.

Transient Creep (unsealed specimen) = Transitional Thermal Creep (TTC) (sealed specimen) + Drying Creep

TTC (Transitional thermal creep) - TTC develops irrecoverably during, and for a few day following, first-time heating of sealed concrete under load. It appears in addition to the increase in elastic strain and basic creep (flow and delayed elastic) components with temperature. TTC is generally developed within a month from the start of heating (Khoury 1985a).

Khoury's description on LITS provides a foundation for experimental study and theoretical modeling of LITS. From aspect of mathematical modeling, additive decomposition of the total strain rate may be separated into as follows:

$$\dot{\varepsilon}_t(T,\sigma) = \dot{\varepsilon}_e(T,\sigma) + \dot{\varepsilon}_{th}(T,\sigma) + \dot{\varepsilon}_{cr}(T,\sigma) + \dot{\varepsilon}_{th}^{\sigma}(T,\sigma) \tag{2.18}$$

in which, the first term on the right represents the instantaneous elastic component, the second term = the thermal expansion component, and the last two terms account for the load induced thermal strain. In the rheological model proposed by Thelandersson (1987) the load induced thermal strain rate was assumed to be comprised of a viscous creep term and an additional term which is mobilized by the rate of temperature,

$$\dot{\varepsilon}_{cr}(T,\sigma) + \dot{\varepsilon}_{th}^{\sigma}(T,\sigma) = \left(\frac{1}{\eta} + \frac{k}{f_c^0}\alpha\dot{T}\right), \quad \eta : \text{viscosity} \tag{2.19}$$

The two contributions to the load induced thermal strain are comprised of a temperature-dependent creep term and the thermo-mechanical strain, respectively. Although it is recognized that the two components cannot be separated experimentally, one reason for the subdivision is that the two terms have different characteristics. The creep component takes place under heating and cooling and shows creep recovery, whereas the thermo-mechanical strain is only observed during first heating and not during subsequent cooling or heating cycles. Thelandersson (1987) assumed proportionality between the thermo-mechanical strain and the thermal strain because of its simplicity. In the following, a more general formulation is adopted according to Nielsen, Pearce and Bicanic (2004) for application to transient fire scenarios. In their LITS model the dashpot (associated with the viscosity) is neglected, however in the case of long term load histories with mechanical and thermal loads, the temperature-dependent creep strain should be included in the total strain rate expression. The parabolic temperature-dependent formulation reads:

$$\begin{aligned} &\varepsilon_{th}^{\sigma} = \frac{\sigma}{f_c^0} y \\ &y: \ A\theta^2 + B\theta \qquad\qquad 0 \le \theta \le \theta^* = 4.5 \\ &\quad C(\theta - \theta^*)^2 + A(2\theta - \theta^*)\theta^* + B\theta \qquad \theta^* < \theta \end{aligned} \tag{2.20}$$

The temperature-dependent coefficient of load-induced thermal strain is calculated as a bilinear function of temperature from the slope $\partial\varepsilon_{th}^{\sigma} / \partial T = \beta\sigma / f_c^0$ from Eq. (2.20)):

$$\beta = \begin{cases} 10^{-2}(2A\theta + B) & 0 \le \theta \le \theta^* = 4.5 \\ 10^{-2}\left[2C(\theta - \theta^*) + 2A\theta^* + B\right] & \theta^* < \theta \end{cases} \tag{2.21}$$

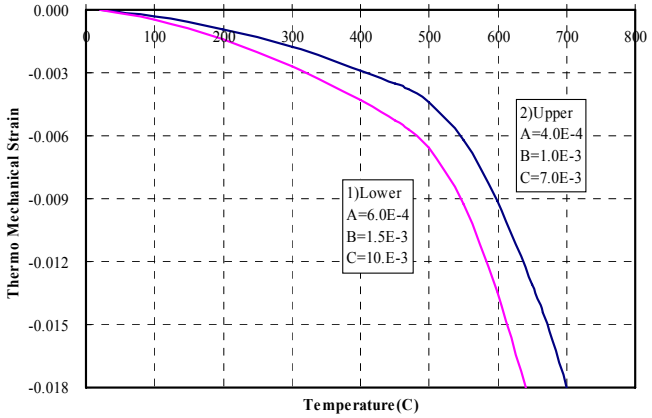

Fig. 2.47 Thermo-Mechanical Strains

Figure 2.47 illustrates two evolutions of the thermo-mechanical strain component of LITS under increasing temperature. The two bounds exhibit at T > 500°C a sharp increase of contraction due to preloading in compression.

2.8 Porosity and weight loss of concrete under high temperatures

Measurements of porosity after exposure to different temperatures were performed by Noumowe et al (1996) using a mercury porosimeter. Figure 2.48(a) shows the results of porosity measurements. Figure 2.48(b) illustrates the percentage loss in mass for different temperatures. Porosity measurements indicated that between 25˚C and 120˚C, the porosity of both NSC and HSC was not altered. As the temperature increased, NSC became increasingly more porous compared with HSC. Mass losses in both concretes were also similar up to 110˚C. The highest rate of mass loss occurred in the temperature range of 110˚C to 350˚C. The rate of weight loss stabilized at temperatures above 350˚C. At any temperature, mass loss in NSC was higher than that in HSC.

Lee et al. (2008) obtained weight loss test data as shown in Figure 2.49, in which two different initial relative humidities in concrete were studied. In general, the weight loss increases with increasing target temperature. However, the weight loss and the target temperature are not proportional over the entire temperature range. The slope of the weight loss vs. temperature above 200 °C is considerably less than that in the range of 25 – 200 °C, which is due to different mechanisms of weight loss. In the lower temperature range, the weight loss is due mainly to the evaporation of the free water present in the voids and capillary pores. After the evaporation of all free water further weight loss comes from the removal of the adsorbed water in smaller pores, which takes more energy. Moreover, at higher temperatures, some phase transformations take place and a certain amount of chemically bound water is released and evaporated. The amount of adsorbed water and chemically bound water released due to the phase transformation is less than

the free water in the concrete specimens with 90% and 100% initial relative humidity (RH). This leads to the reduced slope in the weight loss curves above 200 °C.

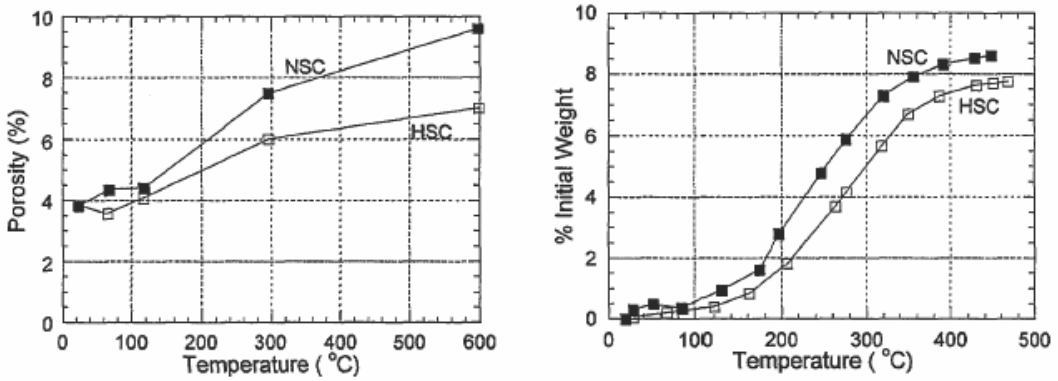

(a) Porosity vs. temperature (b) Mass loss vs. temperature

Fig. 2.48 Porosity and weight loss of concrete obtained by Noumowe et al. (1996)

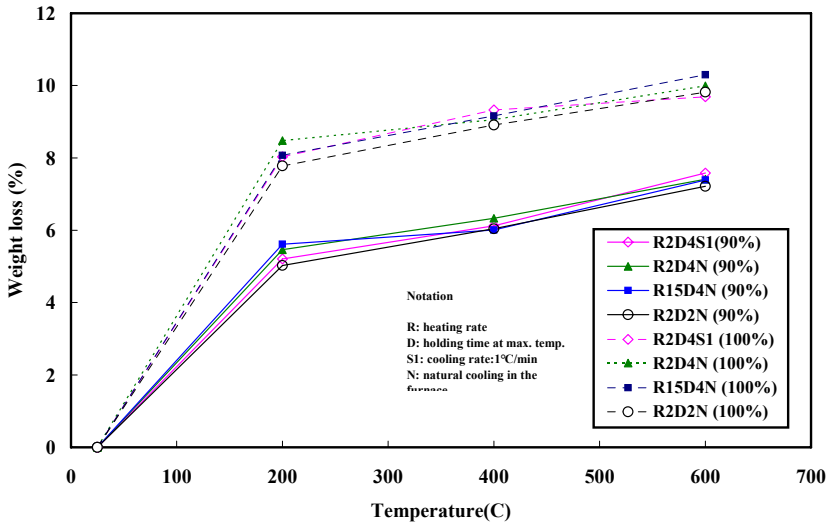

Fig. 2.49 Weight loss of concrete after heating at various temperatures (Lee et al. 2008).

The initial weight loss of fully saturated specimens is steeper than those 90% saturated specimens up to 200 ˚C. This is because the fully saturated specimens contain more free water than the specimens of 90% saturated. At temperatures higher than 200 ˚C, the slopes for both types of specimens are almost the same. This means that the evaporation of the free water in the voids and capillary pores is almost complete at 200°C. Therefore, regardless of the initial moisture content of concrete, after 200°C, the rate of weight loss is similar for all specimens. The constant slope after 200°C indicates that the weight loss of concrete is governed by the same mechanism from 200°C up to 800°C.

The test results, for both 90% and 100 % saturation showed that the weight loss is governed primarily by the target temperature, not by the heating rate, the cooling method, or the holding time (2 hrs and 4 hrs in this research).

2.9 Thermal transport properties of concrete under high temperatures

Assuming isotropy, there are three scalar material parameters to describe the heat transfer in a solids: thermal conductivity λ, specific heat (also called heat capacity) c, and density ρ. Often these parameters are built into a single variable κ which is called the thermal diffusivity.

$$\kappa = \frac{\lambda}{c\rho} \tag{2.22}$$

According to Rigberth (2000), the temperature dependent thermal conductivity of siliceous concrete can be described as a decreasing parabolic function of temperature T as shown in Eq. (2.23). The plot of the equation is shown in Figure 2.50:

$$\lambda_c = 2 - 0.24\frac{T}{120} + 0.012\left(\frac{T}{120}\right)^2 \tag{2.23}$$

in which T = temperature in °C, and λ_c = thermal conductivity of concrete in W/(mK).

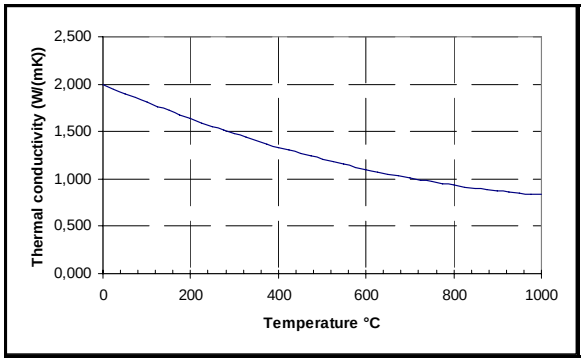

Fig. 2.50 Thermal conductivity of concrete as a function of temperature

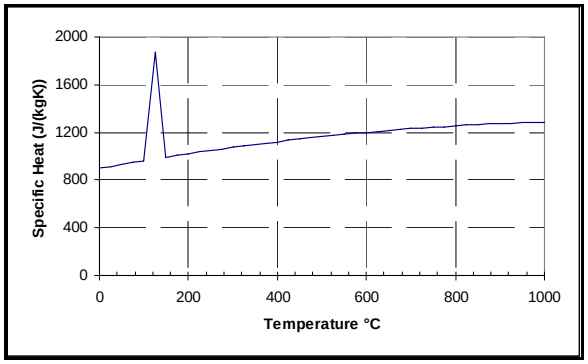

Fig. 2.51 Specific heat of concrete as function of temperature

The specific heat is assumed to be a quadratic function of the temperature according to Eq. (2.24). However, due to phase transformations of free and bound water in heated concrete, the specific heat exhibits a peak between 100°C and 200°C with a top value at 120°C. This peak varies with the concrete properties, water content, and other parameters. According to Eurocode (ENV 1992-1-2, 1995) this peak of concrete heat capacity is c_c(T=120°C) = 1875 J/(kg.K), as indicated in Figure 2.51.

$$c_c = 900 + 80\frac{T}{120} - 4\left(\frac{T}{120}\right)^2 \tag{2.24}$$

Note: for simplified studies the thermal diffusivity may be assumed to be constant where $\kappa_c = 0.83\times10^{-6}$ m^2/s for normal weight concrete and $\kappa_c = 0.32\times10^{-6}$ m^2/s for lightweight concrete respectively (Khoury 1984). Figure 2.52 shows recently obtained test data on thermal diffusivity of concrete (Lee et al. 2008). One can see a large drop in the thermal diffusivity up to 200 ˚C, which is primarily related to the loss of free water. Beyond this temperature the thermal diffusivity shows relatively little variation with increasing temperature up to 800˚C. This result confirmed that a constant thermal diffusivity may be used in the analysis for high temperature ranges.

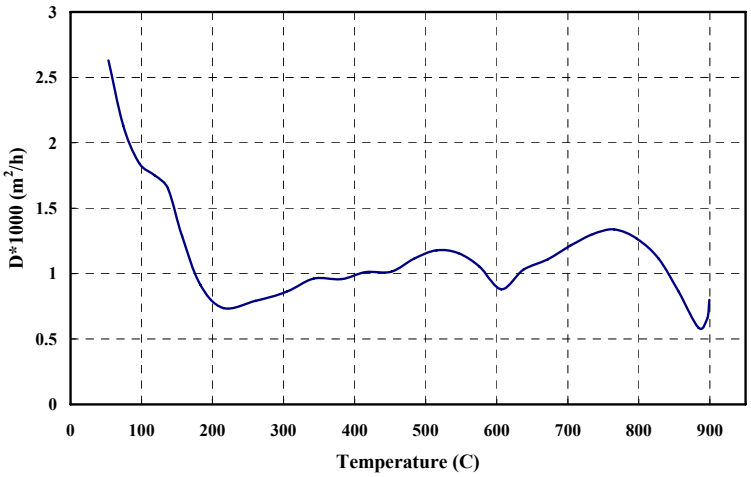

Fig. 2.52 Thermal diffusivity of concrete vs. temperatures (Lee et al. 2008)

As a summary for properties of concrete under high temperatures, Table 2.5 lists some of the prediction models for the properties of concrete, including mechanical properties and thermal transport properties. The table is from the recent paper by Kodur et al. (2008).

Table 2.5 Constitutive relationships for high-temperature properties of concrete (Kodur et al. 2008)

	ASCE manual 1992 (NSC)[12]	Kodur et al. 2004 (HSC)[28]	EN1992-1-2:2004 (NSC and HSC)[24]
Stress-strain relationships	$\sigma_c = \begin{cases} f'_{c,T}\left[1-\left(\frac{\varepsilon-\varepsilon_{max,T}}{\varepsilon_{max,T}}\right)^2\right], & \varepsilon \le \varepsilon_{max,T} \\ f'_{c,T}\left[1-\left(\frac{\varepsilon_{max,T}-\varepsilon}{3\varepsilon_{max,T}}\right)^2\right], & \varepsilon > \varepsilon_{max,T} \end{cases}$ $f'_{c,T} = \begin{cases} f'_c & ,\ 20\ ^\circ\text{C} \le T \le 450\ ^\circ\text{C} \\ f'_c\left[2.011-2.353\left(\frac{T-20}{1000}\right)\right] & ,\ 450\ ^\circ\text{C} < T \le 874\ ^\circ\text{C} \\ 0 & ,\ 874\ ^\circ\text{C} < T \end{cases}$ $\varepsilon_{max,T} = 0.025 + (6.0T + 0.04T^2) \times 10^{-6}$	$\sigma_c = \begin{cases} f'_{c,T}\left[1-\left(\frac{\varepsilon_{max,T}-\varepsilon}{\varepsilon_{max,T}}\right)^H\right], & \varepsilon \le \varepsilon_{max,T} \\ f'_{c,T}\left[1-\left(\frac{30(\varepsilon-\varepsilon_{max,T})}{(130-f'_c)\varepsilon_{max,T}}\right)^2\right], & \varepsilon > \varepsilon_{max,T} \end{cases}$ $f'_{c,T} = \begin{cases} f'_c[1.0-0.003125(T-20)] & ,\ T < 100\ ^\circ\text{C} \\ 0.75f'_c & ,\ 100\ ^\circ\text{C} \le T \le 400\ ^\circ\text{C} \\ f'_c[1.33-0.00145T] & ,\ 400\ ^\circ\text{C} < T \end{cases}$ $\varepsilon_{max,T} = 0.0018 + (6.7f'_c + 6.0T + 0.03T^2) \times 10^{-6}$ $H = 2.28 - 0.012f'_c$	$\sigma_c = \frac{3\varepsilon f'_{c,T}}{\varepsilon_{c1,T}\left(2+\left(\frac{\varepsilon}{\varepsilon_{c1,T}}\right)^3\right)}, \varepsilon \le \varepsilon_{cu1,T}$ For $\varepsilon_{c1,T} < \varepsilon \le \varepsilon_{cu1,T}$, the Eurocode permits the use of linear as well as nonlinear descending branch in the numerical analysis. For the parameters in this equation, refer to Table A.2.
Thermal capacity	*Siliceous aggregate concrete:* $\rho c = \begin{cases} 0.005T+1.7 & 20\ ^\circ\text{C} \le T \le 200\ ^\circ\text{C} \\ 2.7 & 200\ ^\circ\text{C} < T \le 400\ ^\circ\text{C} \\ 0.013T-2.5 & 400\ ^\circ\text{C} < T \le 500\ ^\circ\text{C} \\ 10.5-0.013T & 500\ ^\circ\text{C} < T \le 600\ ^\circ\text{C} \\ 2.7 & 600\ ^\circ\text{C} < T \end{cases}$ *Carbonate aggregate concrete:* $\rho c = \begin{cases} 2.566 & 20\ ^\circ\text{C} \le T \le 400\ ^\circ\text{C} \\ 0.1765T-68.034 & 400\ ^\circ\text{C} < T \le 410\ ^\circ\text{C} \\ 25.00671-0.05043T & 410\ ^\circ\text{C} < T \le 445\ ^\circ\text{C} \\ 2.566 & 445\ ^\circ\text{C} < T \le 500\ ^\circ\text{C} \\ 0.01603T-5.44881 & 500\ ^\circ\text{C} < T \le 635\ ^\circ\text{C} \\ 0.16635T-100.90225 & 635\ ^\circ\text{C} < T \le 715\ ^\circ\text{C} \\ 176.07343-0.22130T & 715\ ^\circ\text{C} < T \le 785\ ^\circ\text{C} \\ 2.566 & 785\ ^\circ\text{C} < T \end{cases}$	*Siliceous aggregate concrete:* $\rho c = \begin{cases} 0.005T+1.7 & 20\ ^\circ\text{C} \le T \le 200\ ^\circ\text{C} \\ 2.7 & 200\ ^\circ\text{C} < T \le 400\ ^\circ\text{C} \\ 0.013T-2.5 & 400\ ^\circ\text{C} < T \le 500\ ^\circ\text{C} \\ 10.5-0.013T & 500\ ^\circ\text{C} < T \le 600\ ^\circ\text{C} \\ 2.7 & 600\ ^\circ\text{C} < T \le 635\ ^\circ\text{C} \end{cases}$ *Carbonate aggregate concrete:* $\rho c = \begin{cases} 2.45 & 20\ ^\circ\text{C} \le T \le 400\ ^\circ\text{C} \\ 0.026T-12.85 & 400\ ^\circ\text{C} < T \le 475\ ^\circ\text{C} \\ 0.0143T-6.295 & 475\ ^\circ\text{C} < T \le 650\ ^\circ\text{C} \\ 0.1894T-120.11 & 650\ ^\circ\text{C} < T \le 735\ ^\circ\text{C} \\ -0.263T+212.4 & 735\ ^\circ\text{C} < T \le 800\ ^\circ\text{C} \\ 2 & 800\ ^\circ\text{C} < T \le 1000\ ^\circ\text{C} \end{cases}$	*Specific heat (J/kg·°C):* $c = 900$, for $20\ ^\circ\text{C} \le T \le 100\ ^\circ\text{C}$ $c = 900 + (T-100)$, for $100\ ^\circ\text{C} < T \le 200\ ^\circ\text{C}$ $c = 900 + (T-200)/2$, for $200\ ^\circ\text{C} < T \le 400\ ^\circ\text{C}$ $c = 1100$, for $400\ ^\circ\text{C} < T \le 1200\ ^\circ\text{C}$ *Density change (kg/m³):* $\rho = \rho(20\ ^\circ\text{C})$ = reference density for $20\ ^\circ\text{C} \le T \le 115\ ^\circ\text{C}$ $\rho = \rho(20\ ^\circ\text{C})(1-0.02(T-115)/85)$ for $115\ ^\circ\text{C} < T \le 200\ ^\circ\text{C}$ $\rho = \rho(20\ ^\circ\text{C})(0.98-0.03(T-200)/200)$ for $200\ ^\circ\text{C} < T \le 400\ ^\circ\text{C}$ $\rho = \rho(20\ ^\circ\text{C})(0.95-0.07(T-400)/800)$ for $400^\circ\text{C} < T \le 1200\ ^\circ\text{C}$ *Thermal capacity* = $\rho \times c$
Thermal conductivity	*Siliceous aggregate concrete:* $k_c = \begin{cases} -0.000625T+1.5 & 20\ ^\circ\text{C} \le T \le 800\ ^\circ\text{C} \\ 1.0 & 800\ ^\circ\text{C} < T \end{cases}$ *Carbonate aggregate concrete:* $k_c = \begin{cases} 1.355 & 20\ ^\circ\text{C} \le T \le 293\ ^\circ\text{C} \\ -0.001241T+1.7162 & 293\ ^\circ\text{C} < T \end{cases}$	*Siliceous aggregate concrete:* $k_c = 0.85(2-0.0011T) \quad 20\ ^\circ\text{C} < T \le 1000\ ^\circ\text{C}$ *Carbonate aggregate concrete:* $k_c = \begin{cases} 0.85(2-0.0013T) & 20\ ^\circ\text{C} \le T \le 300\ ^\circ\text{C} \\ 0.85(2.21-0.002T) & 300\ ^\circ\text{C} < T \end{cases}$	All types: *Upper limit:* $k_c = 2-0.2451(T/100)+0.0107(T/100)^2$ for $20\ ^\circ\text{C} \le T \le 1200\ ^\circ\text{C}$ *Lower limit:* $k_c = 1.36-0.136(T/100)+0.0057(T/100)^2$ for $20\ ^\circ\text{C} \le T \le 1200\ ^\circ\text{C}$
Thermal strain	All types: $\varepsilon_{th} = [0.004(T^2-400)+6(T-20)] \times 10^{-6}$	All types: $\varepsilon_{th} = [0.004(T^2-400)+6(T-20)] \times 10^{-6}$	*Siliceous aggregate:* $\varepsilon_{th} = -1.8 \times 10^{-4} + 9 \times 10^{-6}T + 2.3 \times 10^{-11}T^3$ for $20\ ^\circ\text{C} \le T \le 700\ ^\circ\text{C}$ $\varepsilon_{th} = 14 \times 10^{-3}$ for $700\ ^\circ\text{C} < T \le 1200\ ^\circ\text{C}$ *Siliceous aggregate:* $\varepsilon_{th} = -1.2 \times 10^{-4} + 6 \times 10^{-6}T + 1.4 \times 10^{-11}T^3$ for $20\ ^\circ\text{C} \le T \le 805\ ^\circ\text{C}$ $\varepsilon_{th} = 12 \times 10^{-3}$ for $805\ ^\circ\text{C} < T \le 1200\ ^\circ\text{C}$

Note: The superscripts in the table refer to the references in the paper (Kodur et al. 2008).

3 Responses of Reinforcing Steel to High Temperatures

3.1 Experiments on stress-strain curves of steel under high temperatures

Under high temperatures, both strength (proportional limit) and stiffness of steel deteriorate in the manner similar to concrete. Figure 3.1 shows schematically the stress-strain curves of steel under various temperatures. Figure 3.2 illustrates the variation of mild structural steels tested in direct tension at different temperatures. The response behavior exhibits a drastic reduction of the proportional limit under increasing temperatures which is accompanied by a puzzling increase of the ultimate yield strength up to 300°C at reduced ductility. Beyond that temperature range, the ultimate the yield strength decreases rapidly with temperature while the ductility increases.

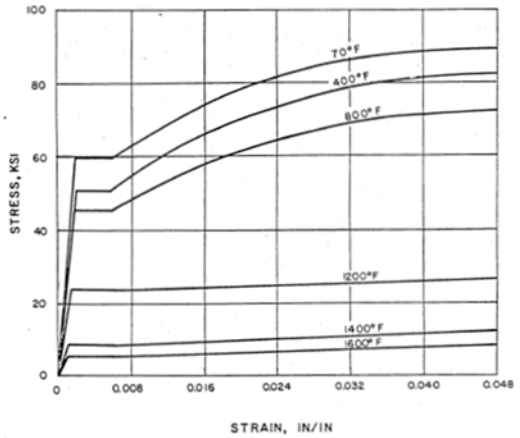

Fig. 3.1 Stress-strain relationship for steel (Freskakis, 1984)

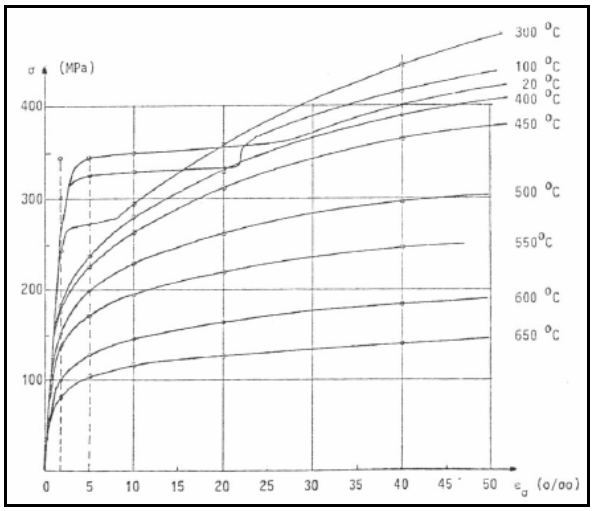

Fig. 3.2 Experimental stress-strain curves for structural steel, St52 (Thor, 1972)

3.2 Predicting responses of steel to high temperatures

3.2.1 Tensile Strength

The provision of ACI 216.1-07 specifies temperature-dependent reduced yield strength of reinforcing steels, $f_{y\theta}$ as shown Figure 3.3.

The temperature dependence of hot-rolled reinforcing steel is specified in Eurocode3 (ENV 1992-1-2, 1995) in the form of Table 3.1. Thereby, the stiffness and strength values have been normalized by the respective values at reference temperature. Figure 3.4 depicts the terminology used to describe the proportional limit and the hardening-softening response up to and beyond the ultimate yield capacity of steel in direct tension.

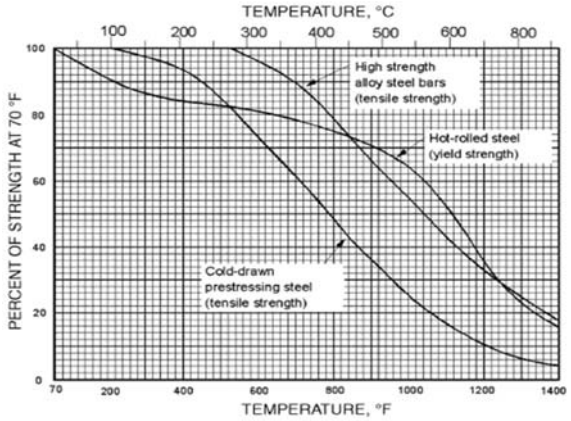

Fig. 3.3 Strength of flexural reinforcement steel bar at high temperature (ACI 216.1-07)

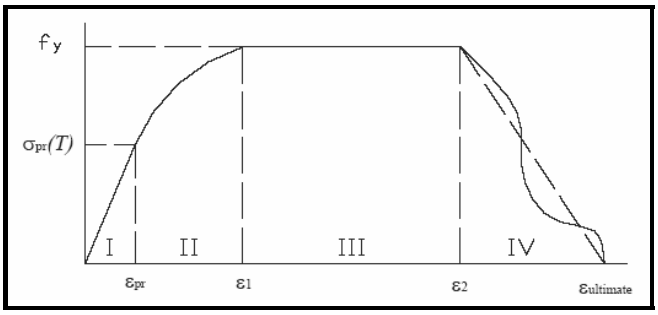

Fig. 3.4 Terminologies used in ENV 1992-1-2.1995(ε_1=2%)

The following expressions are obtained based on Eurocode3 (ENV 1992-1-2, 1995) for reinforcing steel assuming the offset condition ($\varepsilon = 0.2\%$) to determine the proportional limit at the reference temperature. Figure 3.5 compares the model predictions with the tabulated Eurocode3 values and test data obtained by Holmes et al. (1982)

For $0^\circ C < T \leq 350^\circ C$

$$f_y(T) / f_y(20°C) = 1 \quad (3.1)$$

For $350^\circ C < T \leq 706^\circ C$

$$f_y(T) / f_y(20°C) = 1.8848 - 2.528 \times 10^{-3} T \quad (3.2)$$

For 706˚ C < T ≤ 1200˚ C

$$f_y(T) / f_y(20°C) = 0.242992764 - 2.02494 \times 10^{-4} T \quad (3.3)$$

Table 3.1 Hot rolled reinforcing steel (0.2%), ENV 1992-1-2, 1995

Temperature (°C)	$E(T)/E(20°C)$	$\sigma_{pr}(T)/\sigma_{0,2}(20°C)$	$f_y(T)/\sigma_{0,2}(20°C)$
20	1,00	1,00	1,00
100	1,00	1,00	1,00
200	0,90	0,81	1,00
300	0,80	0,61	1,00
400	0,70	0,42	1,00
500	0,60	0,36	0,78
600	0,31	0,18	0,47
700	0,13	0,07	0,23
800	0,09	0,05	0,11
900	0,07	0,04	0,06
1000	0,04	0,02	0,04
1100	0,02	0,01	0,02
1200	0,00	0,00	0,00

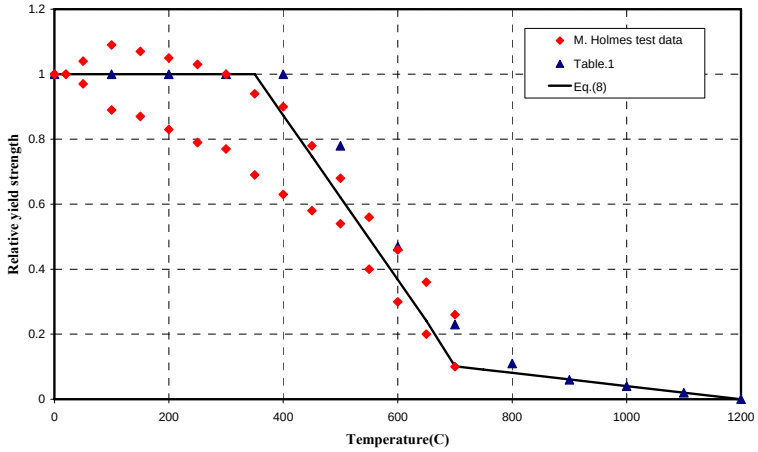

Fig. 3.5 Normalized ultimate yield strength of reinforcing steel vs. temperature

3.2.2 Modulus of Elasticity

The normalized values of the temperature dependent modulus of elasticity, E(T)/E(20°C), described by Eurocode3 (ENV 1992-1-2, 1995) are plotted in Figure 3.6.

For 20˚ C ≤ T < 100˚ C

$$E(T)/E_o(20°C) = 1 \quad (3.4)$$

For 100˚ C ≤ T < 500˚ C

$$E(T)/E_o(20°C) = 1.1 - 0.001T \quad (3.5)$$

For 500˚ C ≤ T < 700˚ C

$$E(T)/E_o(20°C) = 1.775 - 2.35 \times 10^{-3} T \quad (3.6)$$

For 700˚ C ≤ T < 1200˚ C

$$E(T)/E_o(20°C)=0.312 - 2.6\times10^{-4}T \quad (3.7)$$

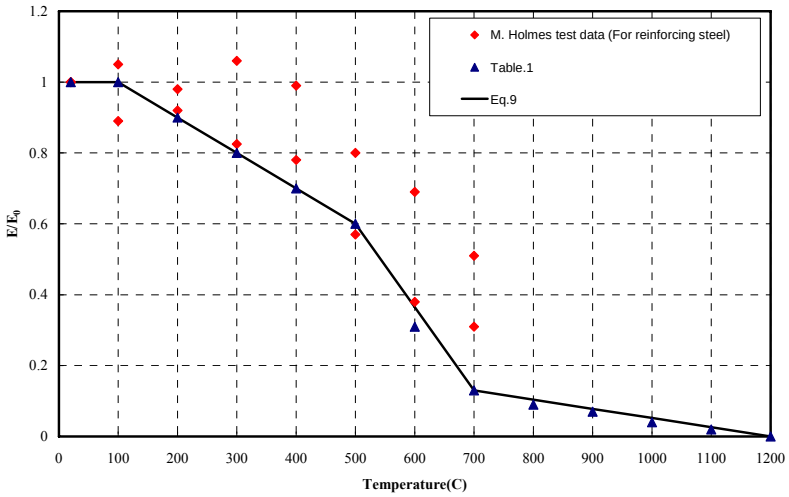

Fig. 3.6 Normalized Young's modulus of reinforcing steel vs. temperature

3.2.3 Thermal expansion and free thermal strain

For typical structural steels, the ASCE Manual and Reports on Engineering Practice No. 78 recommends the expressions below for the thermal expansion of steel which has been plotted in Figure 3.7.

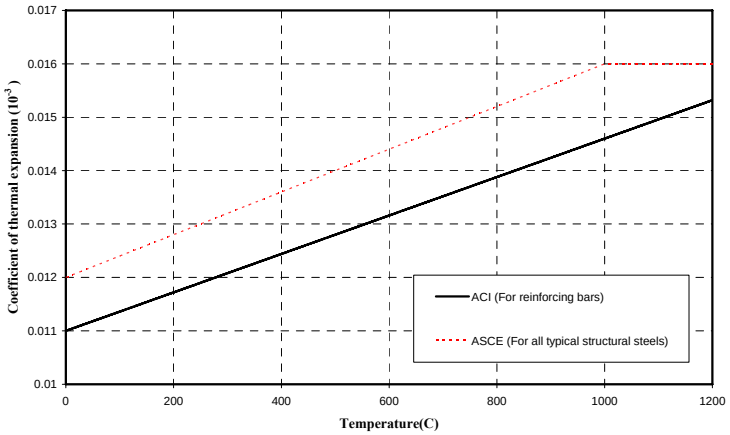

Fig. 3.7 Coefficient of thermal expansion of Steel vs. temperature

For T<1000˚C

$$\alpha_s = (0.004T + 12)\times10^{-6}{}^{\circ}C^{-1} \quad (3.8)$$

For T≥1000˚C

$$\alpha_s = 16\times10^{-6}{}^{\circ}C^{-1} \quad (3.9)$$

ACI suggests

$$\alpha_s = (0.0036T + 11)\times 10^{-6}{}^{\circ}C^{-1} \qquad (3.10)$$

A simplified expression for thermal strain of steel according to Eurocode 3 (ENV 1992-1-2, 1995) is, $\varepsilon_{th} = 14\times 10^{-6}(T-20)$.

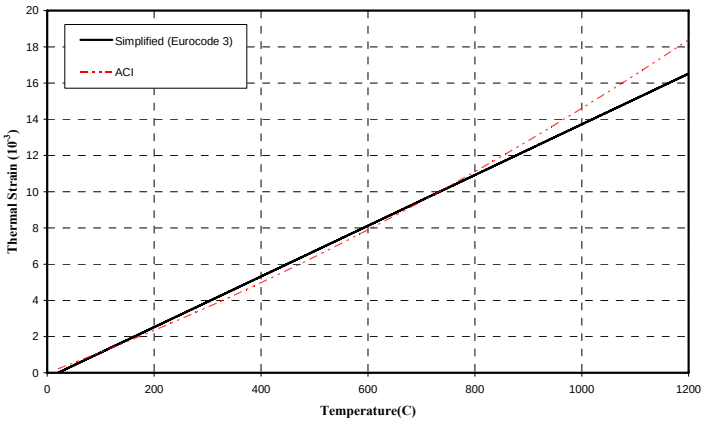

Fig. 3.8 Thermal strain of reinforcing steel vs. temperature

The thermal strain can be directly obtained from the coefficient of thermal expansion suggested by ACI, see ACI, Report no. 216R-81 (Reinforcing bars), $\varepsilon_{th} = \alpha_s(T - T_o)$, $T_o = 20^{\circ}C$. The two recommendations are compared in Figure 3.8.

3.2.4 Thermal transport properties of Steel under high temperatures

Similar to thermal transport properties of concrete, thermal transport properties of steel also include thermal conductivity, density, and specific heat (also called heat capacity). Using Eq. (2.22), thermal diffusivity of steel can be calculated based on thermal conductivity, density, and specific heat. According to Eurocode 3, the thermal conductivity of steel exhibits two branches, one before phase transformation at T=723°C and a constant value thereafter as shown in Figure 3.9.

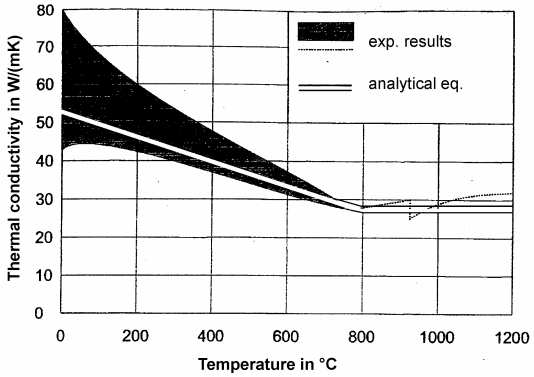

Fig. 3.9 Thermal conductivity of steel (Schneider and Lebeda)

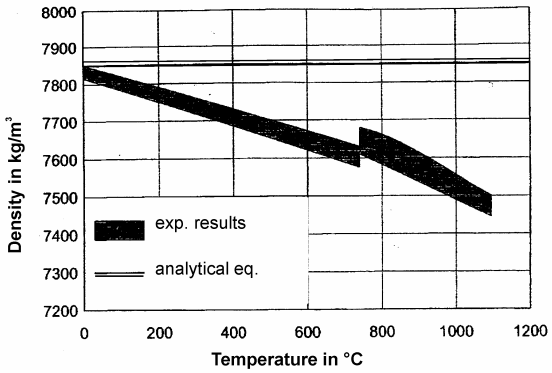

Fig. 3.10 Density of steel varies with temperature (Schneider and Lebeda)

The prediction model used to characterize the variation of thermal conductivity with temperature is as follows

For 20°C $\leq T$<800°C

$$\lambda_s = 54 - 3.33 \cdot 10^{-2} \cdot T \tag{3.11}$$

For 800°C $\leq T \leq$ 1200°C

$$\lambda_s = 27.3 \tag{3.12}$$

in which T = temperature in °C, λ_s = thermal conductivity of steel in W/(mK).

Often the density of steel ρ is assumed to be independent of temperature with a representative value of γ_s = 7850 kg/m^3. However, experimental evidence shows that there is a nearly linear decrease of the density with increasing temperature. As illustrated in Figure 3.10 a small jump occurs at T = 723°C due to the transition of α-into γ-crystals in steel.

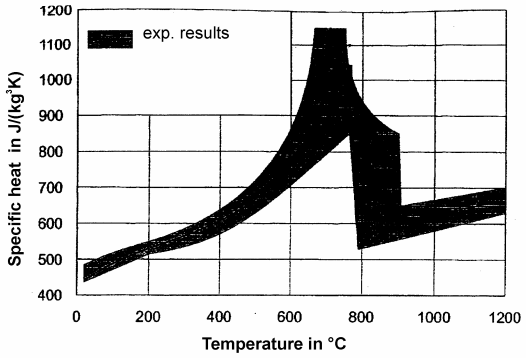

Fig. 3.11 Specific heat of steel from experimental results (Schneider and Lebeda.)

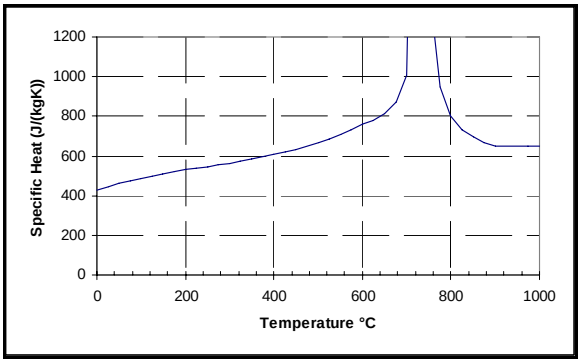

Fig. 3.12 Specific heat of steel (analytical solution)

The variation of the specific heat with respect to the temperature does not show a simple trend, see Figure 3.11. Due to the latent heat effect which occurs at the transition temperature of α-into γ-crystals there are four different ranges according to Rigberth (2000) which are illustrated in Figure 3.12.

The prediction model used to characterize the variation of specific heat with temperature is as follows

For 20°C $\leq T$<600°C

$$c_s = 425 + 0.773 \cdot T - 1.69 \cdot 10^{-3} \cdot T^2 + 2.22 \cdot 10^{-6} \cdot T^3 \tag{3.13}$$

For 600°C $\leq T$<735°C

$$c_s = 666 + \frac{13002}{738 - T} \tag{3.14}$$

For 735°C $\leq T$<900°C

$$c_s = 545 + \frac{17820}{T - 731} \tag{3.15}$$

For 900°C $\leq T$<1200°C

$$c_s = 650 \tag{3.16}$$

in which c_s = specific heat of steel in J/(kg.K).

Note: for simplified studies the thermal diffusivity (calculated by Eq. 2.22) may be assumed to be independent of temperature, where $\kappa_s = 9.6\times10^{-6}$ m^2/s with $\rho_s = 7850$ kg/m^3 (Eurocode 3).

4 The Bond between Concrete and Steel

The reduction or loss of bond strength between steel bars and surrounding concrete under high temperatures is mainly caused by the deformation mismatch between the two materials. The coefficient of thermal expansion at 400 °C is about 20 x 10^{-6}/°C for concrete depending on the aggregate used (Figure 2.33), and about 13 x 10^{-6}/°C for steel (Figure 3.7). The difference in the coefficients of thermal expansion of the two materials results in progressive damage in the interface and thus reduces the bond strength.

4.1 Testing methods for bond strength

The bond strength between concrete and steel reinforcement at high temperatures has been studied by many researchers (Diederichs, U. 1982; Hertz, K. 1980; Sager, H. et al. 1980; Kasami, H et. al 1975). There are two testing methods for measuring residual bond strength and hot bond strength. The residual bond strength can be measured in a way that specimens are heated up to various target temperatures, held at the temperatures for a period of time, cooled down to ambient temperature. Then, a pull-out test is performed to pull the reinforcing steel out of the specimen. The hot bond strength can be obtained with the pull-out test carried out under the hot conditions during the holding period.

Any parameters that change the coefficient of thermal expansion of concrete will have impact on the bond strength, such as mix proportion of concrete and type of aggregate. In addition, there are several other influential parameters on the bond strenth, such as curing conditions, shape of reinforcing bar, surface conditions and type of bars, diameter of bar, shape of concrete specimen, and testing procedure.

4.2 Experimental results on the bond strength

Figures 4.1, 4.2, and 4.3 show differences of the residual bond strengths between plain round bars and shaped bars. For round bars, some of the test data showed that the bond strength was increased after heating below 100 °C. This is similar to the down-up-down trend observed for compressive strength of concrete in the same range of temperature. The bond strength reduction of round bars is more significant than the deformed bars. For example, at 200 °C, the bond strength of round bars dropped to about 60% of original value (Figure 4.1), while the bond strength of deformed bars dropped only to about 85% (Figure 4.2). Therefore, the deformed bars hold better bond under high temperatures.

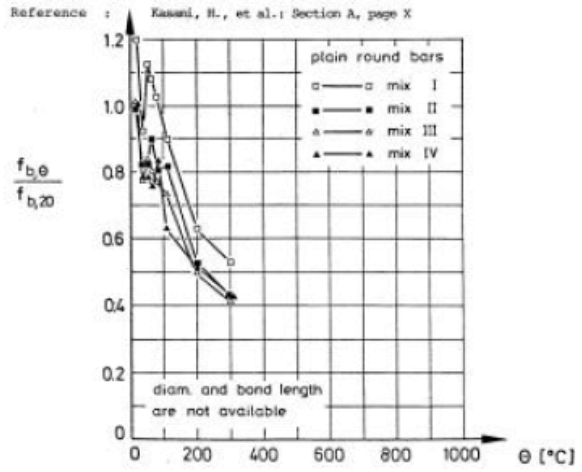

Fig. 4.1 Residual bond strength of plain Round bars in different concrete Mixes (Kasami, H et. al 1975)

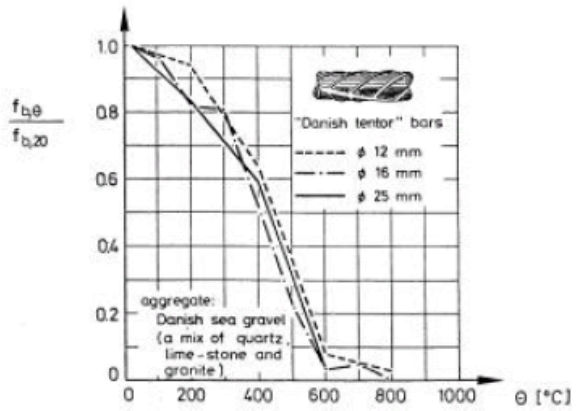

Fig. 4.2 Residual bond strength of Danish "tentor" bars (Hertz 1980)

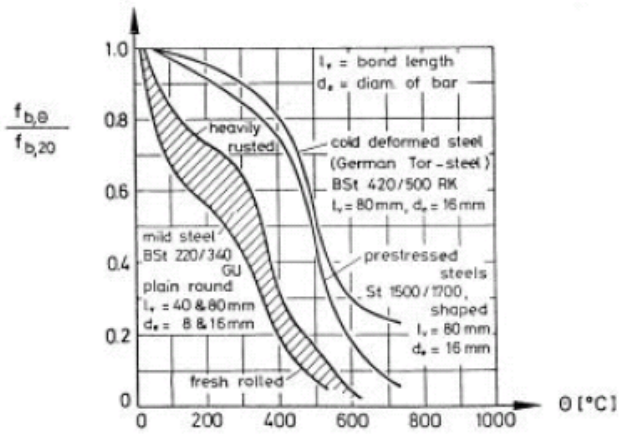

Fig. 4.3 Influence of the surface conditions on the high temperature bond strength (Diederichs, U. 1982)

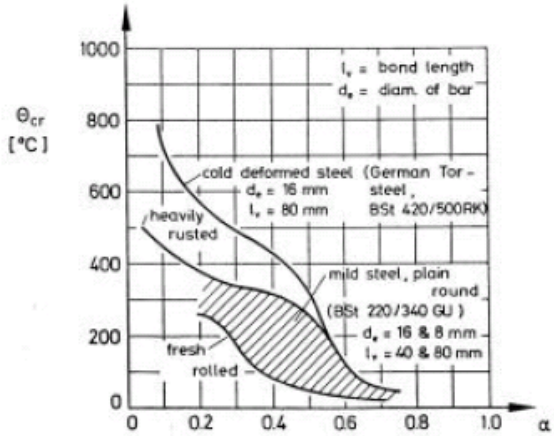

Fig. 4.4 Influence of the surface conditions on the critical bond temperature (Diederichs, U. 1982)

Further tests (see Figure 4.4) on the effect of surface roughness showed that the surface roughness of plain round bars is the main factor affecting the high temperature bond strength. With higher roughness, the bond strength of round bars can be improved. For deformed bars, the rib height is an important factor for the bond strength. Some minimum height should be maintained. When a rib height of approximately 0.2 mm is exceeded, the influence of the rib profile on the bond strength is of minor importance.

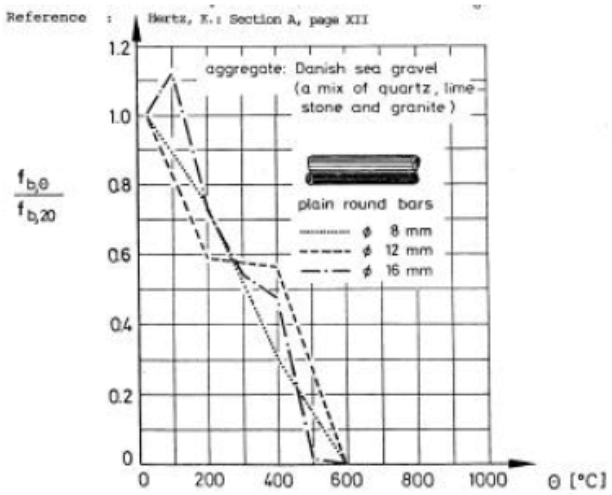

Fig. 4.5 Influence of the diameter of plain Round bars on the residual bond Strength (Hertz 1980)

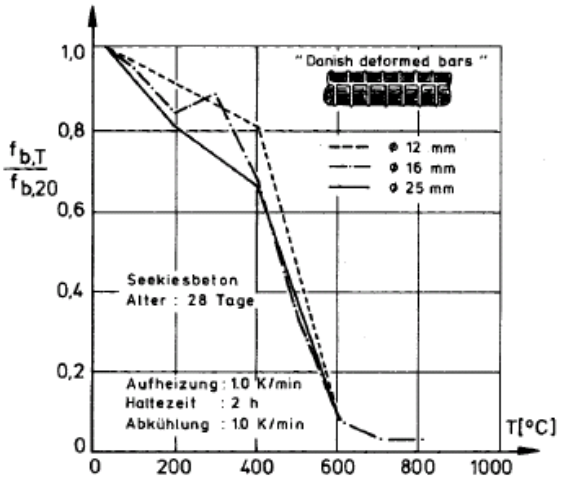

Fig. 4.6 Influence of the diameter of deformed bars on the residual bond strength (Hertz 1980)

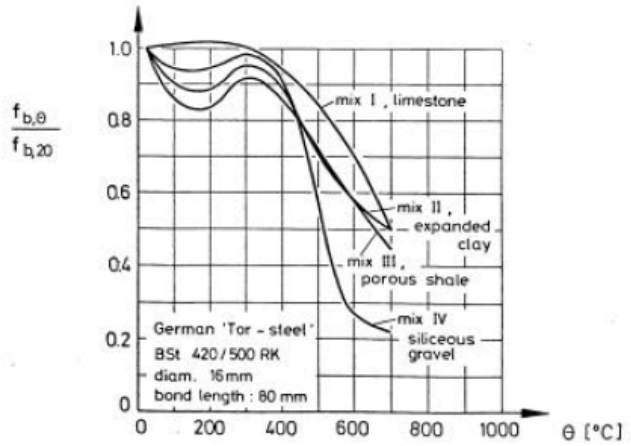

Fig. 4.7 Influence of the type aggregate on the high temperature bond strength (Sager, H. et al. 1980)

Figures 4.5 and 4.6 show that the diameter of the bars has some influence on the bond strength but not very significant. This is observed for both round bars and deformed bars.

Although mix design of concrete has been considered as an influential parameter, qualitative relationship between water/cement ratio and bond strength has not been found in the literature.

The type of aggregate is the main factor determining the hot bond strength. This is due to the fact that the thermal expansion of concrete depends heavily on the aggregate type; and that the lower the thermal strain of concrete, the lower the deformation mismatch between the concrete and the steel; and thus the higher the bond strength at elevated temperatures. This is shown in Figure 4.7, in which the concrete made of the limestone had the highest bond strength (lowest strength reduction) in the testing temperature range. From Table 2.2, one can see that limestone concrete has the lowest coefficient of thermal expansion.

Curing conditions are important at temperatures below 400 °C, and moist cured specimens have a lower bond strength compared to dried specimens. This may be due to the fact that moist cured specimens have higher drying shrinkage upon heating than dried specimens.

The residual bond strength is lower than the bond strengths obtained from hot tests. This is due to the fact that the cooling process generates significant damage in the concrete, which was shown in earlier sections (see Figure 2.29).

The bond strength is significantly influenced by the testing procedure and the shape of specimens. It should be noted that the absolute values of bond strengths of the specimens with conical load bearing ends obtained from Hertz's (Hertz 1980) are twice as high as the values obtained from the specimens with flat load bearing ends from Diederichs et al. (Diederichs, U. 1982).

5 Conclusions of Part I

This report provides a comprehensive review on material properties of concrete and steel under elevated temperatures. The properties of the materials include mechanical properties such as strength and stiffness and transport properties such as thermal diffusivity and heat capacity. There is a detailed description on long-term properties of concrete under elevated temperatures such as creep and shrinkage. The coupling effects among heating, drying, and mechanical loading (the so-called thermo-hygro-mechanical coupling effects) on performance of concrete are discussed. Several aspects are covered for each material property of concrete, including damage mechanisms, available test results, code requirements, and prediction models. The bond between concrete and steel under elevated temperatures is also reviewed.

6 References of Part I

AASHTO TP60-00 (2000) “Standard Test Method for the Coefficient of Thermal Expansion of Hydraulic Cement Concrete”, AASHTO Destination TP60-00.

Abrams, M.S. (1971). “Compressive strength of concrete at temperatures to 1600˚F”, *American Concrete Institute (ACI) SP 25*, Temperature and Concrete, Detroit, Michigan.

ACI 209 (1997) “Factors Affecting Shrinkage, Creep and Thermal Epansion of Concrete and Simplified Models to Predict Strains”, ACI Committee 209, Chairman Al-Manaseer A., and Chairman McDonald, D.B., for subcommittee IV.

ACI 209R-92 (1992) “Prediction of Creep, Shrinkage, and Temperature Effects in Concrete Structures. American Concrete Institute.

American Concrete Institute 216. (1981). “Guide for Determining the Fire Endurance of Concrete Elements”, Concrete International, Feb., 13-47.

American Concrete Institute 318. (2002). “Building Code Requirements for Structural Concrete”, American Concrete Institute

Arthananari, S., and Yu, C.W. (1967) “Creep of Concrete Under Uniaxial and Biaxial Stresses at Elevated Temperatures”, Magazine of Concrete Research, Vol. 19, No. 60, 149-156.

ASCE. (1992). “Structural Fire Protection”, ASCE Manuals and Reports on Engineering Practice, No.78.

Bazant, Z.P. (1988) “Mathematical Modeling of Creep and Shrinkage of Concrete”, John Wiley, New York.

Bazant, Z.P., and Xi, Y. (1994) “Drying Creep of Concrete: Constitutive Model and New Experiments Separating Its Mechanisms”, Materials and Structures, RILEM, 27, 3-14.

Bazant, Z.P., and Kaplan, M.F. (1996) “Concrete at High Temperatures: Material Properties and Mathematical Models”, Longman Group Limited, Longman House, Burnt Mill, Harlow.

Blundell, R., Diamond, C. and Browne, R.G., (1976), “The Properties of Concrete Subjected to Elevated Temperature", CIRIA Underwater Engineering Group, Technical Note No. 9, Concrete Society, London, UK.

Browne, R.D., and Blundell, R., (1969), “The Influence of Loading Age and Temperature on the Long Term Creep Behavior of Concrete in a Sealed Moisture Stable State”, Materials and Structures, RILEM 2, 133-144.

Browne, R.D., and Bamforth, P.B., (1975), "The Long Term Creep Creep of the the Wylfa P.V. Concrete for Loading Ages up to 12.5 Years", Paper H 1/8, 3rd SMIRT Conference, London Sept 1-5, 1975.

Castillo, C., and Durani, A.J. (1990). "Effect of transient high temperature on high-strength concrete", *ACI Material Journal*, Jan/Feb, 87(1), 38-67.

Cruz, C.R. (1968) "Apparatus for Measuring Creep of Concrete at Elevated Temperature, J. of PCA Research and Development Laboratories, PCA Research and Development Bulletin 225, Portland Cement Associations, Vol. 10, No. 3.

Diederichs, U.(1982): Untersuchungen zum Verbundverhalten bei hohen Temperaturen (Investigations on the bond strength at elevated temperatures). Dissertation, TU Braunschweig.

ENV 1992-1-2, (1995). "Design of concrete structures-Part 1-2: General rules-structural fire design", European Committee for Standardization, Brussels.

ENV 1993-1-2, (1995). "Design of steel structures-Part 1-2: General rules-structural fire design", European Committee for Standardization, Brussels.

Furumura, F., Abe, T., and Shinohara, Y. (1995). "Mechanical properties of high strength concrete at high temperature", *Proceedings of the Fourth Weimar Workshop on High Performance Concrete: Material Properties and Design*, Hochschule fuer Architektur und Bauwesen (HAB), Weimar, Germany, Oct., 237-254.

Freskakis, G.N. et al., (1979), "Structural Properties of Concrete of Concrete at Elevated Temperature", Civil Engineering Nuclear Power, Vol. 1, ASCE Natl. Convention, Boston April 1979.

Gvozdev, A.A. (1966) "Creep of Concrete", Mekhanika Tverdogo Tela, Moscow, 137-152.

Gross, H. (1973) "On high temperature creep of concrete", 2nd Int. Conf. on Struct. Mech. in Reactor Techn., Vol. 3, Part H 6/5, Berlin.

Harmathy, T.Z. (1993). "Fire Safety Design & Concrete"., Longman Scientific & Technical.
Hertz, K.(1980), " Bond between concrete and deformed bars exposed to high temperatures", Institute of Building Design, Technical University of Denmark, DK-2800 Lyngby. A paper presented at: CIB W 14 Meeting, Athens, May 19 – 23.

Holmes, M., Anchor, R.D., Cook, G.M.E., and Crook, R.N. (1982). "The effects of elevated temperatures on the strength properties of reinforcing and prestressing steels", *Structural Engineer*, March, 60B(1), 7-13.

Jennings, H.M., and Xi, Y. (1992) "Relationships Between Microstructure and Creep and Shrinkage of Cement Paste", *Material Science of Concrete*, III, Ed. J. Skalny, The Amer. Cer. Soc., Westerville, OH, 37-69

Kasami, H.; Okuno, T., and Yamane, S. (1975) “Properties of concrete exposed to sustained elevated temperature”, Transactions of the 3rd International Confe rence on "Structural Mechanics in Reactor Technology", London, 1.-5. Sept., Vol. 3, paper H 1/5.

Kodur, V.K.R., and Sultan, M.A. (2003). “Effect of temperature on thermal properties of high-strength concrete”, *Journal of Materials in Civil Engrg,* ASCE, March/April, 15(2), 101-107.

Kodur, V.K.R., Dwaikat, M.M.S., and Dwaikat, M.B. (2008) “High-Temperature Properties of Concrete for Fire Resistance Modeling of Structures”, *ACI Materials Journal*, 105(5), September-October, 517 – 527.

Khoury, G.A, Sullivan, P.J.E., and Grainger, B.N. (1984). “Radial temperature distributions within solid concrete cylinders under transient thermal states”, *Magazine of Concrete Research*, 36(128), 146-156.

Khoury, G.A, Sullivan, P.J.E., and Grainger, B.N. (1985a). “Transient thermal strain of concrete: literature review, conditions within specimen and individual constituent behavior”, *Magazine of Concrete Research*, 37(132), 131-144.

Khoury, G.A., Sullivan, P.J.E., and Grainger, B.N. (1985b). “Strain of concrete during first heating to 600˚C under load”, *Magazine of Concrete Research*, 37(133), 195-215.

Khoury, G.A., Grainger, B.N., and Sullivan, P.J.E. (1986). “Strain of concrete during first cooling to 600˚C under load”, *Magazine of Concrete Research*, 38(134), 3-12.

Khoury, G.A., Majorana, C.E. (2001) “Creep of Concrete at High Temperature”, Creep, Shrinkage and Durability Mechanics of Concrete and Other Quasi-Brittle Materials, Edited by F.-J. Ulm, Z.P. Bazant and F.H. Wittmann, Elsevier Science, Ltd., 181-188.

Khoury, G.A., Majorana, C.E., Pesavento, F., and Schrefler, B.A. (2002). “Modelling of heated concrete”, *Magazine of Concrete Research*, 54(2), 77-101.

Lee, J.S., Xi, Y., and Willam, K. (2009a) “A Multiscale Model for Modulus of Elasticity of Concrete at High Temperatures”, *Cement and Concrete Research*, in press.

Lee, J.S., Xi, Y., Lee, K., and Willam, K. (2009b) “Thermo-Hygro Coupling Effect on Strain of Concrete at Elevated Temperatures”, submitted to *ACI Materials Journal*.

Lee, J.S., Xi, Y., and Willam, K. (2008) “Properties of Concrete after High Temperature Heating and Cooling”, *J. of Materials, ACI*, July-Aug. 105(4), 334-341.

Marechal, J.C. (1972) “Creep of Concrete as a Function of Temperature”, In Int. Seminar on Concrete for Nuclear Reactors, ACI Special Publication No. 34, Vol. 1, Ame. Concrete Inst., Detroit, 547-564.

Morita, T., Saito, H., and Kumagai, H. (1992). "Residual mechanical properties of high strength concrete members exposed to high temperature-part 1. Test on material properties", Summaries of Technical Papers of Annual Meeting, Architectural Institute of Japan, Niigata, Aug.

Nasser, K.W., and Neville, A.M. (1965) "Creep of Concrete at Elevated Temperatures, J. of ACI, Vol. 62, Dec., 1567-1579.

Neville, A.M. (1983) "Creep of Plain and Structural Concrete", Construction Press, London.

Neville, A.M. (1970) *Properties of Concrete*, Pitman, London, United Kingdom.

Nielsen, C.V., Pearce, C.J., and Bicanic, N. (2004). "Improved phenomenological modeling of transient thermal strains for concrete at high temperature", *Computers and Concrete*, March, 1(2), 189-209.

Noumowe, A.N., Clastres, P., Debicki, G., and Costaz, J.L. (1996). "Thermal stresses and water vapor pressure of high performance concrete at high temperature", *Proceedings, 4th International symposium on utilization of High-strength/High-Performance Concrete*, Paris, France.

Phan, L.T. (1996). "Fire performance of high-strength concrete: A report of the state-of-the art, Building and Fire Research Laboratory", *National Institute of Standards and Technology*, NISTIR 5934, Dec.

Phan, L.T., and Carino, N.J. (1998). "Review of Mechanical Properties of HSC at Elevated Temperature", *Journal of Materials in Civil Engineering*, ASCE, Feb., 10(1), 58-64.

Phan, L.T. (2004). "Codes and Standards for Fire Safety Design of Concrete Structures in the U.S.", *Workshop fib Task Group 4.3.2, Fire Design of Concrete Structures*, Politecnico di Milano, Italy, Dec.2-4.

Rigberth, J. (2000). "Simplified Design of Fire Exposed Concrete Beams and Columns: An Evaluation of Eurocodes and Swedish Building Code", Report 5063, Department of Fire Safety Engineering, Lund University, Sweden.

Sager, H. et al. (1980), "Hochtemperatur-Verbundverhalten von Beton- und Spannstählen (High temperature behaviour of reinforcing and pre-stressing steels) ", Sonderforschungsbereich 148, Arbeitsbericht 1978 - 1980, Teil II, B 51 - 53, Technical University of Braunschweig, 1980.

Schneider, U., and Herbst, H. (2002). "Theoretical considerations about spalling in tunnels at high temperatures", Technical Report, Technical University Vienna, Austria.

Schneider, U.(1979) "Ein Beitrag zur Klärung des Kriechens und der Relaxation von Beton unter instationärer Temperatureinwirkung" (creep and relaxation of concrete under transient temperature conditions), Forschungsbeiträge für die Baupraxis. Verlag W. Ernst & Sohn, Berlin, S. 133-149.

Schneider, U., and Lebeda, C., “Baulicher Brandschutz, Band 4”, Verlag W. Kohlhammer.

Thelandersson, S. (1987). “Modelling of combined thermal and mechanical action in concrete”, *J. Eng. Mech.,* ASCE, 113(6), 893-906.

Willam, K., Basche, H.D. and Xi, Y. (2004). “Constitutive Aspects of High Temperature Material Models”, *Workshop fib Task Group 4.3.2, Fire Design of Concrete Structures*, Politecnico di Milano, Italy, Dec.2-4.

Willam, K., Rhee, I. and Xi, Y. (2003). “Thermal degradation in heterogeneous concrete materials”, *Proceedings of the EURO-C Conference*, March 17-20, St. Johann i. P., Austria.

PART II:
HIGH TEMPERATURE BEHAVIOR OF RCS

7 Observations of Fire Experiments

There are many available test data in the literature on responses of various reinforced concrete structures under high temperatures. In this chapter, we will first review the test results on structural components like beams and columns, and then on structural systems such as floor slabs.

7.1 Beam tests

- Lin et al. (1981)

Lin et al. (1981) tested 11 RC beams under ASTM E119 standard fire exposure. Their study investigated the influence of a number of factors including beam continuity, moment redistribution and aggregate type on the behavior of RC beams under standard fire conditions. One of the tested beams was simply supported at both ends, while the remaining beams were overhanging at one or both ends. The applied loading on the cantilever was chosen to reflect the continuity effect in RC beams.

With the exception of the beam with simply supported at both end, B-124, all specimens were tested in manner to simulate continuous beams. Six tests were conducted to simulate interior-span conditions, and four to simulated end spans. This was accomplished by maintaining one or both end of the beam at constant elevation by varying load P_2 or loads P_1 and P_2. These cantilever loads generally increased sharply during the first 15 minutes of the fire test, reached a maximum value 30 to 45 minutes after start of test, and more or less remained constant for the reminder of the test. Initial, maximum, and end-of-test values of the P_1 and P_2 cantilever loads are listed in Table 7.1 .

Table 7.1 Loading data (Lin et al., 1981)

Specimen No.	Moment intensity M/M_t at start of test			Span Loads	Cantilever loads						Avg. temp bottom re-inforcement end of test	
					West P1			East P2				
	West support	Midspan	East support		0 hr	Max.	End of test	0 hr	Max.	End of test		
	%	%	%	Kips		kips			Kips		F	C
B-123	50	50	50	11.2	12.9	23.0	20.7	13.6	21.3	22.0	1315	712
B-124	0	50	0	4.5	0	0	0	0	0	0	952	511
B-125	0	50	40	6.4	0	0	0	10.4	20.1	18.1	1123	606
B-126	0	50	40	6.6	0	0	0	10.6	21.4	21.4	1213	655
B-127	55	50	40	10.5	14.9	23.1	19.1	10.2	22.7	20.0	1360	737
B-128	40	50	40	8.8	10.5	19.7	17.4	10.8	19.5	16.7	1450	787
B-129	50	50	50	11.2	13.2	21.6	20.0	13.3	23.3	20.8	1315	712
B-130	60	50	60	13.5	16.1	24.6	24.6	16.1	24.2	24.2	1293	700
B-131	0	50	40	6.4	0	0	0	11.2	21.6	21.6	1280	693
B-132	0	50	60	11.3	0	0	0	33.0	53.1	46.5	1088	586
B-136	55	50	55	13.4	16.2	24.1	24.1	16.0	27.3	22.9	818	436

None of the beams spalled during the fire test. Generally, thin hairline cracks were observed on top surface of the continuous specimens near supports, after the full superimposed loads were

applied but before specimens were heated. Most cracks that developed during the tests opened to widths of 1/16 to 1/8 in. at test completion. Moisture oozed from cracks for different lengths of time.

From the result of simply supported beam, it appears that fire endurance would have been significantly longer if the cutoff bars had been longer. Nevertheless, it is apparent that for simply supported members, fire endurance is the duration of test until moment capacity is reduced to the applied moment. From the results of continuous beams, Except B-136, the mode of failure was flexural. Failure was imminent when three hinges formed. Specimen B-136 failed in shear, possibly because the shear capacity was less than that required by American Concrete Institute (ACI) 318-71. This study concluded that the fire resistance of continuous beams in much higher than that of simply supported beams due to the occurrence of redistribution of bending moment and shear forces in fire conditions.

- Dotreppe and Franssen (1985)

The experimental study, reported by Dotreppe and Franssen, involved testing a simply supported RC beam of rectangular cross section under ISO 834 fire exposure. The loading and heating systems are presented in Fig. 7.1. The beam is loaded and heated symmetrically. The thermal program is applied according to ISO R834. The dimensions of the cross-section and the reinforcement arrangement are indicated in Fig. 7.1.

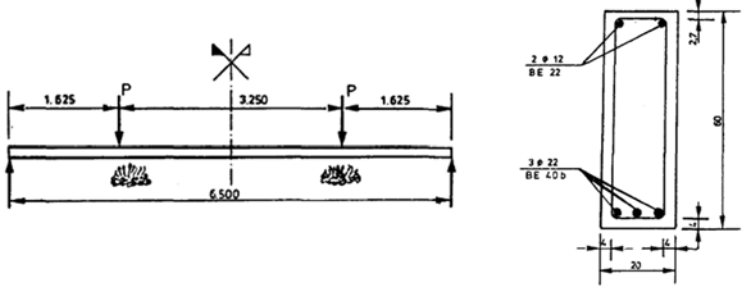

Fig. 7.1 Loading and heating system of the reinforced concrete beam
(Dotreppe and Franssen, 1985)

Fig. 7.2(a) shows the temperature increase in the central bar. In a reinforced concrete beam submitted to a fire test there is a steep thermal gradient on the cross-section producing large deflection even at the beginning of the test when the stiffness properties of materials remain unchanged. Fig. 7.2(b) shows the deflection curve of fire test. The main objective of this fire resistance test was to assess the fire resistance rating of an RC beam.

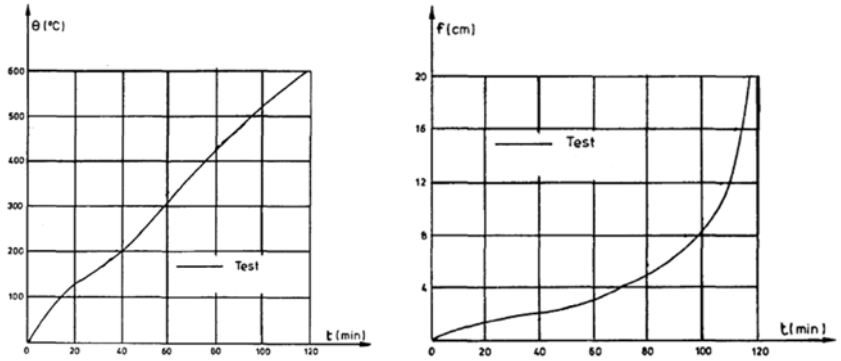

(a) Temperature curve (b) Deflection curve

Fig. 7.2 Temperature curve on the central reinforcing bar and deflection curve (Dotreppe and Franssen, 1985)

- Lin, Ellingwood and Piet (1988)

Lin et al. (1988) conducted fire tests on six full-scale concrete beams subjected to large applied loads for investigating the behavior of reinforced concrete beams exposed to fire. The objectives of the test program were: (a) To examine flexural and shear behavior of beams exposed to fire, and (b) To generate experimental data for validating computer programs developed for calculating thermal and structural behavior of beams exposed to fire.

Test specimens included five 21-in. deep×9-in. wide (533×229mm) and one 24-in. deep×10in. wide (610×254mm) beams. All beams measured approximately 27ft (8.2m) in length, with a 20ft (6.1m) span exposed to fire and an unexposed cantilever loaded so as to provide continuity over one support. They were fabricated with normal-weight concrete. Table 7.2 and Fig. 7.3 show the details of test specimens.

Table 7.2 Details of section and reinforcement layout (Lin et al., 1988)

Specimen	Bar size					Bar end location, from L				
	a	b	c	d	e	A	B	C	D	E
1, 2, 3, 5, 6	#8	#8	#7	#7	-	1in	2ft 2in	12ft 10in	15ft 7in	15ft 11in
4	#8	#8	#7	#7	#8	1in	2ft 8in	12ft 8in	15ft 4in	15ft 5in

Specimen	Cross section H×W	Cover	Dividing line For F stirrup	Stirrup Spacing	
				Left	Right
1, 2, 5	21in×9in	1-1/2in	15ft 7in	8-1/2in	5-3/4in
3, 6	21in×9in	2-1/4in	15ft 7in	8-1/2in	5-3/4in
4	24in×10in	1-1/2in	13ft 11in	10in	4in

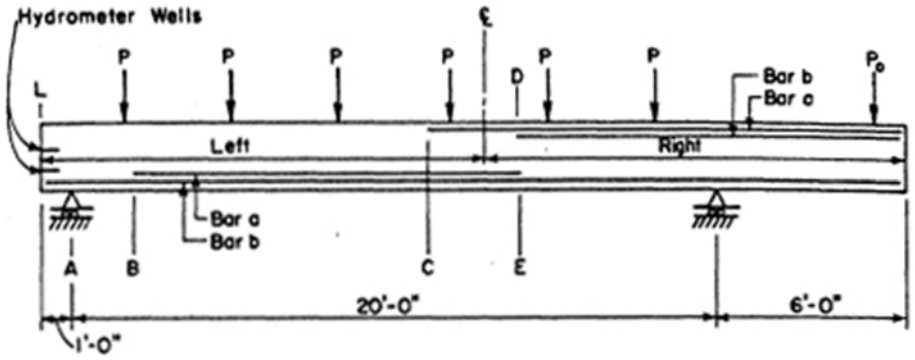

Fig. 7.3 Specimen details (Lin et al., 1988)

Four beams were exposed to the standard fire specified in ASTM E119. The remaining two beams were tested using an exposure denoted as a Short Duration High-Intensity (SDHI) fire. During testing, beams were loaded to produce a negative moment equivalent to 59% of their respective nominal negative flexural strength at the continuous support. And Table 7.3 shows the details of Test conditions

Table 7.3 Details of test conditions (Lin et al., 1988)

Beam No.	Fire exposure type	Specimen age days	Loads		Concrete cover, in	RH** at test	Test duration Hr:Min
			P, kips	P0, kips			
1	ASTM	298	10	26	1-1/2	74	3:40
2	ASTM	369	10	26	1-1/2	73	3:26
3	ASTM	375	10	25	2-1/4	76	4:03
4	ASTM	361	10	39	1-1/2	74	4:08
5	SDHI*	526	10	26	1-1/2	80	4:03
6	SDHI	520	10	25	2-1/4	74	4:03

*: Short duration high intensity fire; **; Relative humidity

In all tests, A few hairline cracks developed across top and side surfaces of the beam over the continuous support. Diagonal shear cracks developed near the continuous support at 1–1/2 hr after the start of the fire and flexural cracks formed in the maximum positive moment region approximately one-half hour later. As the test progressed, shear cracks remained essentially unchanged, but flexural cracks rapidly worsened and surpassed the shear cracks in magnitude during the third hour of the test. All beams formed flexural failure mechanisms that caused the termination of tests. The length of the fire tests were: 3 hr 40 min for Beam No. 1; 3 hr 26 min for Beam No. 2; and 4 hr for Beam No 3 to 6. Applied loads, furnace atmosphere, concrete and steel temperatures, deflections, expansions, and slopes were measured in each test. These data were needed to validate the computer program developed in the Center for Building Technology of the National Bureau of Standards.

This investigation has shown that thermo-mechanical structural analysis, coupled with appropriate material constants, can predict the behavior of reinforced concrete structural elements exposed to different fire exposures, at least within the limits of accuracy required for states limit states design. The ability of the analysis to predict structural behavior is limited by the quality of data available on the structural materials at elevated temperatures, and to a lesser extent by the analytical model which neglects the effect of localized cracks and spalling of concrete. The most important factor affecting predicted beam behavior is the calculated temperature history in the reinforcement. The computation of these temperatures directly from temperatures in the concrete obtained from a two-dimensional thermal analysis tends to be conservative because the capacity of the reinforcement to conduct heat longitudinally is not taken into account. In contrast, accuracy in predicting temperature distribution in the concrete is not as important in predicting load-carrying capacity of reinforced concrete beams.

- Maruta, Yamazaki and Miyashita (1995)

This study undertakes to determine the shear behavior of reinforced concrete members in nuclear power plant facilities following sustained heating to high temperature. A total of nine specimens were tested. Fig. 7.4 shows the details of test specimens. All specimens were of the same size and contained the same reinforcement. The specimens were beams with cross-sections 200mm wide and 400mm deep. The yield strength of the main and transverse bars was 380 MPa. The specified design strength of the concrete was 24 MPa.

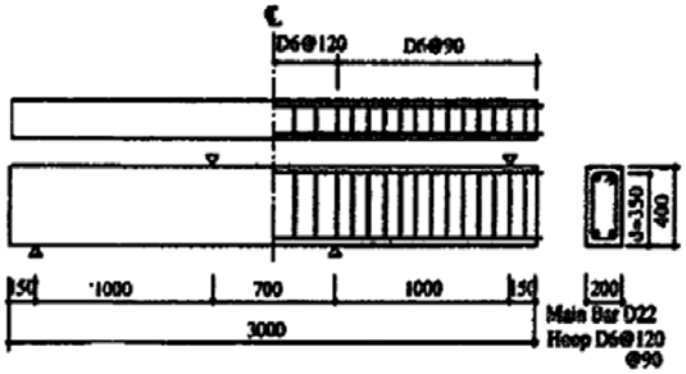

Fig. 7.4 Dimensions and reinforcing details of specimens (Maruta et al., 1995)

Plain core specimens were also cast at the same time to estimate the deterioration in concrete strength in the beams subjected to long-term heating. A core specimen is shown in Fig. 7.5. Each core cylinder was 100mm in diameter and 200mm long.

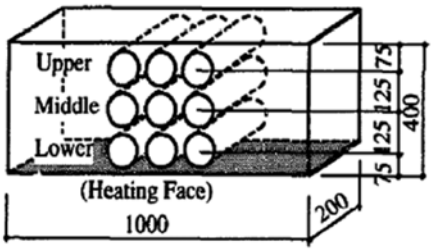

Fig. 7.5 Dimensions of core specimens (Maruta et al., 1995)

The parameters of the test were (1) heating temperature (65, 90, and 175˚C) and (2) heating period (1, 3, 6, and 12 months). A total of nine specimens as shown in Table 7.4 were used with different combinations of these parameters. To examine the core strength, a total of nine plain concrete specimens were cast corresponding to the RC beams and exposed to the same heating conditions

Table 7.4 List of test specimens (Maruta et al., 1995)

Temperature (˚C)	Start(0 months)	1 month	3 months	6 months	12 months
Unheated	F-0	-	-	-	F-12
65	-	L-1	L-3	L-6	L-12
90	-	-	M-1	-	M-12
175	-	E-1	-	-	-

From comparison result of the relationship between the shear force and deformation for specimens heated 65 ˚C and the unheated specimens as shown in Fig. 7.6, No significant difference in behavior was observed between the specimens heated at 65˚C and the unheated specimens.

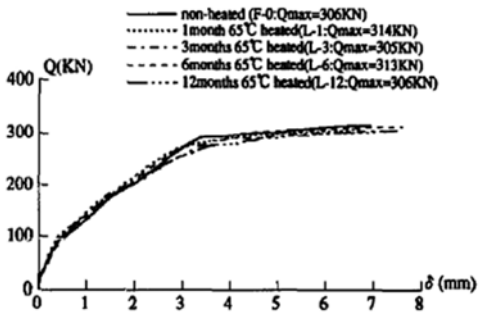

Fig. 7.6 Shear force-deformation relationship for specimens heated at 65˚C and unheated specimen (Maruta et al., 1995)

Fig. 7.7 shows the relationship between the shear force and deformation for specimens heated 90˚C and 175˚C and the unheated specimens. For the specimens heated to 90˚C, the maximum load decreased with increasing heating period. For the specimen heated to 175˚C, approximately 15% degradation of the maximum load was observed, compared with the unheated specimen. The stiffness after cracking of specimens M-12 and H-1 degraded compared with the unheated specimen.

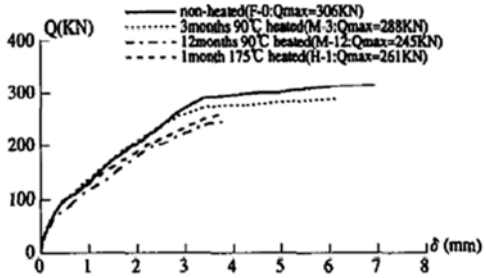

Fig. 7.7 Shear force-deformation relationship for specimens heated at 90˚C and 175˚C and unheated specimen (Maruta et al., 1995)

The deterioration in the shear strength with heating period was investigated. The normalized shear strength ratios of ultimate shear strength of heated specimens divided by that of the unheated specimen were calculated. Fig. 7.8 shows the shear strength ratio plotted against the heating period. For 65˚C heating, no deterioration was observed. For 90˚C heating, the shear strength fell by 6% in 3 months and by 20% in 12 months. For 175˚C heating, the shear strength fell by 15% in 1 month.

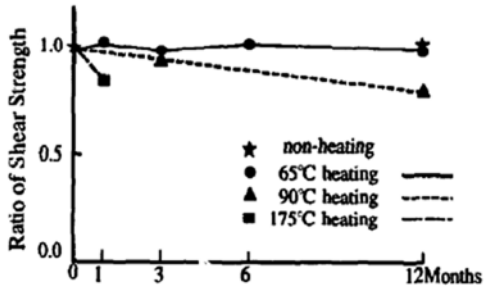

Fig. 7.8 Shear strength ratio with change in heating period (Maruta et al., 1995)

All shear test specimens had the same failure mode in which crushing of the concrete occurred, showing a shear compressive failure. The strength of the core cylinder compared with the shear test under the same heating conditions is discussed. Fig. 7.9 shows the compressive strength ratio plotted against the heating period. From the Figure, the degradation ratio of core strength was greater than that of shear strength in all portions. However, the core strength ratio of the upper portion approximately corresponded to the shear strength ratio. For the specimen heated at 65˚C

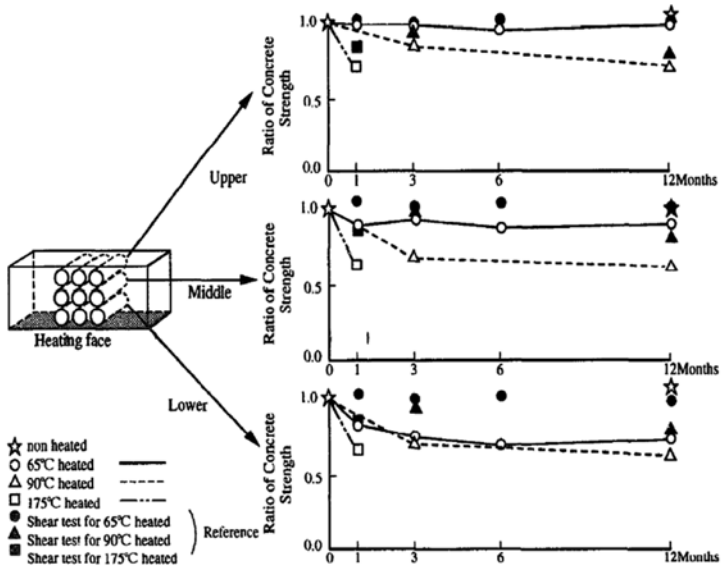

Fig. 7.9 Compressive strength ratio vs. heating period (Maruta et al., 1995)

Fig. 7.10 shows young's modulus plotted against the heating period. The tendency for young's modulus to deteriorate was approximately the same as for the compressive strength ratio.

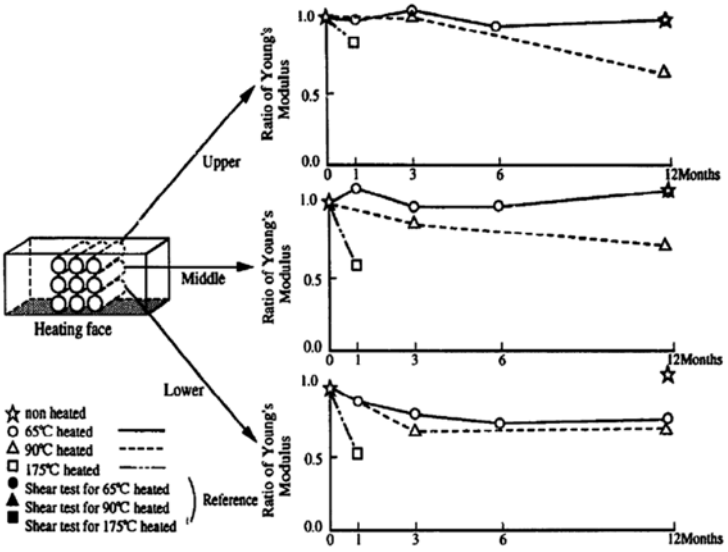

Fig. 7.10 Young's modulus vs. heating period (Maruta et al., 1995)

The results are summarized as follows: (1) The shear strength of the RC beam subjected to 65˚C heating on one side for 12 months showed no degradation. (2) The shear strength after 90˚C heating for 3 months fell by 6%, and after 12 months by 20%. (3) The shear strength after 175˚C heating for 1 month fell by 15%. (4) The deterioration ratio of shear strength was less than that of core strength near the heating side for all temperatures (65, 90 and 175˚C). (5) The shear strength deterioration rate roughly corresponded to that of core strength near the outside air which was subjected to the lowest internal temperature of concrete.

- Shi, Tan, Tan, and Guo (2002)

The effect of force-temperature paths on behaviors of reinforced concrete flexural members were investigated by Shi et al. (2002). These paths are expressed simply by two basic paths: the path of constant forces but subjected to elevated temperature (FT path), and the path of constant temperature but subjected to applying forces (TF path). A total of 13 beam specimens subjected to two such basic paths were tested. Fig. 7.11 and Table 7.5 show details and test result of specimens

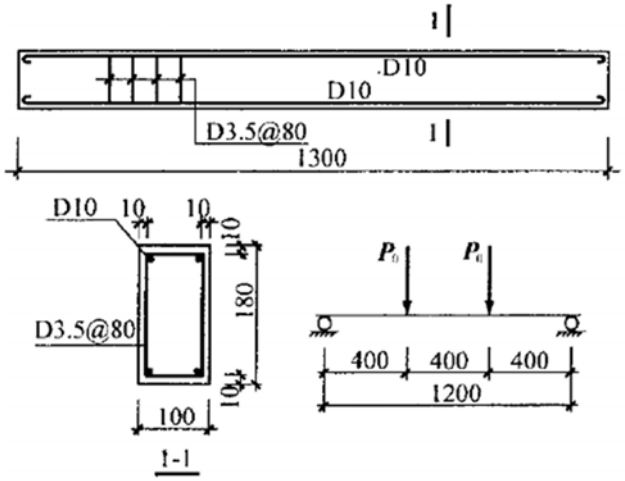

Fig. 7.11 Specimen dimensions, detailing and loading positions (Shi et al., 2002)

Table 7.5 Test results of specimens (Shi et al., 2002)

(a) Specimens subjected to FT path

Specimen no.	Predetermined external load P_0 (kN)	α_{FT}	Ultimate temperature T_u (˚C)
TSB1-0	0.0	0.000	>850.0
TSB1-1	2.0	0.103	727.5
TSB1-2	4.0	0.206	670.0
TSB1-3	6.0	0.308	555.0
TSB1-4	8.0	0.411	540.0
TSB1-5	10.0	0.514	526.0
TSB1-6	12.0	0.617	513.0

(b) Specimens subjected to TF path

Specimen no.	Predetermined temperature T_0 (˚C)	Ultimate temperature P_u^T (kN)	α_{FT}
TSB1-1	20	19.46	1.00
TSB1-2	200	21.47	1.09
TSB1-3	300	18.99	0.98
TSB1-4	400	14.99	0.76
TSB1-5	500	9.08	0.47
TSB1-6	600	5.49	0.28
TSB1-0	850	1.00	0.05

The comparison of ultimate fire resistance between the FT and TF paths is shown in Fig. 7.12. It can be clearly seen that there is little difference between them when T_0 exceeds 525˚C. This is because the value of M_u^T is mainly dependent on the yield strength of tensile reinforcement f_y^T, and the temperature of the tensile reinforcement approaches T_0 after T_0 exceeds 525˚C regardless of the FT or TF path. But when T_0 <525˚C, the converse becomes true. The ultimate temperature for the FT path is always greater than 500˚C when $\alpha_{FT} \le 0.617$. In summary, the specimen fire resistance for the FT path is always greater than that for the TF path.

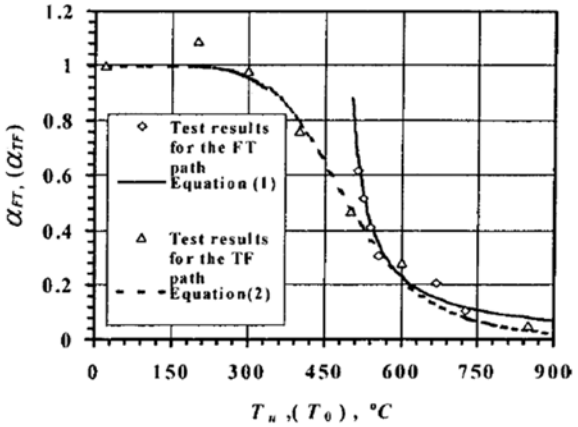

Fig. 7.12 Fire resistances and corresponding comparison for FT and TF paths (Shi et al., 2002)

Since concrete subjected to different stress-temperature paths has different mechanical properties and there is redistribution of stress at a section due to the non-uniform temperature distribution, there will be a great difference in curvature, ϕ, when the specimens are subjected to the same magnitudes of loading and elevated temperature, but undergo different force-temperature paths. Fig. 7.13 shows the comparison of deformations between the FT and TF paths at T_0 =400˚C and 600˚C, respectively. Form comparison of curvatures for specimens subjected to the FT and TF paths, it can be seen that specimen curvatures for different force-temperature paths will experience very different variations.

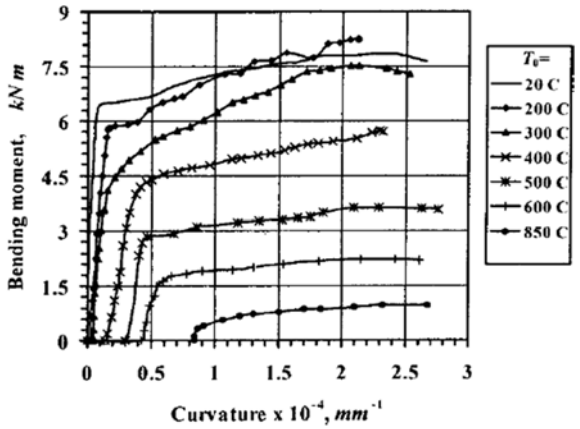

Fig. 7.13 Comparison of deformations at given temperatures for FT and TF paths (Shi et al., 2002)

Thus, in fire-resistant design, especially for statically indeterminate structures, to more accurately ascertain their fire resistances the force-temperature path factor cannot be neglected.

7.2 Column tests

- Lie, Lin, Allen, and Abrams (1984)

Lie *et al.* (1984) conducted experimental study for investigating the effects of axial loading, cross-sectional dimension, moisture content and various types of aggregates on the residual strength of interior concrete columns. Twelve tied, reinforced concrete columns were fabricated and tested. Ten of the columns had a cross-section of 12×12in (305×305mm), one of 8×8in (203×203 mm) and one of 16×16in (406×406 mm). All columns were 12ft 6in (3810mm) long. Three specimens were made with carbonate aggregate and nine with siliceous.

The tests were carried out by exposing the columns to heat in a furnace specially built for this purpose. The heat input into. The test furnace was controlled in such a way that the average temperature followed as closely as possible the standard temperature/time curve given by following:

$$T_f = 20 + 750\left(1 - \exp\left(-3.79553\sqrt{t}\right)\right) + 170.4\sqrt{t} \tag{7.1}$$

Where, t is the time in hours and T_f is the fire temperature in ˚C. Several of the columns were tested under a load, which was concentric. The loads were applied about one hour prior to the test. Table 7.6 shows load and performance of test columns.

Of the variables studied in this report, load, cross-section size and type of aggregate have the largest influence on the fire resistance of reinforced concrete columns. Particularly the use of carbonate aggregate instead of siliceous aggregate will substantially increase the fire resistance of the column. The influence of concrete moisture content on fire resistance is in the practical range, insignificant. The fire resistance of the columns studied is considerably higher than those assigned to them in the National Building Code and in the ACI 216. They also enable the

evaluation of assumptions used for calculating fire resistance by methods based on heat transfer and structural analyses.

Table 7.6 Load and performance of test columns (Lie et al., 1984)

Specimen no.	Load kN (kips)	Length of test Hr : min	Mode of failure
Siliceous aggregate			
1	0	4:00	None
2	1333 (300)	2:50	Compression
3	800 (180)	3:38	Compression
4	711 (160)	3:40	Compression
5*	0	5:00	None
6**	169 (38)	3:00	Buckling
7	1067 (240)	3:28	Compression
8	1778 (400)	2:26	Compression
9	1333 (300)	3:07	Compression
Carbonate aggregate			
10	800 (180)	8:30	Compression
11	1067 (240)	6:06	Compression
12	1778 (400)	3:36	Compression

Cross section 12×12in (305×305 mm) unless otherwise indicated; *=cross section 16×16in (406×406 mm); **=cross section 8×8in (203×203 mm)

- Lin, Zwiers, Burg, Lie and McGrath (1992)

Lin et al. (1992) conducted column tests to study the fire resistance of concentrically and eccentrically loaded reinforced concrete columns. In this study, each fire tests carried according to test purpose and major characteristics as follows: a) standards, b)carbonate aggregate, c)lightweight aggregate, d)high-strength concrete, e)restraint, f)doubled reinforcement, g)size and extra steel, h)shape, i)end conditions, j) other than standard fire, k)eccentric load, and l) eccentric load with constraints. Columns were 12ft 6in (3.8mm) long and had 1-1/2in (38mm) cover to the tie bars. They were fabricated with either siliceous, carbonate, or lightweight aggregate concrete. Specimens included columns with 8×8, 12×12, 16×16, 12×18, 8×36in (203×203, 304×304, 406×406, 304×457, 203×914mm) cross sections and circular columns with 14in (356mm) diameter. Table 7.7 shows details of column specimens

Table 7.7 Details of column specimens (Lin et al, 1992)
(a) concentrically loaded columns

Spec. No.	Cross Section	Aggregate Type	Steel %	Age at Test, Months	Concrete Strength psi	Concrete Relative Humidity %	Test Load, kips	Test Duration, Hr:Min	Type of Failure	Test load/ Allowable Load (%)
1	12"×12"	Siliceous	2.19	27	4950	5	0	4:00	None	0.00
2(1)	12"×12"	Siliceous	2.19	47	5350	15	300(8)	2:50	Comp.	0.65
3	12"×12"	Siliceous	2.19	33	4960	70	180	3:38	Comp.	0.41
4	12"×12"	Siliceous	2.19	33	5090	63	160	3:40	Comp.	0.36
5	16"×16"	Siliceous	2.19	42	5900	9	0	5:00	None	0.00
6(1)	8"×8"	Siliceous	2.19	56	6140	29	38	3:05	Buckled	0.16
7	12"×12"	Siliceous	2.19	35	5230	74	240	3:28	Comp.	0.53
8	12"×12"	Siliceous	2.19	37	5050	NA	400(8)	2:26	Comp.	0.90

9	12"×12"	Siliceous	2.19	42	5560	NA	300[8]	3:07	Comp.	0.63
10	12"×12"	Carbonate	2.19	52	5930	75	180	8:30	Comp.	0.36
11	12"×12"	Carbonate	2.19	50	5350	75	240	6:06	Comp.	0.52
12	12"×12"	Carbonate	2.19	53	5790	75	400	3:35	Comp.	0.81
13	12"×12"	Siliceous	2.19	69	5850	65	77	5:40	Comp.	0.15
14	12"×12"	Siliceous	2.19	38	6320	75	235/461[2]	3:21	Comp.	0.44
15	12"×12"	Siliceous	2.19	33	5130	75	206/465[2]	3:30	Comp.	0.46
16	12"×12"	Siliceous	2.19	32	7680	75	265	3:47	Comp.	0.43
17	12"×12"	Siliceous	2.19	38	7300	75	240	3:54	Comp.	0.41
18	12"×12"	Lightweight	2.19	39	6760	79	242	3:08	Buckled	0.43
19	12"×12"	Lightweight	2.19	42	6160	80	213	4:19	Comp.	0.41
20	12"×12"	Siliceous	2.19	13	6170	61	220	4:12	Comp.	0.36
21	12"×12"	Siliceous	2.19	26	5380	80	300	3:45	Comp.	0.53
22	12"×12"	Siliceous	2.19	41	5630	70	544	4:22	Comp.	0.62
23	12"×12"	Siliceous	2.19	33	5570	75	629	4:45	Comp.	0.65
24[6]	12"×12"	Siliceous	2.19	15	6700	68	670	3:33[7]	None	-
25[4]	12"×12"	Siliceous	2.19	42	5750	60	180	4:02	Comp.	0.37
26[4]	12"×12"	Siliceous	2.19	41	5700	67	225	3:40	Comp.	0.46
27	12"×12"	Siliceous	2.19	19	6150	65	318	5:56	Comp.	0.41
28	12"×12"	Siliceous	2.19	35	6100	NA	170	5:35	Comp.	0.16
29	12"×12"	Siliceous	2.19	13	6040	75	322	4:04	Comp.	0.51
30	12"×12"	Siliceous	2.19	20	6140	76	322	3:45	Comp.	0.50
31[5]	12"×12"	Siliceous	2.19	NA	6030	NA	230	3:41	Comp.	0.45

(1) Force Dry, all other Natural Dry; (2) Initial Load/Max. Load due to full restraint; (3) Compression; (4) Fixed/hinged, other columns fixed/fixed except (5); (5) Hinged/hinged, other columns fixed/fixed except (4); (6) 2.5in. cover to outside steel; (7) Not completed due to furnace malfunction; (8) Exceeded the allowable design load; (9) Fixed/free, other columns fixed/fixed except (4), (5)

(b) eccentrically loaded columns

Test No.	Aggregate Type	Age at Test Months	Concrete Strength psi	Test Load, kips			Eccentricity In.	Initial End Con.	Test Duration, hr:min	Failure Mode
				Concentric	Eccentric	Total				
1	Carbonate	57	5700	-	225	225	1	Hinged/ hinged	3:02	Comp.*
2	Siliceous	45	6100	219	11	230	20	Hinged/ hinged	2:50	Ex-Defl*
3	Siliceous	38	6200	222	11	233	20	Hinged/ hinged	3:45	Ex-Defl
4	Siliceous	37	6500	200	11	211	20	Hinged/ hinged	3:30	Ex-Defl
5	Siliceous	39	5600	210	10	220	20	Hinged/ hinged	2:47	Ex-Defl
6	Siliceous	49	5500	-	265	265	0.96	Hinged/ fixed	3:03	Ex-Defl

*: Comp. = Compression Failure, Ex-Defl = Excessive Lateral Deflection

From the test results on 31 concentrically-loaded reinforced concrete columns exposed to the standard ASTM E119 fire, it clearly indicated that concentrically-loaded 12×12in. columns designed according to ACI 318 will have at least a 3-hour rating. Furthermore, it showed that increasing the cross section size even in only one direction or utilizing a carbonate aggregate concrete rather than a siliceous aggregate concrete would significantly increase fire resistance. The test results also indicated that full restraint on a column did not significantly decrease its fire resistance.

From the test results on 6 eccentrically-loaded reinforced concrete columns, it appear that in spite of a different failure mode, cast-in-place columns supporting loads with eccentricities designed in accordance with ACI Code provisions should also have a three-hour fire resistance. However, the data indicate that while carbonate aggregate concrete columns under concentric loads may have fire resistance times that are several hours longer than siliceous aggregate concrete columns, under eccentric loads, the increase in fire resistance for the carbonate aggregate concrete columns may be only about 10%.

In the concentrically-loaded columns, fire resistance depends primarily on type of aggregate, load/strength ratios, and cross section size. Since eccentrically-loaded columns will fail in excessive lateral deflection rather than in compression, additional factor must be considered in developing rational-design methods for these columns. Rational design methods for these columns would have to include construction of load/moment interaction diagrams as well as calculation of critical buckling loads. These calculations would have to account for end conditions as well as reduction in material strength and reduction in effective cross-section size due to high temperatures.

- Diederichs, Jumppanen, and Schneider (1995)

Diederiches et al.(1995) reported general information on fire test of three short HSC columns (250×250×1000mm), tests by VTT Fire Technology Laboratory (Finland) of ten short HSC columns (150×150×900mm), and a fire test on a full scale column (400×500×5590mm) by the institute für Baustoffe, Massivbau and Brandschutz.

The three columns tested by Diederichs et al. were made of three different concrete mixtures (I, II, and III). Mixture I had specified cube strength of 101MPa and contained fibers (not clearly specified). Mixture II had specified cube strength of 105MPa and contained no fibers. Mixture III had specified cube strength of 90MPa and contained fibers. The columns were subjected to 100% of the design load prior to fire testing.

The two columns with fibers experienced minor spalling (mixture I) and no spalling (mixture III) during fire tests. Fire tests on these columns were terminated at 125minutes after the start of the tests. The mixture II column (without fibers) experienced spalling at about 6 minutes into the fire test. Spalling continued until 30 minutes into the test when it reached the longitudinal reinforcement at the edges of the column. The test was terminated at 45 minutes, which is significantly less than the time of 125 minutes for specimens with fibers.

In the VTT fire tests, the ten HSC specimens were made of three different concrete mixtures, all contained variable fiber contents.

Group 1: Portland cement PZ 55 F with a concrete cube strength of 85 MPa
Group 2: Portland cement PZ 55 F with a concrete cube strength of 105 MPa
Group 3: Portland cement PZ 45 F with a concrete cube strength of 45 MPa

VTT's fire tests were conducted according to the German standard DIN 4102 (similar to International Standard ISO 834). None of the columns experienced spalling. All columns were reported to have failed due to loss of compressive strength at high temperature. The fire resistance times were 51 minutes for the HSC columns (Groups 1 and 2) and 72 minutes for the NSC columns (Group 3).

In the full scale column test, the specimen was made of concrete with a specified cube compressive strength of 110 MPa and contained fibers. The column was eccentrically loaded

with 100% of its design load and exposed to ISO 834 standard fire from all four sides. Shallow spalling occurred at about 10 minutes after starting the test and stopped after 30 minutes. At 181 minutes, the column collapsed due to compressive failure of the concrete near the maximum stressed cross section.

This study indicated that the use of capillary forming fibers help reduce the potential for spalling in HSC columns and suggested that further studies be conducted on the effects of variations in fiber contents.

- Dotreppe et al. (1996)

Dotreppe et al. (1996) conducted experimental studies on the determination of the main parameters affecting the behavior of reinforced concrete columns under fire conditions. The parameters used were the load level, the dimension of the cross section, the length of columns, the main reinforcement, the concrete cover and the eccentricity of the axial load.

The fire resistance tests were performed according to the Belgian Standard NBN 713.020 and the columns were exposed to fire on four sides. The support conditions of the columns were hinges at both ends. The dimensions of the cross section were: 200×300mm, 300×300mm, and 400×400mm. The column lengths were 3.95m and 2.10m. Concrete covers of 25mm, 35mm, and 400mm were used. Eccentricities of (-20 mm, 20mm), (20mm, 20mm), and (0.0mm, 0.0mm) were used with respect to the central axis of the 300×300mm cross section.

Longitudinal reinforcing bars of 12mm, 16mm, and 25mm in diameter were used. Although the type and arrangement of stirrups was not a parameter buckling of some individual longitudinal reinforcements may occur between two stirrups at column failure. Therefore, decreasing the spacing between stirrups might improve the behavior of the column under fire conditions, however theoretical and experimental research should be performed in order to quantify this effect. A summary of the test results follows:

(1) In all problems involving fire resistance, the load level (column stress) is the most important factor. The fire resistance decreases when load increases. (2)The dimensions of the cross section influence the fire resistance. The fire resistance of 200×300mm sections was between 1 hour and 2 hours, while in most of the 300×300mm sections the fire resistance was greater than 2 hours. However the applied load must be limited and reinforcement with large diameters rebars should be avoided. (3) In the case of 400×400mm columns, the fire resistance time was appreciably shorter than expected. For one of the columns, the fire resistance time was shorter than 1 hour, and for the other, the fire resistance time was between 1 hour and 2 hours. These inconsistent results may be partly explained by the existence of reinforcement with large diameters in one case, and by the use of a section with large dimensions and small concrete cover in both cases. (4) The increase of column length had a negative influence on column failure at normal as well as at high temperature because of geometrically nonlinear effects. (5) In principle, the increase of the concrete cover should result in an increase of the fire resistance or of the admissible load level, since the temperature in the main reinforcement increases less rapidly when the column begins to deflect laterally. The test results showed that the increase of concrete cover had a positive effect on the fire resistance. (6) The use of eight 16mm diameter reinforcement instead of four 25mm diameter reinforcement showed a positive effect on the fire resistance in terms of strength. But, additional tests on columns involving reinforcing with large diameter bars are still required to clarify the effect of the bar diameters of longitudinal reinforcement. (7) Test results of eccentrically loaded columns (-20mm, 20mm) and (0mm, 0mm) showed approximately the

same failure results. On the contrary, the use of eccentricities (20mm, 20mm) exhibited a decrease of the load capacity levels.

- Franssen and Dotreppe (2003)

Feanssen and Dotreppe (2003) performed fire tests of circular concrete columns to examine the influence of the circular shape on the behavior under fire conditions. Test specimens, four columns with circular cross section (diameter 300mm) and a length of 2100mm, have been tested. Two columns are reinforced with 6φ20 longitudinal bars (A_s/A_c=2.67%) and two with 6φ12 (A_s/A_c=0.96%). For each specimens the transversal reinforcement is realized with 8φ circular stirrups with a spacing of 100mm until 400mm from the supports, and a spacing of 200mm in the central part. The concrete cover is c=30mm on the stirrups and c=38mm on the main bars, i.e. for the longitudinal bar an axis distance a=44mm for φ12 bars and a=48mm for φ20 bars. The material qualities are C60 siliceous for concrete and S 500 for the steel reinforcing bars. The temperature in the furnace varied according to standard ISO 834 (very similar to the ASTM E119). The test results are summarized in Table 7.8 .

The following conclusions were drawn from this study: (1) Observations made during experiments show that surface spalling was noticed between 20 and 60 minutes of fire test. The circular shape of the cross-section does not prevent the occurrence of this phenomenon. (2) No explosive spalling occurred with the high strength concrete C60 used here. (3) The diameter of the longitudinal reinforcement #12 or #20 had no significant influence on surface spalling. (4) An increase of the load level leads to a significant decrease of the fire resistance. (5) Two simplified calculation procedures developed previously at the University of Liege have been used to evaluate the ultimate capacity of the four columns at elevated temperature. In order to take account of the short length of the specimens, a new formulation has been proposed for the buckling coefficient used in the second method. (6) With this new formulation, both methods lead to acceptable and safe values for design purposes.

Table 7.8 Test results (Feanssen and Dotreppe, 2003)

(a) Load applied and fire resistance obtained for the four columns

Column	Main reinforcement	Load applied (kN)	Load applied/ Design strength, N_{sd}	Fire resistance (min)
C1	6φ12	1260	0.59	156
C2	6φ12	1770	0.83	131
C3	6φ20	1450	0.57	187
C4	6φ20	1900	0.75	163

(b) Main observations during the tests

Column	Time (min)	Observations
C1	25	Sloughing off of concrete in many places of the external layer
C2	20	Large cracks (mainly longitudinal)
	29	Sloughing off of concrete of almost the whole external layer
C3	34	Large cracks at the bottom of the column a few moments later sloughing off of concrete at the same place
	60	Significant increase of the damage
C4	30	Large cracks at the bottom of the column a few moments later sloughing off of concrete at the same place
	38	Significant increase of the damage

- Kodur and McGrath (2003)

In this study, full-scale fire endurance tests on six HSC columns were conducted to determine the behavior of full-scale HSC structural columns under standard building fire exposures, and to evaluate its fire endurance.

Table 7.9 Summary of test parameters and results (Kodur and McGrath, 2003)

Column	Size (square, mm)	Reinf. Qty-size	Tie-conf. spacing	Agg. Type	Factored Resistance (kN)	Comp. strength (MPa)	RH %	Test load (kN)	Test Load /Serv. Load	Fire End. (Min.)
HSC1	406	8-25M	90˚@ h	S	6436	100	69	3080	0.63	239
HSC2	406	8-25M	90˚@ h	S	5900	86	86	2406	0.54	224
HSC3	406	8-25M	90˚@ h	C	7400	96	57	4919	0.90	104
HSC4	305	8-25M	135˚@ h/2	C	3145	120	50	1979	0.82	266
HSC5	305	8-25M	135˚@ h/4	C	3145	120	68	2363	0.98	290
HSC6	305	8-25M	135˚@ h/4	C	3145	120	64	2954	1.23	266

h: width of the column, S: Silceous, C: Carbonate, RH: Relative humidity

All six columns were made of HSC and were of 3810mm length. Three of the columns, HSC1 to HSC3, were of 406mm cross sections, while the remaining three, HSC4 to HSC6, were of 305mm, The dimensions of the column cross section and other specifics of the column are given in Table 7.9. The elevation and cross-sectional details of the columns together with the locations of the ties are given in Fig. 7.14. And Full details on fabrication of these columns, including rebar arrangement, concrete placement, curing, and instrumentation is given by Kodur et al. (2000). Table 7.9 also shows the results of the six column tests.

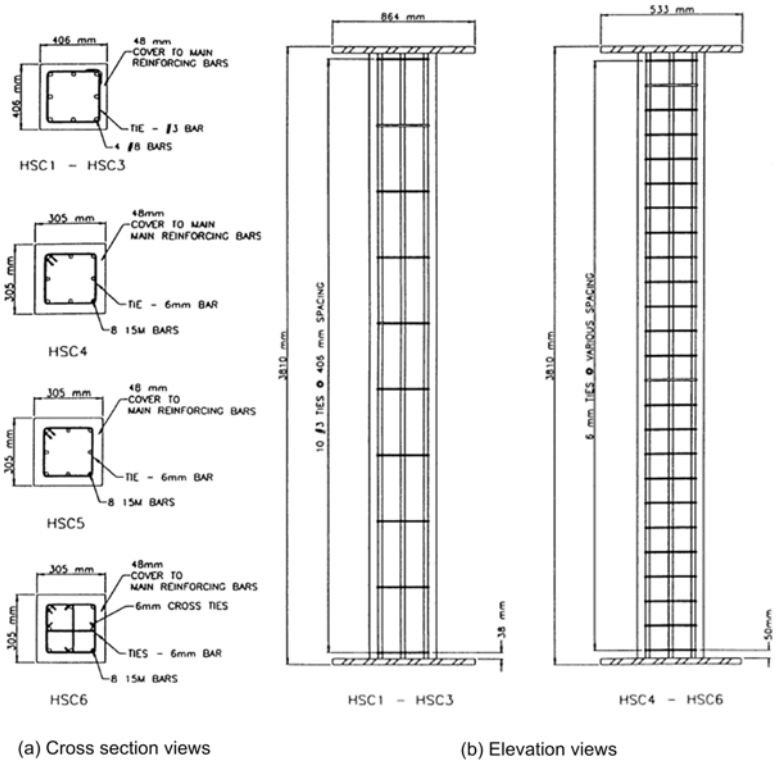

Fig. 7.14 Elevation and cross sectional details of HSC columns (Kodur and McGrath, 2003)

Based on the analysis of test data and the visual observations made during and after the fire tests, some of the factors that influence the fire endurance of HSC columns are briefly discussed below.

• Effect of Concrete Strength

Data from these experimental studies indicate that good fire endurance can be obtained for HSC columns. However, a comparison of the fire endurance in Table 7.9, with that of normal strength concrete columns (kodur & Sultan, 1998; Lie & Woollerton, 1994) indicates that the HSC columns have the lower fire endurance of the two. While for NSC columns a fire endurance of about six hours was obtained in Lie's Report (1993), for HSC columns, with similar confinement, fire endurance of about four hours was obtained. Data from the Table shows that high fire endurance (three hours or more) can be obtained for HSC columns even under full service loads. However, HSC columns must be reinforced with increased levels of confinement reinforcement (as prescribed in CSA-A23.3-M94) over that used in NSC columns, if the same fire endurance ratings are to be achieved by both types of columns.

• Effect of Lateral Reinforcement

Results from experimental studies can be used to study the influence of confinement on the fire performance of HSC columns. The higher fire endurance in columns HSC4 to HSC6, as compared to columns HSC1 to HSC3, can be attributed to the closer spacing, and better detailing of the column ties (ties were bent 135˚ back into the core of the column and increased lateral reinforcement).This is in spite of the fact that the 90˚ ties enclosed larger columns, which characteristically exhibit better fire resistance than smaller column sections. Also, despite the

smaller section size for columns HSC4 to HSC6, these columns with higher levels of confinement, demonstrated better fire performance than the larger columns with 90˚ ties at a larger spacing. It should be noted that for column HSC5, where additional confinement was provided, fire endurance as high as 290 minutes was obtained even under full service load. Further, Column HSC6 has attained a high fire resistance of 266 minutes under an increased load level, as a result of enhanced confinement provided by the provision of cross-ties.

• Effect of Load Intensity

The influence of load on the fire endurance of HSC columns can approximately be gauged by comparing the performance of columns HSC5 and HSC6. The fire endurance of a column increases with decreasing load. The fire endurance of Column HSC6, with a load intensity of 1.23, is 266 minutes as compared to 290 minutes for Column HSC5 with a load intensity of 0.98. This lower fire endurance occurred in spite of Column HSC6 having a higher confinement (additional cross-ties) than Column HSC5. Also, the lower fire resistance of Column HSC3, as compared to that of Columns HSC1 and HSC2, is due to higher load intensity on this column.

• Effect of Aggregate Type

The effect of the aggregate type on the fire endurance of HSC columns is illustrated by comparing the performance of Columns HSC1 and HSC4. While there are other differences in the configuration of these two columns, such as the concrete strength and load level, one of the major variables is the type of aggregate. The fire endurance of column HSC4 made with carbonate aggregate concrete is 10% higher than Column HSC1 made with siliceous aggregate concrete. This occurs mainly because carbonate aggregate has a substantially higher heat capacity (specific heat) than siliceous aggregate, due to an endothermic reaction that takes place in carbonate aggregate at about 700˚C (Lie, 1993).

The aggregate type also influences the spalling phenomenon. In Columns HSC1 and HSC2, the extent of spalling, before the failure of the column, was quite high as compared to the other columns. This could be partly attributed to the effect of aggregate type used in the concrete mix. Of the two concrete types, carbonate aggregate concrete provides better spalling resistance than siliceous aggregate concrete. The higher specific heat and lower thermal expansion of carbonate aggregate concrete at higher temperatures, contributes to this spalling resistance. The specific heat of carbonate aggregate concrete, above 600˚C temperature, is generally much higher than that of siliceous aggregate concrete. This specific heat is approximately ten times the heat needed to produce the same temperature rise in siliceous aggregate concrete. The increase in specific heat is likely caused by the dissociation of the dolomite in the carbonate concrete, and is beneficial in preventing the spalling of the concrete.

- Ali , Nadjai, Silcock, and Abu-Tair (2004)

Ali et al. (2004) conducted the fire tests of 99 high and normal strength concrete columns to investigate the effect of restraint degree, loading level and heating rates on the performance of concrete columns subjected to elevated temperatures with a special attention directed to explosive spalling. A diagram detailing this experimental program is shown in Fig. 7.15. The parameters involved include:

(1) Applied loads: Four loading levels were involved α_L =0, 0.2, 0.4, and 0.6 of BS8100 column design strength.

(2) Axial restraint: Three levels of restraint degrees α_K were involved 0, 0.1, and 0.2. Restraint degree = Applied axial stiffness/column axial stiffness.
(3) Two heating rates: High (HR1) and low (HR2) as shown in Fig. 7.16. The high rates represent the BS476 fire curve.
(4) Two concretes: High (106 N/mm^2) and normal (43 N/mm^2) strength were involved in the research.
It is important to emphasize that 3 specimens were tested in each case (factor combination). A total of 93 half-scale columns (column length = 180mm) constructed from normal and high strength concrete were involved in the tests representing 31 combinations of parameters (see Fig. 7.15). The final part of program included an experimental investigation of methods designed to prevent explosive spalling of 6 columns

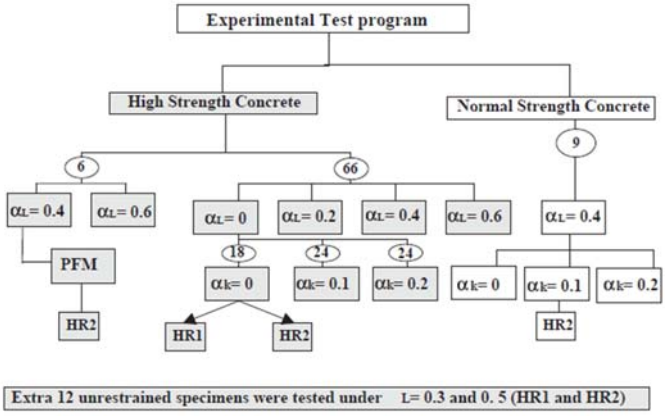

Fig. 7.15 Experimental research program (Ali et al., 2004)

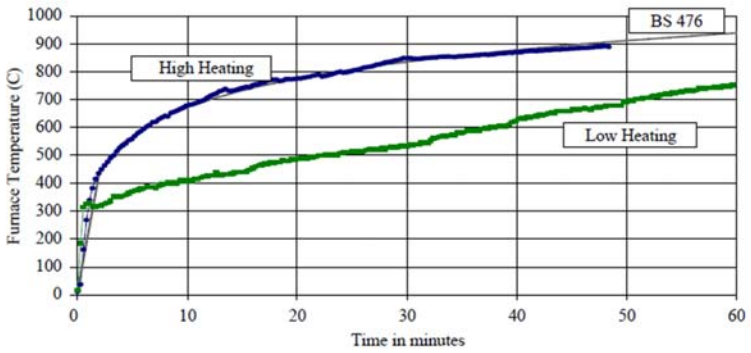

Fig. 7.16 Heating rates adopted during the tests (Ali et al., 2004)

Based on the analysis of test data and the visual observations made during and after the fire tests, the following conclusions were drawn from this study:
(1) In all of the tests conducted, explosive spalling occurred during the first 45 min of the heating. Always minor spalling took place first followed by major and severe spalling. (2) Tests showed that increasing the loading level not increase concrete spalling for both of the high and low heating regimes. Low heating rate reduced the risk of explosive spalling. (3) Increasing the degree of restraint increased the value of the generated forces in the columns. And the generated

restraint forces in normal strength concrete columns were very close to those generated within the high-strength concrete columns. (4) Normal and high-strength concrete columns showed similar susceptibility to explosive spalling under loading only (without restraint) tests. Normal strength concrete columns showed higher spalling degrees when tested under restraint. (5) The tests showed that restraining the column's expansion did not increase the risk of spalling. Increasing the loads imposed on the column reduces the maximum value of the generated restraint forces. And unloaded columns generated restraint forces that reached 0.25 of the column design strength, while loaded columns (0.2 loading levels) generated forces around 0.12 of the design strength.

- Benmarce and Guenfoud (2005)

Benmarce and Guenfoud (2005) conducted fire tests of twelve high strength concrete columns under two heating rates to investigate the effect of boundary condition factors including restraint against thermal expansion and load level at failure temperature. There are two extremes of natural fires to be used in this experimental work. The first curve represents the BS476, defined as the high heating rate (HH) with high energy, high temperatures and short duration, likely to induce high surface gradients, promoting spalling. The other curve represents the ISO standard heating, defined as low heating rate (LH), producing lower peak temperatures but is of longer duration sufficient to permit significant heat conduction, which may produce a large build up of vapor pressure and also create significant thermal expansion producing restraint force.

Table 7.10 Test results (Benmarce and Guenfoud, 2005)

Ref.	Restraint ratio	Load ratio	Heating rate	Axial displacement (mm)	Additional generated force (kN)	Failure Time (min)	Failure temperature (˚C)
HSC1	0.1	0.2	High	1.67	66.80	70	973
HSC2	0.1	0.2	Low	1.90	78.03	102	890
HSC3	0.1	0.4	High	1.03	38.96	43	927
HSC4	0.1	0.4	Low	1.01	43.50	73	705
HSC5	0.1	0.6	High	0.31	10.00	21	802
HSC6	0.1	0.6	Low	0.48	15.59	42	639
HSC7	0.2	0.2	High	1.51	104.10	59	981
HSC8	0.2	0.2	Low	1.61	116.67	119	786
HSC9	0.2	0.4	High	0.89	49.60	44	925
HSC10	0.2	0.4	Low	0.97	69.05	78	727
HSC11	0.2	0.6	High	0.50	38.55	25	790
HSC12	0.2	0.6	Low	0.59	42.67	51	654

Two principal factors of this study are the load ratio (LR) and the restraint ratio (RR). The load ratio (LR) is defined as the ratio of the applied load to the BS8110 design load. The restraint ratio (RR) is defined as the ratio of the column (k_c) to the restraint stiffness provided by the structure (k_c).

Twelve high strength concrete columns were tested at load ratio (LR) of 0.2, 0.4, and 0.6 under restraint ratio (RR) of 0.1 and 0.2, behaved in a similar manner. All specimens failed by axial deflection, no buckling took place. The main findings from this research are presented in Table 7.10 . It is worth noting that most of the additional forces have generated less than 15% of the

design load, under both high heating rates. The additional generated forces depend on the load ratio but are independent on the restraint ratio. The temperature gradients within the concrete columns exposed to both high and low heating rates is shown in Fig. 7.10.

The main conclusions that can be drawn from this experimental research are as follows:
(1) All specimens failed by axial deflection, no buckling took place. There has been no premature failure. (2) Most of the additional forces have generated less than 15% of the design load, under both high heating rates. The additional generated forces depend on the load ratio but are independent on the restraint ratio. An increase of restraint against axial column expansion generated less additional forces. (3) The peak value of axial deformation occurs just as the temperature of the concrete centre reaches 180˚C causing explosive spalling. The maximum value of axial displacement is independent of the rate of heating and it is dependent on the load that has been applied during the test. (4) Spalling of concrete has been observed in many tests. Evaporation of moisture occurred when the temperature within the concrete centre reaches approximately the value 200˚C. The water was boiling and evaporating through these points releasing by that the internal pressure and causing explosive spalling.

- Jau and Huang (2008)
This study investigated the behavior of corner columns under axial loading, biaxial bending and asymmetric fire loading. Corner columns are usually under high biaxial eccentricity. Furthermore, during a fire, only the interior two faces of corner columns may be exposed to fire in contrast to interior columns of which all four faces are exposed. The material asymmetry of concrete after fire further complicated the behavior of corner columns. Six RC corner columns were manufactured for this research under high temperatures.

All experiments were performed in the fire laboratory of the Architecture and Building Research Institute (ABRI) in Gui-Ren, Tainan, Taiwan. The fire curve followed the Chinese National Standards (CNS) 12514, which is the same as the curve from International Organization for Standardization (ISO) 834. RC columns with dimensions of 300×450×2700 mm were cast for this study. The design material strength were f_c' =27.6MPa (the test strength was 33.7 MPa) and f_y = 413.8 MPa (the test strength was 475.87 MPa). Two rebar sizes, No. 8 (φ25mm) and No. 10 (φ32mm), were used as longitudinal reinforcement and No. 4 (φ13mm) steel was used for ties spaced at 100 mm. The design follows the ACI 318 code. Column size is commonly used for 3-storey buildings. The steel ratio was 2% and 3%; the cover was 50 mm (non pre-cast, exposed to earth) and a cover of 70 mm for comparison.

Table 7.11 Column specimen data (Jau and Hwang, 2008)

Specimen	Thickness of cover (mm)	Longitudinal reinforced (mm)	Steel ratio (%)	Fire duration (h)
A12	50	No. 8 (φ25mm)	1.8	2
A22	50	No. 10 (φ25mm)	2.9	2
B12	70	No. 8 (φ32mm)	1.9	2
A14	50	No. 8 (φ25mm)	1.8	4
A24	50	No. 10 (φ32mm)	2.9	4
B24	70	No. 10 (φ32mm)	3.0	4

The test parameters were: fire duration, steel ratio (longitudinal reinforcement) and cover

thickness. The eccentricity was a constant in this experiment. Table 7.11 shows the details of each column. The temperature changes and appearance of the columns were observed and recorded during fire loading. The longitudinal and lateral displacements were measured during the strength tests, which were performed after the columns were exposed to high temperatures.

Based on the result of the experimental studies, the following conclusions can be drawn: (1) The dimensions of the core of the column are very important for the residual strength. For the same fire duration, the larger core area gives a higher residual strength. The thicker the cover, the earlier the cover tends to fall off. The column strength depends mainly on the core of concrete. Therefore, if the core area is increased, the RC column will have a higher residual strength after high temperature exposure. This statement also holds for columns not affected by high temperature. (2) The factors affecting initiation of cracks are, in sequence of importance, fire duration, concrete cover thickness, and steel ratio. However, the existence and the characteristics of surface cracking after fire are not directly related to strength loss. (3) The temperature in the interior part of the specimen continued to rise even after the furnace was turned off. That is, the temperature of the exterior part of the specimen was decreasing while the temperature of the interior was increasing. This difference may cause secondary damage to the column and further complicates analysis. (4) The investigation of the residual strength ratios shows that: (a) the longer the fire, the less the residual strength ratio, (b) the less the steel ratio, the less the residual strength ratio, and (c) the thicker the cover, the less the residual strength ratio. (5) Fire safety behavior of concrete was and is an important topic in building. This study only focused on low-rise buildings, which have a lower axial load. High-rise building is a different issue. It involves high strength material, slender columns, and high axial forces. Their behavior is more complex and they were not included in this study. The findings of this study of residual strengths can be used for future evaluation, repairs and strengthening.

7.3 Reinforced concrete structure systems for floor and slab

- Gustaferro and Abrams (1971)

Fire tests (ASTM E 119-69) were conducted on two concrete waffle flat-slab floor specimens. The 14×18ft specimens were made with carbonate-aggregate concrete. Joists were 6in. wide and 8in. deep (nominal) and the main domes were 30×30 in. in plan. One specimen had a 3 1/2in., deck slab and the other, a 5in. slab. Specimens were supported at the four corners.

Fig. 7.17 shows the important features of the two specimens. The main difference between them was in the thickness of the deck slab. Specimen S-53 had a 5in. thick (nominal) slab, whereas the slab of S-54 was 3in. thick. Because the specimen size was fixed by the dimensions of the floor furnace, three sizes of domes were necessary to obtain the desired joist configuration. Twelve domes were 30×30 in.; six were 20×30 in.; and eight were 14 1/2×30in. In addition, 14 partial domes were used around the perimeter of each specimen. All domes were 8in, deep. Joists were 6in. wide at the bottom with 1:12 side drafts.

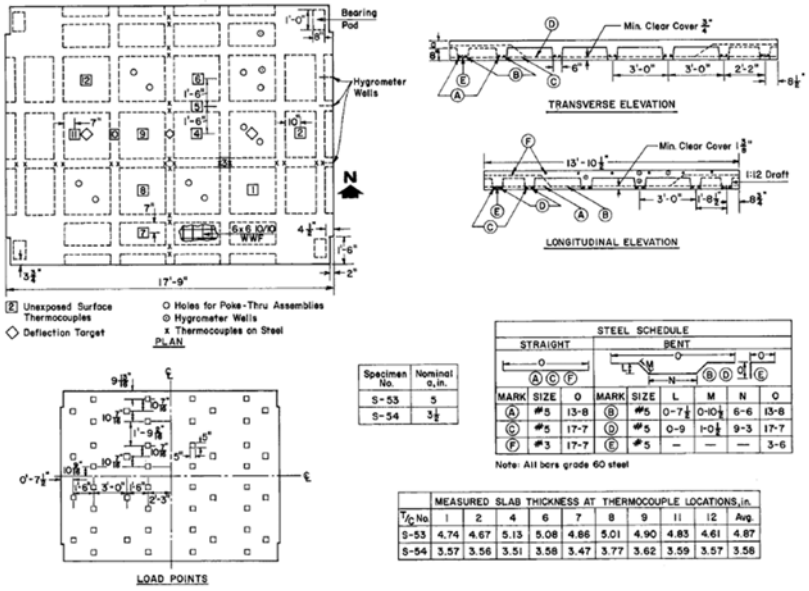

Fig. 7.17 Principal features of the specimens (Gustaferro and Abrams, 1971)

Principal results are summarized in Table 7.12 . Fig. 7.18 shows data on unexposed surface temperature, reinforcement temperature, midpoint deflection, expansion, and thermal restraint forces.

Table 7.12 Summary of Fire test data (Gustaferro and Abrams, 1971)

Data	Specimen S-53			Specimen S-54		
Average slab thickness, in.	4.87			3.58		
Age at test, days	345			253		
Concrete compressive strength at test, psi	4,030			4.850		
Average relative humidity at slab middepth, persent	54			60		
Equivalent live laod, psf	139			102		
Live load deflection at mid point, in	0.35			0.24		
Fire exposure duration, hr: min	4:03			4:03		
Adjusted time for avg. temp rise of 250˚F, hr: min	2:18			1:38		
Adjusted time for max temp rise of 325˚F, hr: min	2:04			1:28		
Date at time indicated	1hr	2hr	4hr	1hr	2hr	4hr
Longitudinal expansion, in.	0.60	0.60	0.60	0.75	0.75	0.75
Lateral expansion, in	0.48	0.48	0.48	0.60	0.60	0.60
Longitudinal thermal thrust, kips	260	420	590	115	250	320
Lateral thermal thrust, kips	225	410	560	115	290	340
Midpoint deflection, in	1.11	1.00	1.00	0.90	0.59	0.49
Avg. longitudinal reinforcement temp, deg F	922	1186	1463	867	1164	1429
Avg. lateral reinforcement temp, deg F	724	1038	1322	707	1038	1321

Live load deflections at midpoint prior to testing were 0.35 and 0.24 in. for S-53 and S-54. The greater deflection for S-53 was probably a result of the higher load and lower concrete modulus of elasticity. During the fire tests, the deflection increased to about an inch during the first hour of test, and then either remained constant or gradually diminished, as shown in Fig.

7.18. Specimens were permitted to expand certain amounts and then further expansion was stopped. Most of the allowed expansion occurred within the first half hour of test, as shown in Fig. 7.18. Thermal thrusts that developed because the specimens were not entirely free to expand are shown in Fig. 7.18. Thrusts were greater for S-54 than for S-53 because S-54 was not permitted to expand as much as S-53. Fire endurances were determined by the criteria for temperature rise of the unexposed surface. In both tests, the fire endurances were longer than results of 3×3ft fire tests had indicated, probably because of the heat sink effect of the joists.

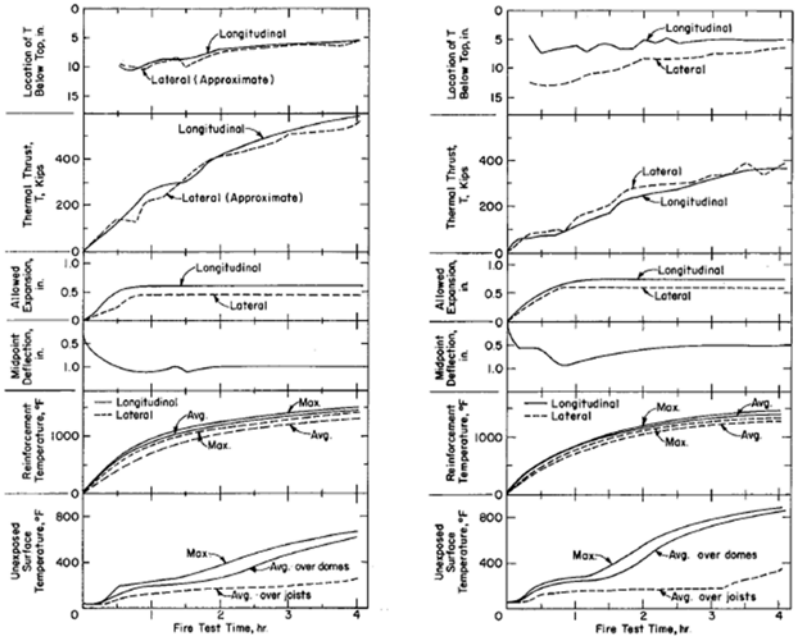

Fig. 7.18 Data from fire test of specimens (Gustaferro and Abrams, 1971)

- Abrams, Gustaferro, and Sales (1971)

In this study, fire tests were conducted on eight concrete pan-joist floor specimens. The 14×18ft specimens were made with carbonate, siliceous, or expanded shale aggregates. Specimens were approximately 14×18 ft in plan, with the joists spanning the 18ft direction, as shown in Fig. 7.19. Metal pans, 30 in. wide by 10 in. deep, were used as forms. Joists were 5 in. wide at the bottom with 1:12 side draft. A transverse beam, 6 in. wide, was cast integrally with the specimen at each end to facilitate handling.

The fire endurance of each of the eight full-scale pan-joist floor specimens was determined by the rise of the unexposed surface temperature, rather than by structural considerations. Fire endurances of the full-scale specimens (temperature rise of unexposed surface) correlated well with results of similar 3×3ft slab specimens, as shown in Fig. 7.20. Specimens supported the design loads during the standard fire tests from 1 to 4 hours even though the temperature of the reinforcing steel reached 1,300 to 1,800 deg. F. A wide range of restraint of thermal expansion was used in various tests, with expansions ranging between 0.3 and 1.1 in. in 18 ft, Resulting maximum thermal thrusts ranged between 780 and 110 kips in the longitudinal direction, The

structural integrity of the specimens can be explained in terms of thermal thrust "interaction diagram envelopes."

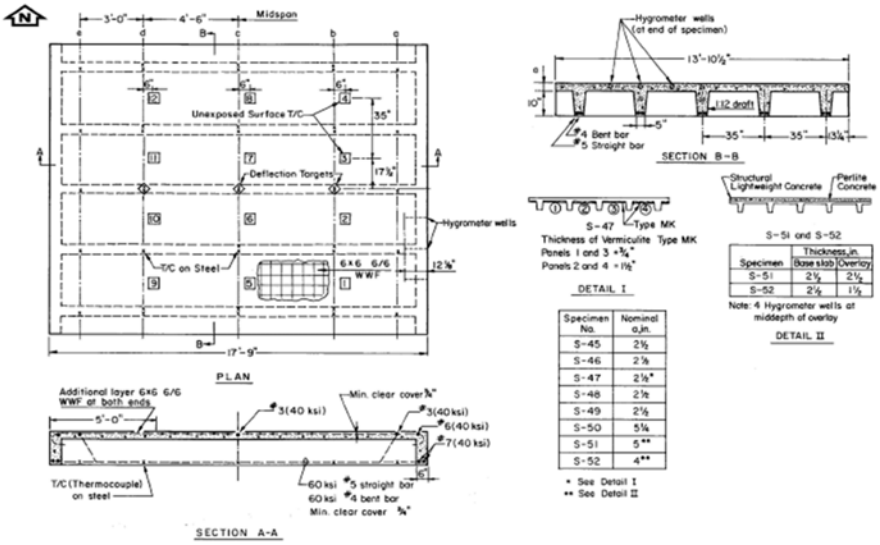

Fig. 7.19 Specimen details and instrumentation locations (Abrams et al., 1971)

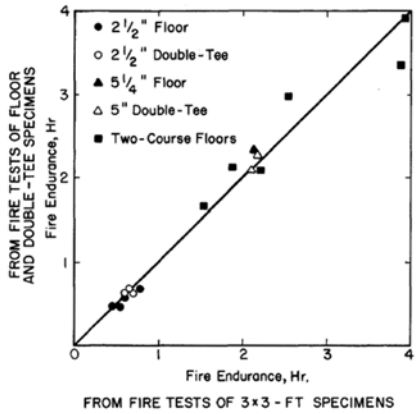

Fig. 7.20 Comparison of fire endurances determined from full-scale and 3×3ft specimens (Abrams et al., 1971)

- Cooke (2001)

Cooke (2001) conducted fire tests of 14 simply supported pre-cast reinforced concrete floor slabs exposed to two standardized heating regimes used in fire resistance furnace tests. The tests were designed to show the effect of varying the slab thickness, type of concrete, imposed load, soffit protection and nature of fire exposure on the mid-span flexural deflection and axial movements of the slab ends. For the slab specimens of BRE (Building Research Establishment), the following parameters were varied: slab thickness (150 and 250mm), type of concrete (normal weight and light weight), live load (zero and two different gypsum board systems) and severity of standard of fire exposure (ISO 834 and the Norwegian Petroleum Directorate (NPD) temperature-time curves). Table 7.13 lists the chosen combinations.

Table 7.13 Fire test parameters (Cooke, 2001)

Test	Specimen	Thickness (mm)	No. of rebar	Concrete	Live load	Heating	Comments
1	1	150	10	NWC	No	BS 476	BRE slab
1	2	150	10	NWC	Yes	BS 476	BRE slab
2	3	150	10	NWC	No	NPD	BRE slab
2	4	150	10	NWC	Yes	NPD	BRE slab
3	5	250	6	NWC	No	BS 476	BRE slab
3	6	250	6	NWC	Yes	BS 476	BRE slab
4	7	150	10	LWC	No	BS 476	BRE slab
4	8	250	6	LWC	No	BS 476	BRE slab
5	9	150	10	NWC	No	NPD	BRE slab
5	10	250	6	NWC	No	NPD	BRE slab
6	11	150	10	NWC	No	BS 476	BRE slab + soffit (1)
6	12	150	10	NWC	No	BS 476	BRE slab + soffit (2)
7	13	185		NWC	No	BS 476	Ronan Point slab
7	14	185		NWC	Yes	BS 476	Ronan Point slab

Live load = 1.5 kN/m^2, Soffit (1) = 10mm thick glass reinforced gypsum board with 37mm air gap, Soffit (2) = 12.5mm gypsum Fireline board with 37mm air gap, NWC = Normal weight concrete, LWC = Light weight concrete, BS 476 = BS 476: Part 8:1972 (ISO 834), NPD = Norwegian Petroleum Directorate (hydrocarbon "re simulation).

Based on the result of the experimental studies, the following conclusions can be drawn: (1) Mid-span deflections were dominated by thermal bowing during the 90 min design period of fire exposure; the effect on deflections of imposing the design live load of 1.5 kN/m^2, Fig. 7.21, was very small and this suggests that BS 8110 is conservative.

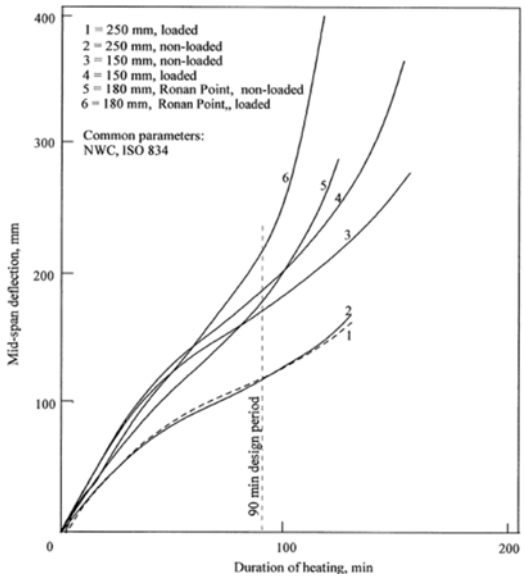

Fig. 7.21 Effect of imposed load (Cooke, 2001)

(2) The higher rate of heating associated with the NPD hydrocarbon fire exposure caused almost a doubling of mid-span deflection obtained using the ISO 834 fire exposure in the first 20 min, Fig. 7.22.

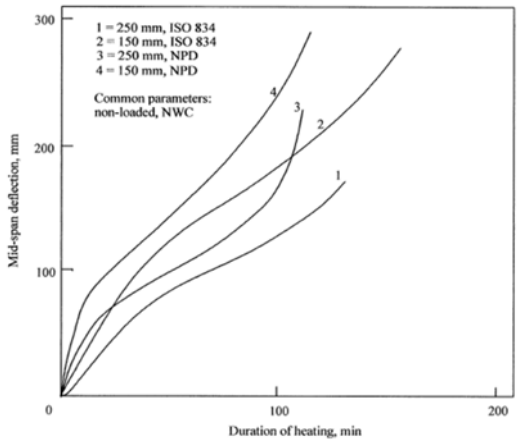

Fig. 7.22 Effect of heating rate (Cooke, 2001)

(3) The effect of using lightweight concrete employing Lytag coarse aggregate is to reduce the mid-span deflection associated with normal weight concrete by roughly 30% at the 90 min design period of fire resistance, Fig. 7.23. The reduced deflections are probably due to the lower coefficient of thermal expansion and lower thermal conductivity of light weight concrete.

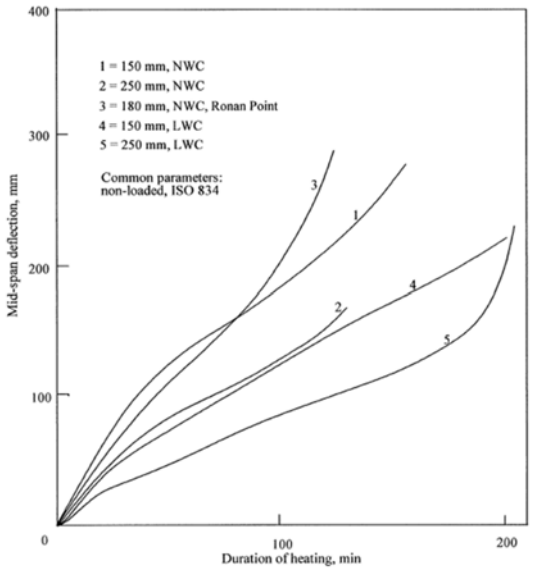

Fig. 7.23 Effect of slab thickness and concrete type (Cooke, 2001)

(4) The effect of soffit protection is, as one might expect, to reduce the mid-span deflection. Fig. 7.24(a) shows that the mid-span deflection of the 150mm NWC slab with soffit protection was roughly a quarter that of the unprotected slab. Fig. 7.24(b), however, shows that the slab having a soffit protection which remained in place suffers almost the same magnitude of axial deflection at mid-slab depth as the same slab with no soffit protection, although the peak deflection occurred much later for the soffit-protected slab.

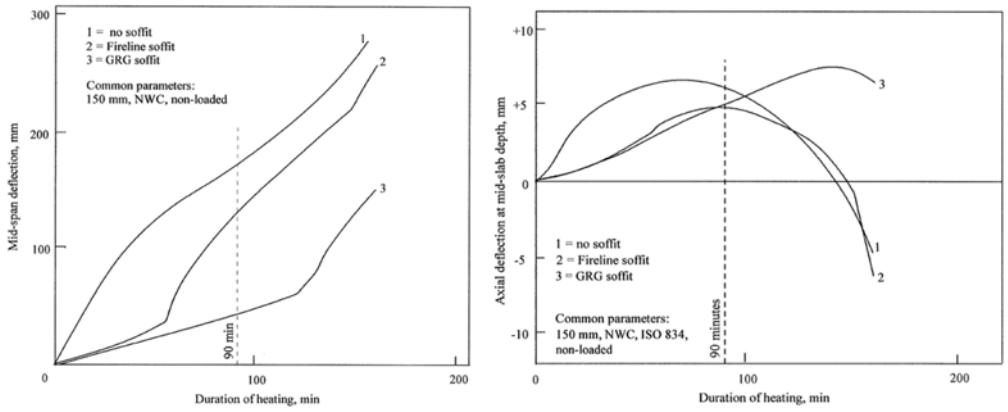

(a) mid-span deflection (b) axial deflection

Fig. 7.24 Effect of soffit protection (Cooke, 2001)

- Bailey and Toh (2007)

This study presents test results of forty-eight horizontally unrestrained two-way spanning reinforced concrete slabs at ambient and elevated temperatures. The test allowed a direct comparison between the modes of failure observed at ambient and elevated temperatures. Both mild steel and stainless-steel welded smooth wire meshes, with varying bar diameters and spacing, were used as reinforcement.

The test program comprised four series of slabs as follows:
(1) M-series: 14 slabs with mild steel mesh reinforcement at ambient temperature.
(2) S-series: 12 slabs with stainless steel mesh reinforcement at ambient temperature.
(3) MF-series: 10 slabs with mild steel mesh reinforcement at elevated temperatures.
(4) SF-series: 12 slabs with stainless steel mesh reinforcement at elevated temperatures.

In each series, half of the slabs had a size of 1.2m×1.2m, and the other half had a size of 1.8m×1.2m with a target thickness of 20mm, except for Slabs M13 and M14 which had a thickness of 36mm.

Twenty-six small-scale slabs have been tested at ambient temperature, with a further 22 similar small-scale slabs tested at elevated temperatures. The slabs were reinforced with either mild-steel or stainless-steel welded mesh. The ambient temperature tests highlighted two modes of failure comprising fracture of the reinforcement (across the shorter span of the rectangular slabs or one of the spans of the square slabs) or crushing of the concrete in the corners of the slab. The mode of failure, together with the magnitude of enhancement, which provides an indication of the magnitude of membrane action and is defined as the maximum sustained load divided by the theoretical yield load, seemed to depend on the reinforcement ratio. Provided the mode of failure was by fracture of the reinforcement, an increase in reinforcement ratio resulted in an increase in enhancement. However, continually increasing the reinforcement ratio finally led to compressive failure where a further increase in reinforcement ratio led to a decrease in enhancement.

The ambient tests also highlighted that the square slabs had a higher enhancement compared to rectangular slabs for a given vertical displacement. The square slabs were shown to fail at a

lower vertical displacement compared to rectangular slabs, even though both slabs had the same shortest span of 1.1 m. This was due to the strains of the reinforcement in the shorter span of the rectangular slab being relieved as the longer span edges of the slab are pulled inwards as the slab deflects vertically. The enhancement, considering all the tests, ranged from 1.33 to 3.66. It was also shown from the ambient tests that increasing the cover to the reinforcement, and increasing the slab's depth, decreases the membrane enhancement above the theoretical yield load. Due to the similar geometry and mesh reinforcement a direct comparison of the failure mode could be made between the twenty-two elevated temperature tests and the ambient temperature tests.

For the elevated temperature tests all failure modes comprised fracture of the reinforcement, due to the reinforcement's high temperatures which reduced its strength. For compressive failure to occur at elevated temperature the reinforcement ratio, based on the elevated temperature strength of the reinforcement and concrete, would have to be of similar magnitude to the ratio, based on normal room temperature values, of the slabs which failed by crushing at ambient temperature. In the fire tests presented in this paper, the reinforcement lost greater strength compared to the concrete in the corners of the slab where crushing was observed in the ambient tests resulting in reinforcement fracture being the critical failure mode.

The theoretical yield-line load of the slabs at the failure temperature was calculated using the reduction factors given in EN1993-1-2 and EN1994-1-2. The slabs tested had to support a static load between 2.2 and 7.5 times the yield load, with maximum vertical displacements at failure ranging from span/6 to span/12, showing that membrane action occurred.

8 Analysis of Reinforced Concrete Structures under High Temperatures

There are many results in the literature on analysis of various reinforced concrete structures under high temperatures. In this chapter, we will first review the analysis results on structural components like beams and columns, and then on structural systems such as floor slabs.

8.1 Fire analysis of RC Beams

- Freskakis (1984)

Freskakis (1984) examined the behavior of a reinforced concrete section by means of moment-curvature-axial force relationships that account for both the effect of temperature on the material properties and the mechanical effects induced by the tendency for thermal expansion. Particular interest was the load carrying capacity, the thermal forces, and the deformation capacity. The effects on these properties due to variation in strength with temperature, the temperature level and its distribution across the section, the amount of reinforcing steel (0.75, 1.0, and 2.0%), and limiting values of compressive strain (0.003 and 0.004) were considered.

Stress-strain relationships for the concrete based on the lower and upper bound relations in these Figures are presented in Fig. 8.1. Stress-strain relationships at various temperatures used for the Grade 60 reinforcing bars are presented in Fig. 8.2.

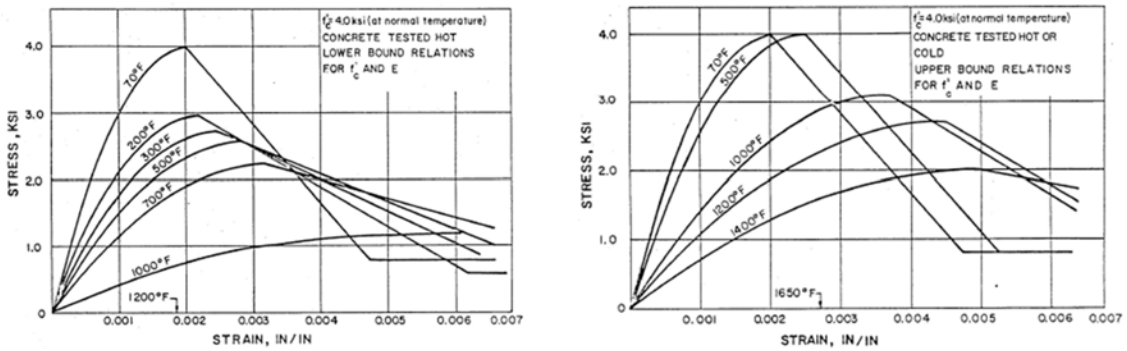

(a) Lower bound (b) Upper bound

Fig. 8.1 Stress-strain relationship for concrete (Freskakis, 1984)

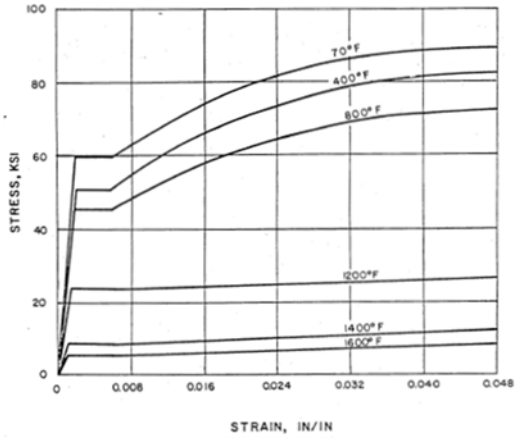

Fig. 8.2 Stress-strain relationship for steel (Freskakis, 1984)

Thermal gradients considered in the study that had temperatures either of 149, 260, or 427°C at the face of the concrete section are presented in Fig. 8.3. The three thermal gradients in Fig. 8.3 represent short (Type I), intermediate (Type II), and long (Type III) duration thermal exposures. Results from this study for selected parameters are presented in Fig. 8.4.

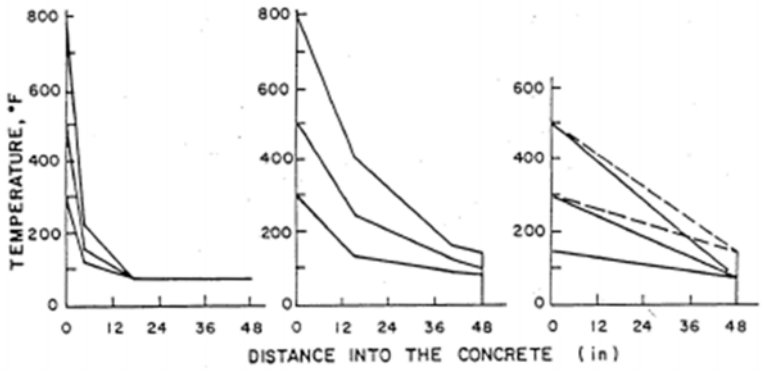

(a) Type I (b) Type II (c) Type III

Fig. 8.3 Temperature gradient (Freskakis, 1984)

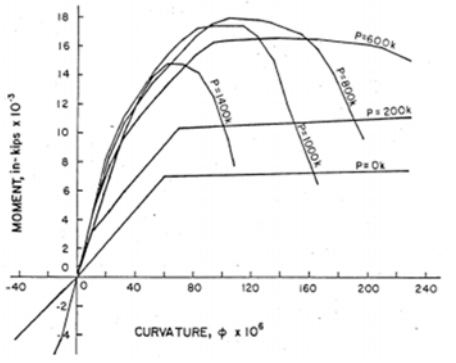

(a) M-φ-P relationship – normal temp.

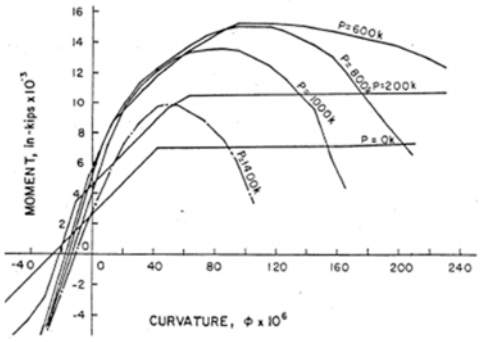

(b) M-φ-P relationship – T=300˚F

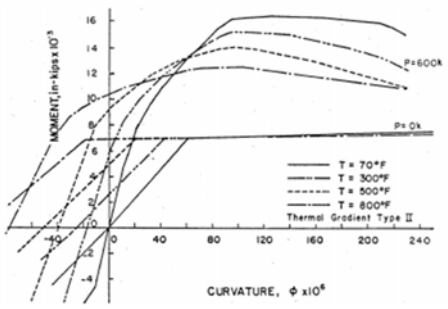

(c) Effect of temperature level on behavior

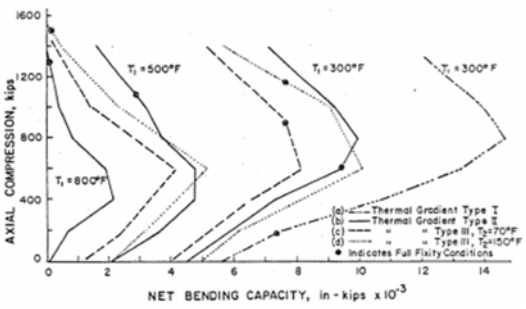

(d) Effect of temperature distribution

(based on L. B. relationship) on net bending capacity

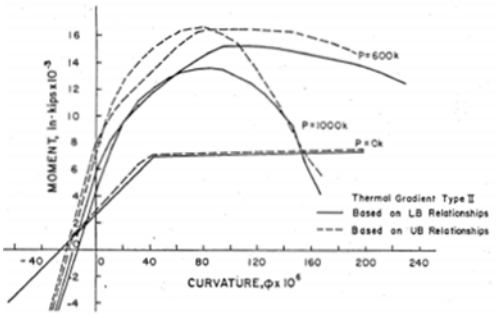

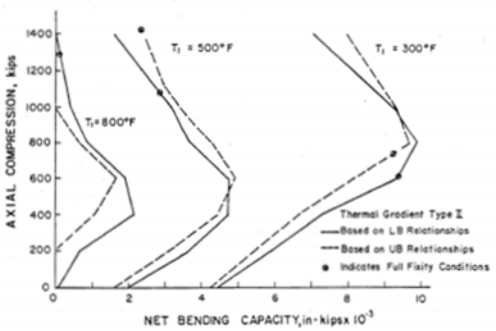

(e) M-φ-P diagrams based on UB and LB strength relationships (f) Net bending capacity based on UB and LB strength relationships

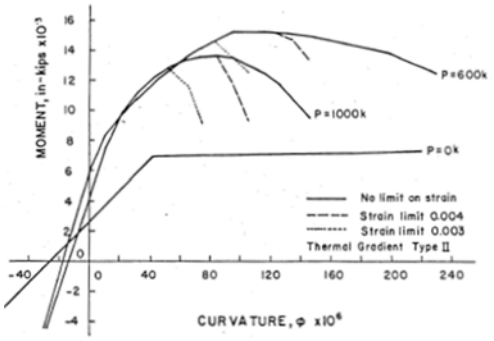

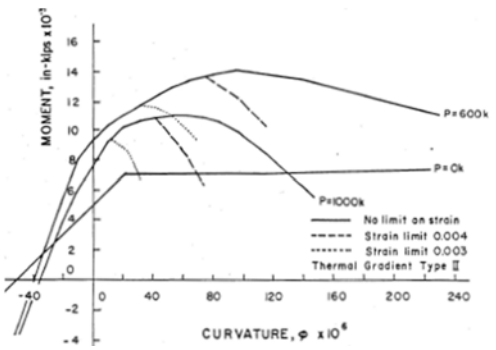

(g) Effect of strain limit on behavior T=300˚F (h) effect of strain limit on behavior T=500˚F

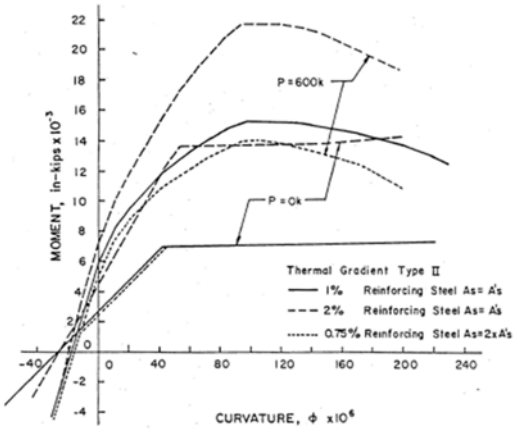

(i) Effect of reinforcing steel on behavior (based on Lower bound)

Fig. 8.4 Results for selected parameters (Freskakis, 1984)

From these results, it was concluded that (1) the effect of elevated temperature is to decrease the section capacity when axial forces are present, and the net carrying capacity decreases significantly with the buildup of thermal forces; (2) in terms of bending and axial force capacity, reinforced concrete sections can be designed to sustain severe temperature gradients

with levels of temperature much higher than allowed by present codes; (3) comparison of net moment capacity results based on the upper and lower bound strength and modulus of elasticity relationships indicates that either upper or lower bound relations may govern the design depending on the level and distribution of temperature across the section and the axial compression (e.g., upper bound should be considered for temperatures above 260°C and where heat of exposure is of short duration); (4) addition of reinforcing steel improves the net capacity of the sections, but the steel must be properly located in the section or a significant reduction in capacity can result; (5) where strain limits are imposed, increases in the temperature level result in significant reductions in rotational ductility; (6) for temperatures up to about 205°C, the use of a limiting concrete strain of 0.003 does not result in a significant loss in member strength, but at higher temperatures a significant reduction of strength occurs in the presence of compressive forces; and (7) the concrete tensile strength is important in the calculation of thermal forces at low elevated temperatures, but is insignificant where severe temperatures are present.

- Dotreppe and Franssen (1985)

Dotreppe and Franssen (1985) developed numerical methods for the analysis of reinforced concrete and composite structures under fire conditions. They are based on the finite element method using beam elements with subdivision of the cross-section in a rectangular mesh. The structure submitted to increasing temperatures is analyzed step-by-step using the Newton-Raphson procedure. To validate this method, a comparison between theoretical and experimental results is made for a reinforced concrete and a composite beam. Fig. 8.5 and Fig. 8.6 present comparison results of reinforced concrete beam and compsite beam.

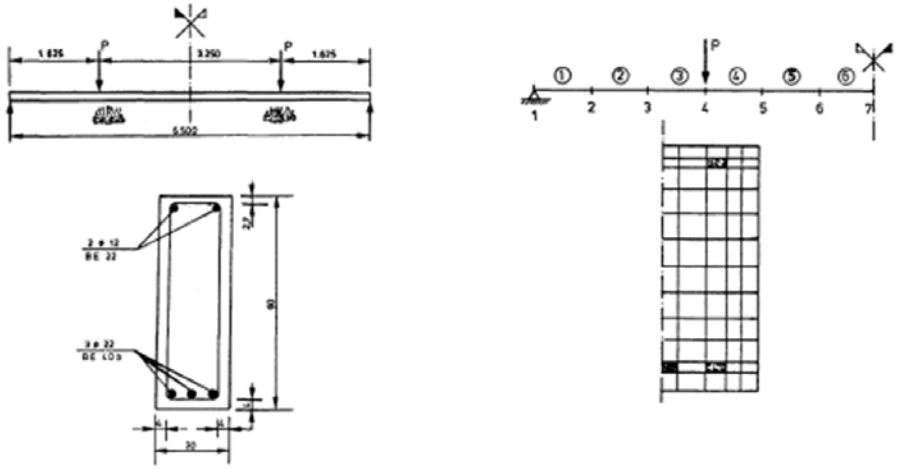

(a) loading and heating system (b) Element and section division

From these result, it was conclude that (1) The accuracy of the numerical results obtained from the described procedure has been proved by comparing them with test results. (2) Concerning the numerical treatment of the problem, however, further difficulties arise when going from reinforced concrete to composite structures. (3) They are mainly due to the fact that in composite structures the percentage of steel becomes significant and this leads to a serious increase of the computation time for the thermal analysis. (4) This computation time can be reduced if some attention is paid in order to avoid steel meshes of very small size. It must also be pointed out that the analysis of the failure mode is more complicated for composite structures.

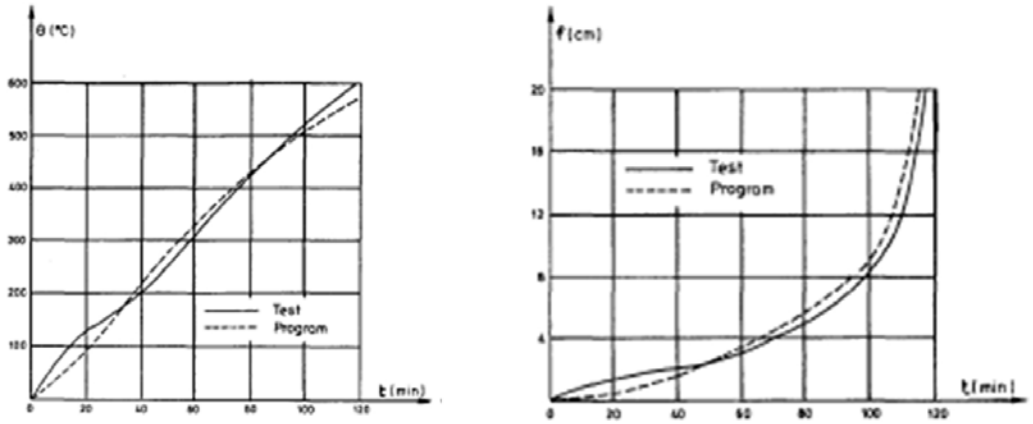

(c) temperature curve (d) deflection curve

Fig. 8.5 Information and comparison results of reinforced concrete beam (Dotreppe and Franssen, 1985)

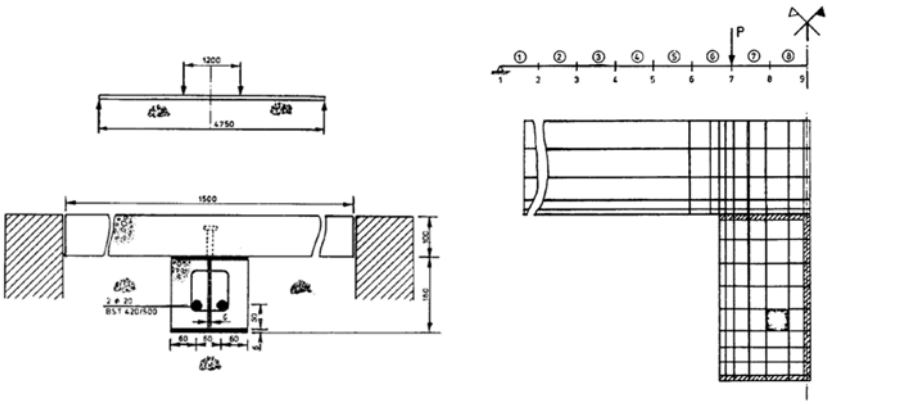

(a) loading and heating system (b) Element and section division

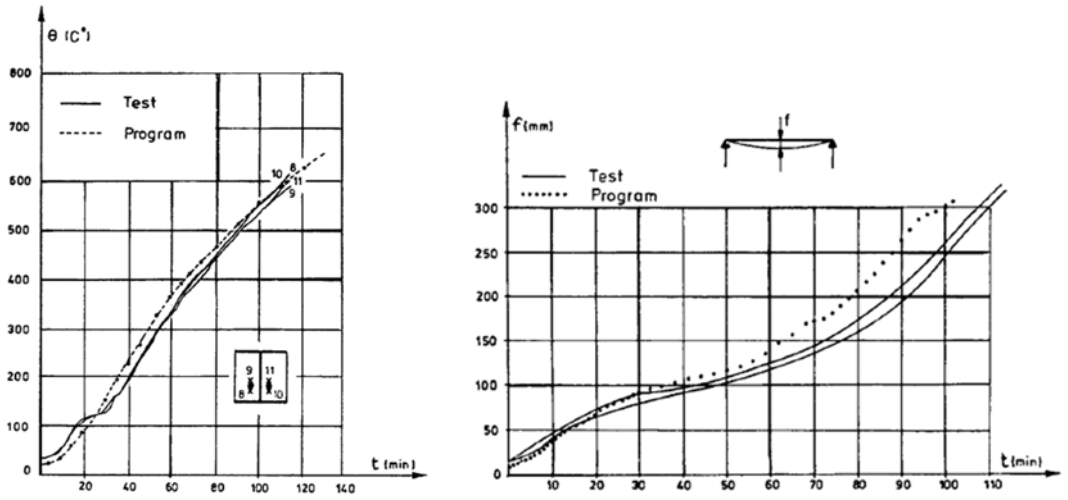

(c) temperature curve (d) deflection curve

Fig. 8.6 Information and comparison result of composite beam (Dotreppe and Franssen, 1985)

- Zha (2003)

In this study, the behavior of reinforced concrete beam (Fig. 8.8) subjected to a fire is investigated by three-dimensional non-linear finite elements. The temperature distribution in the section of concrete member is calculated by Hertz's simplified method, which is then input into the FE program for doing the time-dependent thermal stress analysis. Fig. 8.7 shows the typical temperature distributions for concrete members exposed to fire on one side and three sides, respectively.

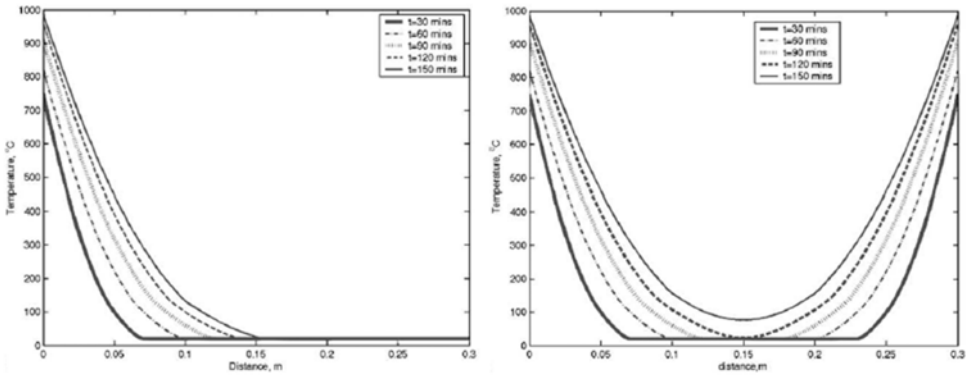

(a) subjected to a fire on one side (b) subjected to a fire on three sides

Fig. 8.7 Temperature distributions at different times (Zha, 2003)

The time-dependent thermal stress analysis is performed using DYNA3D, a three-dimensional non-linear finite element transient analysis program. The rectangular cross-section members are defined by depth *d* and width *w*, and have a length *L*. The two ends were assumed to be simply supported and are subjected to equal compressed loads for column and pure bending loads for beam. Because of the symmetry of the problem, only one quarter of the members is analyzed. Fig. 8.8 shows that of beam which consists of 1400 eight-node solid elements with 1890 nodes. The load is applied to the plate which is only allowed to move longitudinally and rotate about symmetric axis.

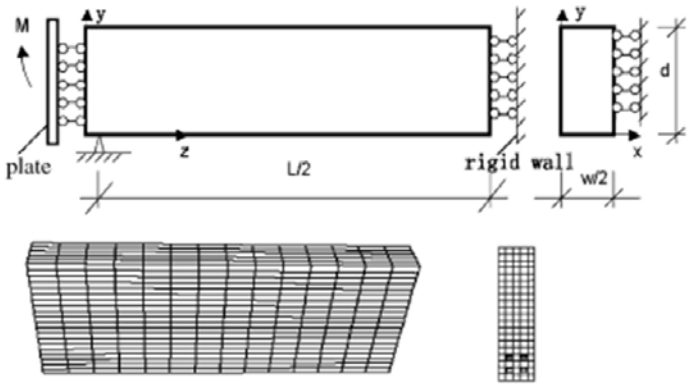

Fig. 8.8 Finite element analysis and element mesh of concrete beam (Zha, 2003)

Fig. 8.9 shows the time–lateral displacement relationship of the beam at the centre of the mid-

section for three different applied loads. It can be seen that the lateral displacement of the mid-section of the beam increases with the time and the maximum failure time of fire resistance decreases with the proportion of bending load to the beam. The various lateral displacements show that the collapse of a beam is caused mostly by excessive deflection. Since the load is pure moment, a beam bends at the beginning of load. During the fire the temperature-induced expansion at the lower part is larger than the temperature induced expansion at the upper part of the concrete section which leads to additional directional bending and deflection. The collapse of beam is caused by reduction of material strength and excessive displacement at high temperature.

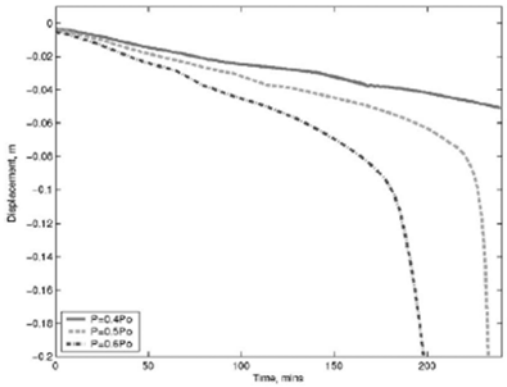

Fig. 8.9 Time-lateral displacement relationship of the beam
at the center of the mid-section at various loads (d=0.6m, w=0.3m) (Zha, 2003)

Fig. 8.10 shows the influence of the concrete cover and dimensioning of the reinforcing steel bars on the lateral displacement of the beam at the centre of the mid-section. As is expected, an increase in the concrete cover results in an increase of fire resistance. Fig. 8.10(b) shows the influence of beam dimension on the lateral displacement of the beam at the centre of the mid-section. It can be seen that the increase of beam dimension results in a significant increase of fire resistance, which means the fire resistance of beams is proportional to their size. It gives the evidence for recent codes and recommendations to present a tabulation of data for beams related to the minimum width of the member.

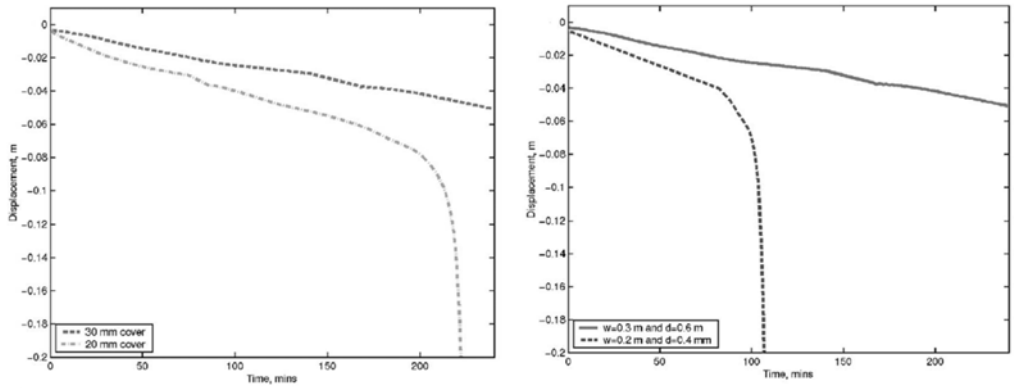

(a) concrete cover (b) dimension

Fig. 8.10 Influence of concrete cover and dimension on the fire resistance of concrete beam when subjected to fire on three sides (w=0.3m, d=0.6m, P=0.4P_o) (Zha, 2003)

The studies of influence of parameters on the fire resistance of the concrete members have shown that, increasing concrete cover, size and a greater number of reinforcing steel element can increase the fire resistance. The results obtained from the two different fire cases have shown that three sides fire exposures is much worse than the one-side fire exposure, not only with respect to fire resistance but also with respect to deformation and deflection. The example demonstrates that the results of the method provided in this paper agree well with the current standards.

- Pisani (2004)

This study presents a numerical method apt to analyze compact cross-sections of general shape under bending, compression and given non-linear strain distributions of general shape. The method can take into account holonomic hardening or perfectly plastic constitutive models of generic shape. The proposed method is implemented in a computer program permitting the analysis of the effect of the non-linear thermal loads (owing to daily and seasonal changes in shade air temperature, solar radiation, re-radiation, etc.) on the cross-section behavior of reinforced concrete or pre-stressed concrete bridge decks, roof planks and slab, reinforced either with steel or with carbon, aramid or glass fiber reinforced polymers.

The outcome of this investigation is that the non-linear thermal load does not significantly affect the load carrying capacity of the sections both when dealing with steel reinforcement and when adopting FRP reinforcement. The tensile stress in the reinforcement does not markedly change either, both under service loads and at failure. On the contrary, the stress and strain distribution in concrete under service loads markedly varies because of the non-linear thermal load, but this effect becomes feasible at ultimate load.

- Capua and Mari (2007)

Capua and Mari (2007) developed a nonlinear structural analysis program of cross-sections of three-dimensional reinforced concrete frames exposed to fire. This analysis program includes two steps: the first step is the calculation of the transient temperature field in cross-sections exposed to fire and the second step is the determination of the mechanical response due to the effect of thermal and mechanical load. A nonlinear finite-element procedure is proposed to predict the temperature field history. In this thermal analysis, the effect of moisture has been taken into account by introducing a water vapor fraction function to define the variation of enthalpy. A mechanical nonlinear analysis of the cross-sections is performed for each temperature distribution and for the applied exterior load using an algorithm of arc-length control. The mechanical and thermal properties of concrete and steel are taken according to the European Standard ENV 1991-1-2 (ENV. Eurocode 2, design of concrete structures, part 1-2: general rules - structural fire design ENV 1992-1-2, 1995).

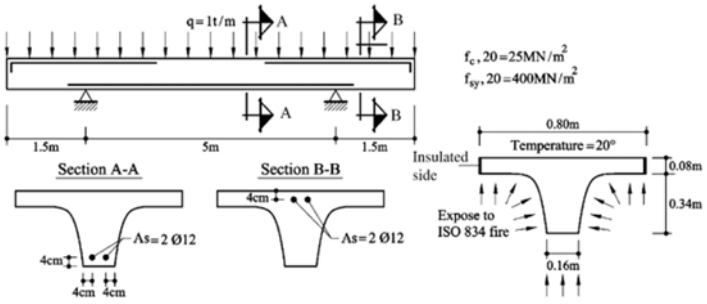

Fig. 8.11 Simply supported beam with cantilever ends (Capua and Mari, 2007)

In order to show the applicability of the model, a simply supported reinforced concrete beam representing a rib of a waffle slab with two cantilever ends, exposed to the ISO 834 fire load is analyzed. Fig. 8.11 shows geometric, material and loading data of the beam.

The flange is considered laterally insulated, and the upper side is exposed to ambient temperature (20˚C). The thermal properties of concrete and steel are assumed to take into account the European Standard ENV 1992-1-2 (1995). The convection coefficient is assumed to be h=25 W/(m^2˚C) for the fire-exposed surfaces and h=9 W/(m^2˚C) for the upper surface. The convection power factor is assumed to be n=1. The emissivity of the concrete surface is assumed to be ε_s =0.8, the emissivity of fire e ε_f =0.8 and the absorption of surface a=1.

Fig. 8.12 shows the temperature distribution at time t=60 min. The stress distribution in the midspan and over the support cross-section, both at time t=60 min, can be seen in Fig. 8.13. It is interesting to observe the compressive stress in the regions close to the exposed surfaces.

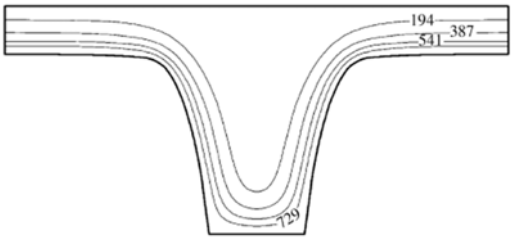

Fig. 8.12 Temperature distributions at t=60min, values in ˚C

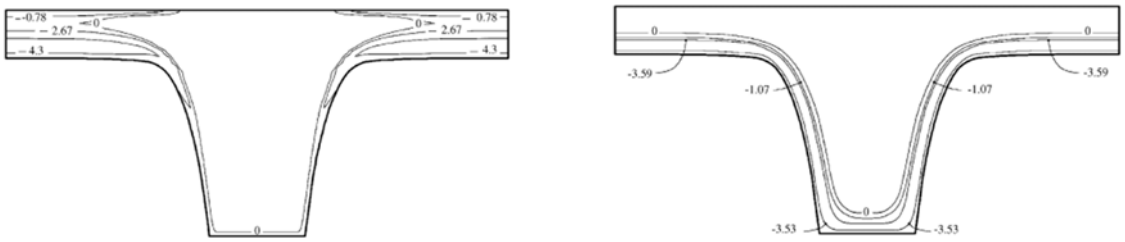

(a) In midspan cross-section (b) Over support cross-section

Fig. 8.13 Stress distributions at t=60min, values in MN/m^2 (Capua and Mari, 2007)

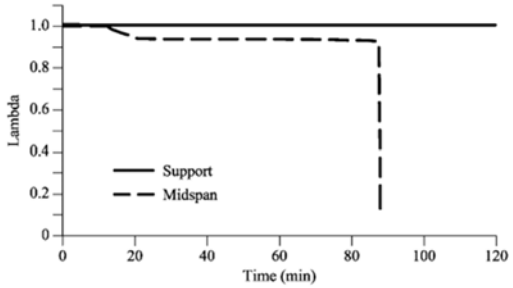

Fig. 8.14 Time evolution of the load level in the midspan and over the support cross-section (Capua and Mari, 2007)

Fig. 8.14 shows the time evolution of the load level (λ) in the midspan and over the support cross section. It is important to note that the cross-section over the support is able to resist for a longer time than the section in the midspan. And it is observed that when the reinforcing steel reaches the critical temperature the moment capacity drops dramatically.

- Bratina, Saje and Planinc (2007)

This study presents a two-step formulation, consisting of separate thermal and mechanical analyses, for the thermo-mechanical analysis of reinforced concrete planar frames subject to fire conditions. The heating and the cooling phases are considered. Standard planar, four-node quadrilateral finite elements are employed in the non-linear time-dependent thermal analysis of cross-sections, while the recently proposed strain-based planar beam finite elements are used in the non-linear mechanical analysis of the frame.

The formulation includes both exact geometric and material nonlinearities, and considers the temperature dependence of thermal and material parameters, the plastic, creep and thermal strains in concrete and steel, the transient strain in concrete and the strain localization as a consequence of softening of material at high temperatures. A so called 'constant strain element' is introduced to resolve numerically the loss of uniqueness of strain measures at the point of localization. The formulation is validated by comparing some of the present numerically predicted results with the data, measured in experiments.

The numerical example is a simply supported concrete beam with overhangs. This beam has been extensively tested by Lin et al. (1988) and their results will be used to validate the present numerical model. In what follows three variants of this beam will be analyzed and marked as B_1, B_3 and B_5. Geometric, material and loading data are given in Fig. 8.15 and in Table 8.1 , where f_{co} and f_{yo} denote the compressive strength of concrete and the ultimate strength of steel at room temperature, respectively

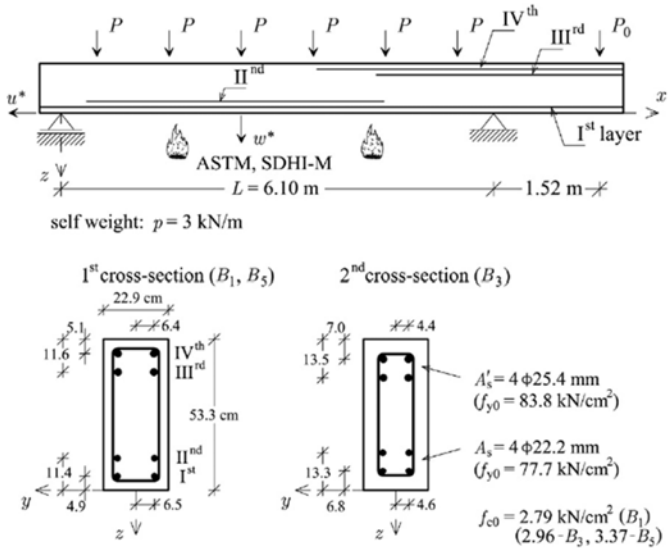

Fig. 8.15 A simply supported concrete beam with overhangs (Lin et al., 1988)

Table 8.1 Details of beam specimens B_1, B_3 and B_5 (Lin et al., 1988)

Beam specimen	B1	B3	B5
Concrete cover (mm)	38	57	38
Fire curve	ASTM E119	ASTM E119	SDHI-M
Test duration (min)	220	243	243
P_0 (at t = 0 min) (kN)	115.7	115.7	115.7
P_0 (at t = 240 min) (kN)	166.5	160.1	166.5

Four analyses were performed to assess the effect of various strain parts on the mechanical response of the beam, see Table 8.2 .

Table 8.2 Strains considered at each analysis (Bratina et al., 2007)

Type of analysis	Strains considered
Case A	D_{th}
Case B	D_{th} and $D_{cr,c}$
Case C	D_{th}, $D_{cr,c}$ and $D_{tr,c}$
Case D	D_{th}, $D_{cr,c}$, $D_{tr,c}$ and $D_{cr,s}$

The comparisons between various experimental and numerical values are for the instant t = 200 min presented in Table 8.3 .

Table 8.3 Comparisons between predicted and measure values at t = 200 min. (Bratina et al., 2007)

	Experiment		Present			
	B_{1a}	B_{1b}	Case A	Case B	Case C	Case D
w^* (cm)	12.4	14.6	8.31	8.66	10.16	12.43
u^* (cm)	6.2	7.5	5.16	5.12	4.99	5.22
Fire resistance time (min)	220	206	>250	>250	>250	224

In case A, our results for the deflection w^* well agree up to about t = 150 min (see Fig. 8.16). At t = 200 min the measured deflection in B_{1a} is w^*_{exp} = 12.4 cm and w^*_{exp} = 14.6 cm in B_{1b}, while the finite-element analysis gives w^* = 8.31 cm, which is a lot less than the measured one. The related calculated horizontal displacement in the left outermost point of the beam, u^* agrees well with the measured one up to time t = 180 min (Fig. 8.17). Later on, at t = 200 min, the differences are somewhat bigger: values, given by experiments B_{1a} and B_{1b}, are u^*_{exp} = 6.2 cm and 7.5 cm, respectively, compared to u^* = 5.16 cm, obtained in the calculation. In case B, The result is that w$^{\llcorner}$ increased somewhat (see Fig. 8.16), yet the error still grows with time. At t = 200 min, the deflection is w^* = 8.66 cm and the horizontal displacement is u^* = 5.12 cm. The fire resistance time is greater than 250 min. This indicates that the creep of concrete is not essential for the loss of stability of the simply supported beam in fire. In case C, The resulting deflections again increase, while the horizontal displacement u^* decreases. At t = 200 min, the deflection is w^* = 10.11 cm and the horizontal displacement is u^* = 5.02 cm. The fire resistance time is still

greater than 250 min. The analysis of case D considers all kinds of strain contributions. It clearly shows a decisive effect of the viscosity of steel at temperatures above 400 C. Williams-Leir (1983) provided the data for steel with different creep characteristics. If we consider the steel with mild creep characteristics (steel Austen 50), the agreement between measured and predicted response curves is sufficient (see Fig.s 8.16 and 8.17). At t = 200 min the calculated displacements are w^* = 12.41 cm and u^* = 5.28 cm. It is obvious that the creep of steel accelerates the collapse of the simply supported beam - the numerically obtained fire resistance time is now 223 min and the related collapse temperature is 1098°C. The results show that w^* increases during fire and that u^* does so only if the creep in steel is considered (Fig. 8.16).

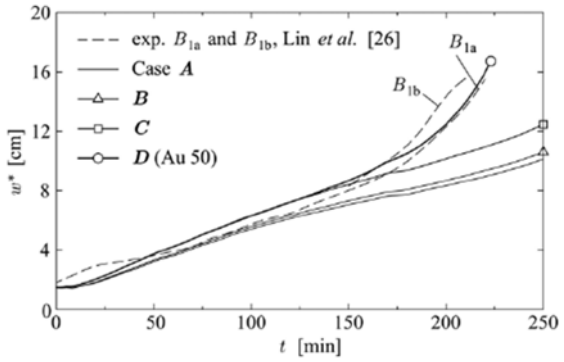

Fig. 8.16 Comparison of the variation of the predicted and measured vertical deflection w^* with time. (Bratina et al., 2007)

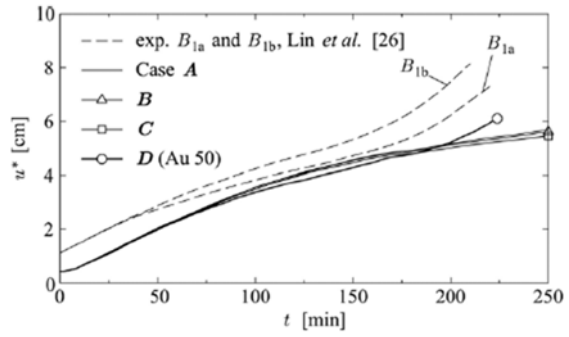

Fig. 8.17 Comparison of the variation of the predicted and measured horizontal displacement u^* at the left outermost point of beam with time. (Bratina et al., 2007)

From these results, it was concluded that (1) although the present model is essentially a 1D stress-strain model, and is thus simple in terms of the number of degrees of freedom used and ignores transfer of water in concrete during heating, the comparisons with the measured data are found to be satisfactory. (2) The agreement of the fire resistance times and critical deflections between the predicted and the experimental values was found to be very satisfactory. (3) In contrast, a disagreement was found in distributions of temperature over the beam cross-sections. The results make it possible to draw several conclusions concerning behavior of structures in fire.

(4) It is established that the consideration of creep and transient strains in concrete has little effect on the fire resistance time of statically determinate beams under bending; their effect on displacements is, however, remarkable.

- Kodur and Dwaikat (2008)

Kodur and Dwaikat (2008) present a numerical model for tracing the behavior of reinforced concrete (RC) beams exposed to fire. The three stages associated with the numerical procedure for evaluating fire resistance of RC beams; namely, fire temperature calculation, thermal analysis and strength analysis, are explained.

The numerical model, proposed here, uses moment-curvature relationships to trace the response of an RC beam in the entire range of loading up to collapse under fire. The model considers the case of loading where the bending moment is the dominant action on the beam and the effect of both shear force and axial force is neglected. The RC beam is divided into a number of segments along its length (as shown in Fig. 8.18) and the mid-section of the segment is assumed to represent the behavior of the whole segment.

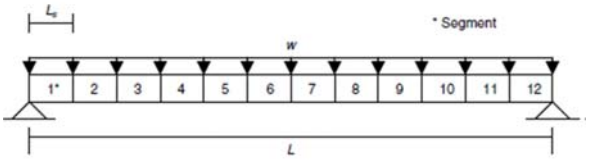

Fig. 8.18 Layout of a typical RC beam and its idealization for analysis
(Kodur and Dawaikat, 2008)

At any time step, the temperatures due to fire exposure are established and then a thermal analysis is carried out to determine temperatures in each segment. Following this, a moment-curvature (M-κ) relationship is generated for each segment at various time steps. It has been well established that M-κ relationships appropriately represent the behavior of a RC beam at ambient conditions. In the current model, such M-κ relationships are established as a function of time for all longitudinal segments in the beam and they are in turn used to trace the response of the beam under fire conditions. The M-κ relationships, at various time steps, are generated using the changing properties of constituent materials namely concrete and reinforcement. In this way, the material nonlinearity will be implicitly accounted for in the analysis.

Using the M-κ relationships, the load (moment) the beam can carry at a particular time step is evaluated. Also, the deflection of the beam at that time step can be calculated through a stiffness approach by evaluating average stiffness of the beam. The average stiffness of the beam is computed using segmental stiffness, which is estimated by means of known M-κ relationships. The moment carrying capacity decreases with time, and the beam is said to attain failure if thermal, strength or deflection limit states are exceeded. A flowchart showing the numerical procedure for fire resistance calculations is given in Fig. 8.19.

The temperatures and strength capacities for each segment, and computed deflections in the beam are used to evaluate failure of the beam at each time step. At every time step, each beam segment is checked against pre-determined failure criteria, which include thermal and structural considerations. The time increments continue until a certain point at which the thermal failure criterion is met or the capacity (or deflection) reaches its limit state. At this point, the beam is assumed to have failed. The time to reach this failure point is the fire resistance of the beam. The

model generates various critical output parameters, such as temperatures, stresses, strains, deflections and moment capacities at various given fire exposure times.
At each time step, the numerical calculations are performed in four steps: namely, calculation of fire temperatures to which the beam is exposed, calculation of temperatures in the beam, generation of M-κ relationships for each beam segment, and calculation of resulting beam deflection and strength through nonlinear structural analysis.

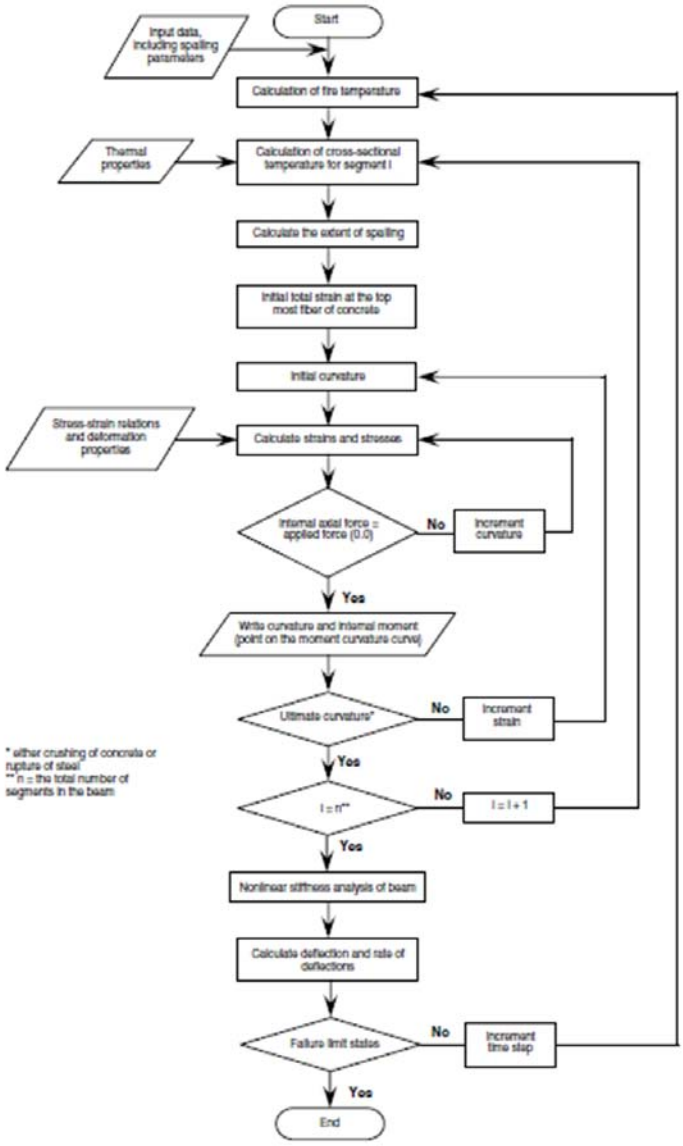

Fig. 8.19 Flowchart for the analysis of RC beams exposed to fire (Kodur and Dawaikat, 2008)

The validity of the computer program is established through a set of numerical studies on two RC beams. Two beams, selected from literature, were analyzed to compare model predictions with fire test data. Details of the beam dimensions, material properties and load level are given in Table 8.4.

Predicted results from the analysis are compared to measured values from fire tests in Fig.s 8.20~23. In Fig. 8.20, the calculated average temperatures in the rebar are compared with the

measured values for Beam II reported by Lin et al. (1981). It can be noted that there is good agreement between the predicted and measured values in the entire range of fire exposure. The steep increase in rebar temperature in the early stages of fire exposure is due to the occurrence of high thermal gradient at the beginning of fire exposure time as a result of faster increase in fire temperature (see ASTM E119 fire curve in Fig. 8.20). A review of predicted temperatures in concrete at various depths indicated that the model predictions follow the expected trend with lower temperatures at larger depths from fire exposed surface. However, the predicted concrete temperatures could not be compared with test data since the measured temperatures were not reported by Lin et al. (1981).

Table 8.4 Properties and results for RC beams (Kodur and Dawaikat, 2008)

Property	Beam II	Beam III
Description	Lin et al., 1981	Dotreppe and Franssen 1985
Cross section	305mm×355mm	305mm×355mm
Length (m)	6.1	6.5
Reinforcement	2φ19mm top bars 4φ19mm bottom bars	2φ12mm top bars 3φ22mm botto bars
f_c' (MPa)	30	15
f_y (MPa)	435.8	300
Loading ratio	0.42	0.263
Applied total load (kN)	80	65
Concrete cover thickness (mm)	25 (bottom) 38 (side)	40
Aggregate type	Carbonate	Siliceous
Fire resistance based on failure criterion:		
Rebar temperature	110	120
Strength	140	145
Deflection (BS476)	102	123
Rate of deflection (BS 476)	105	115
Fire resistance based on ACI 216	180	154
Fire resistance as obtained in test	80	120

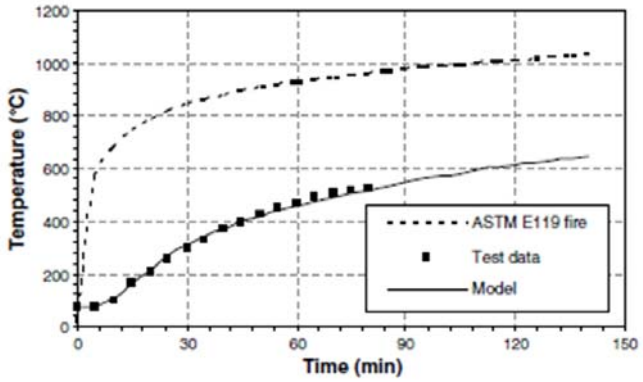

Fig. 8.20 Predicted and measure rebar temperatures for test beam, Beam II (Kodur and Dawaikat, 2008)

Fig. 8.21 shows predicted and measured mid-span deflections as a function of fire exposure time for Beam II. It can be seen that model predictions are in close agreement with the measured deflections, throughout the fire exposure time.

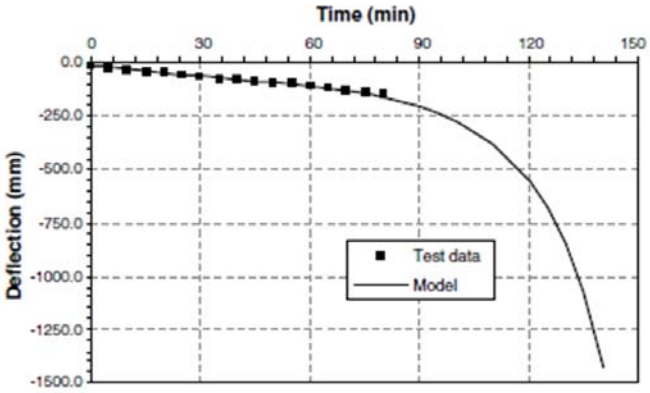

Fig. 8.21 Predicted and measured deflections for test beam, Beam II (Kodur and Dawaikat, 2008)

The fire resistance of this beam was evaluated based on four failure criteria and its values are given in Table 8.4 . The measured fire resistance, for Beam II, is lower than that predicted by the program for all failure criteria. This is mainly because the test was terminated after 80 min of fire exposure and before the beam attained complete failure probably due to sever conditions experienced towards the final stages in fire tests. Thus, the fire resistance of this beam would have been slightly higher if the test was continued till the complete failure. In addition, the difference between measured and predicted fire resistance can be partially attributed to variation in the material properties incorporated in the model from those of the actual beam. As an illustration, the current high temperature material property relationships do not take into account the variation of strength, heating rate, and other factors. There variations, though marginal, will have some influence on the results from the analysis. The fire resistance predicted based on rebar temperature (110 min) is much lower than that for strength failure criterion (140 min). This is because the rebar temperature failure criteria is based on load level of 50% of the room temperature capacity of the beam, however, the load level on this beam is lower than 50% and this results in higher fire resistance from strength failure criterion. In addition, the model predicted lower fire resistance based on deflection and rate of deflection failure criteria probably because the span/depth ratio for Beam II is large Overall, the predicted fire resistance from deflection failure criteria (102 min) is a reasonable estimate to the measured value in the fire test (when the test was terminated).

Fig.s 8.22 and 8.23 show the comparison of rebar temperatures and deflections for beam, Beam III, tested by Dotreppe and Franssen (1985). It is clear from Fig. 8.22 that the model predictions match closely with measured values of rebar temperature from fire test. The predicted and measured mid-span deflections for Beam III are compared in Fig. 8.23. It can be noted that the deflections from the model compare well with the measured values throughout the fire exposure time. The good agreement in deflections can be attributed to capturing all the components of strain (in the model) that occurred during fire exposure. The slight differences

that appear at later stages of fire exposure are probably because the high rate of deflection, at later stages of fire tests, makes the measuring process very difficult, and also reduce the reliability of the measured deflections.

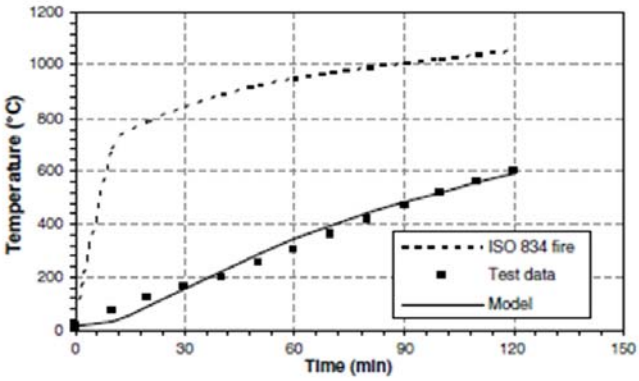

Fig. 8.22 Predicted and measured rebar temperatures for test beam, Beam III (Kodur and Dawaikat, 2008)

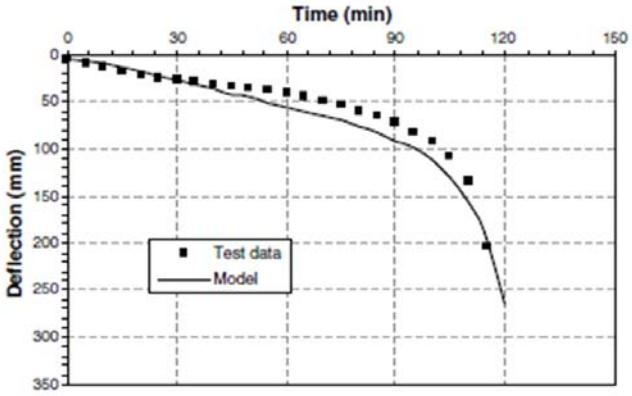

Fig. 8.23 Predicted and measured deflections for test beam, Beam III. (Kodur and Dawaikat, 2008)

Based on the results of this study, the following conclusions can be drawn: (1) There is limited information on the fire performance of reinforced concrete beams, especially under design fire and realistic loading scenarios. (2) The moment-curvature based macroscopic finite element model, presented in this study, is capable of predicting the fire behavior of reinforced concrete beams, in the entire range: from pre-fire stage to collapse stage, with an accuracy that is adequate for practical purposes. Using the model the fire resistance of a reinforced concrete beam can be evaluated for any value of significant parameters such as beam length, type of aggregate, section dimensions, without the necessity of testing. (3) The limiting criterion, used for determining failure of a reinforced concrete beam exposed to fire, has significant influence on the fire resistance values. The conventional failure criterion such as limiting rebar temperature or strength consideration may not be conservative under some scenarios. The deflection and rate

of deflection failure criterion should be considered in evaluating fire resistance of reinforced concrete beams.

8.2 Fire analysis of RC Columns

- Lie and Irwin (1993)

This study presents mathematical models for the calculation of the fire resistance of columns of various sizes and shapes. The calculation of the fire resistance of columns is carried out in various steps. The column temperatures are calculated by a finite difference method. This method has been previously applied to the calculation of temperatures of various building components exposed to fire. The cross-sectional area of column is subdivided into a number of elements, arranged in a triangular network (Fig. 8.24). For reason of symmetry, only one-quarter of the section needs to be considered when calculating the temperature distribution in columns with square or rectangular cross-section.

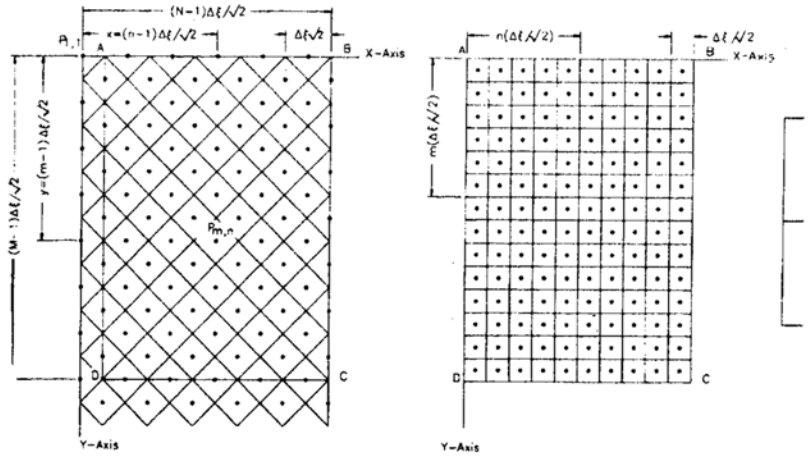

Fig. 8.24 Thermal and stress-strain network in one-quarter cross section (Lie and Irwin, 1993)

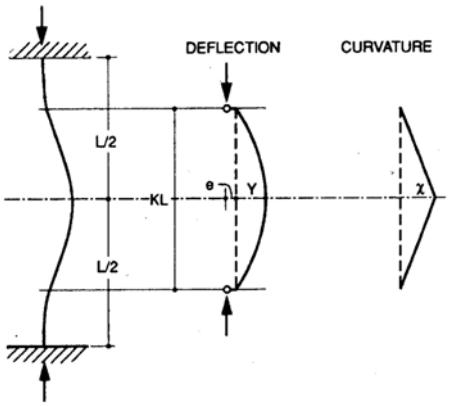

Fig. 8.25 Load-deflection analysis (Lie and Irwin, 1993)

During exposure to fire, the strength of the column decreases with the duration of exposure. The strength of the column can be calculated by a method on a load-deflection analysis. In this

method, the columns, which are fixed at the ends during the tests, are idealized as pin-ended columns of length KL (Fig. 8.25). The curvature of the column is assumed to vary from pin-ended to midheight according to a straight line relation, as illustrated in Fig. 8.25. For such a relationship, the deflection at midheight Y, in term of curvature χ of the column at this height, can be given by

$$Y = \chi \frac{(KL)^2}{12} \tag{8.1}$$

For any given curvature, and thus for any given deflection at mid-height, the axial strain is varied until the internal moment at the mid-section is in equilibrium with the applied moment given by the product: *Load×(deflection+eccentricity)*

In this way, a load deflection curve can be calculated for specific times during the exposure to fire. From these curves, the strength of the column, i.e., the maximum load that the column can carry, can be determined for each time. Using the mathematical model, calculated temperature for various locations in the columns and calculated axial deformations of the columns compared with the measured temperature and axial deformation reported in Lie and Woollerton (1988).

In the Fig. 8.26, the calculated and measured axial deformations of the columns, during exposure to fire, are shown. It can be seen that the mathematical model predicts, reasonably well, the trend in the progression of the axial deformations with time.

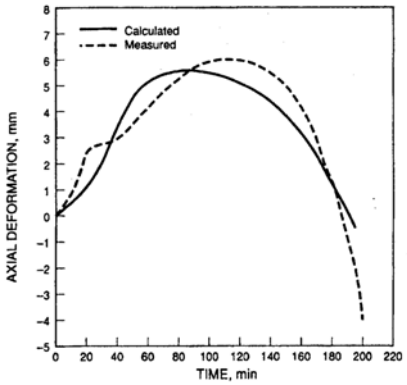

(a) Column No. 1

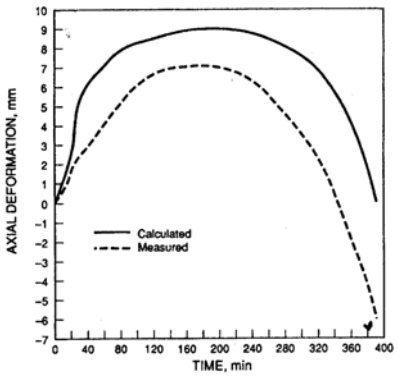

(b) Column No. 2

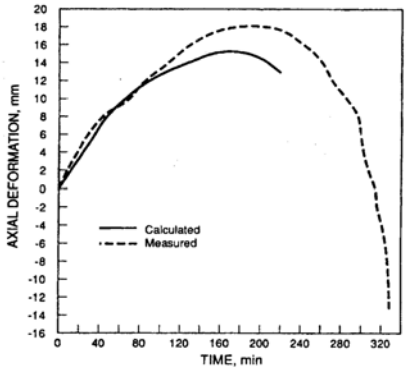

(c) Column No. 3

Fig. 8.26 calculated and measured axial deformations of columns as function of exposed time (Lie and Irwin, 1993)

In Fig. 8.27, the calculated strengths of the columns are shown as a function of the time exposure. The strength decreases with time until it becomes so low that the column can no longer support the load. The time to reach this point is the fire resistance of the column.

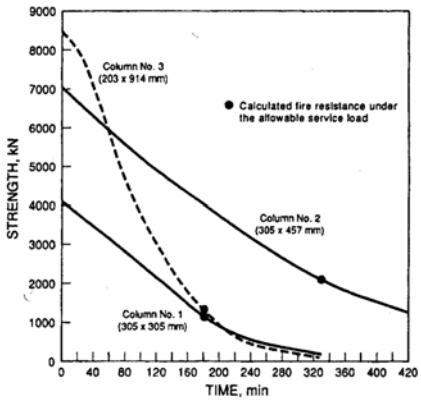

Fig. 8.27 Calculated strengths of columns as function of exposure time and calculated column fire resistance under the allowable service load according to ACI 318 and CSA A23.333-M84 (Lie and Irwin, 1993)

Based on the results of this study, the following conclusions can be drawn: (1) The mathematical model employed in this study is capable of predicting the fire resistance of rectangular reinforced concrete columns with an accuracy that is adequate for practical purposes. (2) The model will enable the expansion of existing data on the fire resistance of reinforced concrete columns, which at present consists predominantly of data for square columns, with that for rectangular columns. (3) Rectangular columns have, under commensurate loads substantially higher fire resistances than square columns of the same thickness. (4) Using the model, the fire resistance of square and rectangular reinforced concrete columns can be evaluated for any value of the significant parameters, such as load, column, section size, column length, concrete strength, percentage of reinforcing steel and concrete cover to the steel without the necessity of testing. (5) The model can also be used for the calculation of the fire resistance of column made with concretes other than those investigated in this study; for example, lightweight or carbonate aggregate concretes, if the relevant material properties are known.

- Poh and Bennetts (1995)

A general numerical method to calculate the nonlinear behavior of load-bearing members under elevated temperature conditions is presented by Poh and Bennetts (1995). The method, although similar in concept to earlier approaches, differs with respect to both solution procedure and capability.

It is assumed that the thermal and structural behavior of a member in fire is uncoupled. For the purpose of analysis, the thermal behavior of the member is obtained separately- either from heat-transfer analysis or from test data – usually in the form of temperature at a multitude of member locations at discrete time steps. The structural behavior of the member is then determined based on the time-temperature information.

The member is divided into a series of segments of appropriate lengths. Each segment is represented at its midlength by a cross section. The cross section, in turn, is divided into a number of small subareas of appropriate shapes and sizes (Fig. 8.28). Each subarea is referred to

as level 1 element, and the cross section and member are levels 2 and 3 elements, respectively. Temperature variations over the cross section and along the member are incorporated through the combination of the subarea temperatures, which are assumed uniform over each subarea.

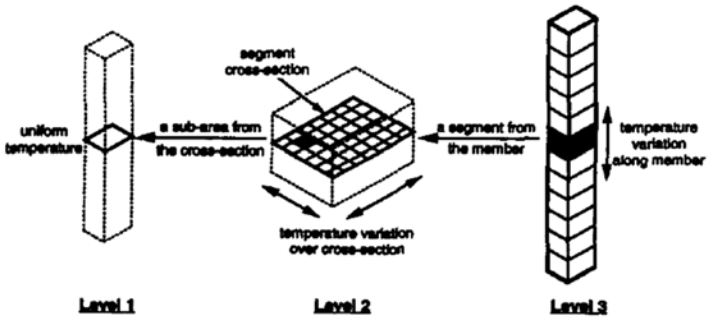

Fig. 8.28 Geometric discretization (Poh and Bennetts, 1995)

The structural behavior of each element level is characterized by appropriate actions (internal or external) and deformations (including strains and curvatures) associated with the element. The actions and deformations for the three element levels are:

1. Force and strain of the subarea.
2. Force and strain, and moment and curvature of the cross section.
3. Force and displacement, and moment and rotation of the member.

Having defined the actions and deformations, succinct equations are formulated to relate the actions and deformations of the three element levels. These actions and deformations are related by material behavior, boundary conditions, compatibility, and requirements for static equilibrium (Fig. 8.29). To determine the structural behavior of the member, the solution sought is a set of actions and deformations for the three levels such that all the requirements are satisfied.

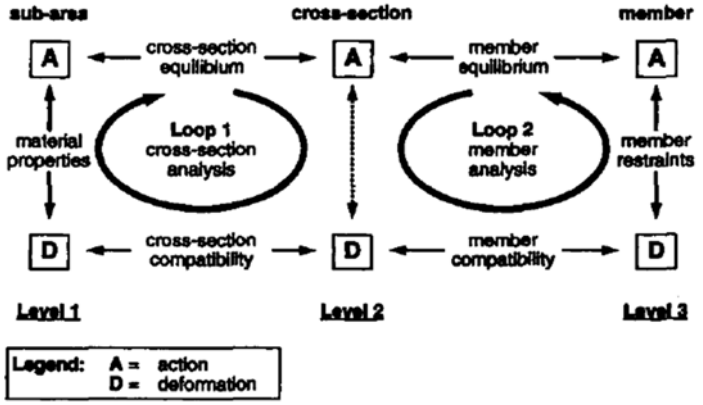

Fig. 8.29 Action-deformation relationships and solution procedure (Poh and Bennetts, 1995)

A simple iterative approach is adopted to obtain the solution, in which the actions and deformations of the three levels are calculated successively in loops till the solution converges. The procedure comprises two iterative loops (Fig. 8.29). The behavior of the cross section is

determined in the first loop (cross-section analysis) and the behavior of the member is determined in the second loop (member analysis). While loop 1 iterates on material nonlinearity, loop 2 iterates on geometric nonlinearity.

The application of the model was demonstrated in relation to a practical example in which the fire resistance of an unprotected steel column of large cross-sectional area was evaluated.

- Kodur, Wang, and Cheng (2004)

Kodur et al. (2004) presents a numerical model, in the form of a computer program, for tracing the behavior of high performance concrete (HPC) columns exposed to fire. The numerical procedure used in the model is similar to the one which was previously applied to the fire resistance calculations of NSC columns (Lie & Irwin, 1993; Kodur & Lie, 1996). The fire resistance calculation is performed in three steps; namely, the calculation of the temperatures of the fire to which the column is exposed, the calculation of the temperatures in the column, and the calculation of the resulting deformations and strength, including an analysis of the stress and strain distribution. In the strength analysis calculations, the extent of spalling is accounted for through a simplified approach.

The column temperatures are calculated by a finite difference method. The cross-sectional area of the column is subdivided into a number of elements, arranged in a triangular network (Fig. 8.30). The elements are square inside the column and triangular at the column surface. The temperature rise in the column can be derived by creating a heat balance for each element.

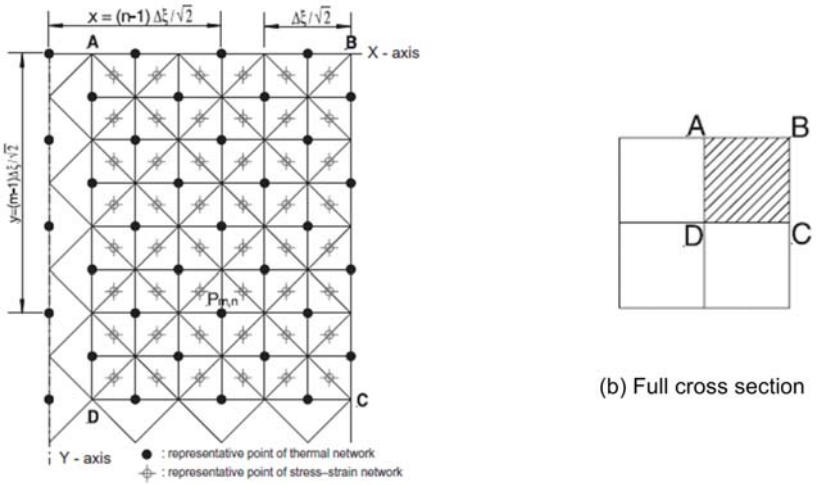

Fig. 8.30 Thermal and stress-strain network in one-quarter cross-section (Kodur et al., 2004)

In order to calculate the strains and stresses in the column and its strength during fire exposure, the triangular network described above is transformed into a square network. In Fig. 8.30, a quarter section of this network, consisting of square elements, arranged parallel to the x- and y-axis of the section, is shown. The arrangement of the elements in the three other quarter sections is identical. The temperatures, deformations and stresses in each element are represented by those at the centre of the element. The temperature at the centre of each element is obtained by averaging the temperatures of the elements in the triangular network noted above.

For the steel reinforcing bars, an approximate average bar temperature is obtained by considering the column as consisting entirely of concrete and selecting the temperature at the

center of the bar section as the representative bar temperature. The strain in an element of concrete can be given as the sum of the thermal expansion of the concrete, the axial strain due to compression and the strain due to bending of the column. A similar calculation is performed for the steel reinforcing bar elements.

The stresses at mid-section in the concrete elements can be calculated for any value of the axial strain, e, and curvature, $1/\rho$. From these stresses, the load that each element carries and its contribution to the internal moment at mid-section can be determined. By adding the loads and moments, the load that the column carries and the total internal moment at mid-section can be calculated. The fire resistance of the column is derived by calculating the strength.

The following guidelines were incorporated into the model to determine the extent of spalling; (1) Spalling occurs when the temperatures in an element exceed 350 ˚C; (2) Spalling is influenced by the tie configuration adopted for the column. Spalling occurs throughout the cross-section when the ties are bent in a conventional pattern. Spalling occurs only outside the reinforcement cage when the ties are bent at 135˚ into the concrete core; (3) The extent of spalling is dependent on the type of aggregate, presence of fiber reinforcement and spacing of ties. The extent of spalling is higher (100%) in the siliceous aggregate HSC than that for carbonate aggregate HSC (40%). No spalling occurs when polypropylene fibers are present in the concrete mix. The extent of spalling in HPC columns with steel fiber is about 50%. No spalling occurs inside the reinforcement core when the tie spacing is 0.7 times the standard spacing. The extent of spalling is also influenced by relative humidity. A higher relative humidity in the HPC column (90% or higher) leads to higher spalling .

The above guidelines have been incorporated into the computer program and the user can select the extent of spalling based on the design parameters. The numerical procedure described above was incorporated into a computer program. For any time step, the analysis starts with the calculation of temperatures due to fire. The next stage is to determine the cross-sectional temperatures by making use of the thermal properties of the column materials. In the third stage, the strength of the column, during exposure to fire, is determined by successive iterations of the axial strain and curvature until the internal moment at mid-height is in equilibrium with the applied moment. The extent of spalling in the section is accounted for based on the above set of guidelines.

The validity of the computer program is established through numerical studies on four HPC columns. The measured and predicted fire resistances of four HPC columns are compared in Table 8.5 . The time to reach failure is defined as the fire resistance for the column.

Table 8.5 Summary of test parameters and results for HPC columns (Kodur et al., 2004)

Column	Dimensions (mm)	Concrete strength (f_c')		Factored Resistance	Test load	Load intensity	Fire resistance	
		28day (MPa)	Test day (MPa)	(Cr)(kN)	(C) (kN)	(C/Cr)	Test (h:min)	Model (h:min)
THC4	305×305	60.6	99.6	3697	2000	0.54	3:22	3:06
THC8	305×305	60.4	72.7	2805	2000	0.71	5:05	4:31
TSH11	305×305	63.2	89.1	3349	2200	0.66	3:26	2:56
THP14	305×305	51.9	86.8	3266	2200	0.67	3:53	3:03

Fig. 8.31 the calculated and measured axial deformations are shown for four columns. It can be seen that the computer model predicts reasonably well, the trend in the progression of the axial deformations with time. However, the variation between predicted and measured deformations

could be partly attributed to the ‘‘spalling factor’’ assumed in the analysis, since the extent of spalling used in the analysis has a moderate influence on the axial deformations.

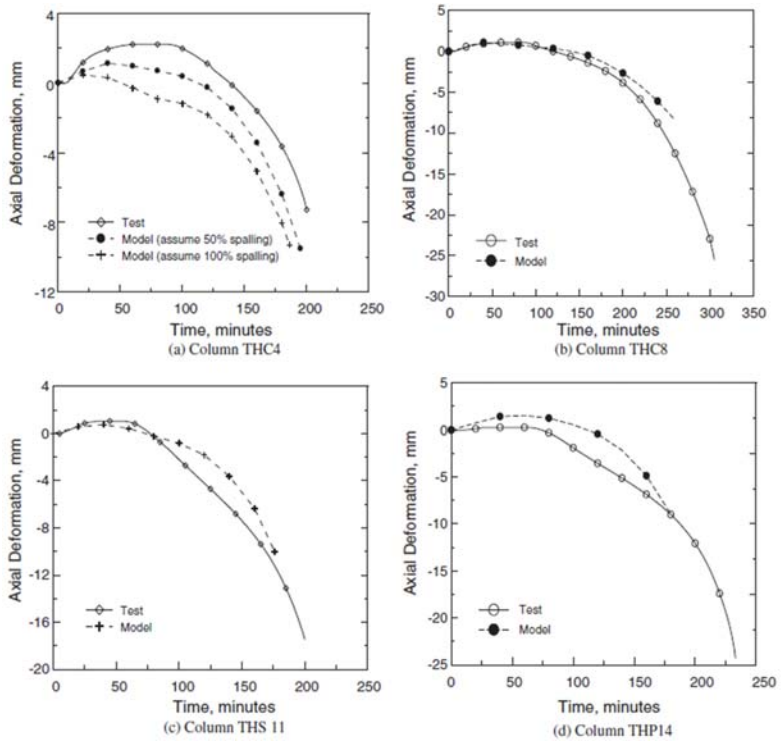

Fig. 8.31 Comparison of axial deformation for HPC columns (Kodur et al., 2004)

Based on the results of this study, the following conclusions can be drawn: (1) The computer program presented in this study is capable of predicting the fire resistance of HPC columns, within the limitations of the basic test parameters, with an accuracy that is adequate for practical purposes. (2) The numerical model accounts for spalling of HPC under fire conditions. The simplified approach used for calculating spalling accounts for tie configuration, aggregate type and presence of fibers. (3) Using the model, the fire resistance of HPC columns can be evaluated for any value of the significant parameters, such as load, section dimensions, column length, concrete strength, aggregate type and fiber reinforcement, without the necessity of testing. (4) The model can also be used for the calculation of the fire resistance of columns made with concrete other than those investigated in this study; for example, lightweight aggregate concrete or rectangular cross-section, if the relevant material properties are known. (5) Data on the mechanical and deformation properties of fiber reinforced HPC, at elevated temperatures, is needed for more accurately predicting the fire resistance of HPC columns.

8.3 Numerical studies of other RC members and systems

- Lim, Buchanan, Moss, and Franssen (2004)

This study presents the computer modeling of axially restrained, one-way reinforced concrete slabs in fire conditions. This study was carried out using a special purpose nonlinear finite element program, SAFIR, developed at the Univ. of Liege, Belgium, for analyzing the behavior

of structures in fire. SAFIR is an integrated thermal and structural analysis program for performing nonlinear two-dimensional (2D) and three-dimensional (3D) analysis of steel, concrete, and composite structures in fire (Franssen, 2003). The behavior of a structure in fire is simulated as a function of time using the temperature distributions in the structural elements evaluated from a thermal analysis. The structural analysis is performed using a variety of structural finite elements such as beam and shell elements. SAFIR can account for geometrical nonlinearity due to large displacements and material nonlinearity in the thermal and mechanical properties. For the analysis of concrete structures, concrete crushing and cracking are taken into account.

The study was carried out for slabs with pin supports and slabs with rotationally restrained supports (See Fig. 8.32). A single span, 5m slab, carrying a uniformly distributed load was analyzed using a special purpose, nonlinear finite element program, SAFIR.

(a) pin supported slab (b) rotationally restrained slab

Fig. 8.32 Structural model for analysis (Lim et al, 2004)

The study for pin-supported slabs considered the effects of the position of the thrust force at the supports and different axial restraint stiffness. The position of the line of the thrust is measured as the distance, x_0, from the fire-exposed face of the slab. Separate analyses were conducted for different positions of line of thrust at the end supports, ranging from -25 mm (25 mm below the exposed face) to 125 mm into the depth of the slab (Fig. 8.33 (a)). The position of line of thrust is fixed for each analysis and does not move during the fire exposure. Fig. 8.33 (b) shows the variation of the midspan deflections of the slabs during the exposure to the ISO fire.

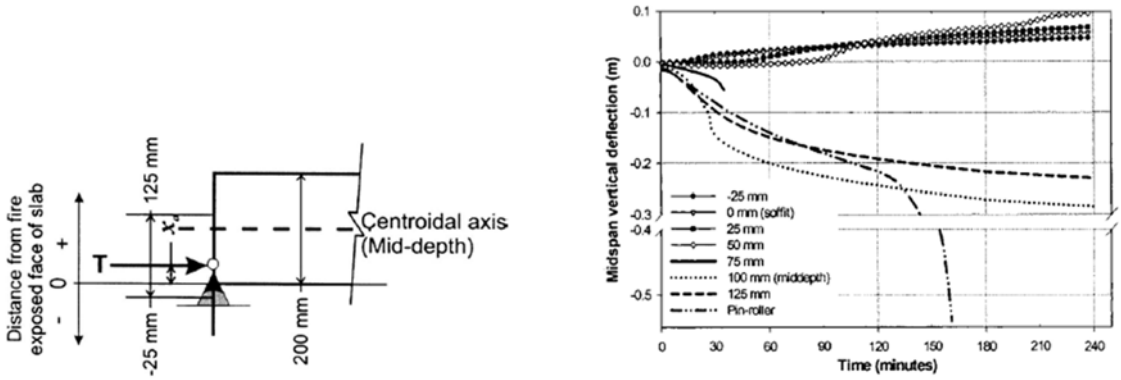

(a) Range of different positions of line of thrust (b) Midspan vertical deflection

Fig. 8.33 The effects of the position of the thrust force at the support (Lim et al, 2004)

In order to investigate the behavior of a slab in a structure with different axial restraint stiffness, the axial spring stiffness of the slab was varied. The analysis was carried out with xo fixed at 50

mm above the exposed face of the slab, representing a precast slab with a shim at the end supports. Fig. 8.34 shows the deflections of the slabs with different axial restraint stiffness

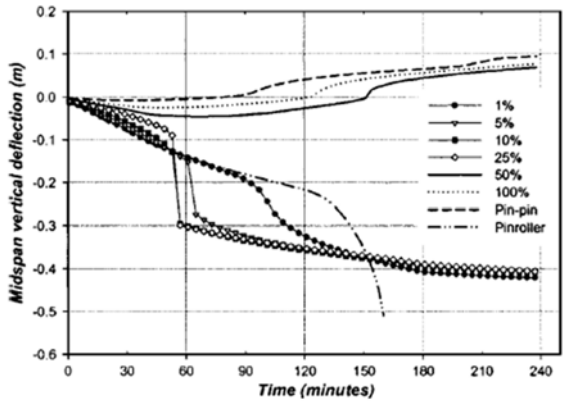

Fig. 8.34 Midspan vertical deflection with different axial restraint stiffness (Lim et al, 2004)

The effects of axial restraint on slabs with rotationally restrained supports were also investigated. The midspan vertical deflections of the slab with rotationally restrained supports and with different axial restraint stiffness are illustrated in Fig. 8.35. The deflections of the *pin-roller* slab are also plotted for comparison. The graph shows that slabs with rotationally restrained end supports have much better performance under fire conditions compared with the pin-roller slab.

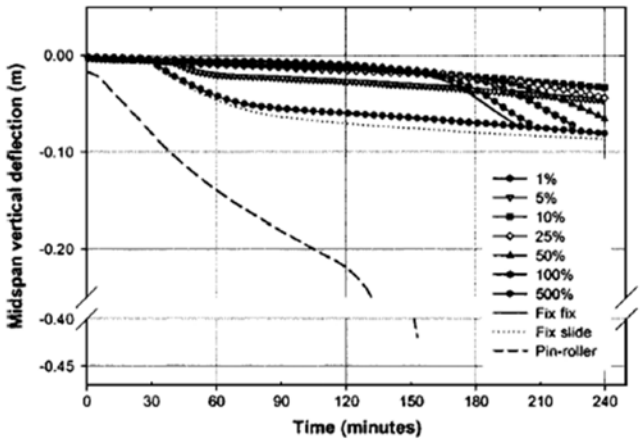

Fig. 8.35 Midspan vertical deflection of rotational restrained slab with different axial restraint stiffness (Lim et al, 2004)

The results of the study have shown that: (1) The behavior of one-way slabs under fire conditions is very sensitive to the end support conditions and the axial restraint stiffness. (2) For pin supported slabs, compressive axial restraint is beneficial only if the line of thrust at the supports is located well below the centroidal axis and if the centroid axis of the slab remains above the line of thrust during the fire exposure. (3) Pin-supported slabs with high axial restraint have good fire resistance. Slabs with intermediate axial restraint have less fire resistance than simply

supported slabs and slabs with low axial restraint behave similarly to simply supported slabs. (4) Slabs with rotationally restrained end supports have much better fire resistance than equivalent pin-supported slabs and they are less sensitive to the axial restraint stiffness.

- Moss, Dhakal, Wang, and Buchanan (2007)

This study investigates the fire performance of a two-way reinforced concrete slab subjected to fire over its whole area in a multi-story multi-bay building. The building is square, with three bays in each direction. The concrete slab is supported by a perimeter frame, four internal columns and no internal beams. It is assumed that all nine bays of the concrete slab at one level are subjected to fire from below. Two fires were used; the standard ISO834 fire for a four hour duration, and a parametric fire based on the ISO834 fire for one hour with the temperatures decaying to ambient in another two hours. Fig. 8.36 shows the distribution of temperatures in the slab when exposed to the same fire without a decay phase and with a decay phase.

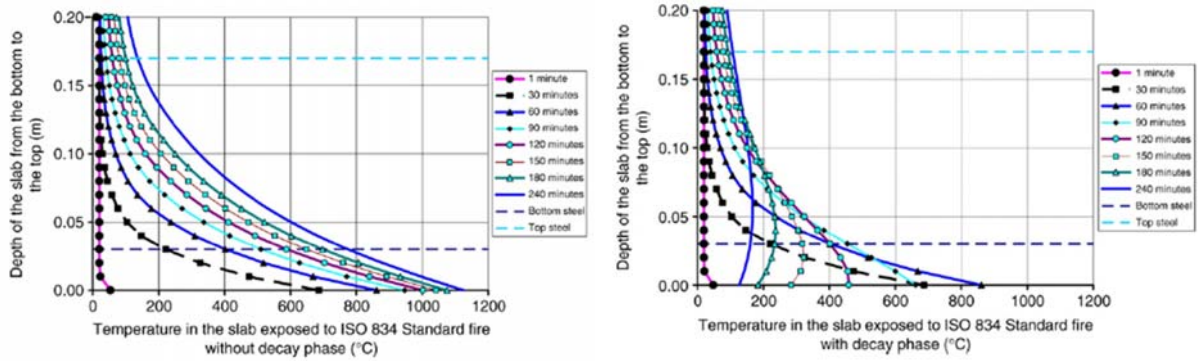

(a) Without a decay phase (b) With a decay phase

Fig. 8.36 Distribution of temperatures in the slabs exposed to an ISO 834 standard fire without a decay phase and with a decay phase (Moss et al., 2007)

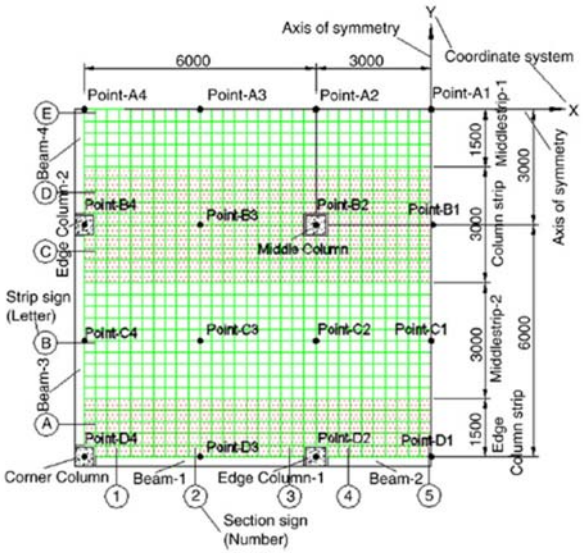

Fig. 8.37 Reference diagram for the nine-bay flat slab (showing one quarter of the slab) (Moss et al., 2007)

Using symmetry, only one quarter of the structure was modelled by SAFIR (Franssen, 2003). The columns were taken as fully fixed at the base, and restrained against all but vertical movement at the top. The columns above and below the fire-exposed floor were discretized into nine beam elements. The beam members were discretized using a number of 0.3m long beam elements. The concrete slab was modelled using 0.3m × 0.3m square shell elements. The top view of a quarter of the nine-bay flat slab is shown in Fig. 8.37. Results from this study for the effect of the fires are presented in Fig. 8.38 and Fig. 8.39.

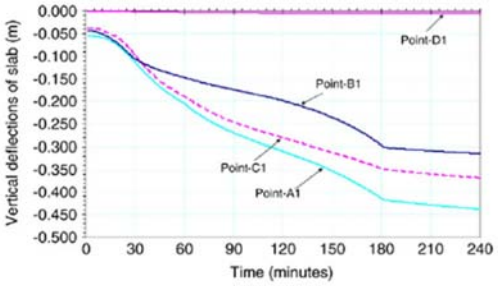

(a) Vertical deflection

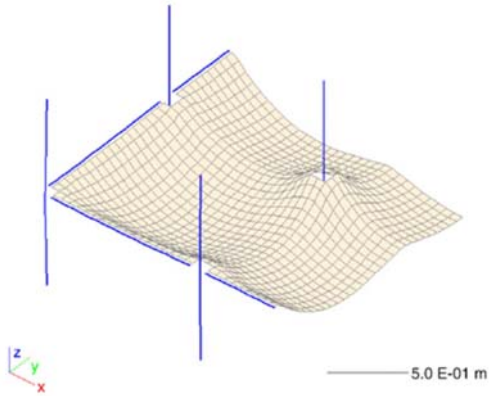

(b) Vertical deflected shape at 180min

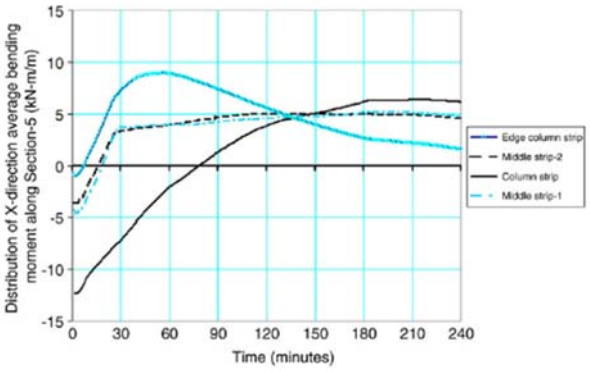

(c) X-direction average bending moments

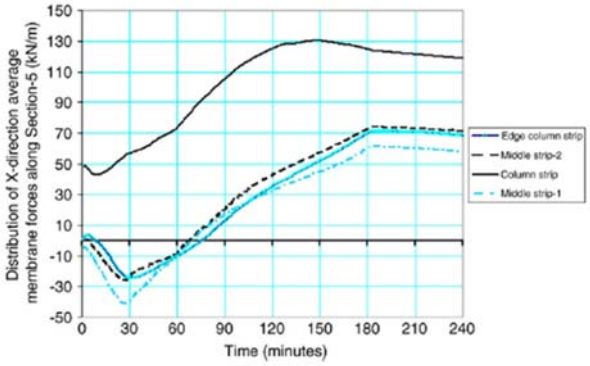

(d) X-direction membrance force

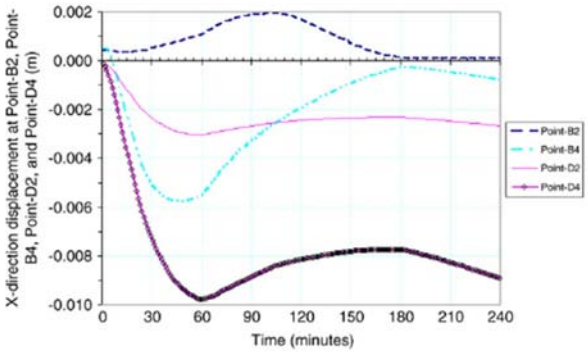

(e) x-direction displacements

Fig. 8.38 Result of flat slab exposed to an ISO 834 standard fire without a decay phase (Moss et al., 2007)

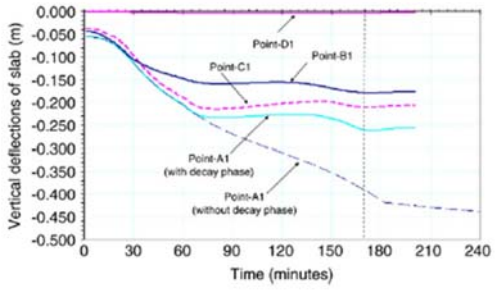

(a) Vertical deflection

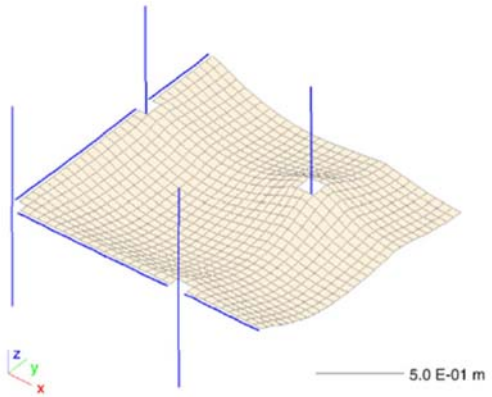

(b) Vertical deflected shape

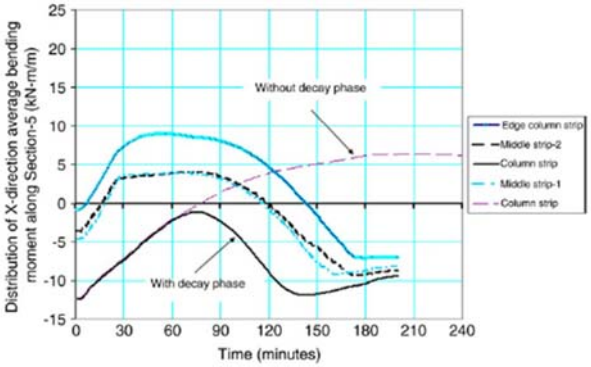

(c) X-direction average bending moments

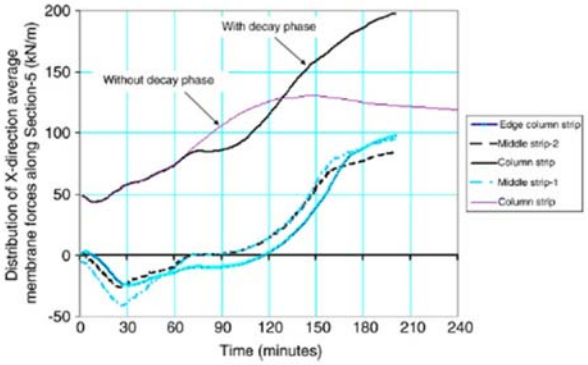

(d) X-direction membrance force

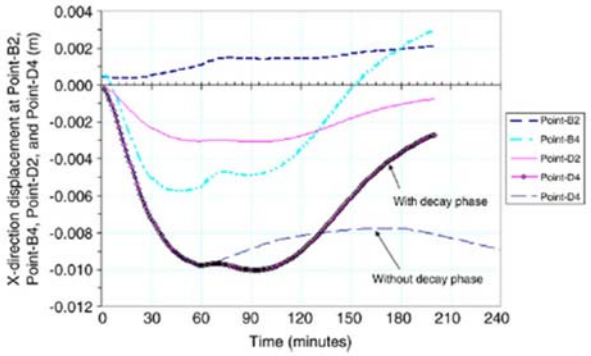

(e) x-direction displacements at point B2, B4, D2 and D4

Fig. 8.39 Result of flat slab exposed to an ISO 834 standard fire with a decay phase (Moss et al., 2007)

For a fire without a decay phase: (1) The bending moments in the slab reach a peak when the bottom steel reaches 300-400˚C and the slab loses strength as the bars heat up further. (2) The tensile membrane forces are limited by the loss of strength in the reinforcing bars as they heat up, and by increasing vertical deflections. (3) No failure occurred, even after four hours of fire exposure, due to the beneficial effects of large displacements and tensile membrane action.

For a fire with a decay phase, the slab behaves differently in the following ways: (1) The bottom of the concrete slab starts to cool once the temperatures start to drop, so that the yield strength of the bottom reinforcing increases and it starts to contract, along with the lower part of the slab. (2) Vertical deflections stop increasing after the fire goes out. (3) The average bending moments in the slab change from positive to negative as the slab cools down and the thermal gradients diminish. (4) The membrane forces become tensile and keep increasing long after the fire goes out, due to increasing strength and continuing thermal contraction. These membrane forces become much greater than those predicted during the continuous four hours of fire exposure. Therefore, designers must ensure good anchorage of all slab reinforcing, especially the top steel, into the edge beams to resist the tensile membrane forces.

- Yu and Huang (2008)

It is evident from a series of tests on simply supported reinforced concrete slabs that the failure of the slabs at large deflections is due to the formation of individual large cracks. In this study, a non-linear layered procedure with embedded weak discontinuity is developed to quantitatively model the progressive tensile failure of reinforced concrete slabs subjected to large deflections. The current model inherits the advantage of the smeared approach, and at the same time, introduces the opening width of crack explicitly by taking the advantage of the better description of the kinematical characteristics of the embedded (EFEM) approach.

In order to demonstrate the capability of the formulation described above to model reinforced concrete slabs under fire conditions, a total of 3 two-way simply supported reinforced concrete slabs tested at the University of Manchester (Bailey and Toh, 2007) and the University of Sheffield (Foster, 2006) were modelled in this study. All the slabs were uniformly loaded during the test. Linear temperature distribution between the top and bottom surfaces was assumed in the model. The layered temperatures were then calculated according to the measured surface temperature data. The tested material properties at ambient temperature were used in the modeling.

Fig. 8.40 shows the comparisons of the central deflections of the slabs predicted by the current model against test results, together with the predictions of the previous smeared model. It can be seen that reasonable agreements between the current model's predictions, test results and the smeared model's predictions were achieved. This again confirms that current model can predict well the global behaviors of reinforced concrete slabs in fire. The predicted cracking pattern of the test slab MF1 (Bailey and Toh, 2007) is shown in Fig. 8.41. It is evident that a large through crack was formed along short span of the slab in which the opening width of the crack is about 62 mm. The cracking pattern of Slab-MF1 observed in the test is shown in Fig. 8.42. It can be seen that the maximum crack opening along the short span was about 75 mm. This comparison further validates the ability of the non-linear procedure proposed in this study for modeling integrity failure of reinforced concrete slabs subjected to extreme loading conditions, such as fire.

From the result, it shows that the model developed in this study is not sensitive to the FE mesh size and the aspect ratio of the slab. The results predicted by the model developed agreed well with the test data in terms of deflection and crack open width, also agreeing well with those modeled by the smeared model. Hence, this new approach provides a numerical method to predict the load capacity as well as identifying the occurrence and severity of crack failure in reinforced concrete slabs subjected to extreme loading conditions, such as fire.

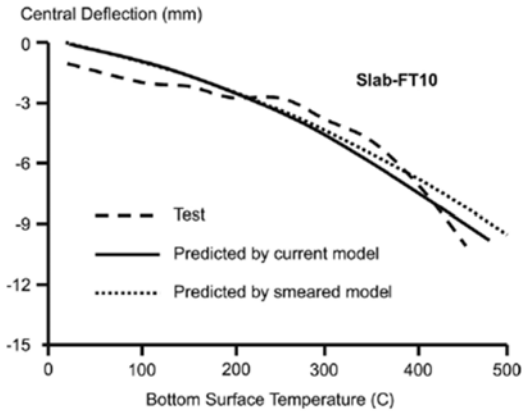

(a) Slab FT10

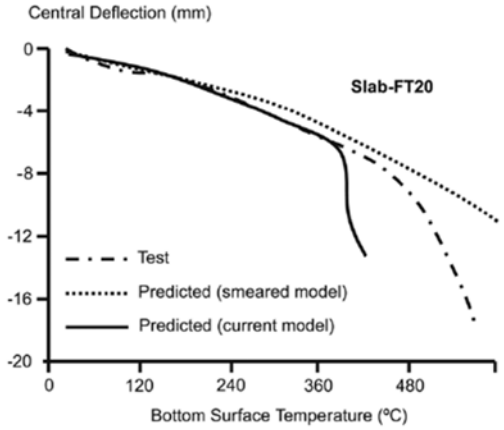

(b) Slab FT20

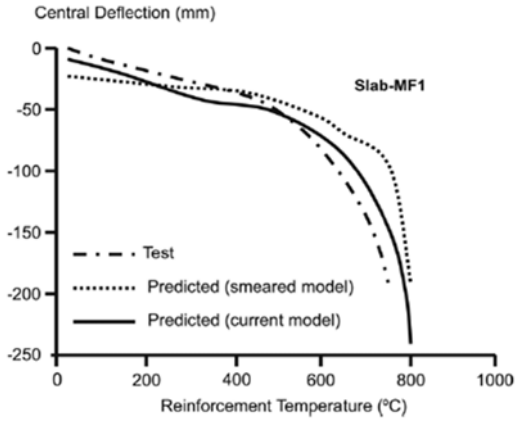

(c) Slab MF1

Fig. 8.40 Comparisons of the central deflections of the slabs (Yu and Huang, 2008)

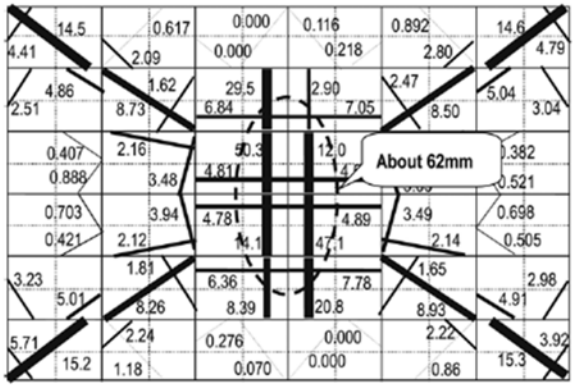

Fig. 8.41 Predicted cracking pattern of the bottom layer of the Slab-MF1 at 800˚C of reinforcement temperature (Yu and Huang, 2008)

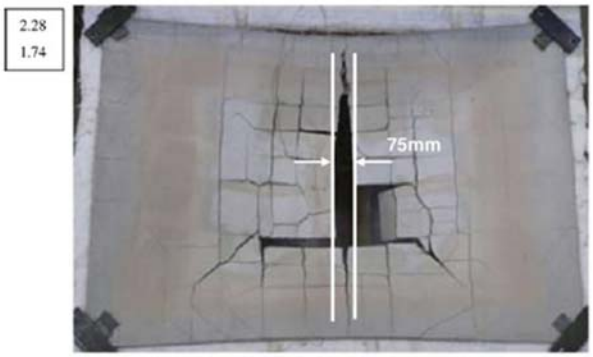

Fig. 8.42 Predicted and tested cracking pattern of the top surface of the Slab-MF1 (Bailey and Toh, 2007)

9 Performance Study of RC Flexural Members under High Temperatures

9.1 Sectional analysis

Generally, sectional analysis can be used an analysis method for evaluating structural behavior of reinforced concrete members under fire. Sectional model for analysis with fire effect should be considered the nonlinear temperature distribution of section and the stress-strain relationship of materials with temperature effect for considering reduction effect of material strength and stiffness due to fire. The stress-strain relationship of materials with temperature effect can be derived by applying analytical model to address temperature effect on strength and stiffness of materials to the stress-strain relationship at the ambient temperature. Kent & Park's model (1971) as stress-strain relationship of concrete at normal temperature is used as following equations.

$$f_c^0 = f_c'\left[\frac{2.0\varepsilon_c}{\varepsilon_o} - \left(\frac{\varepsilon_c}{\varepsilon_o}\right)^2\right] \qquad 0 \le \varepsilon_c \le \varepsilon_o (= 0.002) \tag{9.1a}$$

$$f_c^0 = f_c'\left[1 - z^o(\varepsilon_c^o - \varepsilon_o)\right] \qquad \varepsilon_o \le \varepsilon_c^o \le \varepsilon_{20C}^o \tag{9.1b}$$

$$z^o = \frac{0.5}{\varepsilon_{50u}^o + \varepsilon_{50h}^o - \varepsilon_o}, \quad \varepsilon_{50u}^o = \frac{3 + \varepsilon_o \times 145 f_c'}{145 f_c' - 1000} \tag{9.1c}$$

Where, f_c^o, f_c', ε_c^o, and ε_o are concrete compressive stress at ambient temperature, concrete compressive strength at ambient temperature, concrete compressive strain corresponding to concrete compressive stress, f_c^o, and concrete compressive strain at the compressive strength, f_c'. z^o is slope of the decaying branch of the concrete stress-strain curve at ambient temperature. ε_{50u}^o and ε_{50h}^o are strain component that take into account effect of concrete strength on the slope of the descending branch of unconfined concrete at ambient temperature and strain component that gives the additional ductility due to the transverse reinforcement. ε_{50h}^o is assumed to be zero due to using unconfined concrete condition in this study.

Analytical model to address temperature effect on the strength and stiffness of concrete is used as the model of Nielsen at al. (2004). The following equations are for considering temperature effect on strength and stiffness of concrete.

$$\text{Strength: } f_c^T = \alpha_{c,strength} f_c^o, \ \alpha_{c,strength} = 1 - 0.016\theta^2, \quad \theta = \frac{T - T_o}{100}, \quad 0 \le \theta \le 7.9 \tag{9.2a}$$

$$\text{Stiffness: } E_c^T = \alpha_{c,stiffness} E_c^o, \quad \alpha_{c,stiffness} = \left(1 - 0.1\theta\right)^2, \quad \theta = \frac{T - T_o}{100}, \quad 0 \le \theta \le 10.0 \tag{9.2b}$$

Where, T and T_o are elevated temperature and reference temperature of concrete. The stress-strain relationship of concrete with temperature effect is given as;

$$f_c^T = \alpha_{c,strength} f_c' \left[\frac{2.0\varepsilon_c^T}{\varepsilon_o^T} - \left(\frac{\varepsilon_c^T}{\varepsilon_o^T} \right)^2 \right], \quad \varepsilon_o^T = \frac{\alpha_{c,strength}}{\alpha_{c,stiffness}} \varepsilon_o, \quad 0 \le \varepsilon_c^T \le \varepsilon_o^T \tag{9.3a}$$

$$f_c^T = \alpha_{c,strength} f_c' \left[1 - z^T (\varepsilon_c^T - \varepsilon_o^T) \right], \quad \varepsilon_o^T \le \varepsilon_c^T \le \varepsilon_{20C}^T \tag{9.3b}$$

$$z^T = \frac{0.5}{\varepsilon_{50u}^T + \varepsilon_{50h}^T - \varepsilon_o^T}, \quad \varepsilon_{50u}^T = \frac{3 + \varepsilon_o^T \times 145 \cdot \alpha_{c,strength} f_c'}{145 \cdot \alpha_{c,strength} f_c' - 1000} \tag{9.3c}$$

Where, f_c^T, ε_c^T and ε_o^T are concrete compressive stress at elevated temperature, concrete strain corresponding to concrete compressive stress, f_c^T, and concrete strain at compressive strength at elevated temperature. Fig. 9.1(a) shows the stress-strain relationship of concrete at ambient temperature and Fig. 9.1(b) shows the modified stress-strain relationship considering temperature effects on strength and stiffness of concrete with $f_c' = 20.7MPa$.

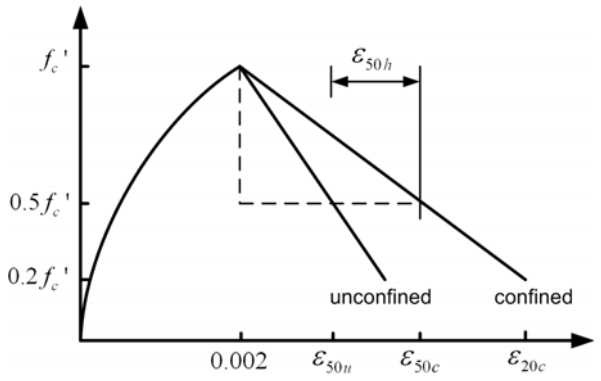

(a) Ambient temperature (Kent and Park, 1971)

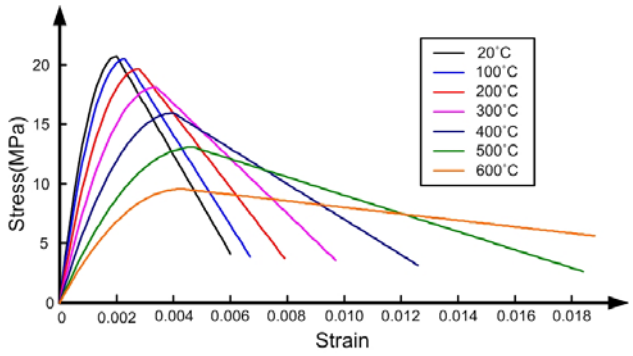

(b) Elevated temperature

Fig. 9.1 Stress-strain relationship of concrete

The stress-strain relationship of steel at normal temperature is assumed to be that of elastic-perfect plastic material. Analytical model to address temperature effects on strength and stiffness of steel is used as Enrocode3's model (1992). The following equation is for considering temperature effects on strength and stiffness of steel.

Strength: $f_y^T = \alpha_{s,strength} f_y^o$

$$\begin{aligned}
\alpha_{s,strength} &= 1 && (0^\circ C \le T \le 350^\circ C) \\
\alpha_{s,strength} &= 1.8848 - 2.528\times10^{-3} T && (350^\circ C \le T \le 706^\circ C) \\
\alpha_{s,strength} &= 0.002992764 - 2.02494\times10^{-4} T && (706^\circ C \le T \le 1200^\circ C)
\end{aligned} \tag{9.4a}$$

Stiffness: $E_s^T = \alpha_{s,stiffness} E_s^o$

$$\begin{aligned}
\alpha_{s,stiffness} &= 1 && (0^\circ C \le T \le 100^\circ C) \\
\alpha_{s,stiffness} &= 1.1 - 0.001T && (100^\circ C \le T \le 500^\circ C) \\
\alpha_{s,stiffness} &= 1.775 - 2.35\times10^{-3} T && (500^\circ C \le T \le 700^\circ C) \\
\alpha_{s,stiffness} &= 0.312 - 2.6\times10^{-4} T && (700^\circ C \le T \le 1200^\circ C)
\end{aligned} \tag{9.4b}$$

Once Eq. (9.4) of analytical model is substituted to the stress-strain relationship of steel at normal temperature, the stress-strain relationship of steel with temperature effect can be derived as follows;

$$f_s^T = E_s^T \varepsilon_s^T = \alpha_{s,stiffness} E_s^o \varepsilon_s^T, \quad \varepsilon_y^T = \frac{\alpha_{s,strength}}{\alpha_{s,stiffness}} \varepsilon_y^o, \quad (0 \le \varepsilon_s^T \le \varepsilon_y^T) \tag{9.5a}$$

$$f_s^T = f_y^T = \alpha_{s,strength} f_y^o, \quad (\varepsilon_y^T \le \varepsilon_s^T) \tag{9.5b}$$

Where, f_s^T, ε_s^T and ε_y^T are steel stress at elevated temperature, steel strain corresponding to steel stress, f_s^T, and steel strain at yield strength at elevated temperature. Fig. 9.2(a) shows the stress-strain relationship of steel at ambient temperature and Fig. 9.2(b) shows the modified stress-strain relationship considering temperature effects on strength and stiffness of steel with $f_y{}^o = 413MPa$.

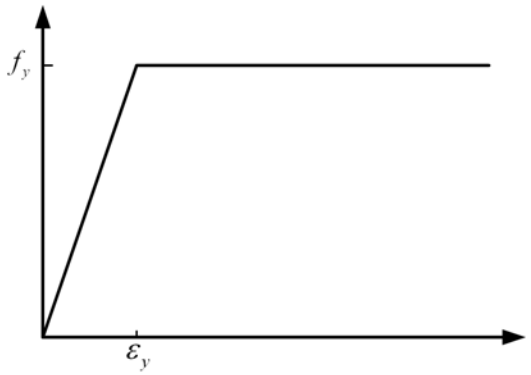

(a) Ambient temperature

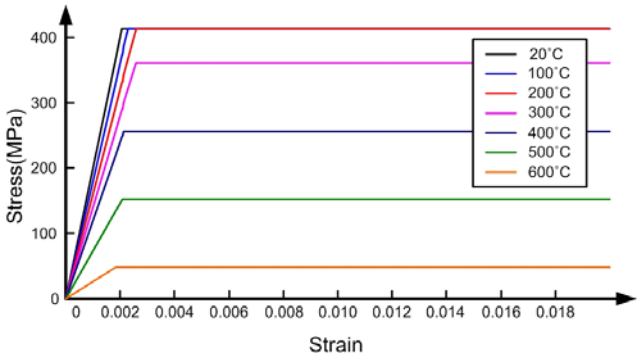

(b) Elevated temperature

Fig. 9.2 Stress-strain relationship of steel

Sectional analysis can be classified Layered sectional analysis and fiber sectional analysis in accordance with how to divide a section. Layered sectional analysis can be used for structural member with 1-side heating condition such as slab because the section divides several layer elements along one direction as shown in Fig. 9.3(a). Fiber sectional analysis can be used for structural member with 2, 3 and 4-side heating condition such as beam and column. The section of fiber sectional analysis divides several fiber elements along two directions as shown in Fig. 9.3(b).

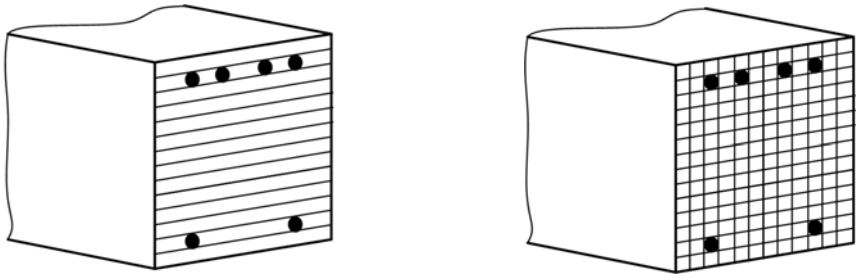

(a) Layer section (b) Fiber section

Fig. 9.3 Sectional analysis

In this study, in order to estimate structural response of reinforced concrete beam under exposure of fire, fiber section analysis is developed. In this analysis, the section consists of fiber element to consider the 3-side heating condition of actual beam under fire. Also, nonlinear section temperature distribution and the stress-strain relationship of concrete and steel with temperature effect are applied.

Temperature distribution of beam under fire depends on heating rate as well as thermal properties of materials such as thermal conductivity, specific heat, and density. Basically, In order to accurately reflect temperature distribution of beam section under fire in the analysis, fiber section analysis should be conducted by using temperature distribution of beam section from thermal transient analysis over time. However, this analysis procedure needs much longer analysis time due to repeatedly carry out the fiber section analysis and thermal transient analysis each time. In this study, as shown in Fig. 9.4, the temperature distribution selected from the thermal transient of ABAQUS(2007) is constantly applied to fiber section analysis at every time

step to simplify the repetitive analysis procedure. Once the temperature ratio of each fiber element is decided by the fraction of the maximum temperature among fiber elements to that of each fiber element, the temperature of fibers at each time step can be calculated with applied temperature and the temperature ratio of fibers.

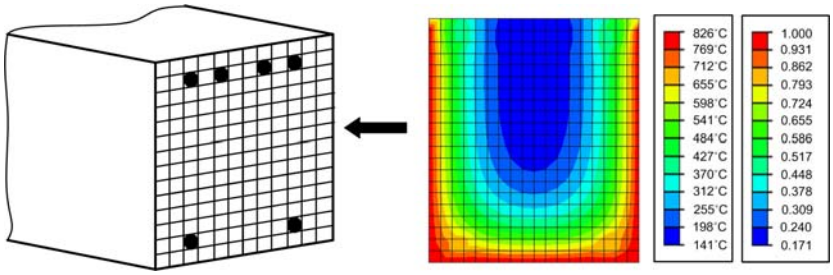

Fig. 9.4 Temperature distribution of the section

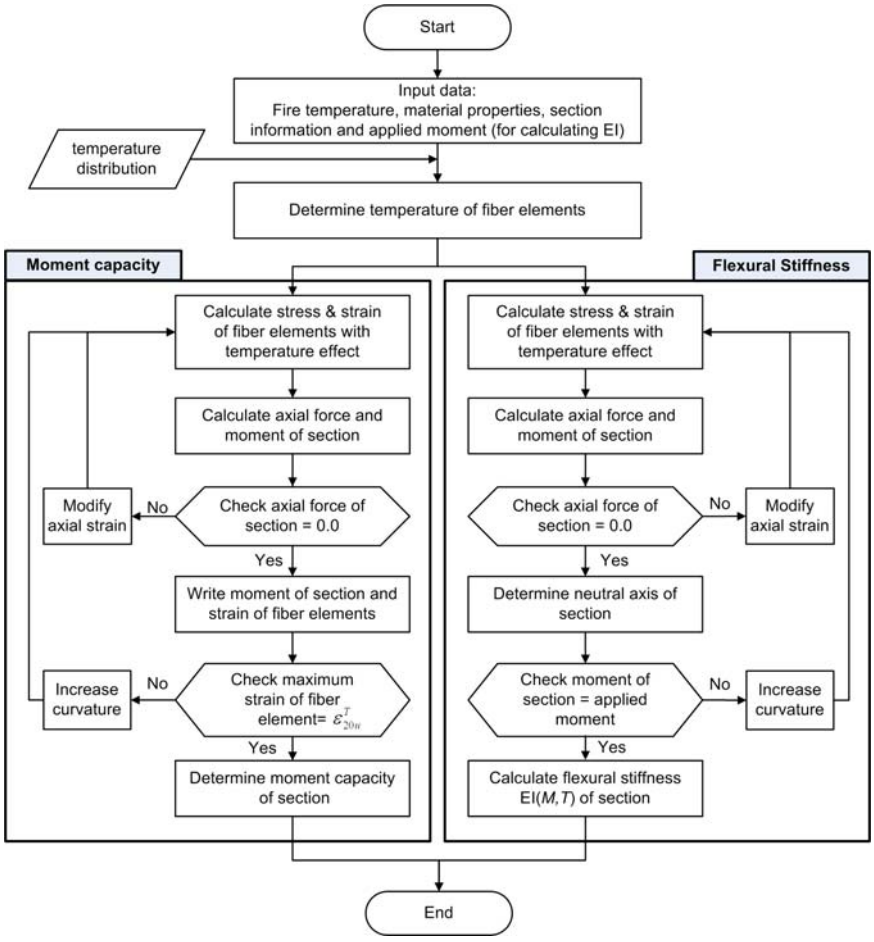

Fig. 9.5 Flowchart for fire resistance and flexural stiffness using fiber section analysis

This study evaluates fire resistance and flexural stiffness (EI) of beams under fire, using fiber section analysis with nonlinear section temperature distribution and the stress-strain relationship of materials with temperature effects. In the calculation of flexural stiffness using fiber section analysis, mechanical moment, temperature, and reinforcement layouts of section are considered. Fig. 9.5 shows the calculation procedure of fire resistance and flexural stiffness (EI) of beam under fire using simplified fiber section analysis.

9.2 Response behavior of unrestrained vs. restrained RC beams

In this study, fire resistance and deflection of beams under fire using fiber section analysis are estimated. Three beams with different restrained boundary conditions are employed as the selected members; simple supported beam, continuous 2-span beam, and continuous 3-span beam (Lin et al., 1981). In the evaluation of fire resistance of beam, structural fire resistance of critical beam section calculated by simplified fiber section analysis is compared with actual moment of fire test and that of ACI 216.1-07 code (2007).

Total deflection of beam under fire is defined by the sum of deflections due to mechanical moment, thermal moment occurred by restrained boundary condition of the continuous span and thermal curvature. In the calculation of deflection, fiber section analysis is used to consider the change of flexural stiffness according to mechanical moment, temperature, and reinforcement layouts of section. And thermal strain equation of Eurocode3 (1992) is used to consider the variation of thermal expansion coefficient depending on temperature.

9.2.1 Experimental results

Three types of beam selected for evaluation have same geometry and reinforcement layout. And boundary condition of these beams is changed as applied different cantilever loading (P_1, P_2) condition at the end of both side. Fig. 9.6 is shown that the details of geometry and reinforcement layout of beams. In the Fig. 9.6, the loadings, P_3 are applied as the mechanical loadings. And the cantilever loadings, P_1 and P_2 are applied to keep zero deflection at the both end for reflecting the continuity effect in the beams.

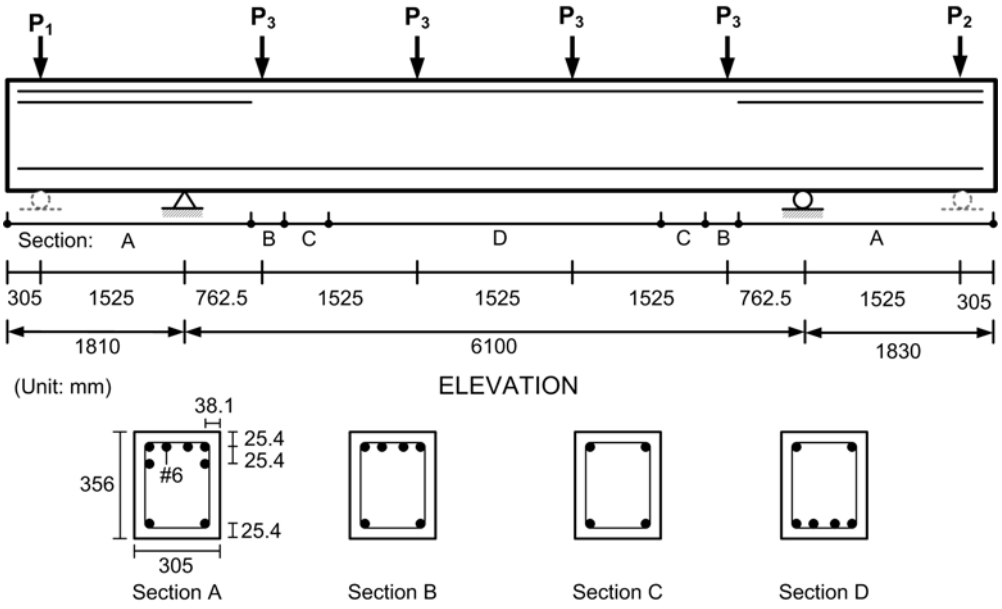

Fig. 9.6 Geometry and section information of specimens

Material property of the specimens and the applied loadings of the fire test are shown in Table 9.1. The cantilever loading, $P_1 = P_2 = 0$ is used for simple supported condition in the beam B-124. The cantilever loading, $P_1 = 0$ is used for continuous 2-span supported condition in the beam, B-125. Fire standard, ASTM E119 (2001) is applied as the fire condition at the middle span of the specimens.

Table 9.1 Material information and test data (Lin et al, 1981)

Specimen No.	f_c' (MPa)	E_c (MPa)	f_y (MPa)	E_s (MPa)	Span loads P_3 (kN)	Cantilever loads					
						West, P_1 (kN)			East, P_2 (kN)		
						0 hr.	Max.	End of test	0 hr.	Max.	End of test
B-123	29.7	26889.6	453.7	2.0E+5	49.8	57.4	102.3	92.1	60.5	94.7	97.9
B-124	30.1	26889.6	453.7	2.0E+5	20.0	0.0	0.0	0.0	0.0	0.0	0.0
B-125	27.0	25511.0	453.7	2.0E+5	28.5	0.0	0.0	0.0	46.3	89.4	80.5

Fig. 9.7 shows the applied loadings, mid-span deflection, and bottom steel temperature of the beams as the fire test result. In the result of simple supported beam, actual moment is constant due to pin condition at the both end. Mid-span deflection is increased in the same proportion until 60 minutes of fire test time. However, after then, the deflection is dramatically increased. In the result of continuous 2-span beam, the cantilever loading, P_2 is increased until 45 minutes, and then, constant. If the beam has enough moment capacity in fire test, P_2 should be continuously increased. So the result of fire test means that plastic hinge is formed in the critical section of the beam at the 45 minutes. In the result of continuous 3-span beam, the cantilever

loadings, P_1 and P_2 have the constant value after 60 minutes as the result of the continuous 2-span beam. The variety of loading means that plastic hinge is formed in the critical section of beam at the 60 minutes. Mid-span deflection of the beam is steeply increased after 150 minutes.

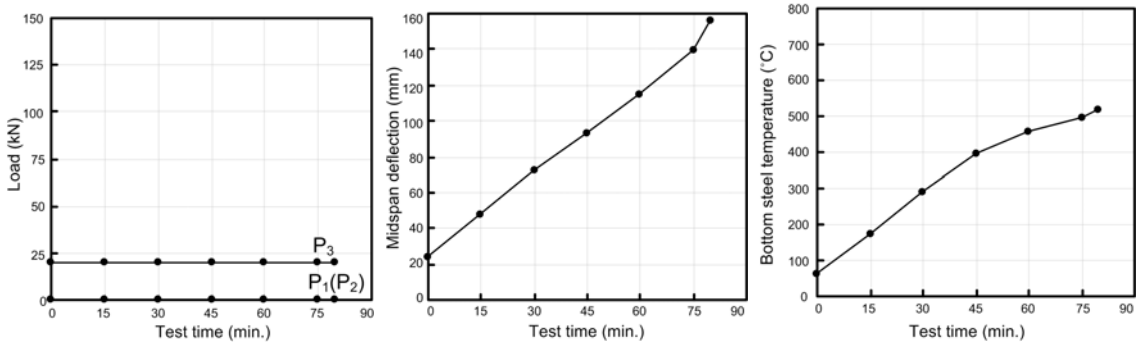

(a) Simple supported beam; B-124

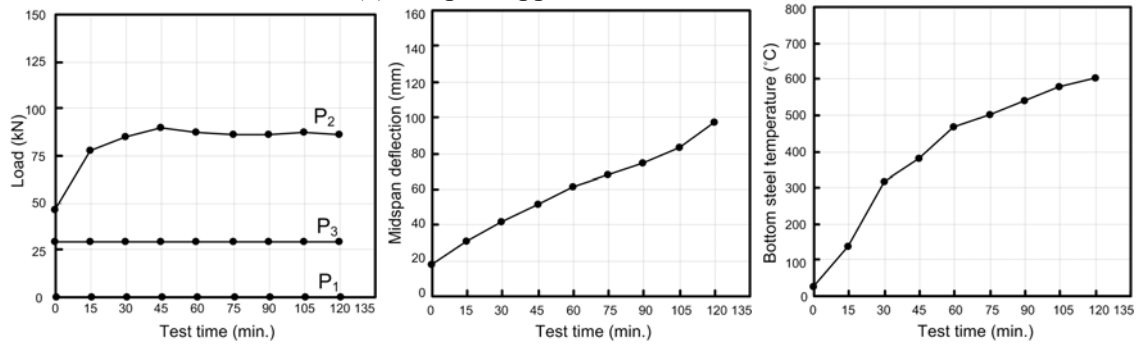

(b) Continuous 2-span beam; B-125

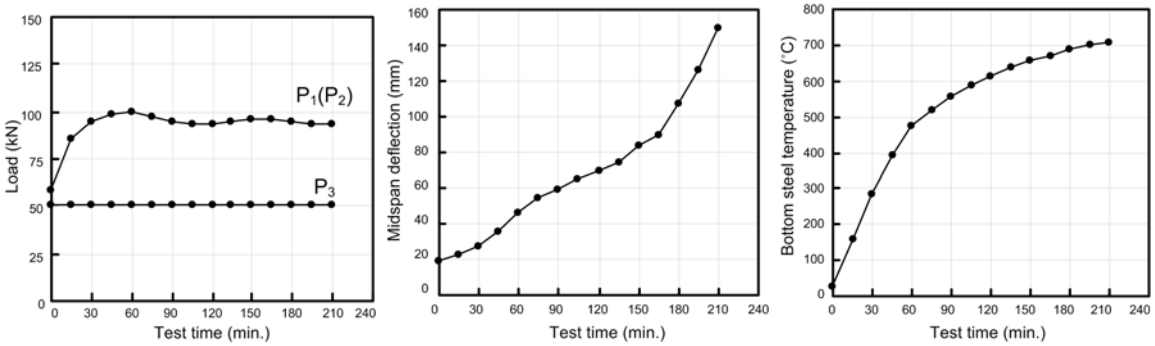

(c) Continuous 3-span beam; B-123

Fig. 9.7 Fire test results (Lin et al, 1981)

9.2.2 Residual moment capacity of the beams

Calculation of residual moment capacity using ACI 216.1-07 code

ACI 216.1-07 code (2007) describes acceptable methods for determining the fire resistance of concrete and masonry construction assembles and structural elements. In the ACI 216.1-07 code, residual moment capacity of the RC beam under elevated temperature can be calculated by the following equation.

Positive moment capacity: $M_{n\theta}^{+} = A_s f_{y\theta}(d - a_\theta / 2)$ (9.6a)

Negative moment capacity: $M_{n\theta}^{-} = A_s f_{y\theta}(d_{ef} - a_\theta / 2)$ (9.6b)

Where, A_s, $f_{y\theta}$, d, d_{ef}, and a_θ (= $A_s f_{y\theta} / 0.85 f_{c\theta}' b$, b = width of concrete beam, $f_{c\theta}'$ =reduced compressive strength of concrete at elevated temperature) are cross-sectional area of the longitudinal tension reinforcement, reduced yield strength of reinforcing steel at elevated temperature, effective depth, reduced effective depth, and depth of equivalent concrete rectangular stress block at elevated temperature. Reduced effective depth, d_{ef} is the distance from the centroid of tension reinforcement to most extreme concrete compressive fiber at which point temperature does not exceed 760˚C (1400˚F).

In the calculation of residual moment capacity of the beam using ACI 216.1-07 code, temperature of concrete for calculating $f_{c\theta}'$ uses average temperature of rectangular stress block and the temperature of steel for calculating $f_{y\theta}$ uses each temperature located in steel in Fig. 9.8. Reduced compressive strength of concrete, $f_{c\theta}'$ is calculated by using Fig. 9.10 and reduced yield strength of reinforcing steel, $f_{y\theta}$ is calculated by using Fig. 9.10.

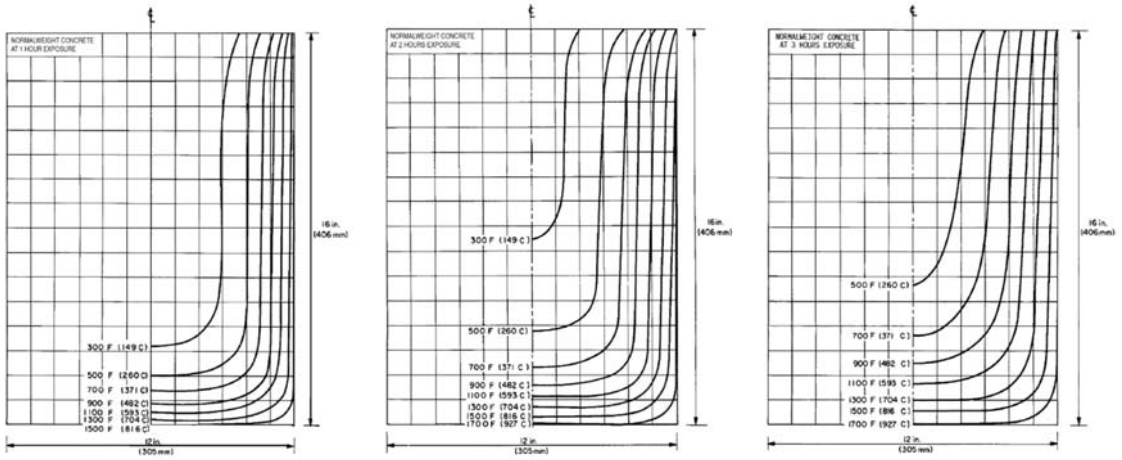

Fig. 9.8 Temperature distribution in a normal-weight concrete beam at the fire exposure (ACI 216.1-07, 2007)

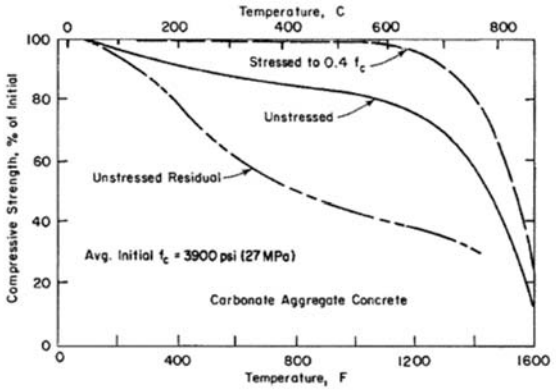

Fig. 9.9 Compressive strength of carbonate aggregate concrete at high temperature and after cooling (ACI 216.1-07, 2007)

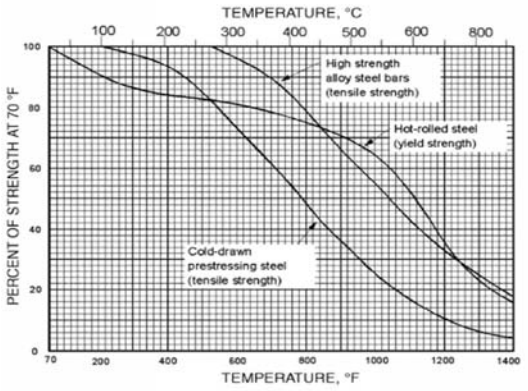

Fig. 9.10 Strength of flexural reinforcement steel bar at high temperature (ACI 216.1-07, 2007)

Calculation of residual moment capacity by fiber section analysis

Residual moment capacity of fiber section analysis is calculated by the flowchart of Fig. 9.5. Once the analysis is executed until compressive strain of any fiber element for concrete in the beam section is reached by concrete strain corresponding to a stress equal to 0.2 of the concrete strength at elevated temperature, ε_{20u}^{T}. Most large value of residual moment capacity in the analysis results is decided as residual moment capacity at elevated temperature.

Comparison of actual moment and residual moment capacity of three type beams

The actual moment distribution of simple supported beam is always constant because of no restrained boundary condition during fire test. When it has generally positive value, structural fire resistance of simple supported beam is decided by residual positive moment capacity of beam section.

Fig. 9.11 shows the actual moment and residual moment distribution of the simple supported beam before and after fire test. In the Fig. 9.11(a), residual negative moment capacities by two methods, fiber section analysis and ACI 216.1-07 code, are almost same before and after fire test. In the comparison of residual positive moment capacity, the values by two methods are almost same before the fire test. However, the value of ACI 216.1-07 code is larger than that of fiber

section analysis after fire test. In order to compare in detail the change of residual moment capacity according to temperature, residual moment capacity variation of the section at the right border in the region C (refer to Fig. 9.6) during fire test is shown as Fig. 9.11(b). In the first Figure of Fig. 9.11(b), the residual positive moment capacity by ACI 216.1-07 code is gradually reduced during fire time, but the residual positive moment capacity by fiber section analysis is dramatically reduced after the fire time, 30 minutes. Because of the difference of the variation of residual positive moment capacity, the result by ACI 216.1-07 code is larger than that of fiber section analysis at end of fire test. And the results by ACI 216.1-07 code do not show the occurrence of plastic hinge during fire test. On the other way, the results by fiber section analysis show the occurrence of plastic hinge at the fire time, 60 minutes. The difference of results indicates that ACI 216.1-07 code overestimates actual positive moment capacity of beam under fire, comparing with fiber section analysis.

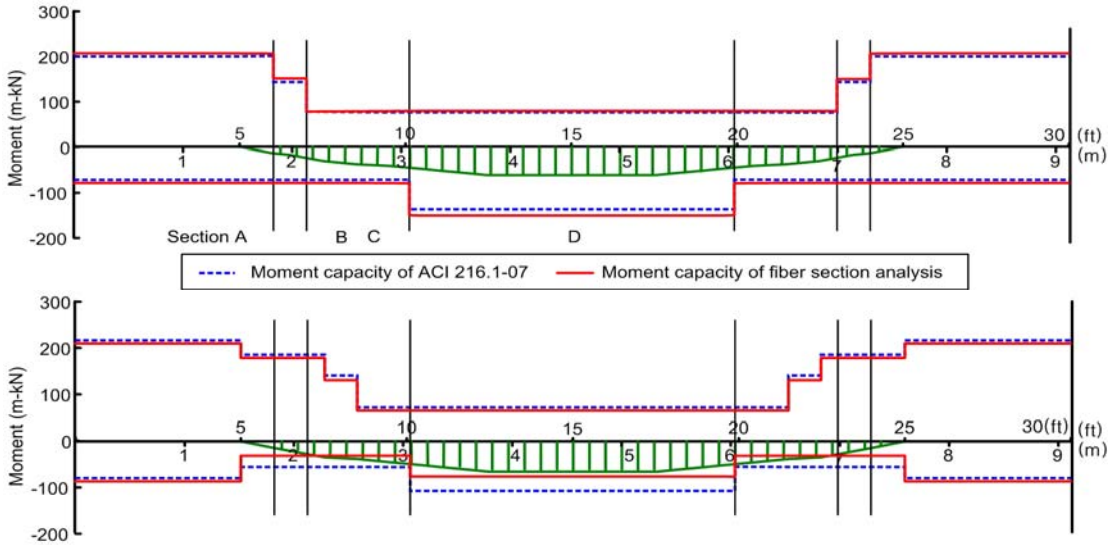

(a) Distribution of actual moment and moment capacity at the start and end of test

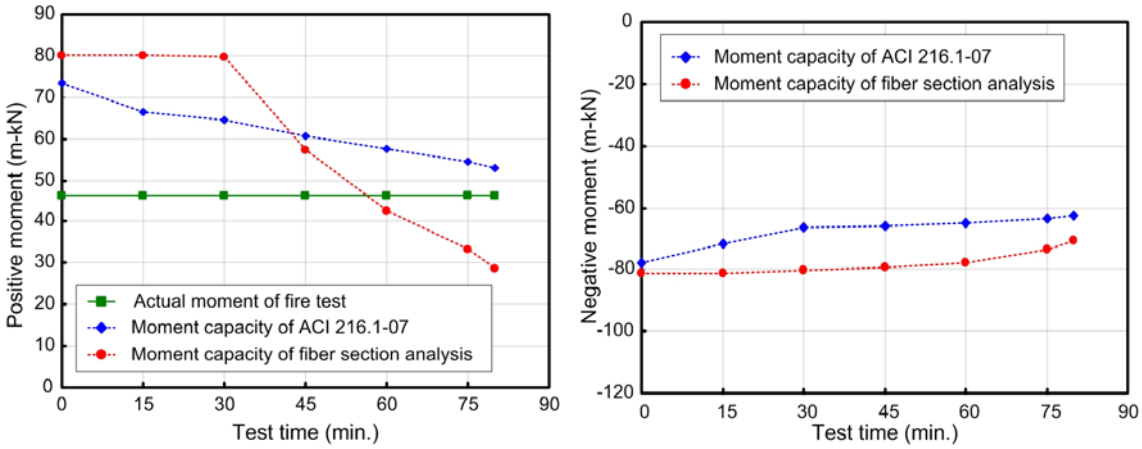

(b) Moment variation at right border of region C

Fig. 9.11 Comparison of actual moment and moment capacity of simple supported beam

In the second Figure of Fig. 9.11(b), the result by ACI 216.1-07 code is smaller than that of fiber section analysis during fire test. These results show that ACI 216.1-07 code underestimates actual negative moment capacity of beam under fire rather than fiber section analysis.

The actual moment distribution of continuous beam is changed by the moment redistribution due to restrained boundary condition of continuous span during fire test. Because the moment occurred by moment redistribution has generally negative values, the actual positive moments of the beam decrease, and the actual negative moments increase. Fire resistance in the continuous beam is decided by residual negative moment capacity of beam because of the decrease of residual negative moment capacity and simultaneously the increase of actual negative moment. But, when the decrease rate of residual positive moment capacity is larger than that of actual positive moment due to moment redistribution, fire resistance of the continuous beam is decided by residual positive moment capacity of beam.

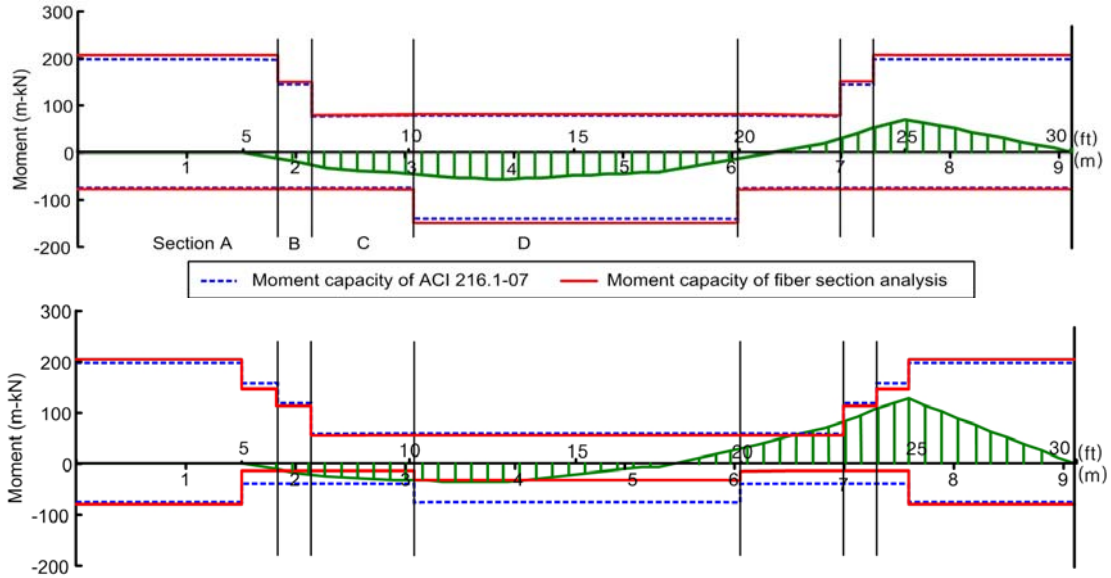

(a) Distribution of actual moment and moment capacity at the start and end of test

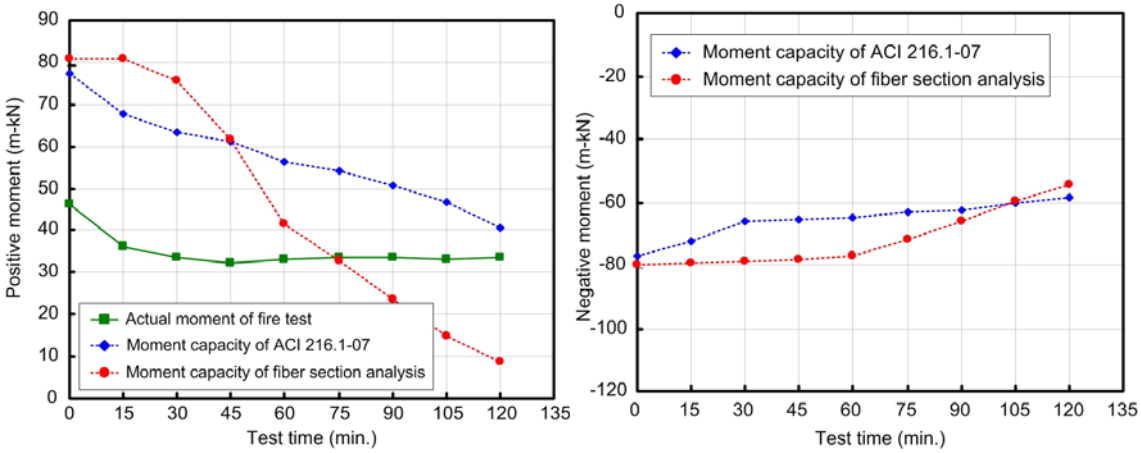

(b) Moment variation at right border of region C

Fig. 9.12 Comparison of actual moment and moment capacity of continuous 2-span beam

Fig. 9.12 shows the comparison of the actual moment and residual moment capacity of the continuous 2-span beam during fire test. In Fig. 9.12 (a), the results of continuous 2-span by two methods shows same trend in comparison with that of simple supported beam. In other words, ACI 216.1-07 code properly estimates the residual negative moment capacity of beam under fire, but it overestimates the residual positive moment capacity of beam under fire. In the first Figure of Fig. 9.12 (b), the results of ACI 216.1-07 code does not show the occurrence of plastic hinge during fire test. On the other way, the result of fiber section analysis shows the occurrence of plastic hinge at the fire time, 75 minutes. Specially, the location of plastic hinge is not negative moment region generally expected in the continuous beam, but positive moment region. The difference of results indicates that ACI 216.1-07 code overestimates actual positive moment capacity of beam under fire, rather than fiber section analysis. Also, it shows that in order to accurately estimate the fire resistance of continuous beam, the residual negative moment capacity as well as positive moment capacity should be calculated carefully.

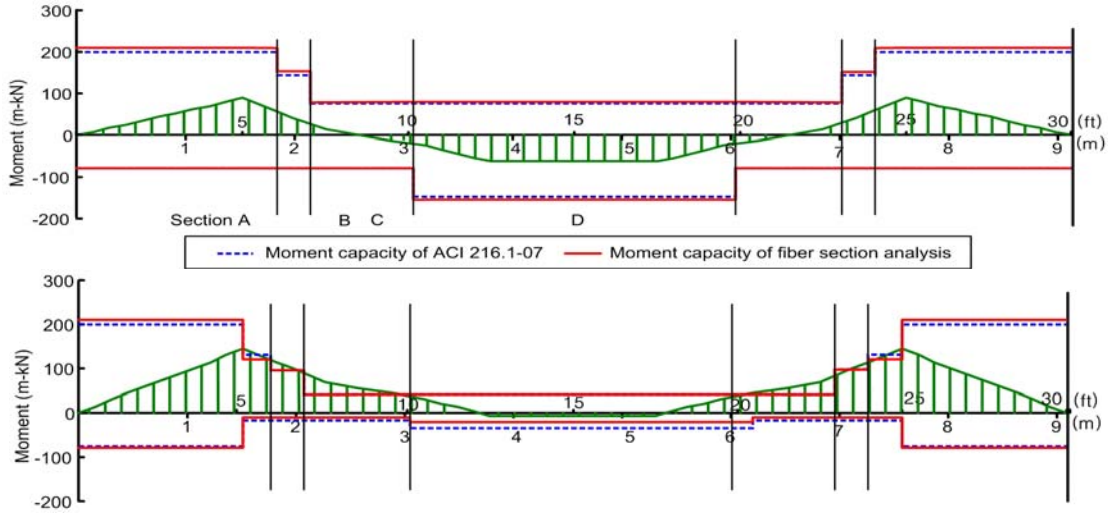

(a) Distribution of actual moment and moment capacity at the start and end of test

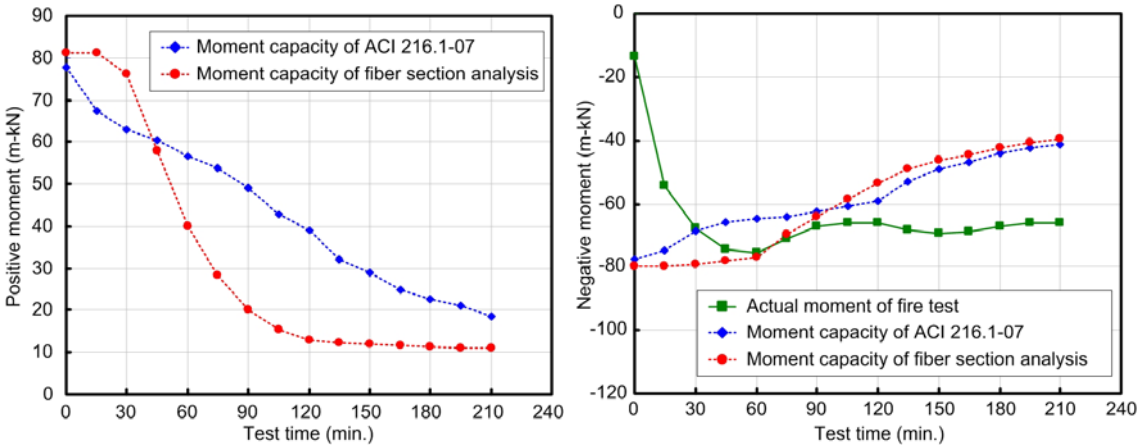

(b) Moment variation at left border of section C

Fig. 9.13 Comparison of actual moment and moment capacity of continuous 3-span beam

Fig. 9.13 shows comparison results of the actual moment and residual moment capacity of the continuous 3-span beam during fire test. Form Fig. 9.13(a), the results of continuous 2-span by two methods shows same trend in comparison with that of simple supported beam. In the second

Figure of Fig. 9.13(b), the result by ACI 216.1-07 code has smaller or similar values in compared with that by fiber section analysis. These results show that ACI 216.1-07 code properly estimates actual negative moment capacity of beam under fire.

In the view of fiber section analysis can predict more realistic residual moment capacity of beam compared with ACI 216.1-07 code, the equation of ACI 216.1-07 for residual negative moment capacity is suitable for design code. However, the equation of ACI 21.1-07 for residual positive moment capacity is not appropriate for design code due to overestimation of residual positive moment capacity of beam.

9.2.3 Deflection of the beams

Calculation of deflection by analytical model

In this study, the sum of deflections due to mechanical moment, thermal moment occurred by restrained boundary condition of the continuous span and thermal curvature is defined as total deflection of beam under fire. In the calculation of deflection, fiber section analysis is used to consider the change of flexural stiffness according to mechanical moment, temperature, and reinforcement layouts of section. And thermal strain equation of Eurocode3 (1992) is used to consider the variation of thermal expansion coefficient depending on temperature. Deflection of the beam at elevated temperature can be calculated by the following equations

$$v = v_{M,me} + v_{M,th} + v_{\phi,th} \tag{9.7}$$

Where, $v_{M,me}$, $v_{M,th}$ and $v_{\phi,th}$ are the deflections by the mechanical moment, the thermal moment and the thermal curvature. The deflections of the mechanical moment and the thermal moment can be calculated by following equations using dummy unit load method.

$$v_{M,me} = \int_0^l \frac{M_Q M_{me}}{EI(M,T)} dx, \quad v_{M,th} = \int_0^l \frac{M_Q M_{th}}{EI(M,T)} dx \tag{9.8}$$

Where, M_Q, M_{me}, M_{th}, and $EI(M,T)$ are the moment due to the unit load, the mechanical moment, the thermal moment by the restrained boundary condition of continuous span and flexural stiffness. In order to consider the variation of flexural stiffness according to mechanical moment, temperature, and reinforcement layouts of section, the beam is divided into several segments with 1ft in length. The flexural stiffness of each segment is calculated by simplified fiber section analysis according to the flowchart of Fig. 9.5.

The deflection of the thermal curvature, $v_{\phi_{th}}$ can be calculated by the following equation using double integration method.

$$v_{\phi,th} = \frac{\phi_{th}}{2} x^2 - \frac{\phi_{th}}{2} lx, \quad \phi_{th} = \frac{\varepsilon_{th}(T)}{h} \tag{9.9}$$

Where, ϕ_{th}, x, l, $\varepsilon_{th}(T)$ and h are the thermal curvature, the distance between the end of the beam and the location that wants to calculate deflection, length of the beam, thermal strain, and

depth of the measured temperature variation. The thermal strain, $\varepsilon_{th}(T)$ in the Eq. (9.9), uses that of concrete as the following equation suggested by the Eurocode3 (1992).

$$\varepsilon_{th} = -1.8\times10^{-4} + 9\times10^{-6}\cdot(T-20°C) + 2.3\times10^{-11}\cdot(T-20°C)^3 \le 14\times10^{-3} \text{ for siliceous} \quad (9.10a)$$

$$\varepsilon_{th} = -1.2\times10^{-4} + 6\times10^{-6}\cdot(T-20°C) + 1.4\times10^{-11}\cdot(T-20°C)^3 \le 12\times10^{-3} \text{ for carbonate} \quad (9.10b)$$

The calculated deflection of three beams by this analytical model according to elevated temperature is shown as Fig. 9.17.

Calculation of deflection by ABAQUS

In this study, 3-dimensional beam element with 25 integration point on section of ABAQUS uses for calculating deflection of three beams under fire. The numerical model using beam element for analysis of beams under fire is composed sixty elements with 0.5ft length for each element and sixty one nodes.

In the analysis model of ABAQUS for beams, Temperature dependent concrete smeared cracking model is used as Concrete failure model in analysis. Kent & Park's model and fracture based tension stiffening model are used as concrete constitutive model for compression and tension. Temperature dependent J2 model is used as Steel failure model of the model. And Elastic-perfect plastic model is used as steel constitutive model. Development length of steel reinforcement, 12in (minimum development length of ACI 318-05) is considered in the analysis model of ABAQUS in order to reflect rapid reduction effect of adhesive strength between concrete and steel in end zone of steel reinforcement of the beam under fire.

The analysis model of beam is analyzed using implicit and full integration analysis of ABAQUS. And If Convergence problem occurs in the analysis global stabilization option is used to solve it. Global stabilization values used in the analysis is smaller than that of suggested value(10^{-3}) of ABAQUS. So it has no effect to accuracy of deflection

Fig. 9.14, 9.15 and 9.16 show the results of three beams under fire by ABAQUS. In these Figures, it appears that the beam analysis using ABAQUS is well enough to predict the moment distribution variation of beam and presence of plastic hinge of beam due to fire. The deflection of three beams by ABAQUS is shown in Fig. 9.17.

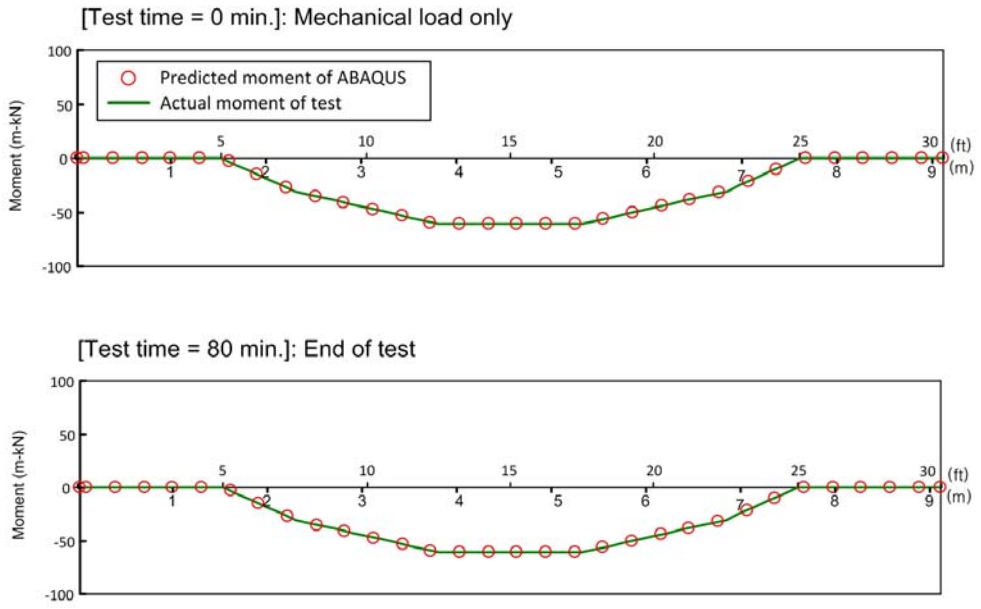

(a) Moment distribution

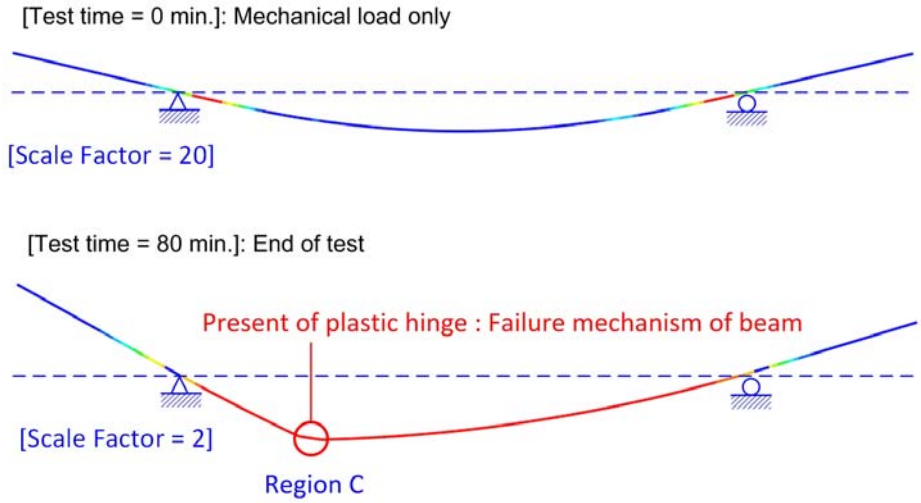

(b) Deformed shape of beam

Fig. 9.14 Result of simple supported beam, B-124 by ABAQUS

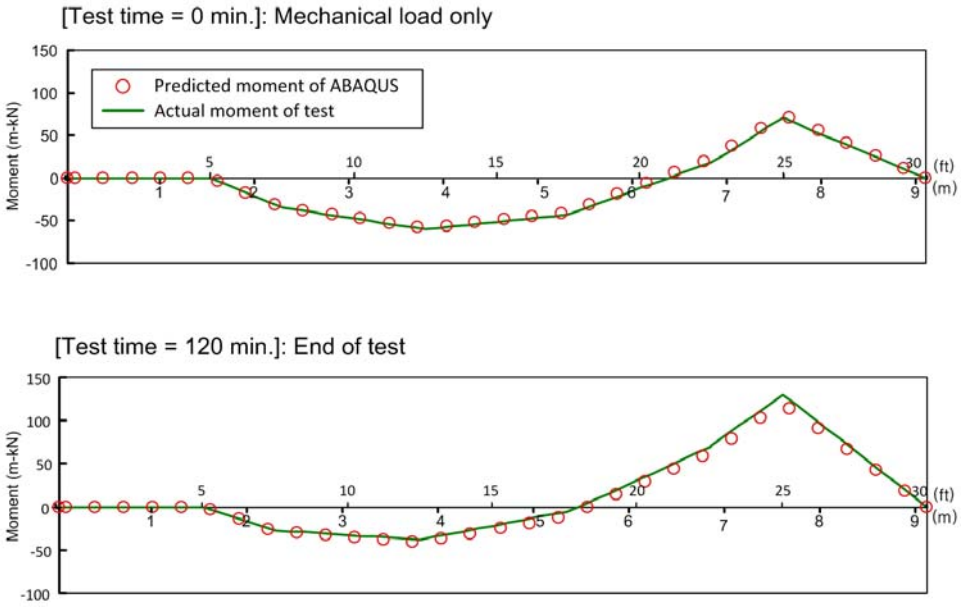

(a) Moment distribution

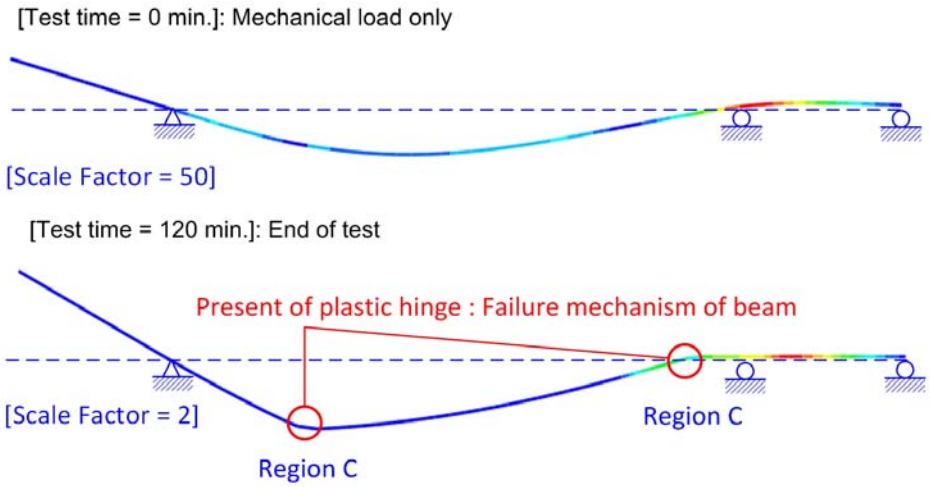

(b) Deformed shape of beam

Fig. 9.15 Result of continuous 2-span beam, B-125 by ABAQUS

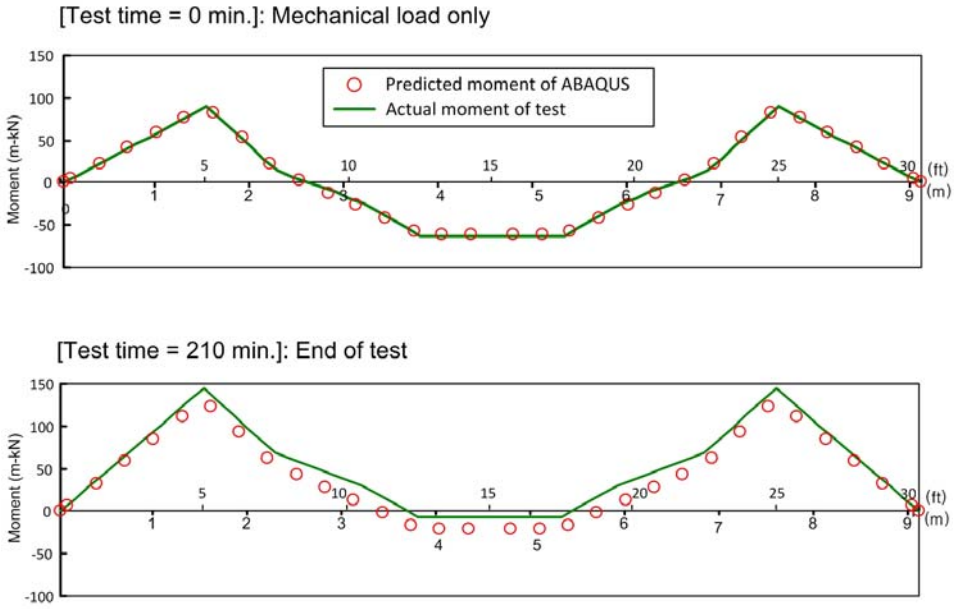

(a) Moment distribution

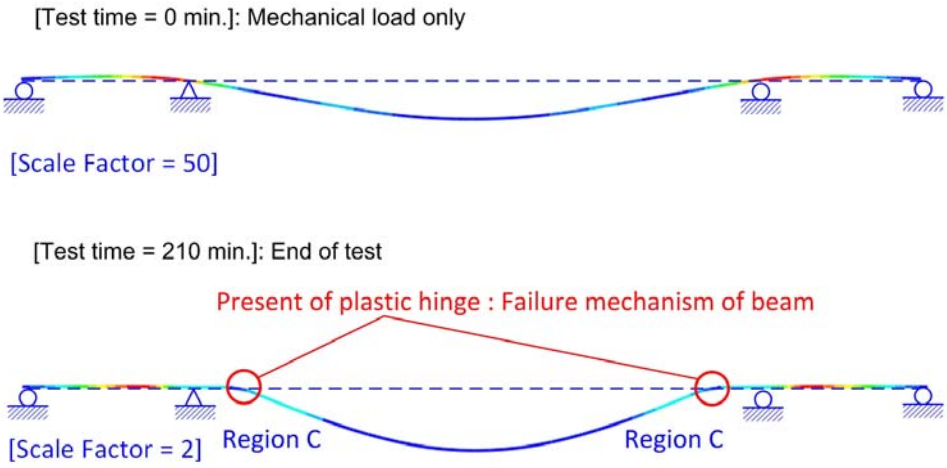

(b) Deformed shape of beam

Fig. 9.16 Result of continuous 3-span beam, B-123 by ABAQUS

Comparison of the deflection of three type beams

The comparison of actual mid-span deflection, calculated deflection by the analytical model using Eq. (9.7) and predicted deflection by ABAQUS is shown in Fig. 9.17. In the beam analysis of ABAQUS, two models are analyzed to evaluate deflection variation of beam according to whether the consideration of the reduction effect of adhesive strength between concrete and steel in the end zone of steel reinforcement in beam or not.

In the Fig. 9.17(a) for simple supported beam, the calculated deflection using Eq. (9.7) shows somewhat the error during fire test. But at the end of the fire test, it properly captured the trend of actual deflection. The predicted deflection using beam model of ABAQUS without development length shows somewhat the error during fire test. And the error increases as progressing fire test. But the predicted deflection by the beam model of ABAQUS with development length is well predicted with actual deflection during fire test.

In the Fig. 9.17(b) for continuous 2-span beam, the calculated deflection using Eq. (9.7) is well predicted with actual deflection during fire test. But at the end of fire test, it shows a little difference with actual deflection. The predicted deflection by the beam analysis of ABAQUS without development length properly evaluates actual deflection in the early region of fire test, but it can not capture the trend of actual deflection that is rapidly varied as progressing fire test. However the predicted deflection using beam model of ABAQUS with development length is well evaluates actual deflection during fire test. And it can also capture the trend of actual deflection.

In the Fig. 9.17(c) for continuous 3-span beam, calculated deflection using Eq. (9.7) shows somewhat the error during fire test. But at the fire time, 210 minutes, it properly captures the trend of actual deflection.. The predicted deflection by the beam analysis of ABAQUS without development shows somewhat the error during fire test. And the amount of this error increases more and more as progressing the fire test. it means that beam model of ABAQUS without development length can not capture the trend of actual deflection of beam. However the beam analysis of ABAQUS with development length properly evaluates actual deflection during fire test unlike the result of analysis without development length.

Based on the comparison results of deflection for three beams with different restrained condition under fire, the results indicate that even if calculated deflections by the analytical model, Eq. (9.7) have somewhat difference with actual deflection, the prediction of actual deflection is acceptable because it captures the trend of actual deflection. And it also indicate that The reduction effect of adhesive strength between concrete and steel in the end zone of steel reinforcement in the beam is very important factor to evaluate the deflection of beam under fire.

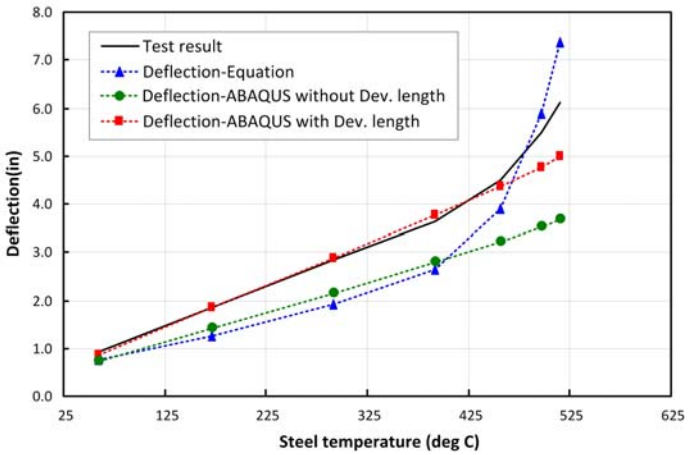

(a) Simple supported beam

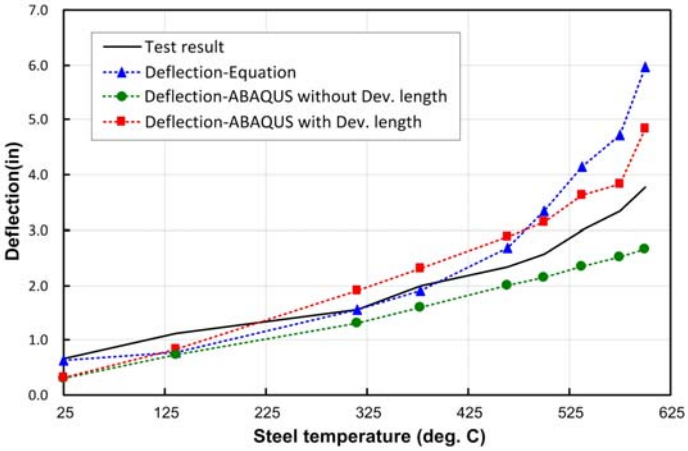

(b) Continuous 2-span beam

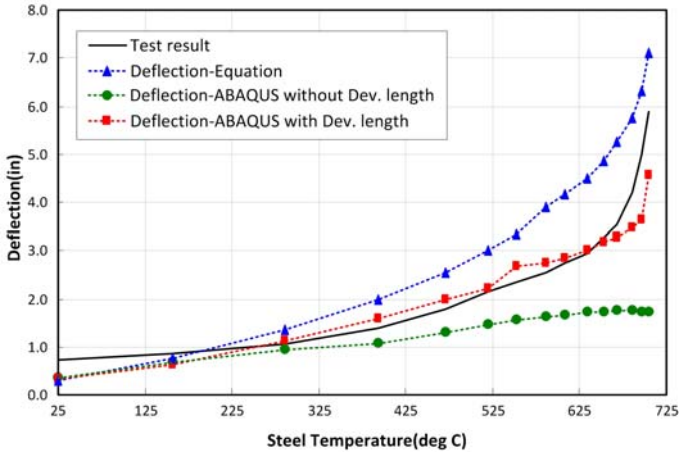

(c) Continuous 3-span beam

Fig. 9.17 Comparison of mid-span deflection of beams

9.3 Summary

Based on the evaluation of structural fire resistance and deflection of three beams with different restrained condition, the following conclusion can be drawn:

(1) In the evaluation of residual moment capacity of the beam, residual moment capacity by the simplified fiber section analysis can be evaluated more actual than that of ACI 216.1-07 code.

(2) The equation for residual negative moment capacity of ACI 216.1-07 code properly evaluates to actual moment capacity of the section at high temperature. However, the equation for residual positive moment capacity of ACI 216.1-07 code overestimates the actual residual positive moment capacity of the section at high temperature.

(3) The equation for positive moment capacity of ACI 216.1-07 code might be formed unexpected plastic hinge in the beam under exposure of actual fire because of overestimation of the residual positive moment capacity of the section. And the formation of this plastic hinge means that continuous beam with large fire resistance capacity changes to simple supported beam with small fire resistance capacity because there is no additional moment redistribution due to formation of plastic hinge.

(4) Based on previous conclusions, the equation for positive moment capacity of ACI 216.1-07 code should be modified to predict more actual residual positive moment capacity. And in order to evaluate actual residual positive moment capacity, the analysis model considering 3side heating condition such as the model presented should be used.

(5) In the evaluation of deflection of beam, the beam analysis of ABAQUS with development length evaluates more accurately the actual deflection of beam during and after fire test than other methods.

(6) Based on the comparison results of actual and predicted deflection of three beams, the deflection by the analytical model defined in this study is acceptable to predict actual deflection of beam under fire.

(7) Based on the comparison result of the beam analysis of ABAQUS according to the consideration of development length in the beam model, the reduction effect of adhesive strength between concrete and steel in the end zone of steel reinforcement in the beam is very important factor to evaluate the deflection of beam under fire.

10 National and International Design Standards

10.1 Standards for Fire Testing

10.1.1 International Standard ISO 834 (1975)

The International Standard ISO 834, *Fire Resistance Tests – Elements of Building Construction*, specifies standard heating and pressure conditions, test procedures and criteria for the determination of the fire endurance of elements of building construction of various categories. This test method provides for the determination of the fire resistance of building elements on the basis of the length of time for which the test specimens satisfy the prescribed criteria.

The scope of ISO 834 includes, but is not limited to, the following structural elements: Walls and partitions; Columns; Beams; Floors (with or without ceilings); Roofs (with or without ceilings). Elements which fall into none of these categories may be tested by analogy with a similar element. ISO 834 specifies that the test specimen is subjected to a furnace temperature rise given by the following equation:

$$T - T_o = 345 \log_{10}(8t + 1) \tag{10.1}$$

Where, t, T, and T_o are time (expressed in minutes), furnace temperature at time t (expressed in ˚C), and initial furnace temperature (expressed in ˚C). The curve representing this relationship, known as the standard time-temperature curve, is shown in Figure 10.1.

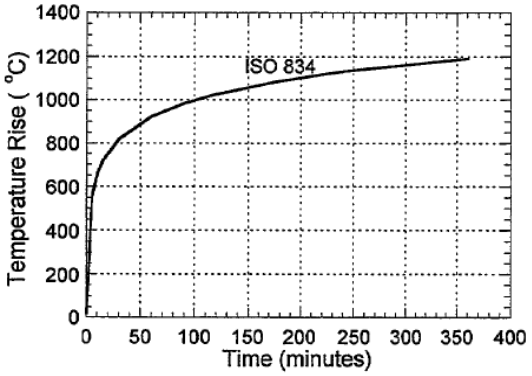

Fig. 10.1 Standard Fire Curve for ISO 834 (1975)

The test specimens are conditioned so that they correspond as closely as possible, in temperature, moisture content and mechanical strength, to the expected state of a similar element in service. The fire resistance of the test specimens is the time, expressed in minutes, of the duration of heating until failure occurs as defined by one of the following criteria:

- *Load-bearing capacity*: Failure is reached when the test specimen collapses in such a way that it no longer performs the load-bearing function for which it was intended.
- *Insulation*: For test elements, such as walls and floors which have the function of separating two parts of a building, failure occurs when: (1) the temperature on the unexposed face of the specimens increases above the initial temperature by more than 140˚C; (2) the maximum temperature at any point on the unexposed face exceeds the initial

temperature by more than 180˚C; and (3) when the surface temperature exceeds 220˚C, irrespective of the initial temperature.

- *Integrity*: For elements such as walls and floors which have the function of separating two parts of a building, failure is reached when: (1) cracks, holes, or other openings, through which flames or hot gases can pass, occur in the test specimen; (2) the 100 mm square by 20mm thick cotton pads, held at a distance of between 20 and 30mm from any opening on the unexposed side, is ignited or when sustained flaming, having a duration of at least 10s, appears on the unexposed face of the test element.

For load-bearing structural elements, the fire resistance is judged by the criterion of load-bearing capacity. For a separating element, the fire resistance is judged by the criteria of insulation and integrity. For a load-bearing and separating element, the fire resistance is determined by all three criteria: load-bearing capacity, insulation and integrity.

10.1.2 ASTM E119 (2007)

The ASTM E119, *Standard Test Methods for Fire Tests of Building Construction and Materials*, specifies the test procedures for evaluating the fire resistance of structural elements for buildings, including bearing and other walls and partitions, columns, girders, beams, slabs, and composite slab and beam assemblies for floors and roofs. The standard is widely used for the fire testing in North America.

The test subjects a specimen to a standard fire exposure, which is characterized by the standard time-temperature curve shown in Figure 10.2. A more detailed tabulation may be found in Appendix X1 of ASTM E119.

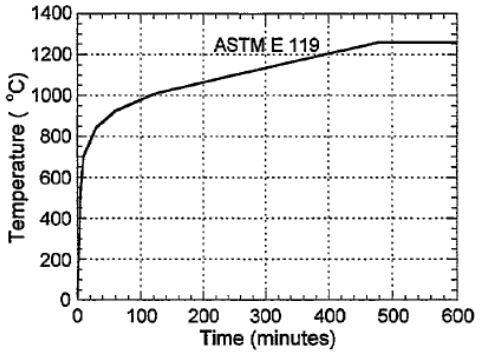

Fig. 10.2 Standard Fire Curve for ASTM E 119 (2007)

The end-point criteria applied to concrete test assemblies are as follows:

- *Heat transmission end point*: As it applies to separating element such as walls, floors, and roofs. This end point occurs when the specimen's unexposed surface exceeds an average temperature rise of 139˚C or when any single point on the unexposed surface exceeds 181˚C above its initial temperature.
- *Flame passage end point*: As it applies to assemblies that function as separating elements, this end point occurs when flames or gases hot enough to ignite combustible material (cotton waste) pass through the test assembly.
- *Structural end point*: As it applies to load-bearing elements, including those that must function as separating elements. This end point occurs when the test assembly can no longer sustain the applied load, or meet other specified conditions of acceptance in ASTM

E119, based on the given type of test specimen (for example, temperature limits on steel reinforcement in concrete beams).

Walls must additionally be subjected to a hose stream test for purposed of evaluating specimen stability, durability and resistance to thermal shock. An assembly is considered to have failed the test if an opening develops such that a projection of water from the hose stream passes beyond the unexposed surface at any time during the stream's application.

10.1.3 Japanese Industrial Standard JIS A (1994)

The Japanese Industrial Standard JIS A 1304, *Method for Fire Resistance Test for Structural Parts of Buildings*, specifies a test method to measure the fire resistance of building elements such as a wall, column, beam, floor, ceiling, roof, etc. The fire endurance rating system in JIS A 1304 classifies the fire resistance of an element by 5 levels (30-minute heat, 1-hour heat, 2-hour heat, 3-hour heat, and 4-hour heat). One major difference between JIS A 1304 and the ISO 834 and ASTM E119 is in the heat transmission criterion. The Japanese standard sets the unexposed surface temperature of walls and floors at 260˚C Assuming an ambient temperature of 20˚C, this allowable temperature rise is about 100˚C greater than that of E119 or ISO 834. This has a significant effect on the fire resistance rating results of assemblies tested to the respective standards. The maximum heat exposure time (duration of the fire test) in JIS A 1304 is limited to 4 hours.

The standard time-temperature curve specified in JIS A 1304 in shown in Figure 10.3. Wall specimens are heated from one side in a vertical position in accordance with the standard time-temperature curve. Column specimens are heated from four sides in a vertical position. Beams and floors are heated from the under side in a horizontal position. The following criteria are used to determine if the concrete test specimens "passes" the fire test:

- Structural failure due to deformation, destructive spalling or harmful change to fireproofing material does not occur during heating.
- During heating, there are no cracks in walls floors and roofs which allow flames to penetrate.
- For walls and floors the temperature on the unexposed side does not exceed 260˚C.
- During heating, all structural materials do not flame remarkably, and after completion of heating any embers do not remain for 10 minute or more.

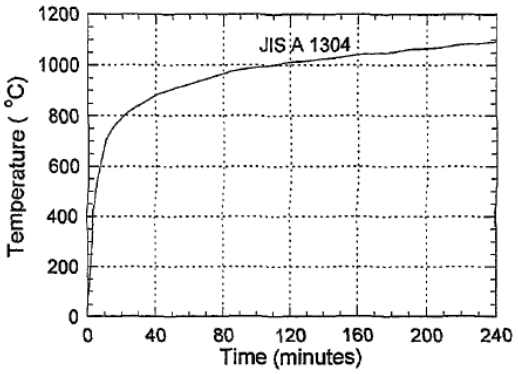

Fig. 10.3 Standard Fire Curve for JIS A 1304 (1994)

10.2 High Temperature Design Specifications for RCS

10.2.1 ACI 349.1R-07 (2007)

ACI 349.1R-07 presents a design-oriented approach for considering thermal effect on reinforced concrete structures. Although the approach is intended to conform to the general provisions of Appendix E of ACI 349-06, "Code requirements for nuclear safety-related concrete structures and commentary.", it is not restricted to unclear power plant structures.

For frame structures, the thermal load is assumed to be represented by temperatures that vary linearly through the thickness of the member. A rationale is described for determining the extent of member cracking that can be assumed for purposes of obtaining the cracked structure thermal forces and moments. The thermal moments due to the linear temperature gradient ΔT and those resulting from the expansion or contraction of the axis of the component T_m - T_B are considered separately. For each type of thermal effect, fixed-end moments, stiffness coefficients, and carryover factors were obtained for two types of cracked components: 1) end cracked and 2) interior-cracked. These factors are presented for the case of an end-cracked component in Fig. 10.4(a).

$$M_A = \left(\frac{\alpha \Delta T L}{2t}\right) K_A \left(1 - CO_{AB}\right)$$
$$M_B = \left(\frac{\alpha \Delta T L}{2t}\right) K_B \left(1 - CO_{BA}\right) \tag{10.2}$$

Although shown only for a component cracked at the ends, the aforementioned expressions for M_A and M_B also apply to a component cracked in its interior. In Eq. (10.2), $\alpha \Delta T L / 2t$ = the angle change of the component ends with the rotational restraints removed; K_A = the stiffness of the component at A with B fixed ($4E_c I_g / L$ for uncracked component); K_B = the stiffness of the component at B with A fixed; CO_{AB} = the carryover factor from A to B (1/2 for uncracked component); and CO_{BA} = the carryover factor from B to A.

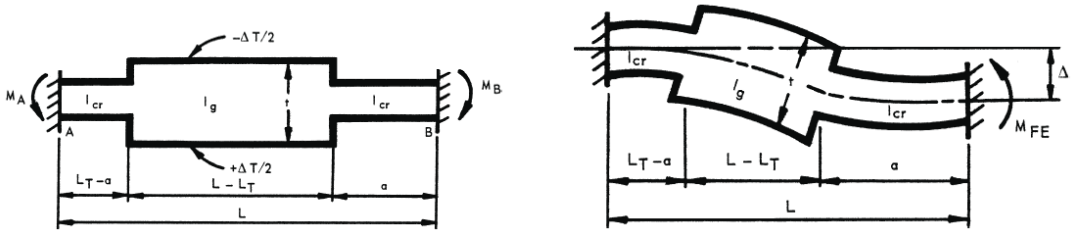

(a) ΔT fixed-end moment (b) T_m - T_B fixed-end moment

Fig. 10.4 Member cracked at ends by mechanical loads (ACI 216.1R-07, 2007)

The expressions for *K* and *CO* can be derived from moment-area principles. Also, *K* can be expressed as

$$K = \frac{E_c I_g}{L} k_s \tag{10.3}$$

where k_s is the dimensionless stiffness coefficient that is a function of L_T / L and a / L_T. Likewise, CO can be expressed as a function of L_T / L and a / L_T. Stiffness coefficients (k_s) and carry-over factors (CO) are presented in graphical form as a function of the extent of member cracking along its length and the reinforcement ratio.

Fixed-end thermal moments for cracked members are expressed in terms of these factors for (1) a temperature gradient across the depth of the member and (2) end displacements due to a uniform temperature change along the axes of adjacent members. The ΔT fixed-end moment at the a end of the component can be expressed as

$$M_{FE} = \frac{E_c \alpha \Delta T b t^2}{12} \frac{k_s (1 - CO)}{2} \tag{10.4}$$

For the purpose of determining the mean temperature effects, it is necessary to develop the $T_m - T_B$ fixed-end moment, which is shown in Fig. 10.4(b) for a component cracked at its ends. The $T_m - T_B$ fixed-end moment at the end cracked a distance a is

$$M_{FE} = \frac{E_c I_g \Delta}{12} k_s (1 + CO) \tag{10.5}$$

The displacement Δ is produced by $T_m - T_B$ acting on an adjacent component.

For the axisymmetric shells, the structure is considered to be uncracked for all mechanical loads and for part of the thermal loads. The thermal load is assumed to be represented by a temperature that is distributed linearly through the wall of the structure (i.e., linear temperature distribution is separated into a gradient ΔT and into a uniform temperature change $T_m - T_B$ where T_m is the mean temperature and T_B the base (stress-free) temperature).

Generally, for most axisymmetric structures, a uniform temperature change ($T_m - T_B$) produces significant internal section forces (moment included) only at the externally restrained boundaries of the structure where movement due to thermal change is prevented, or in regions where $T_m - T_B$ varies fairly rapidly along the structure. The magnitude and extent of these discontinuity forces depend on the specific geometry of the structure and on the external restraint provided. If cracking occurs in this region, a prediction of the cracking reduction of the discontinuity forces is attainable through a re-analysis using cracked section structural properties. Therefore, forces resulting from an analysis for the $T_m - T_B$ part of the thermal effect are considered to be included with corresponding factored mechanical forces. These combined axial forces and moments are denoted as N and M.

The gradient ΔT produces internal section forces (moment included) at externally restrained boundaries, and also away from these discontinuities. At discontinuities, the most significant internal force is usually the moment, primarily resulting from the internal restraint rather than the external boundary restraint. Away from discontinuities, the only significant forces due to T are thermal moments caused by the internal restraint provided by the axisymmetric geometry of the structure. Due to the axisymmetric geometry of the subject structures, the free thermal curvature change $\alpha \Delta T / t$ is fully restrained. This restraint produces a corresponding thermal moment whose magnitude depends on the extent of cracking the section experiences. This in turn depends

on ΔT, the other section forces N and M, and the section properties (Fig. 10.5). With the ratio M/N denoted as e, referenced to the section centerline, and the distance from the concrete compression face to the tension reinforcement denoted as d, two cases of e/d are identified in Sections 4.2 and 4.3 of the ACI 349.1R-07.

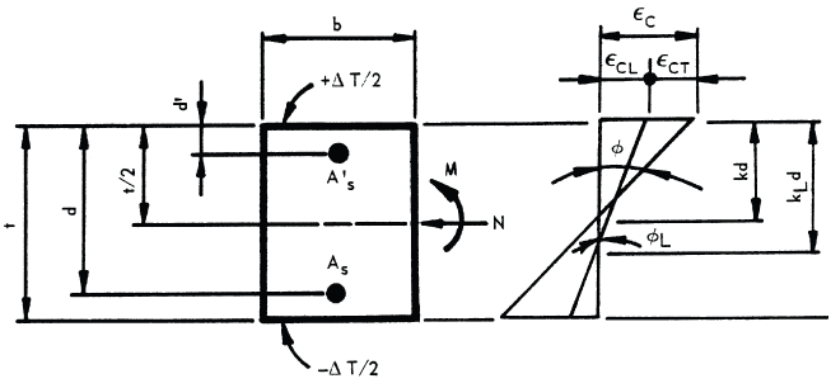

Fig. 10.5 Section under N, M, ΔT (ACI 216.1R-07, 2007)

Normalized cracked section thermal moments are presented in graphical form as a function of the reinforcement ratio and the internal axial forces and moments acting on the section. The moments have been normalized with respect to cross-sectional dimensions and the temperature gradient across the section. Examples are presented for both design of a frame and of an axisymmetric shell under mechanical and thermal loadings.

10.2.2 ACI 216.1-07 (2007)

This standard describes acceptable methods for determining the fire resistance of concrete building and masonry building assemblies and structural elements, including walls, floor and roof slabs, beams, columns, lintels, and masonry fire protection for structural steel columns. These methods shall be used for design and analysis purposes and shall be based on the fire exposure and applicable end-point criteria of ASTM E 119 (2007).

The chapter 2 of this standard introduces the requirement for fire resistance of concrete members and assemblies. Section 2.2 describes the calculation methods of the equivalent thickness and the fire resistance of concrete walls, floors, and roofs with various type. Table 10.1 shows the minimum equivalent thickness of plain and reinforced concrete walls, floor and roof slabs in accordance with fire-resistance ratings of 1 to 4 hour.

Table 10.1 Fire resistance of single-layer concrete wall, floors, and roofs (ACI 216.1-07, 2007)

Aggregate Type	Minimum equivalent thickness for fire-resistance rating, in				
	1 hour	1-1/2 hours	2 hours	3 hours	4 hours
Siliceous	3.5	4.3	5.0	6.2	7.0
Carbonate	3.2	4.0	4.6	5.7	6.6
Semi-Lightweight	2.7	3.3	3.8	4.6	5.4
Lightweight	2.5	3.1	3.6	4.4	5.1

Section 2.3 describes the requirement of concrete cover protection of steel reinforcement.

Cover protection determinations in this section are based on the structural end-point. For purposes of determining minimum concrete cover, classify slabs and beams as restrained or unrestrained in accordance with Table 10.2 .

Table 10.2 Construction classification, restrained and unrestrained (ACI 216.1-07, 2007)

Unrestrained	
Wall bearing	Single spans and simply-supported end spans of multiple bays such as concrete or precast units*
Restrained	
Wall bearing	Interior spans of multiple bays: 1. Cast-in-place concrete slab systems 2. Precast concrete where the potential thermal expansion is resisted by adjacent construction**
Concrete framing	1. Beam fastened securely to the framing numbers 2. Cast-in-place floor or roof systems (such as beam/slab systems, flat slabs, pan joists, and waffle slabs) where the floor or roof system is cast with the framing members 3. Interior and exterior spans of precast systems with cast-in-place joints resulting in restraint equivalent to that of Condition 1, concrete framing 4. Prefabricated floor or roof systems where the structural members are secured to such systems and the potential thermal expansion of the floor or roof systems is resisted by the framing system of the adjoining floor or roof construction**

* It shall be permitted to consider floor and roof systems restrained when they are tied into walls with or without tie beams, provided the walls are designed and detailed to resist thermal thrust from the floor or roof system.

** For example, resistance to potential thermal expansion is considered to be achieved when:
1. Continuous concrete structural topping is used;
2. The space between the ends of precast units or between the ends of units and the vertical face of supports is filled with concrete or mortar, or
3. The space between the ends of the precast units and the vertical face of supports, or between the ends of solid or hollow-core slab units, does not exceed 0.25% of the length for normalweight concrete members or 0.1% of the length for structural lightweight concrete members.

Section 2.3 provides minimum cover for slab, nonprestressed flexural reinforcement and prestressed flexural reinforcement in beam. Table 10.3 shows minimum cover in nonprestressed beams.

Table 10.3 Minimum cover in nonprestressed beams (ACI 216.1-07, 2007)

Restraint	Beam Width, in.	Cover for corresponding fire-resistance rating, in.				
		1 hour	1-1/2 hours	2 hours	3 hours	4 hours
Restrained	5	3/4	3/4	3/4	1	1-1/4
	7	3/4	3/4	3/4	3/4	3/4
	≥ 10	3/4	3/4	3/4	3/4	3/4
Unrestrained	5	3/4	1	1-1/4	NP*	NP
	7	3/4	3/4	3/4	1-3/4	3
	≥ 10	3/4	3/4	3/4	1	1-3/4

* Not permitted

Instead of using methods described in section 2.3, the calculation methods in section 2.4 shall be permitted for determining fire resistance and the adequacy of cover protection in concrete flexural members based on the ASTM E 119 time temperature fire exposure. The provisions in section 2.4 do not explicitly account for the effects of restraint of thermally induced expansion; however, the use of comprehensive analysis and design procedures that take into account the

effects of moment redistribution and the restraint of thermally induced member expansion shall be permitted. In no case shall cover protection be less than that required by ACI 318.

For Simply supported beams, On the basis of structural end-point behavior, the fire resistance of a simply supported, unrestrained, flexural member shall be determined by

$$M_n \geq M_{n\theta} \geq M \tag{10.6}$$

Assume that the unfactored full service load moment M is constant for the entire fire-resistance period. The structural fire resistance or amount of concrete cover u to center of the steel reinforcement of concrete beam is determined by using Fig. 10.6. When determining an average value of u for beams with corner bars or corner tendons, an "effective u," u_{ef}, shall be used in its place. Values of u for the corner bars or tendons used in the computation of u_{ef} shall be equal to 1/2 of their actual u value. Figure 10.6 (Figure 2.8 in ACI 216.1-07) shall be used in conjunction with the computed u_{ef}.

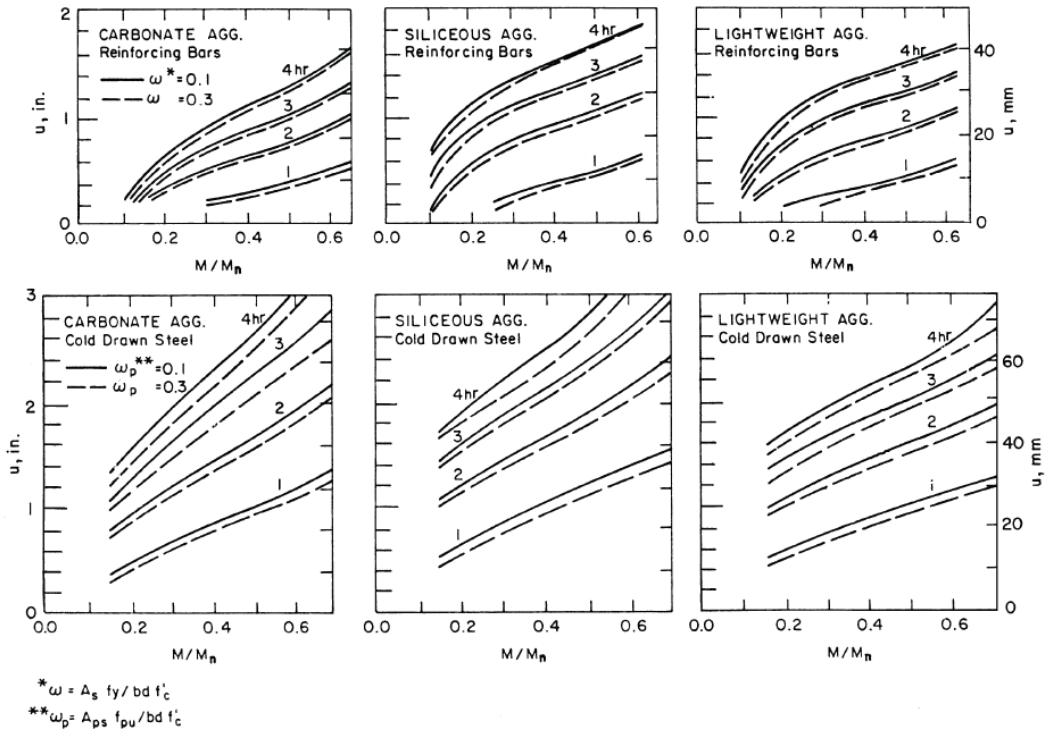

Fig. 10.6 Fire resistance of concrete slabs as influenced by aggregate type, reinforcing steel type, moment intensity, and u (ACI 216.1-07, 2007)

For continuous beams, The Following equations shall be used to determine structural fire resistance based on continuity.

$$M^{+}_{n\theta} = A_s f_{y\theta}(d - a_\theta / 2) \quad \text{for positive moment capacity} \tag{10.7a}$$

$$M^{-}_{n\theta} = A_s f_{y\theta}(d_{ef} - a_\theta / 2) \quad \text{for negative moment capacity} \tag{10.7b}$$

Where, A_s, $f_{y\theta}$, d, d_{ef}, and a_θ (= $A_s f_{y\theta} / 0.85 f_{c\theta}' b$, b = width of concrete beam, $f_{c\theta}'$ =reduced compressive strength of concrete at elevated temperature) are cross-sectional area of the longitudinal tension reinforcement, reduced yield strength of reinforcing steel at elevated temperature, effective depth, reduced effective depth, and depth of equivalent concrete rectangular stress block at elevated temperature. Reduced effective depth, d_{ef} is the distance from the centroid of tension reinforcement to most extreme concrete compressive fiber at which point temperature does not exceed 1400˚F(760˚C).

Reduced compressive strength of concrete, $f_{c\theta}'$ is calculated by using Fig. 10.7 and reduced yield strength of reinforcing steel, $f_{y\theta}$ is calculated by using Fig. 10.8. Temperature of concrete for calculating $f_{c\theta}'$ uses average temperature of rectangular stress block and the temperature of steel for calculating $f_{y\theta}$ uses each temperature located in steel in Fig. 10.9.

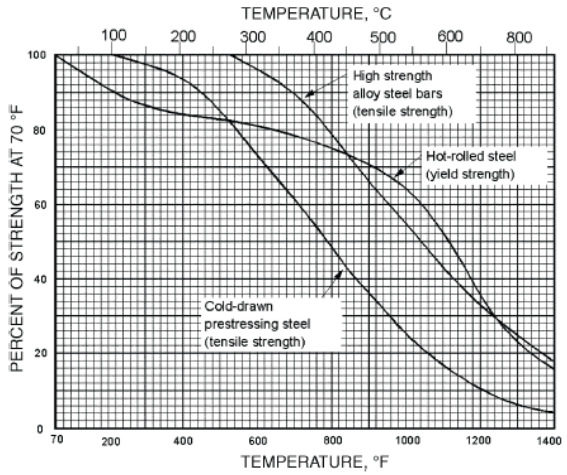

Fig. 10.7 Strength of flexural reinforcement steel bar and strand at high temperatures (ACI 216.1-07, 2007)

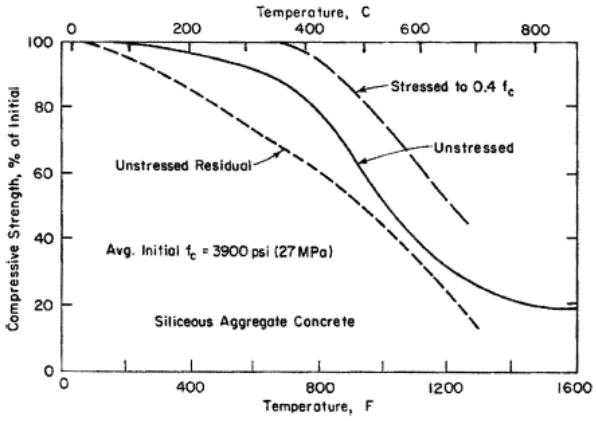

(a) Compressive strength of siliceous aggregate concrete at high temperatures and after cooling (ACI 216.1-07, 2007)

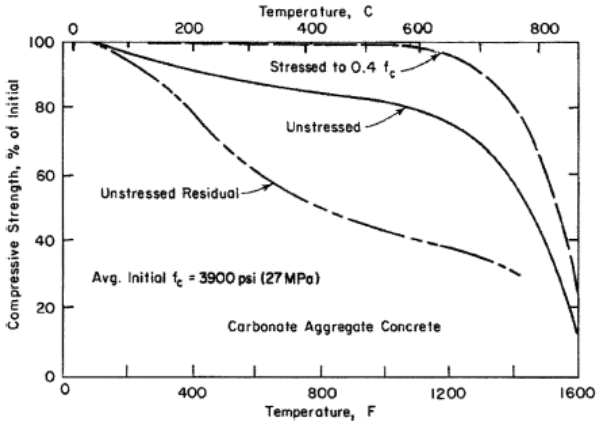

(b) Compressive strength of carbonate aggregate concrete at high temperatures and after cooling

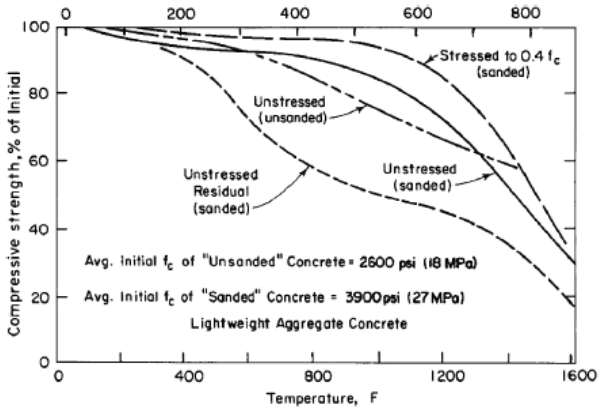

(c) Compressive strength of semi-lightweight concrete at high temperatures and after cooling

Fig. 10.8 Compressive strength of concrete at high temperatures (ACI 216.1-07)

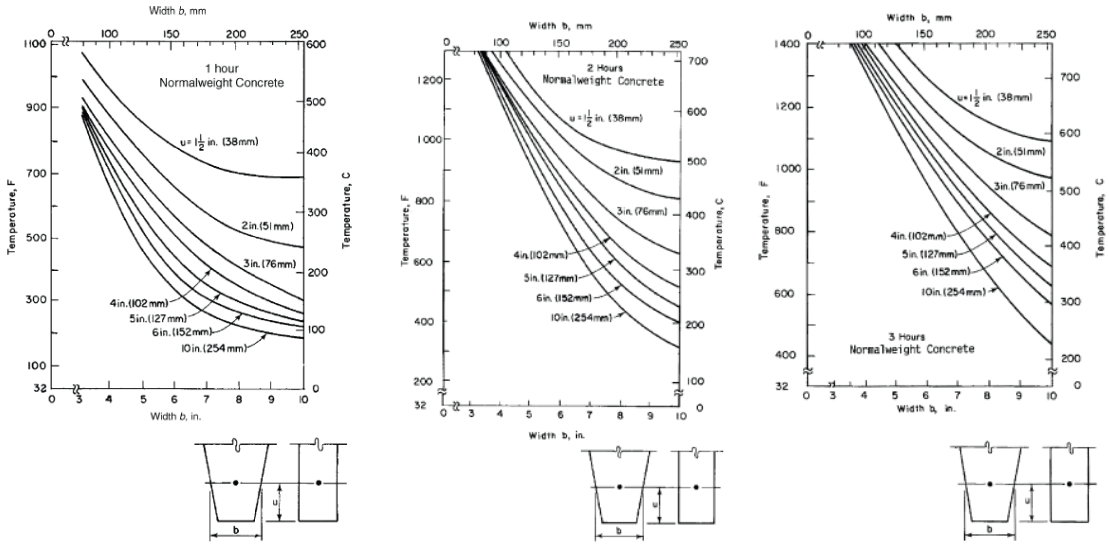

(a)~(c) Temperatures in normalweight concrete rectangular and tapered units at 1, 2, and 3 hours of fire exposure

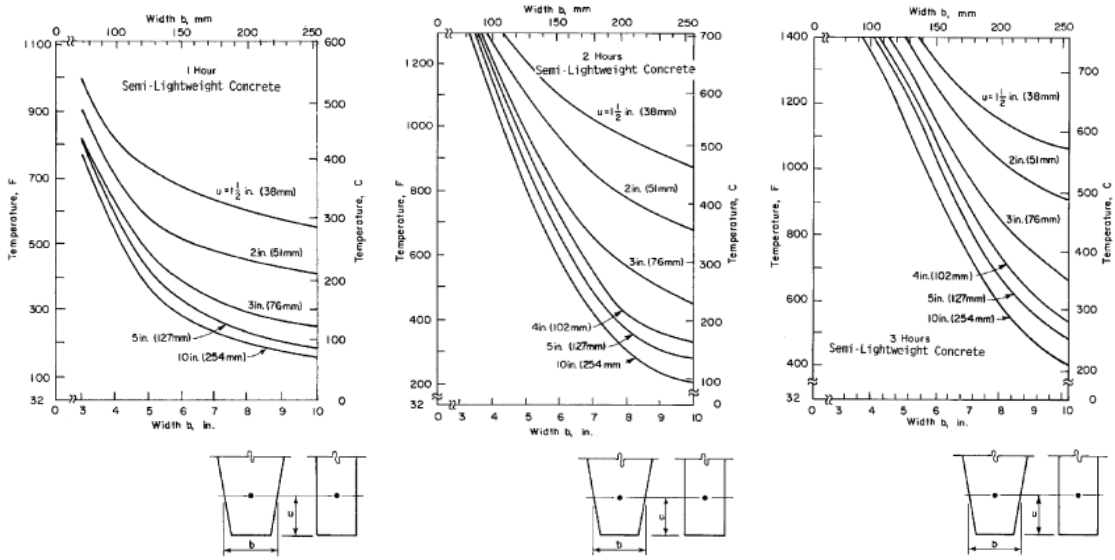

(d)~(f) Temperatures in semi-lightweight concrete rectangular and tapered units at 1, 2, and 3 hours of fire exposure

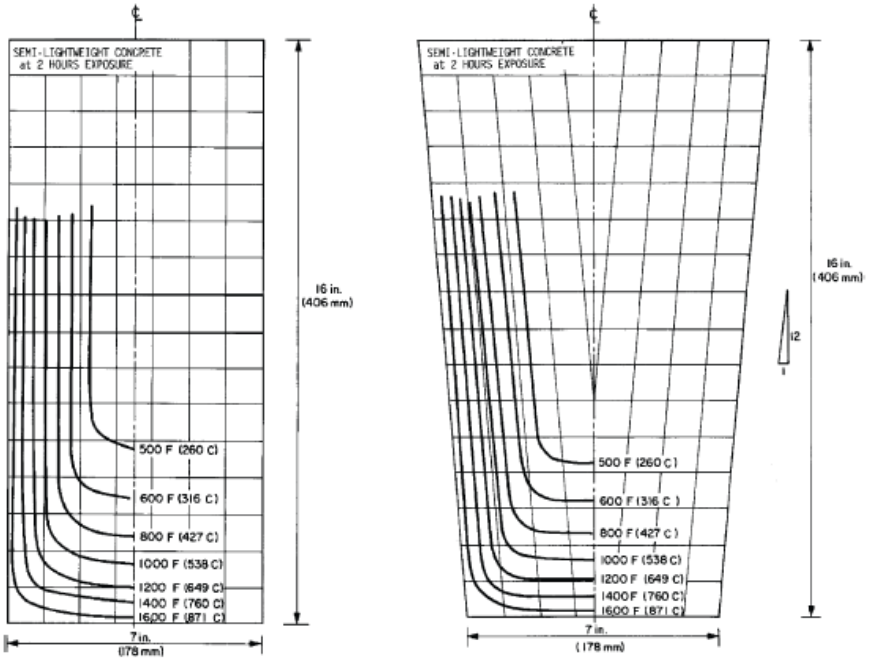

(g)~(h) Measured temperature distribution at 2-hour fire exposure for semi-lightweight concrete rectangular and tapered unit

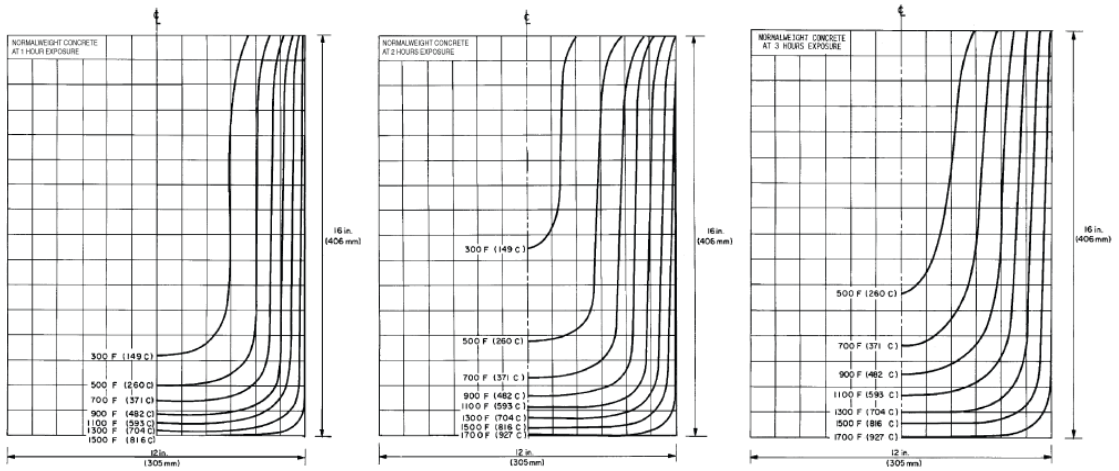

(i)~(k) Temperature distribution in a normalweight concrete rectangular unit at 1, 2, and 3 hours of fire exposure

Fig. 10.9 Temperature distribution in concrete (ACI 216.1-07)

Section 2.5 describes the requirement for reinforced concrete columns. The least dimension of reinforced concrete columns of different types of concrete having a specified compressive strength equal to or less than 12,000 psi for fire-resistance rating of 1 to 4 hours shall conform to values given in Tables 10.4 and 10.5. And the least dimension of reinforced concrete columns having a specified compressive strength greater than 12,000 psi for a fire resistance rating of 1 to 4 hours shall be 24 in.

Table 10.4 Minimum concrete column size

Aggregate Type	Minimum equivalent thickness for fire-resistance rating, in				
	1 hour	1-1/2 hours	2 hours	3 hours	4 hours
Siliceous	8	9	10	11	12
Carbonate	8	9	10	12	14
Semi-lightweight	8	8-1/2	9	10-1/2	12

Table 10.5 Minimum concrete column size with fire exposure conditions on two parallel sides

Aggregate Type	Minimum equivalent thickness for fire-resistance rating, in*				
	1 hour	1-1/2 hours	2 hours	3 hours	4 hours
Siliceous	8	8	8	8	10
Carbonate	8	8	8	8	10
Semi-lightweight	8	8	8	8	10

* Minimum dimensions are acceptable for rectangular columns with a fire exposure condition on three or four sides, provided that one set of the two parallel sides of the column is at least 36 in. long.

11 References of Part II

ABAQUS (2007) "*User's maual-Version 6.7, vol.II : Abaqus Solutions.*", Rocky Mountains.

Abrams, M.S., Gustaferro, A.H. and Sales, E.A.B. (1971) "*Fire tests of concrete joist floors and roofs*.", PCA R&D Bulletin RD006.01B.

ACI Committee 318 (1971) "*Building code requirements for reinforced concrete (ACI 318-71).*", American Concrete Institute, Detroit, Michigan, 353 pp.

ACI Committee 318 (2008) "*Building code requirements for structural concrete and commentary (ACI 318-08/ACI 318R-08).*", American Concrete Institute, Detroit, Michigan, 467 pp.

Joint ACI-TMS Committee 216 (2007) "*Code requirements for Determining Fire Resistance of Concrete and Masonry Construction Assemblies (ACI 216.1-07).*", American Concrete Institute, Detroit, Michigan, 28 pp.

ACI Committee 349 (2006) "*Code requirement for nuclear safety-related concrete structures (ACI 349-06) and commentary.*", American Concrete Institute, Detroit, Michigan, 153 pp.

ACI Committee 349 (2007) "*Reinforced concrete design for thermal effects on nuclear power plant structures.*", American Concrete Institute, Detroit, Michigan, 36 pp.

Ali, F., Nadjai, A., Silcock, G. and Abu-Tair, A. (2004) "Outcomes of a major research on fire resistance of concrete columns.", *Fire Safety Journal*, Vol. 39, pp 433-445.

ASTM (2007) "*Standard methods of fire test of building construction and materials (ASTM E 119-07).*", American Society for Testing and Materials, West Conshohocken, Philadelphia, 22pp.

Bailey, C.G. and Toh, W.S. (2007) "Small-scale concrete slab tests at ambient and elevated temperatures", *Engineering Structures*, Vol. 29, pp 2775-2791.

Benmarce, A. and Guenfoud, M. (2005) "Behaviour of axially restrained high strength concrete columns under fire.", *Construction and Building Materials*, Vol. 19.

Bratina, S., Saje, M., and Planinc, I. (2007) "The effects of different strain contributions on the response of RC beams in fire.", *Engineering Structures*, Vol. 29, pp 418-430.

BS8110 (1985) "*Structural use of concrete. BS8110: part 1.*", British Standards.

Capua, D.D. and Mari, A.R. (2007) "Nonlinear analysis of reinforced concrete cross-sections exposed to fire.", *Fire Safety Journal*, Vol. 42, pp 139-149.

CNS 12514 (2005) "*Method of fire resistance test for structural parts of building.*", Chinese National Standard.

Cooke, G.M.E. (2001) "Behaviour of precast concrete floor slabs exposed to standardized fires", *Fire Safety Journal*, Vol. 36, pp 459-475.

Diederichs, U., Jumppanen, U.M. and Schneider, U. (1992) "High temperature properties and spalling behavior of high strength concrete.", *Proceedings of the Fourth Weimar Workshop on High Performance Concrete: Material Properties and Design*, pp 219-236.

DIN 4102 (1981) "*Behavior of building materials and components in fire.*", German Institute for Standardization.

Dotreppe, J.C. and Franssen, J.M. (1985) "The use of numerical models for the fire analysis of reinforced concrete and composite structures.", *Engineering Analysis*, Vol. 2, pp 67-74.

Dotreppe, J.C., Franssen, J.M., Bruls, A., Baus, R., Vandevelde, P., Minne, R., van Nieuvenburg, D. and Lambotte, H. (1996) "Experimental research on the determination of the

main parameters affecting the behavior of reinforced concrete columns under fire.", *Magazine of Concrete Research*, Vol. 49, pp 117-127.

EN 1992-1-2 (1995) "*Eurocode 2 - Design of concrete structures: Part 1-2: Structural fire design.*", European Committee for Standardization, Brussels.

EN 1993-1-2 (1992) "*Eurocode 3 - Design of steel structures: Part 1-2: Structural fire design.*", European Committee for Standardization, Brussels.

EN 1994-1-2 (1994) "*Eurocode 4 - Design of composite concrete and steel structures, Part 1-2: Structural fire design.*", European Committee for Standardization, Brussels.

Foster, S. (2004) "Experimental behaviour of concrete floor slabs at large displacement.", *Engineering Structures*, Vol. 26, pp 1231-47.

Franssen, J.M. (2003) "SAFIR: A thermal/structural program modeling structures under fire.", North American steel construction conference, American Institute of Steel Construction, Baltimore.

Franssen, J.M. and Dotreppe, J.C. (2003) "Fire tests and calculation methods for circular concrete columns.", *Fire Technology*, Vol. 39, pp 89-97.

Freskakis, G.N. (1980) "Behavior of reinforced concrete at elevated temperature.", *Second ASCE Conference on Civil Engineering and Nuclear Power*, Vol. 1, pp 3-5-1 – 3-5-21.

Gustaferro, A.H. and Abrams, M.S. (1971) "*Fire test of concrete two-way joist floors.*", PCA R&D Bulletin RD007.01B.

ISO 834 (1975) "*Fire resistance tests: elements of building construction.*", International Organization for Standardization (ISO).

Jau, W-C. and Huang, K-L. (2008) "A study of reinforced concrete corner columns after fire.", *Cement & Concrete Composites*, Vol. 30, pp 622-638.

JIS A 1304 (1994) "*Method for fire resistance test for structural parts of building.*", Japanese Industrial Standard (JIS), Japanese Standards Association, Japan.

Kent, D.C. and Park R. (1971) "Flexural members with confined concrete.", *Journal of Structure Division*, Vol. 97, pp 1969-1990.

Kodur, V.K.R. (2000) "Spalling in high strength concrete exposed to fire – concerns, causes, critical parameters and cures.", *Advanced Technologies in Structural Engineering*, ASCE Structures Congress, Philadelphia.

Kodur, V.K.R. and Dwaikat, M. (2008) "A numerical model for predicting the fire resistance of reinforced concrete beams.", *Cement & Concrete Composites*, Vol. 30, pp 431-443.

Kodur, V.K.R. and Lie, T.T. (1996) "A computer program to calculate the fire resistance of rectangular reinforced concrete columns.", *Third Canadian Conference on Computing in Civil and Building Engineering*, pp 11-20.

Kodur, V.K.R. and McGrath, R. (2003) "Fire endurance of high strength concrete columns.", *Fire Technology*, Vol. 39, pp 73-87.

Kodur, V.K.R. and Sultan, M. (1998) "Behaviour of high-strength concrete columns exposed to fire.", *Concrete Canada International Conference Symposium*, Vol. 4, pp 217-232.

Kodur, V.K.R., Wang, T.C. and Cheng, F.P. (2004) "Predicting the fire resistance behavior of high strength concrete columns.", *Cement & Concrete Composites*, Vol. 26, pp 141-153.

Lie, T.T. Ed., (1993) "Structural Fire Protection: Manual of Practice.", *ASCE Manual and Reports on Engineering Practice, No.78*, American Society of Civil Engineers, New York.

Lie, T.T., and Irwin, R.J. (1993) "Method to calculation the fire resistance of reinforced concrete columns with rectangular cross section.", *ACI Structural Journal*, Vol. 90, pp 52-60.

Lie, T.T., Lin, T.D., Allen, D.E. and Abrams, M.S. (1984) "*Fire resistance of reinforced concrete columns.*", DBR paper No. 1167.

Lie, T.T. and Woollerton, J.L. (1988) "*Fire Resistance of Reinforced Concrete Columns: Test Results.*", IR 569, IRC, National Research Council of Canada, 302 pp.

Lim, L., Buchanan, A., Moss, P. And Franssen, J-M. (2004) "Computer modeling of restrained reinforced concrete slabs in fire conditions.", *Journal of Structural Engineering*, Vol. 130, No. 12, pp 1964-1971.

Lin, T.D., Ellingwood, B. and Piet O. (1988) "*Flexural and shear behavior of reinforced concrete beams during fire tests.*", PCA R&D Bulletin, RD091T.

Lin, T.D., Gustaferro, A.H. and Abrams, M.S. (1981) "*Fire endurance of continuous reinforced concrete beams.*", PCA R&D Bulletin, RD072.01B.

Lin, T.D., Zwiers, R.I., Burg, R.G., Lie T.T. and McGrath, R.J. (1992) "*Fire resistance of reinforced concrete columns.*", PCA R&D Bulletin RD101B.

Maruta, M., Yamazaki, M. and Miyashita T. (1995) "A study on shear behavior of reinforced concrete beams subjected to long-term heating.", *Nuclear Engineering and Design*, Vol. 156, pp 29-37.

Moss, P.J., Dhakal, R.P., Wang, G. and Buchanan, A.H. (2008) "The fire behaviour of multi-bay, two-way reinforced concrete slabs.", *Engineering Structures*, Vol. 30, No. 12, pp 3566-3573.

Nielsen, C.V., Pearce, C.J. and Bicanic, N. (2004) "Improved phenomenological modeling of transient thermal strains for concrete at high temperature.", *Computers and Concrete*, Vol. 1, No. 2, pp 189-201.

Pisani, M.A. (2004) "Non-linear strain distribution due to temperature effects in compact cross-sections.", *Engineering Structures*, Vol. 26, pp 1349-1363.

Poh, K.W. and Bennetts, I.D. (1995) "Analysis of structural members under elevated temperature conditions.", *Journal of Structural Engineering*, Vol. 121, No. 4, pp 664-675.

Shi, X., Tan, T.H., Tan, K.H. and Guo, Z. (2002) "Effect of force-temperature paths on behaviors of reinforced concrete flexural members.", *Journal of Structural Engineering*, Vol. 128, No. 3, pp 365-373.

Yu, X. and Huang, Z. (2008) "An embedded FE model for modeling reinforced concrete slabs in fire.", *Engineering Structures*, Vol. 30, No. 11, pp 3228-3238.

Zha, X.X. (2003) "Three-dimensional non-linear analysis of reinforced concrete members in fire.", *Building and Environment*, Vol. 38, pp 297-307.

PART III:
SPALLING OF CONCRETE AND CONCRETE STRUCTURES

12 Concrete spalling under high temperatures

Under high temperatures concrete is exposed to several degradation processes. Multi-physical mechanisms in the porous concrete lead to thermal softening as well as thermal expansion, drying shrinkage and internal pore pressure build-up. When exposed to high temperature, heat is conducted and convected through material, resulting in changes in the chemical composition, physical structure and fluid (water, gas and vapor) contents in the porous material which in turn affect the overall mechanical properties (strength, stiffness, fracture, etc) and other physical properties (thermal conductivity, permeability, porosity, etc). Such degradation processes have come to the forefront in the safety assessment of structures, e.g. tunnel, high rise buildings, and nuclear power plant and the need for a comprehensive understanding of concrete materials exposed to high temperature under fire environment has been reinforced. The basic principles and details of the physical, mathematical and numerical models forming the main system equations of the thermal, hygral and mechanical behavior of concrete structures subjected to heating are presented.

13 Influential Factors on Concrete Spalling

Concrete should behave well at high temperatures. The advantages of concrete in a fire are two-fold: incombustible material when compared with other materials e.g. wood; and a good insulating material possessing a low thermal diffusivity where heat cannot pass through it easily, e.g. when compared with steel, which decreases with increasing temperature. However, a major disadvantage of concrete is spalling. Spalling refers to the ablation of layers or pieces from the surface of a structural concrete when it is exposed to high and rapid elevating temperatures in fires. Spalling of normal strength concrete occurs due to rapid temperature increase - typically 20˚C/min (Khoury 2000). High strength concrete (HSC) has a significantly higher potential for explosive spalling than normal strength concrete (NSC) due to its low permeability. Explosive spalling of HSC may occur even at relatively low heating rate - less than 5˚C/min (Phan, L.T. et al. 2001). However, spalling may occur only in narrow regions near the surface of reinforced concrete specimens, which has been observed by many researchers. There has been no explanation as to why spalling does not occur in all concrete specimens, and it varies according to the structure size, strength, temperature history, and reinforcement, etc. Many studies have been discovering the main cause of especially explosive concrete spalling which can result in significant loss of section leading to reduction in load-bearing capacity. Explosive spalling is the most severe and aggressive type and is due to a combined action of pore pressures built up as moisture evaporates and thermal stresses due to the thermal expansion of the materials and steep thermal gradients between hotter and cooler concrete regions or initial-mechanical loadings. It is mainly dependent on aggregate, moisture content, stress level, heating rate and temperature. Explosive spalling can seriously affect the stability and durability of the concrete structures because of the extensive removal of concrete from reinforcement of concrete structures, which can result in instability or immature failure of concrete structures. Spalling can occur soon after exposure to heat, accompanied by sudden and violent explosions, or it may happen when the concrete has become so weak after heating that cracks develop and pieces fall off the surface. In order to prevent the occurrence of that, it is very important to understand the fundamental mechanisms that cause spalling of concrete. There are many types of spalling and these are discussed in Section 13.1.

13.1 Types of spalling

There are many types of spalling including:

Explosive spalling – This type of spalling occurs during the early time of a fire, usually within the first 30 min. or so of a standard furnace test with standard fire curves. It can occur at an early stage just above 200°C~300°C depending on types of concrete, pore pressure build-up by moisture content and heating rate. It is characterized by large or small pieces of concrete being violently expelled from the surface, accompanied by a loud noise. The pieces may be as small as 100mm or as large as 300mm in length and 15-20mm deep (CIRIA 1984). The phenomenon can occur just once or at intervals even from the previously spalled parts. Multiple spalling layers are more likely in High Strength Concrete (HSC) than Ordinary Strength Concrete (OSC) (Khoury 2003). Occasionally, the severity of explosive spalling can lead to the formation of holes through the thickness of a membrane section. In many cases, this type of spalling is restricted to the

unreinforced part of the section and usually does not proceed beyond a reinforcing layer (CIRIA 1984).

Surface spalling – This type of spalling is associated with local removal of surface material including, pitting and blistering mainly due to thermo-mechanical interaction by the rapid heating of massive concrete components and structures. This occurs when small pieces, up to about 20mm in size, fly off the surface of a concrete element during the early part of its exposure to a fire or a fire test. Surface spalling may result in exposure of the reinforcement (Khoury 2003).

Aggregate splitting – This type of spalling is failure of aggregate near the surface, characterized by a popping sound.

Table 13.1 Transforamtion and decomposition of aggregates under temperature

Temperature [°C]	Transformation and decomposition reactions of aggregates
30 - 120	Evaporation as well as vaporization of free and physically tied water
100 - 300	Gel reduction, beginning of dehydration
250 - 600	Depositing of the chemically bound water
450 - 550	Decomposition of portlandit; $Ca(OH)_2 \rightarrow CaO + H_2O$
573	Only with quartz: quartz conversion; a $\rightarrow$ β SiO_2
600 - 700	Begin of the decomposition of the CSH-phases; formation of β -C_2S
600 - 900	Only with limestone: decalcination; $CaCO_3 \rightarrow CaO + CO_2$
1200 - 1300	Beginning of the melting of cement stone
>1400	cement stone is available as vitreous glasses

It is caused by thermal expansion of the aggregate and splitting of pieces of aggregate close to the surface because with higher temperatures, dehydration reactions occur with different types of aggregates as well as mineral conversions, for example granite, quartz at T=570°C, due to physical or chemical changes, which occur at high temperatures in siliceous aggregates. It has little impact on structural performance as the majority of the cover remains intact and insulates the reinforcement though this may lead to an increase of spalling. The decalcination of the limestone (see Table 13.1) leads to a fired limestone aggregate. From 1200°C to 1300°C some components of the concrete begin to melt. Different concrete aggregates, for example gush rock, like certain basalts, show inflation effects, i.e. the gases which were locked during the rock formation process do escape during the melting. In addition, because aggregate spalling only causes superficial damage to concrete, the insulation function of the structural members in fire is little affected.

Corner separation - This type of spalling occurs during the later stages of a fire exposure when the concrete has become weak and cracks develop as a result of tensile stress along edges and corners where the reinforcement is typically located. Pieces of concrete fall off beams and columns, and may be followed by pieces coming away from the faces as cracks develop further. Because of the advanced stage at which such spalling occurs, the strength of the element may

have already reduced significantly, and therefore this type of spalling may be of limited significance to structural stability because it has already been lost.

Sloughing off – This is a gradual progressive process which is caused by chemical deterioration of cement paste and internal cracking of concrete due to the difference in thermal expansion between the aggregate and the cement paste (Breunese and Fellinger 2004). This type of spalling is related to the attained temperature of concrete and not the heating rate which tends to define explosive spalling.

Post cooling spalling –This is a non-violent process with no sound and is caused by carbonate aggregates in Limestone expanding on re-hydration during the cooling phase of a fire.
Research to date suggests explosive spalling is the most significant form of spalling when the heating rate is rapid e.g. a standard hydrocarbon fire (Marsh 2002). The significant loss of material during explosive spalling leads to a more rapid rise of temperature in the remainder of the section and a reduction in the load bearing and containment functions of the element.

13.2 Factors of influencing spalling

Spalling is influenced by a number of factors; rapid heating, the temperature gradient, chemical composition of the cement, aggregate type, large compressive stresses, loading, restraint to thermal expansion, pore pressures as a result of moisture expanding on evaporation. The factors that affect spalling are reviewed in the following sections.

Moisture content
Moisture content is one of the main factors causing spalling. In the absence of moisture, the potential explosive spalling is reduced (Schneider 1986). However, explosive spalling due to thermal stress can still occur with no moisture in ceramic materials for instance (Khoury 2003). Many researchers have shown that increasing moisture content increases the probability of spalling. Therefore, wet concrete, e.g. an external environment, will tend to spall faster and more extensively than drier concrete. This is because the moisture increases the thermal conductivity and therefore the rate at which the concrete responds to heating and the rate of production of water vapor that builds up inside the concrete, which leads to earlier spalling (SINTEF 1988). It is commonly accepted that the normal weight and ordinary strength concrete with less than 3% moisture content by weight will not give rise to explosive spalling and that concrete in the range of 3-4% moisture content has a limited risk of spalling (Hertz 2003, Newman and Choo 2003, EC2). However, spalling has been observed in some limited instances at low moisture content (<3%) (Shuttleworth 1997). The tests by Both (2000) and SINTEF (1992) were carried out on high strength concretes where the 3% rule of thumb is for normal strength concretes. Sloughing off of concrete at the corners of the columns in the tests by Thomas and Webster (1953) is caused by chemical deterioration of the cement paste and internal cracking of concrete due to the difference in thermal expansion between the aggregate and the cement paste. It is a gradual process and not thought to be as a result of moisture. The tests by Shuttleworth (1997) are significant in that spalling was observed in normal strength concrete at a moisture content of just over 2%. However, the amount of spalling during 2 hours of the standard fire was only 5-20mm. From the test data presented there is only 1 instance where explosive spalling occurred in normal weight concrete at moisture contents below 3% by weight. The amount of spalling observed was 5-20mm. When compared to the spalling rates proposed (ArupFire 2005) of 3mm/min (=180mm

in 2hours) the amount of spalling observed in the test is small. This one case of spalling below a moisture content of 3% is not considered to negate the 3% rule of thumb referenced by many (BS8110-2 1985, Khoury 2000, Newman and Choo 2003, Hertz 2003, Lennon 2004, CIRIA 1984). In some literature, the moisture content is expressed in terms of relative humidity of the concrete. Higher relative humidity levels lead to greater spalling (Lee et. el. 2007). The acceptable relative humility level of concrete to reduce the spalling risk is 75% (Kodur 1999).

Water/Cement ratio, Permeability

Cement paste with a low water cement ratio, produces a dense almost impervious microsturcture (Komonen and Vesa 2003), which keeps the moisture vapor from escaping in a high temperature environment. This can lead to a build up of high internal pore pressure in the cement paste. Consequently the concrete is more likely to explosively spall, and to experience multiple spalling. High strength concrete (HSC) normally has a low water/cement ratio therefore is more likely to spall even at a slow heating rate when compared to normal strength concrete. Permeability is especially important in fires of high heating rate, such as hydrocarbon fires because the low permeability will trap moisture and pressure will build up rapidly under rapid heating causing spalling.

Heating condition

The heating condition is also one of the major factors influencing spalling. The higher the heating rate the higher the probability of spalling, and spalling is much more severe in high fire intensities due to the large temperature and moisture gradients in the fire-exposed surfaces (Kodur 1999). Hydrocarbon fires pose a severe threat in this regard. Explosive spalling seems to be the dominant spalling form in a hydrocarbon type fire (Marsh 2002). In addition, heating of more than one side of a concrete section (e.g. 4 sides of a column) increases the probability of spalling due to the increase of pore pressure by fast vapor flow and thermal stress (Schneider 1986, SINTEF 1988, Lennon 2000).

Aggregate

For normal weight concrete, there are two common aggregate groups: siliceous aggregates such as quartzite, gravel, granite and flint; calcareous aggregates such as limestone, dolomite and anorthosite. It is widely found that siliceous aggregates give the poorest resistance to spalling (Newman and Choo 2003). Flint aggregate is particularly susceptible (Canisius et al 2003). This can be explained partly as a result of the markedly different coefficients of thermal expansion between aggregate and cement paste, particularly at higher temperatures, and partly the result of a volume increase phase transformation at approximately T=570°C from α-quartz to β-quartz. Expansion of the aggregates leads to cracks in the concrete or splitting of the aggregate which contribute to spalling. Calcareous aggregates tend to give good fire performance (Newman and Choo 2003). There are several reasons to explain the improved resistance to spalling. First, the calcareous aggregates typically have a lower coefficient of thermal expansion than siliceous aggregates and they are closer to that of cement paste, producing lower internal stresses on heating. Secondly, there are no solid state phase changes in calcareous aggregates within fire exposure conditions. On heating to temperatures in excess of 660°C calcium carbonates begin to break down, similarly above 740°C for magnesium carbonates. On breaking down the minerals release carbon dioxide and heat transfer is claimed to slow down despite the reaction being endothermic. The residual aggregate particles also have lower thermal conductivity, further

reducing heat transfer into the concrete. During cooling the carbonates, which have broken down during heating, re-hydrate. This re-hydration reaction is believed to cause post-cooling spalling in calcareous aggregate concretes (Khoury 2003). Design guidance on cover and thickness of section based on the provisions of standard BS 476 and ACI 216 fire exposure is purely empirical.

Test condition

Concrete is usually tested at high temperatures in sealed or unsealed conditions, in which the unsealed test condition is closer to reality with respect to a concrete building in a fire. In an unsealed test, vapor can escape from the concrete surface. In a sealed test, moisture and pore pressure gradient at the fire exposed sealed surface equal 0 (Huang et al 1991). Figure 13.1 illustrates the difference between sealed and unsealed test conditions. The primary difference is that moisture can escape towards the fire in an unsealed test but is forced to migrate through the inner concrete in a sealed test. A sealed test is commonly carried out to test concrete pressure vessels used in the nuclear industry where there is a liner between the concrete and the heating regime preventing moisture escaping towards the heat source. The dominant process for unsealed concrete relates to the loss of the various forms of water (free, absorbed and chemically bound), while the dominant process in sealed concrete relates to hygrothermal chemical reactions (Khoury 2000). A mathematical model, simulating the heat and mass transfer in concrete structures under fire (Huang et al 1991), has shown that in both sealed and unsealed test conditions, the pore pressure builds up rapidly across the drying region of the concrete section as a result of high heat flux from the fire and low mass transport capacity of the heated concrete during the period of fire exposure. Consequently, spalling of concrete is expected in the early stages of the fire, e.g. typically the first 20 minutes when the pore pressure exceeds the ultimate tensile strength of the concrete. Pore pressure then reaches a constant or dissipates during the steady state and cooling phase of the fire. Similarly spalling as a result of thermal expansion will reduce because the temperature change slows down in the steady state phase.

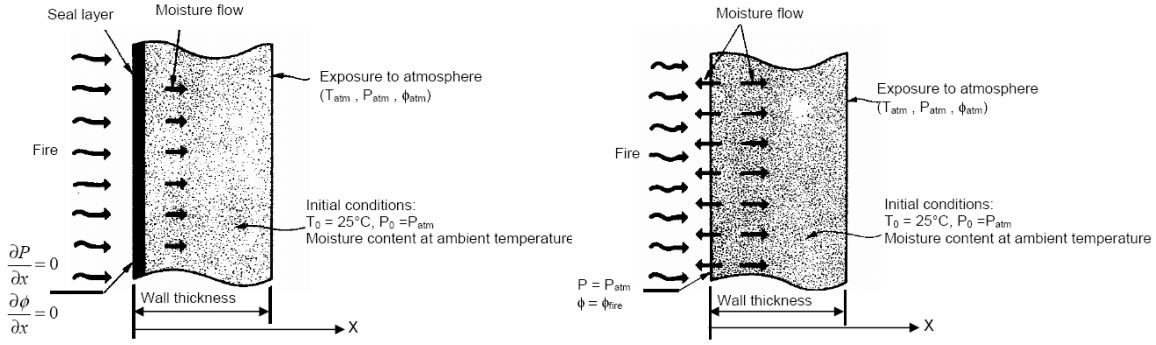

(a) Sealed concrete slab in fire (b) Unsealed concrete slab in fire

Fig. 13.1 Sealed vs. unsealed tests conditions (Huang et al 1991)

Concrete strength

Spalling in part is attributed to strength of concrete. High strength concrete is more susceptible to this pressure build up, because of its low permeability, which inhibits the escape of water vapor, compared to that of normal strength concrete. Available information (Kodur 1999; Long Phan 2001) shows that concrete with strengths higher than 55MPa are more susceptible to spalling and

may result in lower fire resistance. In normal strength concrete, the vapor can be transported much more easily to the unexposed surface, reducing the risk of spalling.

Mix proportions
Mix proportions influence the effect of spalling through alternations in the pore size distributions. In general a low porosity and decreasing pore radius increase the risk of spalling.

Section size
Section size is also an important factor affecting spalling - with thick members the probability of spalling decreases. CIRIA (1984) concluded that beams of 200mm or greater are less likely to suffer serious spalling. A design nomogram in EC2 suggests spalling is unlikely for members with section size > 200mm. Most variables that affect spalling are inter-related. Test results (CIRIA 1984) show that explosive spalling is unlikely to occur if the moisture content of concrete is below 2.5% by weight and the concrete section not less than 80mm thick. For specimens about 120mm in thickness, the moisture content can be as high as 4.5% before spalling occurs.

Applied load
High compressive stresses due to external loading or prestressing in the concrete layer exposed to heating increase probability of explosive spalling because of inducing restraint. Then spalling occurs as a result of thermal buckling as concrete expands, which is usually regardless of moisture content. Normally explosive spalling is unlikely to occur for thick concrete members under small load and the standard fire (EC2 1995, Schneider 1986).

Restraint
Restraint can restrain thermal expansion and give rise to thermal stresses which is similar when an external load applies. Normal strength concrete showed higher levels of spalling when tested under restraint and the standard fire (Ali et al 2004). Structural members can be restrained to thermal expansion as well as thermal gradient. Restraint may be beneficial to a bowing beam under thermal gradient because the tension, experienced on the underside as a result of bending under imposed loading, is reduced by the beam expanding against restraints, closing any tension cracks, but at a internal support of such as a continuous beam restraint increases tensile stresses. A restrained column exposed on 4 sides will be more compressive as it tries to expand resulting in stress induced spalling. From a practical point of view, all structural members can be regarded as being restrained at some level by adjacent cold structures. A slab or beam with free ends in a standard furnace test is the only elements, which could be considered to be unrestrained. Actually it can be considered that all structural elements in real buildings are restrained.

Thermal expansion
Thermal expansion of concrete increases as temperature increases. Siliceous aggregate has higher thermal expansion than calcareous aggregate concrete, therefore is more susceptible to spalling than calcareous aggregates. Thermal strains due to heating of the concrete may lead to tensile or compressive stresses in the area of the heated surface, which can lead to damage, resulting in a degradation of the structural performance.

Reinforcement

The presence of reinforcement in concrete will generally improve the spalling resistance of a concrete section because it halts or delays the development of spalling at the line of the reinforcement. Meyers Ottens (1977) believes that differential expansion of reinforcement and the surrounding concrete causes cracking and contributes to spalling. There is no evidence from other work to prove this conclusion. Moreover the thermal expansion coefficient of normal weight concrete and steel is of the same order ($\sim 10 \times 10^{-6}$) at reference temperature, but internal mismatch between concrete and reinforcement can occur by distinctively different thermal coefficients as temperature increases. Spalling as a result of cracking is generally not associated with explosive spalling although high concentrations of reinforcement in the corners of structural members enhance the occurrence of spalling.

Cover

For normal strength concrete, explosive spalling can often be restricted to the unreinforced part of the section and usually does not proceed beyond a reinforcing layer. Therefore it is believed that the greater the depth of cover, the greater the risk of spalling (Newman and Choo 2003). Standard fire tests (CIRIA 1987) have shown that spalling of limestone aggregate concrete was not observed for covers of up to 50mm within 2 hours of a standard fire. Spalling in gravel aggregate concrete ribs (joists) with covers to the main reinforcement of 35mm or less is not serious for up to two hours in a standard fire test. Significant spalling may occur with increased covers. However BS 8110 Part 2 recommends that additional spalling measures should be taken for cover thickness greater than 40mm for NWC exposed to the standard fire.

Fibers

An effective reduction of explosive spalling of concrete can be obtained by a suitable pore system which leads to a sufficient reduction of high vapor pressures. This can be reached by the addition of polymer fibers. Tests (Shuttleworth 1997, Lennon 2000, Both 2000) have shown that adding polypropylene fibers to the concrete mix is an effective method of reducing explosive spalling. During a fire attack at relatively low temperatures, approximately T=160°C the polypropylene fibres melt and micro pores form a porous transition zone between matrix and concrete surface, i.e. filling pores with fibers help the high pressure vapor escape and then relieve the pressure inside concrete, thus avoiding high pore pressure build-up. Polypropylene fibers are usually used in high strength concrete to improve its permeability. For normal strength concrete, they are rarely used (Shuttleworth 1997, Kodur 1999, Khoury 2000). However this is probably because the concept of spalling is not explicitly considered as the norm in design. It is important in this context to know, that e.g. the procedure of the addition of fibers, for example PP-fibers is a patent in concrete technology for the prevention of spalling in Europe. Adding steel fibers in concrete has no obvious effect on improving the spalling resistance of concrete (Shuttleworth 1997).

Density

The density of a specific concrete depends upon the aggregate used and the water/cement ratio. High strength concrete is densified by additive such a silica fume and as a result has very low water/cement ratio and permeability, therefore this increases the risk of spalling. In normal weight and ordinary strength concrete clear effect on spalling due to the variation in the density has not been verified.

Summarized investigations indicate that the occurrence of spalling depends amongst others on the following factors:

a) Rate of heating has a significant influence on spalling;
b) Temperature of the concrete has a mid-influence on spalling;
c) Moisture content of the concrete has a significant influence;
d) Strength of the concrete has a significant influence;
e) Pore volume and average pore size distribution may be altered to influence the severity of spalling;
f) Stress condition of the structural element has only little influence on spalling;
g) Mineral- and petrological composition of the aggregate has only a great influence if special aggregates are used (e.g. flint, granite);
h) Amount and location of the reinforcement has a mid-influence on spalling;
i) Geometry of the structural element has a mid-influence on spalling.

Due to the large amount of the factors, which partially cause synergetic effects, it is extremely difficult to make statements about the occurrence, degree and size of spalling. It therefore is necessary, to produce the concretes in a way, that the exclusion of spalling in practice is based on experiences and appropriate tests.

13.3 Interaction of key factors on spalling

Researchers have mixed conclusions about the most critical factors which define spalling. This is to be expected given the number of variables involved and their interdependency. Table 13.2 is a summary of key factors as suggested by various researchers. Each factor is either related to moisture and pore pressures or to stress. In general three mechanisms have been debated explaining spalling mechanisms among many researchers: moisture content and pore pressure build-up are the dominant factor; thermal stress as a result of thermal expansion to be the dominant factor; and their combination. Having considered the findings of the literature review and the overview the following views can be taken as to what we will include and comment as follows:

- The primary cause of spalling in concrete is moisture and associated pore pressures as moisture is vaporized when concrete is exposed to elevated temperature during a fire.

- Moisture > 3% by weight is assumed to cause spalling.

- Heating rate is a critical factor on the rate of spalling of concrete. The rapid heating rate can develop very steep temperature gradient, therefore causing a rapid build up in pore pressure near the heating surface and resulting in explosive spalling in the early stages of a fire.

- Stress induced spalling as a result of loading and restraint to thermal expansion is also an important factor although it is not as well defined as moisture. This is primarily because of the many variables which affect stress induced spalling including initial loading, end restraint conditions, magnitude of thermal expansion coefficient, section thickness, magnitude of fire temperature.

– The presence of reinforcement will be considered to promote spalling resistance.

Table 13.2 The interactive key factors affecting spalling under rapid heating

Researcher	Key factors	Secondary factors
Saito (1965)	Initial load + restraint + stress caused by frictional resistance in concrete	Vapor pressure
Hamathy (1965)	Moisture clog	
Meyer-Ottens (1977)	Vapor pressure enhanced by frictional resistance in concrete + initial load +restraint	Initial load + restraint + frictional resistance in concrete, reinforcement expansion
Sertmehmetoglu (1977)	Moisture clog + Internal cracks	Initial load
Akhtaruzzaman and Sullivan (1970)	Vapor pressure	
Gustaferro (1966)	Vapor pressure	Aggregate expansion
Copier (1977)	Vapor pressure + initial load	
Long T. Phan (2002)	Pore pressure	Concrete strength
CU at Boulder (2008)	Moisture + vapor pressure	Concrete strength

14 Experimental Studies

14.1 Concrete cylinder

Introduction

Spalling failure was investigated through numerical analysis and observation of the experimental test phenomena. The experimental tests were performed (J.Lee, K.Lee, Xi and Willam 2007) at the University of Colorado Boulder where two different relative humidity (RH) conditions, wet and oven dried were considered when concrete cylinders were heated to elevated temperature with three different heating rates. The finite element analysis is conducted in order to simulate and detect spalling of the specimen and the experimental test results are compared with the results of the numerical simulation. The analytical and numerical verification of potential spalling is investigated below.

Test set-up and procedure

Experimental tests were performed on concrete cylinders, 50.8mm (2 in) wide and 100.16mm (4 in) high, see Figure 14.1.

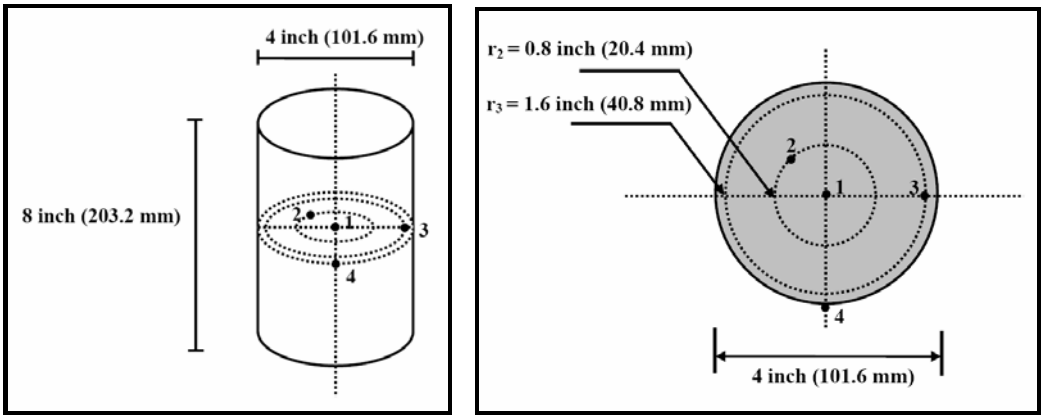

(a) Specimen geometry (b) Positions of thermocouples

Fig. 14.1 Specimen geometry and locations of thermocouples

The test specimens with two different initial humidity conditions were placed into the furnace where three heating elements were attached to each side. When the temperature on the surface of specimen reached the target temperatures of 250˚C, 400˚C, 550 ˚C using two heating rates, the furnace was shut off so that the hot specimens cooled down naturally. The faster heating rate was 22°C/min and the slower one was 1°C/min according to the external sensor in the furnace. However the actual higher heating rate on the surface was measured to be 18°C/min in the case of rapid heating.

Here the following abbreviations are used to describe the test conditions:

WF: Water saturated and Fast heating (30°C/min), OF: Oven dried and Fast heating rate (30°C/min), WS: Water saturated and Slow heating (1°C/min). In total 27 specimens were tested in which each set was comprised of 9 specimens. The 3 sets of specimens were monitored in the

furnace at three temperature levels, 250°C/min, 400°C/min, and 550°C/min. Temperatures were measured through thermo couples positioned in the concrete cylinder as shown in Figure 14.1. During elevating temperatures no mechanical load and no mechanical restraint were applied.

Test results

Figure 14.2 shows the temperature variation at the locations where thermo couples were placed.

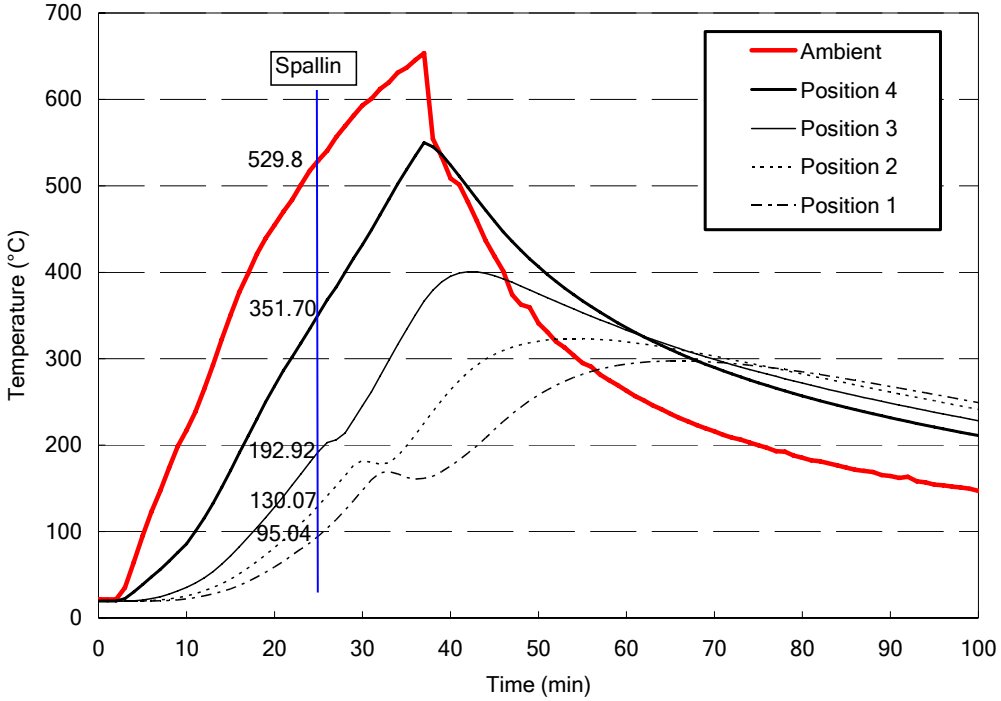

Fig. 14.2 Temperature histories at each position

The interesting aspect is that spalling failures occurred not only near the cylinder surface but also in the axial direction in the specimen series WF400 and WF550 when the surface temperatures reached T=350°C. At position 2 at 20.4mm from the surface the temperature was T=193°C. Hence the temperature in the region from the surface to 10mm inside from the surface can be estimated to reach T=250~300°C.

(a) Spalling Failure under different surface temperatures, T_{surf}=400: WF_400_1

(b) Spalling Failure under different surface temperatures, T_{surf} 550°C: WF_550_TD

Fig. 14.3 Spalling Failure under different surface temperatures, T_{surf}=400 and 550°C

It is also noted that no spalling failure occurred in the specimen series WS (wet and slow heating rate) and OF (oven dried and fast heating). This indicates that the spalling mechanism is closely related to the interaction of moisture migration and the steep thermal gradient which developed during rapid heating and initial moisture conditions. The spalled specimens are shown in Figure 14.3. The residual strengths were measured in compression after naturally cooling the specimen which were heated up to the different temperature levels. The degradation of the compressive strengths and stiffness due to thermal damage is shown in Figure 14.4.

The strength test were performed on the specimens which survived from the heating tests under two conditions: (a) the full-saturated specimen with slow heating and (b) the oven dried specimen with fasting heating. But no strength tests could be performed on the full-saturated specimens with fast heating rate which did exhibit spalling. The ultimate concrete strengths reached 6000psi, 5000psi, and 3600psi which corresponded to the target surface temperatures, T=250°C, 400°C, and 550°C.

Concluding remarks

1. Explosive spalling was observed under the wet concrete cylinders with the rapid heating rate.
2. Spalling was not observed in the wet cylinders subjected to the slow heating rate and oven dried cylinders with the fast heating rate.
3. We can conclude that the explosive spalling is highly affected with initial moisture contents and heating rate from the tests.

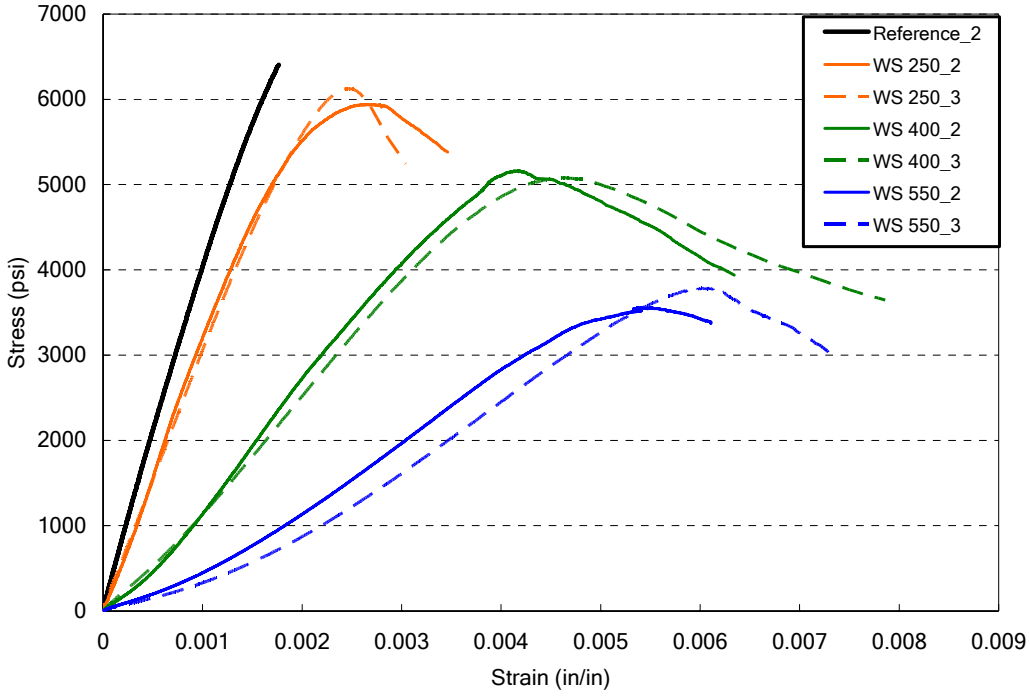

Fig. 14.4 Residual compressive strength at different temperatures

14.2 Reinforced concrete column

Introduction

The study of "Fire Test on Normal and High-strength Reinforced Concrete Columns", NIST Special Publication 919, 1997 was led by Corina-Maria Aldea, Jean-Marc Fransses, and Jean-Claude Dotreppe. The objective of the study was to quantify main parameters influencing spalling of normal and high-strength concrete columns under fire conditions for providing recommendations for fire safety.

Test set-up and procedure

The six reinforced concrete columns were tested at the University of Liege, in Belgium. The short columns are considered as followings: 290mm x 290 mm cross section and 2.10m length. The length of columns was determined by the height of the furnace used. Three mix compositions were designed for normal strength C30 and C50, and high strength concrete C90. Two different longitudinal reinforcement types, 8-ϕ12 and 4-ϕ25, were used as shown Figure 14.5. Concrete cover was 3 cm and stirrups with ϕ8 were placed 200mm spacing along the columns but at the ends of columns 100mm spacing was used. Each column was simply supported at the ends and loaded by hydraulic jacks in the furnace with external frame designed

to apply mechanical loading. Thirty two thermocouples were placed in 4 different sections along column: 9 thermocouples in two sections containing stirrups, and 7 thermocouples in 2 sections without stirrups. Mechanical force that is 50% of the design load was applied first, and then heating was applied in the gas furnace according to the standard ISO 834 curve. The test set-up is summarized in Table 14.1.

Table 14.1 Summary of test set-up

Test specimen	Section & B.C.	Mix type	Thermo couples	Loading
-Total 6 sets Each 2 sets to mix types	-290mmx290mm x2.1m -Simply supported short column	C30,C50,C90	32 thermo couples	-50 % of column design load -Standard ISO834 fire curve in the furnace

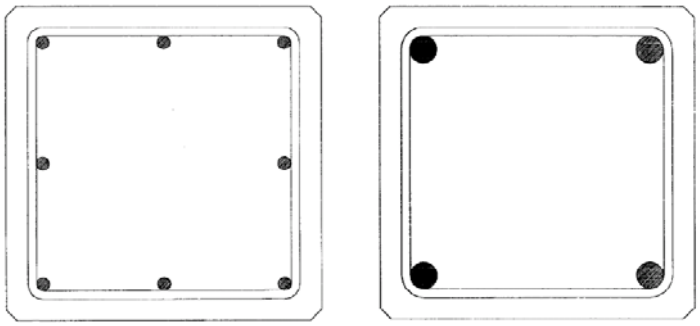

Fig. 14.5 Concrete cross section (29cm x 29cm): 8-ϕ12mm and 4-ϕ 25mm rebars with 3cm concrete cover.

The section types and positions of thermocouples at section and elevation are in Figure 14.6 and 14.7.

Experimental results

A. C20 and C50

Both C20 and C50 columns showed a few longitudinal cracks near edges with progressive crushing of concrete and buckling of steel bars. Fire resistance proved comparable.

B. C90

High strength columns showed early spalling at the corners causing premature heating of the steel rebars in the reduced section. These resulted in buckling of the steel rebars just before a sudden failure by crushing of concrete core, and led to a considerable reduction in fire resistance. The fire resistance is summarized in Table 14.2.

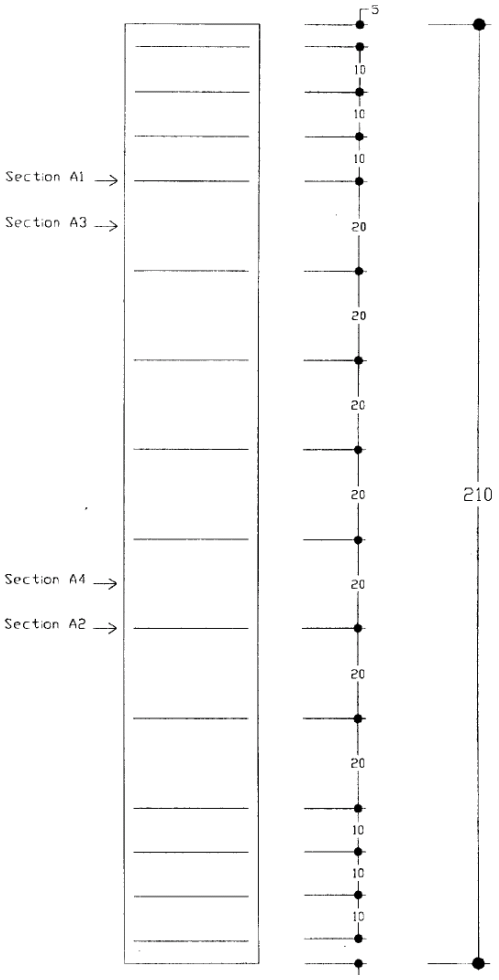

Fig. 14.6 Section types, and positions of thermocouples.

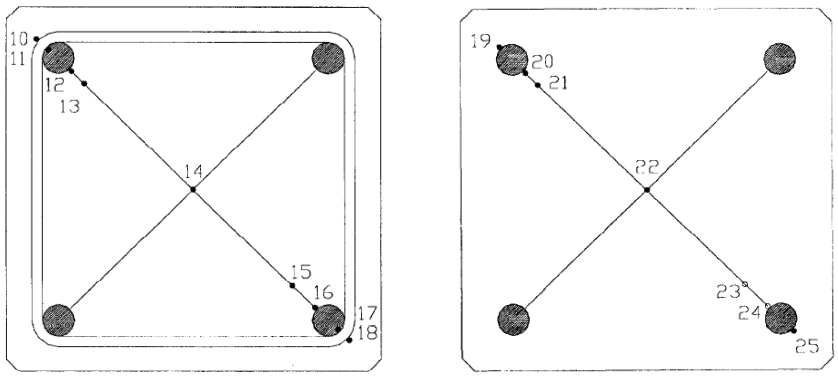

Fig. 14.7 Positions of thermocouples in the cross sections with and without stirrups.

Table 14.2 Fire resistance of different concrete strengths and reinforcements

Concrete	Fire Resistance (hours and minutes)	
	8-ϕ12	4-ϕ25
C20	3 hours 54 minutes	3 hours 13 minutes
C50	2 hours 32 minutes	3 hours 29 minutes
C90	1 hours 46 minutes first spalling after 8 minutes	1 hours 29 minutes first spalling after 12 minutes

Concluding remarks

1. High strength concrete columns showed corner spalling phenomena for C90, 8-ϕ12 and 4-ϕ25 after 8 minutes and 12 minutes. A type of spalling was sloughing-off which was a consequence of losing concrete tensile strength at elevated temperature. The experimental results confirm that high strength concrete is more susceptible to spalling than normal strength concrete where spalling was not noticed during tests.
2. Longitudinal cracks along the main reinforcement were detected for normal strength concrete after one hour of the fire test and propagated until the end of the test failed to crushing.
3. Tests showed that the local behavior at material points has a more significant influence on failure than the structural behavior.

15 Theoretical Background in Poromechanics

Spalling can be modelled explicitly using a porous system of thermo-hygro-mechanical coupling equations. These governing equations can consider all variables that lead to spalling including the build up of pore pressures as moisture evaporates from the concrete in a fire. The individual components of the micro structure of the concrete material are all represented in this type of modeling. Therefore it is very detailed and complicated. This level of accuracy is still firmly in the research domain and still requires significant validation. In this section the equations of two systems of equations are introduced for thermo-hygro-mechanical behavior in concrete: Four-field vs. Three-field formulations.

15.1 Thermohygro processes

The processes of explosive spalling under fire may be explained as a hypothesis in Figure 15.1. Due to high temperature and a rapid heating rate on the concrete surface desorption of physically bounded water occurs first and gel water as well as crystal water from cement paste and aggregates are dissociated in turn. Some vapor water escapes through a porous network in concrete to the free surface while the other one moves inward concrete. When vapor flows colder zones at an inner region the vapor may condensate. As condensation continues a quasi saturation layer called moisture clog can occur and then moisture may not migrate through this moisture block. The condensation may lead to a zone of pressurized water which is very active beyond the temperature, T=250°C. If the pressure increases beyond tensile strength of the concrete, explosive spalling may occur at the front of the saturated layer from the hot surface. Migration of vapor can only flow to the hot surface zone due to the moisture clog. The total pore pressure results from the summation of the partial pressures of all phases, i.e. liquid water, vapor water, air.

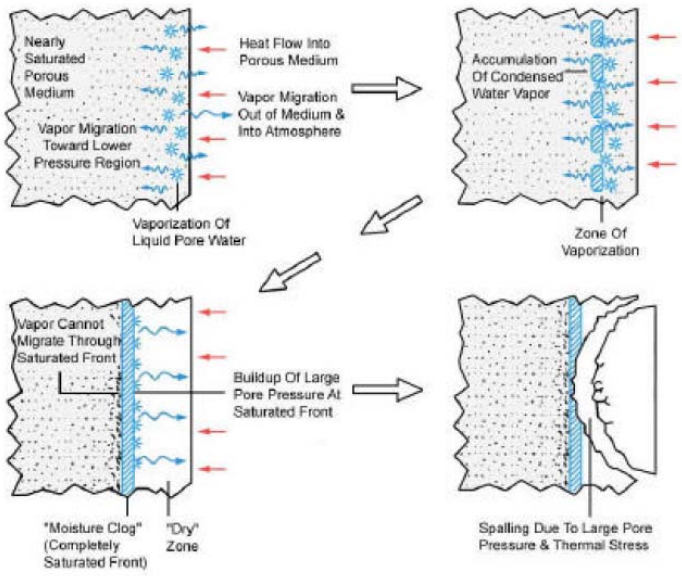

Fig. 15.1 Hypothesis of spalling mechanism

It is obvious that Figure 15.2 indicates with a heating up to approximately 250°C just short after fire, the tensile strength of normal or high strength concrete may reach cracking strength due to the vapor pressure since the capacity of yield strength reduces as temperature increases. This is because around T = 250 ˚C saturated vapor pressure in a saturated region (moisture clog) in concrete increases abruptly according to thermodynamic table.

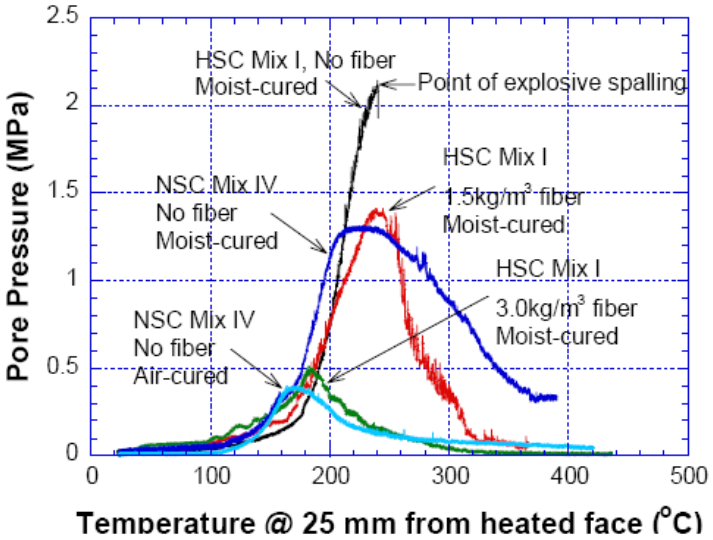

Fig. 15.2 Pore pressure at 25mm deep in different block specimens (Long Phan 2001)

For High Performance Concretes, the saturated water zone develops near the heated surface due to low permeability of the dense concrete structure. The faster the saturated zone on the surface is heated up the higher the vapor pressure increases. This may lead to spalling near surface at even low moisture contents. Also high strength concrete can have the same behavior due to the low water-cement ratio.

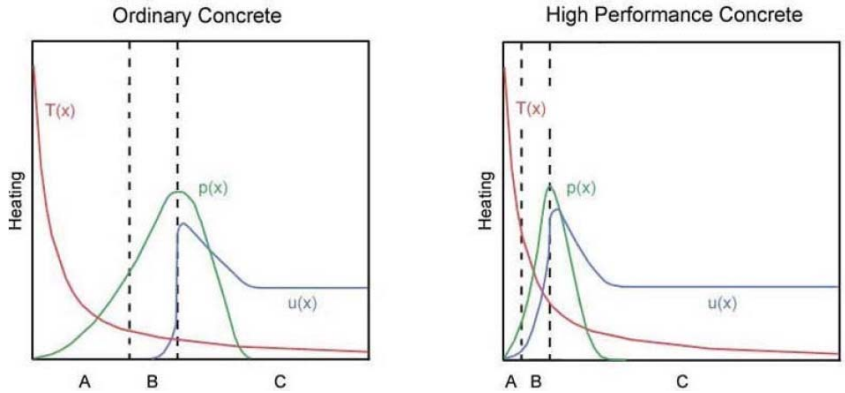

A: Dry zone B: vapor zone C: liquid zone

T(x) : Temperature P(x) : pore pressure m(x) : mositure content

Fig. 15.3 Relationship of temperature, pore pressure and moisture distribution

For ordinary concrete with a strength of less then 40 N/mm^2 and a physical bounded water content of 2 % by weight it is known that it does not spall under standard fire conditions with temperature increase of fire gases less than 60 K/min, which is common for the ISO standard fire test. But the experimental test showed spalling of concrete cylinders with fc'=50 N/mm^2 and quasi saturated condition where relative humidity is 95% (K. Willam, Y. Xi, J. Lee and K. Lee 2007). Therefore crucial factors are the density and porosity as well as absolute water content in concrete structures. Figure 15.3 illustrates pore pressure development and moisture distribution for ordinary concrete and high strength concrete.

15.2 Four Field Formulations vs. Three Field Formulations

Spalling can be modelled explicitly using state of the art thermo-hydro-mechanical system of equations considering all variables. In order to represent behaviors of the individual components of the porous structure of the concrete a system of eqations such as four field formulations or three field formulations is required, which can simulate and lead to spalling behavior including the build up of pore pressures as moisture evaporates in concrete under a fire. These types of modeling are very complicated and in research domain. This section will introduce the fundamental and basic principles of two mathematical models and provided with some numerical results of concrete under rapid temperature using three field formulations.

Concrete contains very fine pores which can be partially filled with water. When modeled as a porous medium, concrete is usually considered to be a triphasic body, consisting of a solid phase (the cement paste and the aggregates), a liquid phase (usually water) and a gaseous phase (usually vapor and dry air). A partially saturated porous medium, in principle, is composed of multiphase constituents of a solid skeleton and porous structures filled with one or more gaseous and liquid phases.

15.3 Mass balances

The mass balance equations are described for the solid and fluid phases. The general form of the local mass balance conservation for the π-th phase is

$$\frac{\partial \rho_\pi}{\partial t} + \nabla \bullet (\rho_\pi \mathbf{v}^\pi) = \rho_\pi e^\pi(\rho_\pi) \tag{15.1}$$

where ρ_π and $\mathbf{v}^\pi$ are the phase-averaged apparent density and the mass averaged phase velocity, respectively. The exchange term, $\rho_\pi e^\pi(\rho)$, represents the average microscopic rate of exchange of density with the other phases.

solid phase

The averaged macroscopic solid mass balance equation is obtained from Eq. (15.1) where we assume there is no solid mass loss to the fluid phases, $\rho_s e^s(\rho) = 0$:

Appling the material derivative yields the following mass balance in following form

$$\frac{D^s \rho_s}{Dt} + \rho_s \nabla \bullet \mathbf{v}^s = 0 \tag{15.2}$$

Eq. (15.2) can be rewritten in terms of intrinsic phase-averaged density of the solid phase, ρ^s, as

$$\frac{(1-\phi)}{\rho^s}\frac{D^s\rho^s}{Dt} - \frac{D^s\phi}{Dt} + (1-\phi)\nabla\bullet\mathbf{v}^s = 0 \tag{15.3}$$

where the first term on the left denotes change in solid density, the second one is the change of porosity and the third term represents the divergence of volumetric strain rate of the solid skeleton in time. Since $D^s\rho^s/Dt = 0$ for an incompressible solid material, the mass balance becomes

$$-\frac{D^s\phi}{Dt} + (1-\phi)\nabla\bullet\mathbf{v}^s = 0 \tag{15.4}$$

where Eq. (15.4) does not mean that the solid skeleton is rigid because rearrangement of the void space may occur.

Liquid water phase

The mass balance Eq. (15.1) for the liquid phase is

$$\frac{\partial\rho_w}{\partial t} + \nabla\bullet(\rho_w\mathbf{v}^w) = \rho_w e^w(\rho_w) \tag{15.5}$$

where the term on the right hand defines the rate of mass transfer from the liquid phase to the vapor phase in time due to evaporation,

$$\rho_w e^w(\rho_w) = -\dot{m} \tag{15.6}$$

By introducing the relative velocity, $\mathbf{v}^{w,s} = \mathbf{v}^w - \mathbf{v}^s$, and re-writing the Eulerian time derivative in terms of material time derivative with respect to the solid skeleton, we get

$$\frac{D^s\rho_w}{Dt} + \mathbf{v}^{w,s}\cdot\nabla\rho_w + \rho_w\nabla\bullet(\mathbf{v}^s + \mathbf{v}^{w,s}) = -\dot{m} \tag{15.7}$$

Incorporating relative velocity vector identities we can derive the following equation:

$$\frac{D^s\rho_w}{Dt} + \nabla\bullet(\rho_w\mathbf{v}^{w,s}) + \rho_w\nabla\bullet\mathbf{v}^s = -\dot{m} \tag{15.8}$$

Summing the mass balance equations for the liquid phase and the continuity equation for an incompressible solid we get

$$\underbrace{\frac{D^s\rho_w}{Dt}}_{(a)} - \underbrace{\frac{\rho_w}{\phi}\frac{D^s\phi}{Dt}}_{(b)} + \underbrace{\nabla\bullet(\rho_w\mathbf{v}^{w,s})}_{(c)} + \underbrace{\frac{\rho_w}{\phi}\nabla\bullet\mathbf{v}^s}_{(d)} = -\underbrace{\dot{m}}_{(e)} \tag{15.9}$$

where term (a) represents the mass variation of liquid water in time; (b) is the change in liquid mass fraction due to the change of porosity in time; (c) is the gradient of liquid mass flux; (d) is the change of saturation by the volumetric strain rate; and (e) is the rate of evaporation between each phases.

We can extend Eq. (15.9) in terms of liquid water and vapor pressures, temperature and displacement assuming the apparent density and porosity are dependent with those variables into

$$\begin{aligned}
&\frac{\rho_w}{\phi}\nabla\bullet\frac{D^s\mathbf{U}}{Dt}+\left(\frac{D^s\rho_w}{D^sP_w}-\frac{\rho_w}{\phi}\frac{D^s\phi}{D^sP_w}-\frac{D^s\rho_w e^w(\rho_w)}{D^sP_w}\right)\frac{D^sP_w}{Dt}+\left(\frac{D^s\rho_w}{D^sP_{gw}}-\frac{\rho_w}{\phi}\right)\frac{D^s\phi}{D^sP_{gw}}\frac{D^sP_{gw}}{Dt}\\
&+\left(\frac{D^s\rho_w}{D^sT}-\frac{\rho_w}{\phi}\frac{D^s\phi}{D^sT}\right)\frac{D^sT}{Dt}+\nabla\bullet\left[\left(-D_{ww}\frac{\partial\rho_w}{\partial P_w}-D_{wg}\frac{\partial\rho_{gw}}{\partial P_w}\right)\nabla P_w\right]\\
&+\nabla\bullet\left[\left(-D_{ww}\frac{\partial\rho_w}{\partial P_{gw}}-D_{wg}\frac{\partial\rho_{gw}}{\partial P_{gw}}\right)\nabla P_{gw}\right]+\nabla\bullet\left[\left(-D_{ww}\frac{\partial\rho_w}{\partial T}-D_{wg}\frac{\partial\rho_{gw}}{\partial T}-D_{wT}\right)\nabla T\right]=0
\end{aligned}\tag{15.10}$$

Eq. (15.10) requires interactive relationships among liquid water mass, vapor water mass and temperature. Also porosity is dependent to temperature and water masses, which can show removal of absorbed water on the inner surface of pores.

water vapor phase

The macroscopic water vapor balance can be derived in the same manner as the liquid water balance except for using the gas phase as a reference phase. The result is

$$\frac{D^g\rho_{gw}}{Dt}+\nabla\bullet J_g^{\,gw}+\rho_{gw}\nabla\bullet\mathbf{v}^g=\rho_{gw}e^{gw}(\rho_{gw})\tag{15.11}$$

where $J_g^{\,gw}=\rho_{gw}\mathbf{v}^{gw,g}=\phi S^g\rho^{gw}\mathbf{v}^{gw,g}$ indicates the relative motion of the water vapor mass to the gas phase, and the rate of evaporation, $\rho_{gw}e^{gw}(\rho_{gw})=\dot{m}$, is positive when evaporation of vapor water occurs. Rewriting Eq. (15.11) in terms of the material time derivative with respect to the solid skeleton and incorporating the relative velocity, $\mathbf{v}^{g,s}$, we arrive at:

$$\frac{D^s\rho_{gw}}{Dt}+\nabla\bullet(\rho_{gw}\mathbf{v}^{g,s})+\rho_{gw}\nabla\bullet\mathbf{v}^s+\nabla\bullet J_g^{\,gw}=\dot{m}\tag{15.12}$$

The macroscopic and incompressible solid balance Eq. (15.4) is added to Eq. (15.11), and we get

$$\underbrace{\frac{D^s\rho_{gw}}{Dt}}_{(a)}-\underbrace{\frac{\rho_{gw}}{\phi}\frac{D^s\phi}{Dt}}_{(b)}+\underbrace{\nabla\bullet(\rho_{gw}\mathbf{v}^{g,s})}_{(c)}+\underbrace{\frac{\rho_{gw}}{\phi}\nabla\bullet\mathbf{v}^s}_{(d)}=\underbrace{\dot{m}}_{(e)}\tag{15.13}$$

where (a) denotes the mass variation of vapor water in time; (b) is the change in vapor mass fraction due to the change of porosity in time; (c) is the gradient of vapor mass flux; (d) is the saturation change by volumetric strain rate; and (e) is the rate of evaporation. The water vapor mass flux driven by the relative motion of gas and water vapor, J_g^{gw} is neglected in concrete medium.

Eq. (15.13) can also be extended in terms of liquid water and vapor pressures, temperature and displacement assuming the apparent density of vapor and porosity are dependent with those variables as

$$\begin{aligned}&\frac{\rho_{gw}}{\phi}\nabla\bullet\frac{D^s U}{Dt}+\left(\frac{D^s\rho_{gw}}{D^s P_w}-\frac{\rho_{gw}}{\phi}\frac{D^s\phi}{D^s P_w}-\frac{D^s\rho_{gw}e^{gw}(\rho_{gw})}{D^s P_w}\right)\frac{D^s P_w}{Dt}+\left(\frac{D^s\rho_{gw}}{D^s P_{gw}}-\frac{\rho_{gw}}{\phi}\right)\frac{D^s\phi}{D^s P_{gw}}\frac{D^s P_{gw}}{Dt}\\&+\left(\frac{D^s\rho_{gw}}{D^s T}-\frac{\rho_{gw}}{\phi}\frac{D^s\phi}{D^s T}\right)\frac{D^s T}{Dt}+\nabla\bullet\left[\left(-D_{gw}\frac{\partial\rho_w}{\partial P_w}-D_{gg}\frac{\partial\rho_{gw}}{\partial P_w}\right)\nabla P_w\right]\\&+\nabla\bullet\left[\left(-D_{gw}\frac{\partial\rho_w}{\partial P_{gw}}-D_{gg}\frac{\partial\rho_{gw}}{\partial P_{gw}}\right)\nabla P_{gw}\right]+\nabla\bullet\left[\left(-D_{gw}\frac{\partial\rho_w}{\partial T}-D_{gg}\frac{\partial\rho_{gw}}{\partial T}-D_{gT}\right)\nabla T\right]=0\end{aligned}\tag{15.14}$$

15.4 Energy balance

The macroscopic energy balance equation for a multiphase medium can be written using the mass balance equation as follows:

$$(\rho C)_{eff}\frac{\partial T^{\pi}}{\partial t}+\rho_{\pi}C_p^{\pi}\mathbf{v}^{\pi}\bullet\nabla T^{\pi}=\nabla\bullet\mathbf{q}^{\pi}-\dot{m}\Delta H_{vap}\tag{15.15}$$

where the effective heat capacity is $(\rho C)_{eff}=\rho_s C_p^{\ s}+\rho_w C_p^{\ w}+\rho_g C_p^{\ g}$, the convective term is $\rho_{\pi}C_p^{\pi}\mathbf{v}^{\pi}=\rho_w C_p^{\ w}\mathbf{v}^{w}+\rho_{gw}C_p^{gw}\mathbf{v}^{g}$, the heat flux is $\mathbf{q}_{\pi}=-D_{TW}\nabla\rho_w-D_{Tg}\nabla\rho_{gw}-D_{TT}\nabla T$, and $\Delta H_{vap}=[(\rho^{gw}H^{gw}-\rho^{w}H^{w})+(\rho^{w}E^{w}-\rho^{gw}E^{gw})]$ is the latent heat energy due to phase change. The energy balance Eq. (15.15) can be expressed in terms of temperature and pressures assuming the phases in the porous medium are locally in a state of thermodynamic equilibrium, $T^{\pi}=T$

$$\begin{aligned}&(\rho C)_{eff}\frac{\partial T}{\partial t}=\nabla\bullet\left[\left(-D_{Tw}\frac{\partial\rho_w}{\partial P_w}-D_{Tg}\frac{\partial\rho_{gw}}{\partial P_w}\right)\nabla P_w\right]+\nabla\bullet\left[\left(-D_{Tw}\frac{\partial\rho_w}{\partial P_{gw}}-D_{Tg}\frac{\partial\rho_{gw}}{\partial P_{gw}}\right)\nabla P_{gw}\right]\\&\nabla\bullet\left[\left(-D_{Tw}\frac{\partial\rho_w}{\partial T}-D_{Tg}\frac{\partial\rho_{gw}}{\partial T}-D_{TT}\right)\nabla T\right]\end{aligned}\tag{15.16}$$

where energy due to convection is assumed to be negligible, and the latent heat due to the phase change can be also neglected if the effective diffusivity can be obtained from a test.

15.5 Momentum balance

The instantaneous momentum balance of all phases e.g. fluid and solid skeleton, occupied in a porous medium reaches

$$\mathbf{L}^{\mathrm{T}}\boldsymbol{\sigma}_{eff} - \mathbf{L}^{\mathrm{T}}P_{\pi}\mathbf{I} + \rho\mathbf{g} = \mathbf{0} \tag{15.17}$$

where $\mathbf{L}^{\mathrm{T}}$ is the differential operator. The effective stress is $\boldsymbol{\sigma}_{eff} = \boldsymbol{\sigma} + P_{\pi}\mathbf{I}$ where $\boldsymbol{\sigma}$ is the total stress, and $P_{\pi} = \left[(1-\chi_w)P_{gw} + \chi_w P_w\right]\mathbf{I} = \left[P_{gw} - \chi_w P_c\right]\mathbf{I}$ is the total fluid pressure in a partially saturated porous medium of concrete. The equilibrium capillary pressure can be defined as $P_c = P_{gw} - P_w$, and material function, χ_w is dependent with saturation degree of pores and capillary pressure, sorption isotherm $S_w(P_c)$, which need to be determined experimentally with various relative humidities to vapor-liquid thermodynamic equilibrium of water in different pore sizes.

The discretized system of equations are compacted and expressed in the matrix form as following,

$$\begin{bmatrix} \mathbf{K}_{uu} & \mathbf{K}_{uw} & \mathbf{K}_{ug} & \mathbf{K}_{uT} \\ \mathbf{0} & \mathbf{K}_{ww} & \mathbf{K}_{wg} & \mathbf{K}_{wT} \\ \mathbf{0} & \mathbf{K}_{gw} & \mathbf{K}_{gg} & \mathbf{K}_{gT} \\ \mathbf{0} & \mathbf{K}_{Tw} & \mathbf{K}_{Tg} & \mathbf{K}_{TT} \end{bmatrix} \begin{Bmatrix} \mathbf{U} \\ \mathbf{P}_w \\ \mathbf{P}_g \\ \boldsymbol{\theta} \end{Bmatrix} + \begin{bmatrix} \mathbf{0} & \mathbf{0} & \mathbf{0} & \mathbf{0} \\ \mathbf{C}_{wu} & \mathbf{C}_{ww} & \mathbf{C}_{wg} & \mathbf{C}_{wT} \\ \mathbf{C}_{gu} & \mathbf{C}_{gw} & \mathbf{C}_{gg} & \mathbf{C}_{gT} \\ \mathbf{0} & \mathbf{0} & \mathbf{0} & \mathbf{C}_{TT} \end{bmatrix} \frac{d}{dt} \begin{Bmatrix} \mathbf{U} \\ \mathbf{P}_w \\ \mathbf{P}_g \\ \boldsymbol{\theta} \end{Bmatrix} = \begin{Bmatrix} \mathbf{F}_u \\ \mathbf{F}_w \\ \mathbf{F}_g \\ \mathbf{F}_T \end{Bmatrix} \tag{15.18}$$

where each row forms a system of the ordinary differential equation in time.

The four field formulation is a system of equations which can represent interactions between liquid water, vapor water, temperature and mechanical behaviors. Applying this system of equations to concrete thermal expansion, shrinkage, and each combined response to the concrete skeleton can be represented by temperature, pressures, and capillary action in porous media. These interactive responses in a partially or fully open system of a concrete may reasonably be simulated during long term processes such as shrinkage and creep in an environmental condition e.g. normal operation of a nuclear power plant subjected to moderate temperatures.

Under severe environmental conditions subject to rapid-elevated temperatures or an accidental steam or water jets in the event of a pipe failure in a nuclear power plant the three-field formulations may model appropriately spalling of concrete and concrete structures for other short term period. This is mainly because significant pore pressure build-up may be directly related to vapor pressure under elevated temperatures which may lead to a localized damage resulting in global failure of structures.

15.6 Mass balances

The mass balance equations are rewritten for each phases from four-field formulations,

solid phase

$$-\frac{D^s\phi}{Dt} + (1-\phi)\nabla\bullet\mathbf{v}^s = 0 \tag{15.19}$$

Liquid water phase

$$\frac{D^s(\phi S^w \rho^w)}{Dt} - S^w \rho^w \frac{D^s \phi}{Dt} + \nabla\bullet(\phi S^w \rho^w \mathbf{v}^{w,s}) + S^w \rho^w \nabla\bullet \mathbf{v}^s = -\dot{m} \tag{15.20}$$

water vapor phase

$$\frac{D^s(\phi S^g \rho^{gw})}{Dt} - S^g \rho^{gw} \frac{D^s \phi}{Dt} + \nabla\bullet(\phi S^g \rho^{gw} \mathbf{v}^{g,s}) + S^g \rho^{gw} \nabla\bullet \mathbf{v}^s + \nabla\bullet J_g^{gw} = \dot{m} \tag{15.21}$$

water species: liquid water +vapor water phase

The rate of evaporation term can be eliminated by combining the liquid water balance Eq. (15.20), with the vapor water balance Eq. (15.21).

$$\begin{aligned}&(S^w \rho^w + S^g \rho^{gw})\nabla\bullet \mathbf{v}^s + \frac{D^s}{Dt}(\phi S^w \rho^w + \phi S^g \rho^{gw}) - (S^w \rho^w + S^g \rho^{gw})\frac{D^s \phi}{Dt} \\ &+\nabla\bullet\left[\phi(S^w \rho^w \mathbf{v}^{w,s} + S^g \rho^{gw} \mathbf{v}^{g,s})\right] + \nabla\bullet J^{gw} = 0\end{aligned} \tag{15.22}$$

We define the effective density as $\rho^e = \phi(S^w \rho^w + S^g \rho^{gw})$, and assume that the average density change due to porosity rate in time, $(S^w \rho^w + S^g \rho^{gw}) D^s \phi / Dt$, is negligible in concrete. This is quantified from various experimental studies (Piasta et al, 1984). Piasta measured the variations of total porosity in structure of hardened cement paste at the range of temperature 20°C and 800°C where the total porosity in hardened cement paste can be considered as total porosity of concrete neglecting porosity of aggregate in concrete. In their test, the variation of the porosity at the range of temperature, T=100~500°C, $\partial\phi / \partial T = 7.8\times10^{-5}$ [cm^3/(g°C)] which is negligibly small. Furthermore we can assume that $\partial\phi / \partial P^e \approx 0$ which is based on the fact that the solid skeleton of concrete experiences very small dilatation before spalling, but this is not quantified from an experimental test.

If we assume that the flux by the relative motion between gas and vapor is also negligible, $\nabla\bullet J_g^{gw} = \nabla\bullet(\phi S^g \rho^{gw} \mathbf{v}^{gw,g}) \approx 0$, then Eq. (15.22) can be written as

$$\frac{\rho^e}{\phi}\nabla\bullet \mathbf{v}^s + \frac{\partial \rho^e}{\partial t} + \nabla\bullet(\rho^e \mathbf{v}^{e,s}) = 0 \tag{15.23}$$

where $\rho^e \mathbf{v}^{e,s} = \phi(S^w \rho^w \mathbf{v}^{w,s} + S^g \rho^{gw} \mathbf{v}^{g,s})$ is the effective flux due to the relative motions in a moving solid. In Eq. (15.23) the first term on the left-hand side indicates the effective mass change due to the averaged mechanical response, the second one represents the effective mass change in time, and the third, $\nabla\bullet(\rho^e \mathbf{v}^{e,s})$, indicates the effective fluid mass flow by Darcy's law.

The effective density ρ^e is defined as a function of the effective pressure or relative humidity, RH and a temperature.

$$\rho^e = \rho^e(P^e, T) \tag{15.24}$$

This sorption isotherm equation can be explained with the degree of effective saturation, S^e, capillary pressure, and the interaction of the surface tension and curvature at the interface between gas and liquid phases. In Eq. (15.23) the third term, mass diffusion equation can be interpreted as $\nabla\bullet[\rho^e(P^e,T)\mathbf{v}^{e,s}]=\nabla\bullet J_e$. The effective flux of moisture in concrete J_e (kg/m^{3}s) consists of the flux due to the gradient of moisture concentration according to Fick's law as well as the Soret flux due to the gradient of temperature.

$$J_e=-D_{ww}\nabla\rho^e-D_{wT}\nabla T \tag{15.25}$$

where D_{ww} and D_{Tw} are the material transport coefficients which depend on T and P^e. The gradient of the effective density can be expanded as $\nabla\rho^e=(\partial\rho^e/\partial P^e)\nabla P^e+(\partial\rho^e/\partial T)\nabla T$ since ρ^e is a function of temperature and the equivalent pore pressure. Then we can obtain the following moisture flux as

$$J_e=-D_{ww}\frac{\partial\rho^e}{\partial P^e}\nabla P^e-(D_{wT}+D_{ww}\frac{\partial\rho^e}{\partial T})\nabla T \tag{15.26}$$

in which $D_{ww}(\partial\rho^e/\partial P^e)$ denotes the permeability (m/s) and the first term on the right–hand side in Eq. (15.26) is known as Darcy's law. It is normally limited to saturated porous media but the Darcy-type law can be applied for both saturated and partially saturated concrete, provided the pressure in the pores of partially saturated concrete is treated as the vapor water pressure rather than the capillary pressure. The time derivative of ρ^e is written as functions of temperature and pressure.

$$\frac{\partial\rho^e}{\partial t}=\frac{\partial\rho^e}{\partial P^e}\frac{\partial P^e}{\partial t}+\frac{\partial\rho^e}{\partial T}\frac{\partial T}{\partial t} \tag{15.27}$$

Substituting of Eq. (15.26) and Eq. (15.27) into the effective mass balance equation leads to the following equation which compares with the mass balance equation proposed by Bazant (Bazant and Thonguthai 1979) except for the leading term introducing the coupling between the rate of skeleton volume change and pore pressure in the above equation.

$$\begin{aligned}&\frac{1}{\phi}\rho^e\underbrace{\nabla\bullet\mathbf{v}^s}_{(a)}+\underbrace{\frac{\partial\rho^e}{\partial P^e}\frac{\partial P^e}{\partial t}}_{(b)}+\underbrace{\frac{\partial\rho^e}{\partial T}\frac{\partial T}{\partial t}}_{(c)}+\nabla\bullet\left[\underbrace{(-D_{ww}\frac{\partial\rho^e}{\partial P^e})\nabla P^e}_{(d)}\right]\\&+\nabla\bullet\left[\underbrace{-(D_{wT}+D_{ww}\frac{\partial\rho^e}{\partial T})\nabla T}_{(e)}\right]=0\end{aligned} \tag{15.28}$$

In Eq. (15.28) the terms (a) is the volumetric strain rate; (b) is the effective mass variation due to the change of pressure; (c) is the effective mass variation due to the change of temperature; (d) is the Darcy flux; (e) is the Soret flux.

15.7 Energy balance equation

The macroscopic energy balance Eq. (15.15) is re-introduced

$$(\rho C)_{eff}\frac{\partial T^{\pi}}{\partial t}+\rho_{\pi}C_{p}{}^{\pi}\mathbf{v}^{\pi}\bullet\nabla T^{\pi}=\nabla\bullet\mathbf{q}^{\pi}-\dot{m}\Delta H_{vap} \tag{15.29}$$

where the effective heat capacity $(\rho C)_{eff}$, the convective term, $\rho_{\pi}C_{p}{}^{\pi}\mathbf{v}^{\pi}$ are defined in the above section and the heat flux is $\mathbf{q}_{\pi}=-D_{TW}\nabla\rho_{e}-D_{TT}\nabla T$. The energy balance Eq. (15.29) can be expanded as

$$(\rho C)_{eff}\frac{\partial T}{\partial t}=\nabla\bullet\left[-D_{Tw}\frac{\partial\rho_{e}}{\partial P_{e}}\nabla P_{w}\right]+\nabla\bullet\left[\left(-D_{Tw}\frac{\partial\rho_{e}}{\partial T}-D_{TT}\right)\nabla T\right] \tag{15.30}$$

where energy due to convection is assumed to be negligible, and the latent heat due to the phase change is neglected.

15.8 Momentum balance

The instantaneous momentum balance of all phases e.g. fluid and solid skeleton, occupied in a porous medium reaches

$$\mathbf{L}^{\mathrm{T}}\boldsymbol{\sigma}_{eff}-\mathbf{L}^{\mathrm{T}}P_{e}\mathbf{I}+\rho\mathbf{g}=\mathbf{0} \tag{15.31}$$

where $\mathbf{L}^{\mathrm{T}}$ is the differential operator. The effective stress is $\boldsymbol{\sigma}_{eff}=\boldsymbol{\sigma}+P_{e}\mathbf{I}$ where $\boldsymbol{\sigma}$ is the total stress, and P_{e} is the effective pressure from combined fluid interactions in a partially saturated porous medium of concrete. The effective pressure, P_{e} can be dependent to relative humidity and temperature.

In three field formulations the major assumptions are as follow:
(1) The Lagrangian and Eulerian porosities are the same

(2) The time-rate of change of porosity is negligible

(3) The divergence of the diffusive velocity term, $J_{g}{}^{gw}$ is negligible

(4) The convection transport of heat due to individual phases flowing relative to the solid phase is negligible

(5) Heat lost due to strain rates of change is negligible

(6) Heat loss due to liquid water evaporating is negligible

(7) No body source of heat is assumed

(8) The deformation tensors are assumed to be small

The discretized system of ordinary differential equations in time are as follows,

$$\begin{bmatrix} \mathbf{K}_{uu} & -\mathbf{K}_{up} & \mathbf{K}_{uT} \\ \mathbf{0} & \mathbf{K}_{pp} & \mathbf{K}_{pT} \\ \mathbf{0} & \mathbf{K}_{Tp} & \mathbf{K}_{TT} \end{bmatrix} \begin{Bmatrix} \mathbf{U} \\ \mathbf{P} \\ \boldsymbol{\theta} \end{Bmatrix} + \begin{bmatrix} \mathbf{0} & \mathbf{0} & \mathbf{0} \\ \mathbf{C}_{pu} & \mathbf{C}_{pp} & \mathbf{C}_{pT} \\ \mathbf{0} & \mathbf{0} & \mathbf{C}_{TT} \end{bmatrix} \frac{d}{dt} \begin{Bmatrix} \mathbf{U} \\ \mathbf{P} \\ \boldsymbol{\theta} \end{Bmatrix} = \begin{Bmatrix} \mathbf{F}_u \\ \mathbf{F}_P \\ \mathbf{F}_T \end{Bmatrix} \tag{15.32}$$

Three filed formulation is much simpler than four field formulation and may predict effective pressure, temperature and mechanical response under elevated temperatures. Also short term process for transport and mechanical bahavior such as an explosive spalling can be explained. But the three field formulation has some limitation for evaluating long term process such as shrinkage in concrete due to a single pressure. In porous mechanics capillary action can occur with difference between water and vapor pressure.

The system of three-field formulations is solved using 2D in-house finite element analysis which was developed (K. Lee 2008), which provides solution coupled with mechanical, temporal variables: pressure and temperature. From the tested concrete cylinder one strip was modeled and subjected to mechanical boundary conditions and transport boundary conditions shown in Figure 15.4 where 4-node axisymmetric element is used.

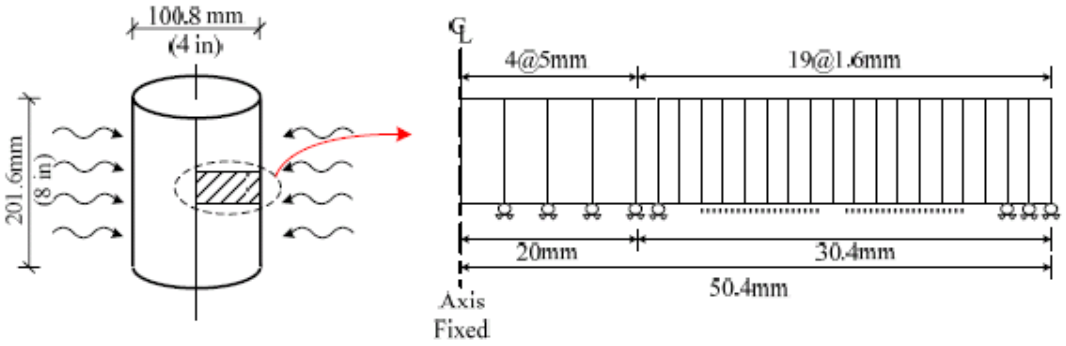

Fig. 15.4 Geometry and meshes extracted from cylinder

The prescribed temperature history, the heating rate, R = 20°C/min, on the surface is shown in Figure 15.5.

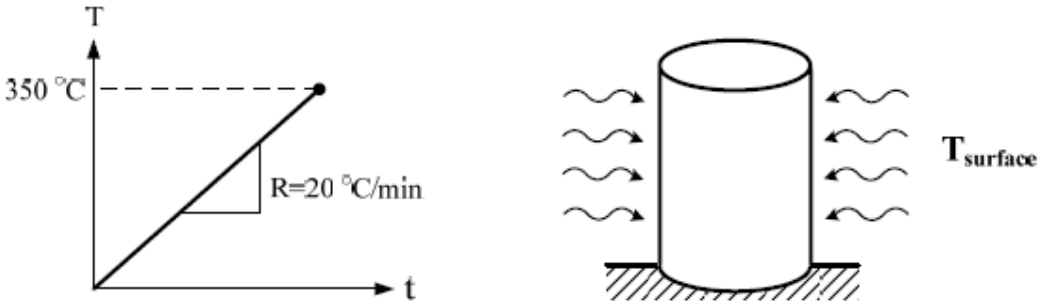

Fig. 15.5 Prescribed surface Temperature history in the specimen

The material properties for moisture, heat and mechanical analysis are summarized in Table 15.1. Pressure variations under different temperatures were computed numerically in the temperature range T=20°C to 350°C. The maximum pressure reaches 3.5MPa at the location $r \approx 10$mm from the surface when the temperature on the surface reaches T=350°C, while pressures at different temperatures, T=100°C and T=200°C on the surface are 1.8MPa and 0.3MPa. The pressure migration at various temperatures is shown in Figure 15.6. The transport of pressure is affected by the relative humidity which is a function of saturation pressure with temperature-dependence. The thermo-hygral process is associated with the transport of heat and mass. Mass is considered the effective water mass in the form of vapor. As temperature increases water partly evaporated. Thereby the evaporation develops an internal pore pressure in the porous network, which is the major driving force for mass transport together with temperature gradients.

Table 15.1 Material properties used in numerical analysis

TYPE	PROPERTIES
Hydraulic Analysis	Intrinsic permeability (m/s) $k_o = 1\times10^{-22}$ Relative permeability (m/s) $k = k_o(T-8.33)/16.67$, T < 100°C $k = 1\times10^{-19}$, 100< T < 350° Sorption curve $\rho_e = \rho_{cem}\left[RH(\rho_L^o/\rho_{cem})\right]^{1/m(T)}$ if $RH \le 0.96$ $\rho_e = \rho_L^o[1+0.12(RH-1.04)]$ if $RH \ge 1.04$ $\rho_e = 0.96\rho_L + (RH-0.96)\frac{1.04\rho_L - 0.96\rho_L}{0.08}$ if $0.96 \le RH \le 1.04$
Heat Analysis	Diffusivity (m^2/sec) $D = Ra^2/(4\Delta T) = 1.60\times10^{-7}$ Heating rate, Ra(°C/min) $Ra = 20$ Radius, a(mm) $a = 50.4$
Mechanical Analysis	Compressive strength (MPa) $f'_c(T_o) = 48.0$ $f'_c(T) = f'_c(T_o) - 0.0315(T-T_o)$ Tensile strength (MPa) $f_t(T_o) = 4.0$

		$f_t(\mathrm{T}) = f_t(\mathrm{T_o})(1 - 0.1356 \times \frac{\mathrm{T\text{-}T_o}}{100})$
	Elastic modulus (GPa)	$E(\mathrm{T_o}) = 27.8$
		$E(\mathrm{T}) = E(\mathrm{T_o})[0.03921 \times \exp(-0.002\mathrm{T})]$
	Thermal coefficient(m/m/°C)	$\alpha_{th} = 8.57 \times 10^{-6}$

Vapor is partially evacuated to the heated surface and also migrates toward the center of the concrete cylinder. Then vapor condenses at a certain point as soon as the thermodynamic conditions are equilibrated, which results in formation of a quasi-saturated layer. The pressure peak is located at the saturated layer where increasing temperature leads to the saturated vapor pressure increase. This mechanism explains partly why pressure peaks dramatically increase around T=200°C~230°C because of abrupt increase of saturated vapor pressure thermodynamically at that temperature. These phenomena are also quantified (Pierre Kalifa, et el 2000). The relationship between pressure and temperature obtained from the current numerical computations shows this mechanism as shown in Figure 15.1. In a fully saturated porous medium, by thermodynamic relationships vapor pressures reach P=1MPa, 2MPa, and 3.5MPa when boiling temperatures are T=197°C, 253°C, and 313°C.

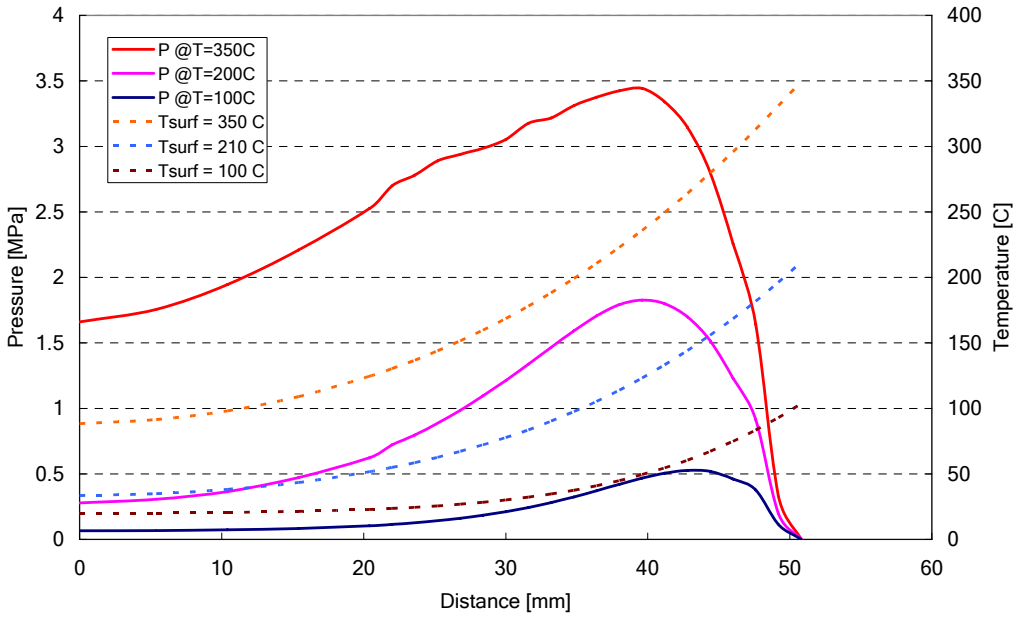

Fig. 15.6 Pressure vs. temperature profile from core to outer surface

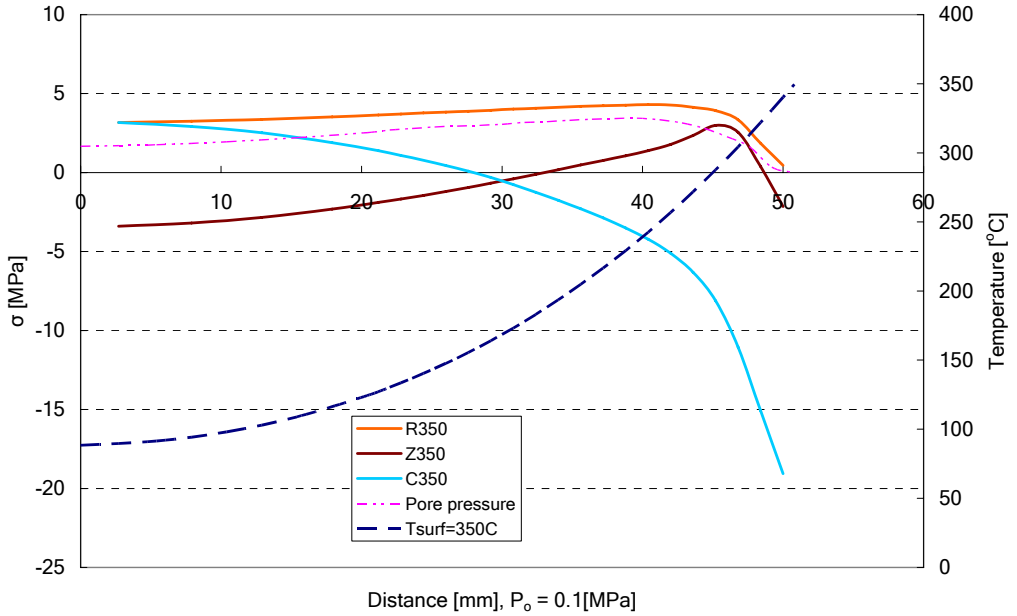

Fig. 15.7 Stress profiles, σ_{rr}, σ_{zz} and $\sigma_{\theta\theta}$ at surface temperature, T=350°C from thermo pore elasto-plastic analysis using parabolic DP model

These pressure levels are in the range of pressures developed in computational simulation which indicates that there can be a potential moisture clog near the surface.

From thermoporoelasto-plastic analysis Figure 15.7 shows stress profiles when the surface temperatures reaches T_{surf}=350°C. The triaxial state of stress in r_1=axis region is tension-tension-compression. The maximum radial stress and circumferential stress in tension reach σ_{rr}=3.2MPa and $\sigma_{\theta\theta}$=3.2MPa at r_1, and the axial stress is in compression, σ_{zz} = -3.4MPa at T_{surf}=350°C. The state of stresses is very similar to the one of thermoelasto-plastic analysis except for axial stresses developed by the internal pore pressure. Neglecting the axial stresses that are relatively small, yields equibiaxial tension. In the second region, r_2=35mm~40mm, since the tensile axial stress and the compressive circumferential stress are negligibly small, an uniaxial state of radial tension, σ_{rr} is the main governing stress.

The maximum radial tension reaches σ_{rr}=4.25MPa at T_{surf} = 350°C and the axial stresse in tension is σ_{zz}=1.0MPa at T_{surf} =350°C, which are bigger than the values from thermoelasto-plastic analysis but still much smaller than the radial stresses. Focusing on the level of tensile radial stress, the uniaxial tensile radial stress, σ_{rr} governs collapse in concrete although three stress components exist. In the third region near the surface, r_3=40mm~47mm the stress states are investigated from the view of thermo-poro-mechanical process for tensile collapsing the form of spalling. The overall stress states are in tension-tension-compression. The radial stress and axial stress at r=42mm are σ_{rr}=3.86MPa and σ_{zz}=2.0MPa where the temperature is T =150°C when the surface temperature reaches T_{surf} =200°C. Meanwhile the uniaxial ultimate tensile

stress is degraded to $f_t(T)$=3.29MPa at T=150°C. The circumferential stress at the same location is $\sigma_{\theta\theta}$=-8.24MPa. At the location, r=45mm where the temperature becomes T =296°C when T_{surf} =350°C, the radial stress, σ_{rr} =3.92MPa and the axial stress σ_{zz}=3.0MPa in tension exceed the ultimate tensile strength, $f_t(T)$=2.48MPa and the circumferential stress increases to $\sigma_{\theta\theta}$=-10.0MPa which is below ultimate compressive stress, $f_c'(T)$=39MPa. In summary the state of stresses is close to equi-biaxial tension and compression where the radial stress and axial stress exceed the ultimate uniaxial tensile strength. The circumferential stress in compression, $\sigma_{\theta\theta}$ could confine the radial tensile stresses near the surface, and therefore combined stress states of equi-biaxial tension and compression may accelerate brittle and sudden failure which leads to surface spalling or ablation in the radial and vertical directions. Such a failure was also observed from the experimental observation as shown in Figure 14.3. These actions are different when compared to thermoelasto-plasticity in case that the ring compression near surface helps radial cracking restrain, which may result in more ductile failure. In addition, most spalling activities occur between 250°C and 400°C, which has been reviewed by Pierre Kalifa (2000) and Long Phan (2001). The current simulation shows that spalling can occur at temperatures in the range, about T =260°C ~310°C.

16 Spalling Risk Category

16.1 Defining spalling risk categories [Arup Group 2005]

Spalling can be modelled explicitly using state of the art thermo-hydro-mechanical system of equations considering all variables such as four field formulations vs. three field formulations shown in the previous chapter, which can lead to spalling including the build up of pore pressures as moisture evaporates from the concrete in a fire. The individual components of the porous structure of the concrete are all represented in this type of modelling therefore it is very complicated. This level of accuracy is still on-going research domain and still requires significant validation. Due to the level of uncertainty still associated with this explicit approach the alternative approach is instead to determine risk categories for spalling, based on the significant factors and available test data as follows.

Definition of the risk associated with each individual variable known to affect spalling – assigning risk factors

Each variable to influence spalling of concrete was split into an upper and lower bound and a "risk" value assigned to each (see Table 16.1) for categories of different concrete types. A value of 1 represents the lower bound of a variable, which is unlikely to affect spalling. A value of 3 is applied to the variables that are believed to have a medium effect on spalling and a value of 5 to those that have a high effect e.g. moisture above 3% by weight. The risk values of 1, 3 and 5 represent an approximating scale that indicates in each case that the characteristic can affect spalling and the values to distinguish the characteristic extent of this effect. Evidence in the literature has not enabled us to distinguish between the relative importance of reinforcement, aggregate type, cover, section size, number of sides exposed, restraint or initial loading on spalling. Consequently they have all been assigned the same values either 1 where the characteristic is at the level which is known to relatively give better performance or 3 where it is known to give relatively worse performance. The literature and test data have shown that the presence of initial moisture and the rate of heating have a more significant impact than the reinforcement, aggregate etc. Therefore these variables have been assigned a higher weighting equal to 5 when the heating rate is equivalent to the hydrocarbon fire or the moisture is greater than 3% by weight. Spalling of high strength concrete in a standard hydrocarbon fire is difficult to quantify. Therefore, for the purposes of this project it is assumed that high strength concrete is never less than Category D when exposed to a hydrocarbon fire. This is a simplistic approach to put the risk categories in perspective. The following limitations should be noted as presented in the data base;

- In general spalling is not expected in concrete with moisture content below 3% but there have been exceptions noted in the test data reviewed here. For the purposes of this work it is assumed that 3% is the critical value for spalling because a greater number of researchers have agreed upon this value.

- Concrete design strength 55MPa is assumed to be the limit between ordinary strength and high strength concrete. Its design strength is not the same as high performance concrete with silica fume and very low permeability, which is very susceptible to spalling.

- Moisture and heating rate have a significant effect on spalling whereas all other variables, which are known to have an effect on spalling, are generally considered to be secondary. This same approach has been adopted when developing the risk factors.

Table 16.1 Factors influencing explosive spalling

	RISK
Design Strength > 55Mpa	Not quantified
Design Strength < 55Mpa	1
Hydrocarbon fire	5
Standard fire (BS 476)	1
Moisture content > 3%	5
Moisture content < 3%	1
No Reinforcement	3
Reinforcement included	1
Cover > 40mm	3
Cover < 40mm	1
Siliceous aggregate	3
Calcareous aggregate	1
No. of sides exposed > 1	3
No. of sides exposed = 1	1
Section size < 200mm	3
Section size > 200mm	1
Restrained	3
Unrestrained	1
Thermal expansion > 10x10E-6	3
Thermal expansion < 10x10E-6	1
Loaded in compression	3
Unloaded	1

Definition of the total risk of spalling associated with a particular concrete – assigning risk categories

In order to arrive at a total risk of spalling for a particular concrete it is proposed that the risk associated with each variable in Table 16.1 can be added together and then further categorised. Five generic categories, from A to E are proposed as set out in Table 16.2 and associated with a "total risk" value.

A quantity of spalling associated with that risk category has then been defined by evidence from fire tests. To arrive at a "total risk" value for a particular concrete, all of the relevant individual "risk" values from Table 16.1 are added together. The value of "total risk" will then fit into the range for each of the categories in Table 16.2.

Table 16.2 Risk Categories with associated spalling quantification

Category	Risk of Spalling	Value of Total Risk	Key factors	Spalling level
A	Very low	<11	Ordinary strength, NWC, Unloaded, Unrestrained, Standard fire exposure, Reinforced, moisture <3%, one side exposure	Zero or minimal
B	Low	12-20	Ordinary strength, NWC, restrained, Standard fire exposure Significant number of key variables likely to promote spalling	Up to the level of reinforcement
C	Mid	21-28	Ordinary strength, NWC, restrained, Standard hydrocarbon fire exposure: Small number of key variables* likely to promote spalling	3mm/min
D	High	29-37	Ordinary strength, NWC, restrained, Standard hydrocarbon fire exposure Significant number of key variables likely to promote spalling	7mm/min
E	Very high	>37	High strength (Design strength >55Mpa), standard hydrocarbon fire exposure.	Unquantifiable

16.2 Assessment of the thermal spalling risk [Gawin, Pesavento, Schrefler 2006]

Three simplified models were introduced for concrete during heating by evaluating the thermally induced stresses and/or vapor pressures. Herein, only a schematic classification and brief description of these criteria are presented in three main categories:

1. Criteria based on pore pressure prediction, which consider the pore pressure as responsible for thermal spalling (N. Khoylou 1997). Usually the models employed for the description of the hygral state of concrete are rather simple. In some cases the so-called ‘‘moisture clog’’ is indicated as the main cause of spalling (T.Z. Harmathy 1965).

2. Criteria based on thermal stresses. These are the simplest ones and are related to the non-uniform thermal stresses.

3. Criteria based on combined action of thermal stresses and pore pressure. This is based on a method for the evaluation of the strain energy density in the direction of the heated surface in which spalling occurs when the strain energy density in normal direction to the heated surface equals the rupture energy density defined on the basis of tensile strength of concrete (Zhukov 1975, Connelly 1995).

In the approaches presented above, the criteria omit the complexity of hygro-thermal and chemo-

physical processes in concrete at high temperature hence they were not able to give a realistic evaluation of the thermal spalling risk.

Hypotheses concerning mechanisms of thermal spalling:
It is assumed that simplified hypotheses for mechanisms leading to thermal spalling which is based on mechanical models can formulate some quantitative criteria in assessment of the risk of the collapse. In particular, first three criteria which were assumed different macromechanisms led to concrete spalling, and one 'intuitive' criterion was deduced from the analysis of physical processes during heating of concrete.

Pressure-induced shear model
This simple criterion is based on the pressure-induced shear model (A. Combescure 2002). Considering a concrete slab heated on one face, it is possible to identify three zones in Figure 16.1.

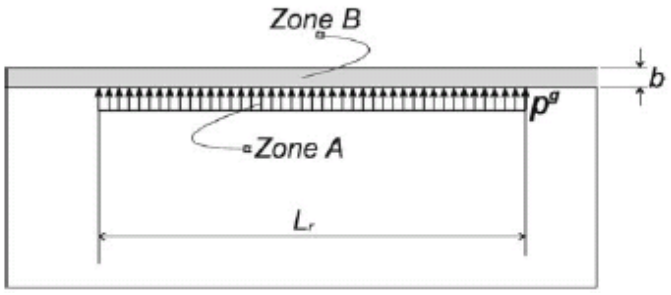

Fig. 16.1 Possible mechanism of thermal spalling: pressure-shear model or buckling

The first zone is a compressed concrete layer directly adjoining the heated surface, which is probably the most damaged one, the second zone is a region where the gas pressure reaches high values, and the third zone consists of partly thermo-chemically deteriorated concrete. This simple criterion predicts the plastic failure of the material constraints for the external layer. Denoting L_r the length of the zone A where gas pressure equal to P^g is assumed to be uniformly distributed which is delaminated from the rest of structure. The following limit condition for shear can be derived:

$$\frac{P^g L_r}{b} = f_t \tag{16.1}$$

where f_t is the tension strength of the material and b the thickness of the zone B of the compressed layer. Despite of its simplicity, this model presents some intrinsic difficulties related to the defining the characteristic parameters L_r and b, determination of which is a non-trivial problem.

Based on the pressure-induced shear model with the L_r/b ratio as a geometrical parameter, the first spalling index, I_{s1}, can be defined as follows:

$$I_{s1} = \frac{(P^g - P_{atm})d}{\bar{f}_t}\left(\frac{L_r}{b}\right) \tag{16.2}$$

where the gas pressure difference between the current position and the surrounding air is P^g- P_{atm}, and a necessary condition for this mode of rupture is pre-existence of a macro-fracture at the b depth. The effect of cracks on the concrete strength properties is described in the model by the mechanical damage parameter, d. $\bar{f}_t$ is the averaged traction strength, while P^g and d are local values.

Buckling model considering gas pressure

This spalling criterion is based on the hypothesis of buckling of the zone B in Figure 16.1 and the heated surface is initially delaminated. For the simple 2D case, the zone B close to the heated surface can be treated as a beam with length, L_r and thickness, b which is simply supported at its ends and subjected to a thermal compressive load and to a lateral pressure by the gas pressure as shown in Figure 16.1. Spalling will occur if $\sigma_{th} = \sigma_E = (\pi^2 E/12)\left(b/L_r\right)^2$ where σ_{th} is the mean-compressive thermal stress in the beam and σ_E is the critical buckling stress according to Euler's formula for columns. A slightly more sophisticated model can be proposed as incorporating lateral displacement by the applied gas pressure $w = w_o/(1-\sigma_{th}/\sigma_E)$ and the stress due to the lateral displacement, $\sigma_b = 6\sigma_{th}(w/b)$

$$P^g = \frac{16}{15}E\left(\frac{b}{L_r}\right)^4\left(1-\frac{\sigma_{th}}{\sigma_E}\right) \tag{16.3}$$

where zero tensile stress is assumed on the heated side when $\sigma_b = \sigma_{th}$. Using the compressive stress on the internal side of compressed zone, $f_c = \sigma_{th} + \sigma_b = \sigma_{th}(1+6w/b)$ and lateral displacement due to the gas pressure yields a definition of the critical value of gas pressure as

$$P^g = \frac{64}{5\pi^2}E\left(\sigma_E - \sigma_{th}\right)\left(\frac{f_c}{\sigma_{th}}-1\right)\left(\frac{b}{L_r}\right)^2 \tag{16.4}$$

Based on the buckling model considering gas pressure and the geometry, $(L_r/b)^2$ the following form, I_{s2} can be obtained as

$$I_{s2} = \frac{64}{5\pi^2}\frac{\left(P^g - P_{atm}\right)d}{\left(\bar{\sigma}_E - \bar{\sigma}_{th}\right)\left(\bar{f}_c/\bar{\sigma}_{th}-1\right)}\left(\frac{b}{L_r}\right)^2 \tag{16.5}$$

where also this rupture mode is necessary to have pre-existence of a macro-fracture and parameters σ_E, σ_{th}, and $\bar{f}_c$ are averaged from the heated surface to a given thickness.

Simplified fracture mechanics model

This hypothesis is based on fracture mechanics. The main mechanism of compressive failure is the sideways propagation of a band of parallel axial splitting cracks. Such a kind of mechanism can lead to a sudden release of the stored elastic energy and to a modification of the original stress field [(Z.P. Bazant 1997), (Z.P. Bazant, J. Planas 1998)]. In this particular case the compressive stresses derive directly from thermal fields and the released energy is related to constrained thermal dilatation. At a certain moment of compressive loading due to thermal stresses, axial cracks forming a band which is illustrated in Figure 16.2 (above) appear and the micro-slabs between them behave like beams with the correlated problems of buckling.

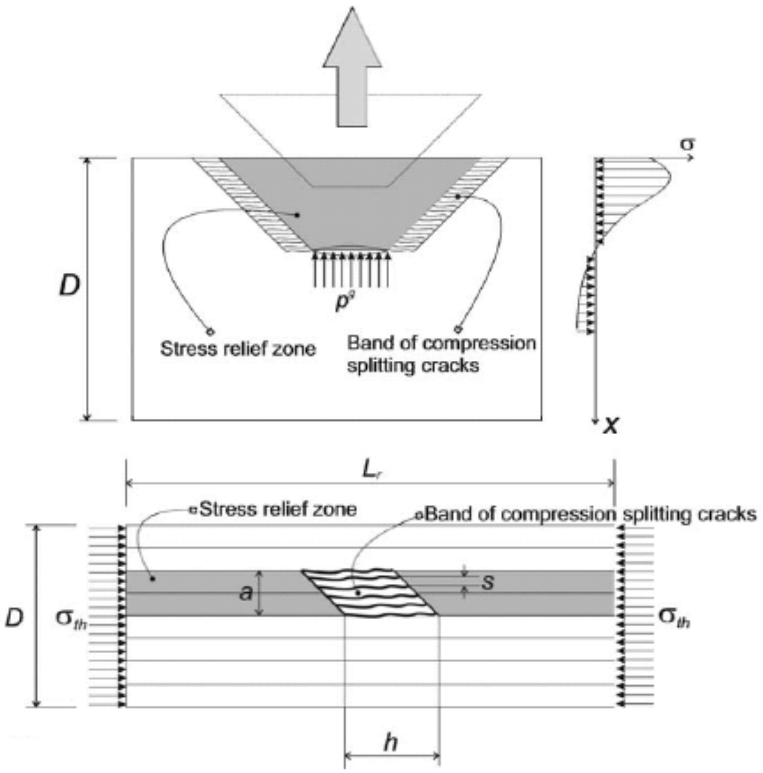

Fig. 16.2 Possible mechanism of thermal spalling: parallel axial splitting cracks propagation model (above) and band of compression splitting cracks with tensile transverse stresses model (below).

It is possible to calculate the variation of strain energy density in the micro-slabs and to define an energy balance by fracture energy using the initial normal stress before any fracturing in the cross-sections, the critical stress in the micro-slab by buckling, and the energy density by the post-buckling. The failure mechanism is formed by the development of two different systems of cracks: compression splitting cracks, and parallel cracks in the direction of compression due to the transverse tensile stresses, Figure 16.2 (below). The global behavior of the concrete element at macro-scale is similar to an orthotropic material. The energy released due to the propagation of axial splitting micro-cracks at practically layers between parallel tensile cracks in Figure 16.2 (below), ΔU, equals

$$\Delta U = \int_V \delta U dV = \frac{\sigma_{th}^{\ 2}}{2E} BaL_r \tag{16.6}$$

where ΔU is the energy density, V is the volume of the stress relief zone and σ_{th} are the compressive thermal stresses. The mechanical energy dissipated by the band of axial splitting micro-cracks is $W_f = ¼ (G_f Bha / s)$ where G_f is the fracture energy, so the energy balance during the fracture processes can be expressed as

$$\frac{\sigma_{th}^{2}}{2EL_r} = G_f \frac{h}{s} \tag{16.7}$$

which clearly shows a size effect (Z.P. Bazant, J. Planas 1998).

Despite of complexity for real concrete structures during heating, it is still possible to model it, in a simplified way. The third spalling index, I_{s3}, deduced from the criterion using fracture energy base is defined as

$$I_{s3} = \left(\frac{\bar{\sigma}_{th}^{2}}{2E}\right)\frac{d}{\bar{G}_f}\left(\frac{L_r s}{h}\right) \tag{16.8}$$

where $\bar{G}_f$ is averaged over the distance from the heated surface to a fractured position.

Intuitive spalling index

An intuitive spalling index, I_{s4}, is based on the analysis of physical phenomena during heating of concrete and leading to thermal spalling (Gawin, Schlefler 2006), which allows to estimate the kinetic energy of spalled material pieces, and to make predictions about explosive or non-violent character of the phenomenon, as well as on the results of several experimental studies. The criterion is formulated in such a way, that all factors regarding the material rupture are put in the numerator of a fraction defining the index, and resisting factors will be placed in its denominator where containing different data about the hygro-thermo-chemo-mechanical state of concrete, can generate a kind of 'averaging' effect and allow to predict thermal spalling. σ_{th} is averaged transversal traction stresses, $\bar{U}$ is a constrained elastic energy, $\bar{f}_t$ is average values of traction strength and $\bar{G}_f$ is specific fracture energy for the material layer between a current position and the heated surface.

$$I_{s3} = \left(\frac{\bar{\sigma}_{th}\bar{U}\,d}{\bar{f}_t\,\bar{G}_f}\right)\frac{P^g - P_{atm}}{P_{atm}} L \cdot C_s \tag{16.9}$$

where C_s is the scaling factor and L is the characteristic element length which are can be determined from experimental test (P.J. Sullivan, A.A. Akhtaruzzaman1971) and geometry of specimen.

16.3 Analytical assessment of spalling risk using concrete model

In the three-field formulations in Section 11.2.2 the parabolic Drucker-Prager model was used to investigate spalling failure mechanism under rapid heating. The yield function and associate flow potential which are temperature-dependent are defined as

$$F = J^{eff}{}_2 + \alpha_F(T) I_1^{eff} - \beta_F(T) \tag{16.10a}$$

$$Q = J^{eff}{}_2 + \alpha_Q(T) I_1^{eff} - \beta_Q(T) \tag{16.10b}$$

The strength parameters $\alpha_F(T)$ and $\beta_F(T)$ may be expressed in terms of the uniaxial tensile and compressive strengths of concrete, which are temperature-dependent as,

$$\alpha_F(T) = \frac{f_c'(T) - f_t'(T)}{3}, \beta_F(T) = \frac{f_c'(T) f_t'(T)}{3} \tag{16.11}$$

$J^{eff}{}_2 = 1/2(\mathbf{S}^{eff} : \mathbf{S}^{eff})$ is the second invariant of the effective deviatoric stresses and $I_1^{eff} = tr(\boldsymbol{\sigma}^{eff})$ is the first invariant of the effective stresses.

States of stresses near surface for thermal and hydraulic loading are assumed to be for the brevity followings:

$$\begin{aligned} \sigma_r^{eff} &= \sigma_z^{eff} = \sigma_H \\ \sigma_c^{eff} &= \sigma_T \end{aligned} \tag{16.12}$$

The first and second invariants of effective stresses are re-written in terms of thermal stress, σ_T and hydraulic stress, σ_H as $I_1^{eff} = 1/3(2\sigma_H + \sigma_T)$ and $J_2^{eff} = 1/3(\sigma_H{}^2 - 2\sigma_T\sigma_H + \sigma_T{}^2)$.
Substituting thermal and hydraulic stresses into yield function, Eq. (16.10) yields the following as

$$F = \frac{4}{5\alpha_F(T)^2 + 12\beta_F(T)} \left[\left(\sigma_H + \alpha_F(T)\right)^2 + \left(\sigma_T + \alpha_F(T)/2\right)^2 - 2\sigma_H\sigma_T \right] \le 1 \tag{16.13}$$

where the strength parameters, $\alpha_F(T)$ and $\beta_F(T)$ are temperature-dependent , which are related to uniaxial compressive and tensile strengths, $f_c'(T)$ and $f_t'(T)$,

$$f_c'(T) = f_c'(T_o) - 0.315(T - T_o) \text{ and } f_c'(T_o = 20C) = 48MPa \tag{16.14a}$$

$$f_t'(T) = f_t'(T_o)[1 - 0.1356 \times (T - T_o)/100] \text{ and } f_t'(T_o = 20C) = 4MPa \tag{16.14b}$$

Two possible states of stresses near surface of concrete cylinder are explored:
Applied temperature is T=300C at a position near surface, and T=350C at surface when the compressive and tensile strength are $f_c'(T) = 39MPa$ and $f_t'(T) = 2.5MPa$ using Eq. (16.14).

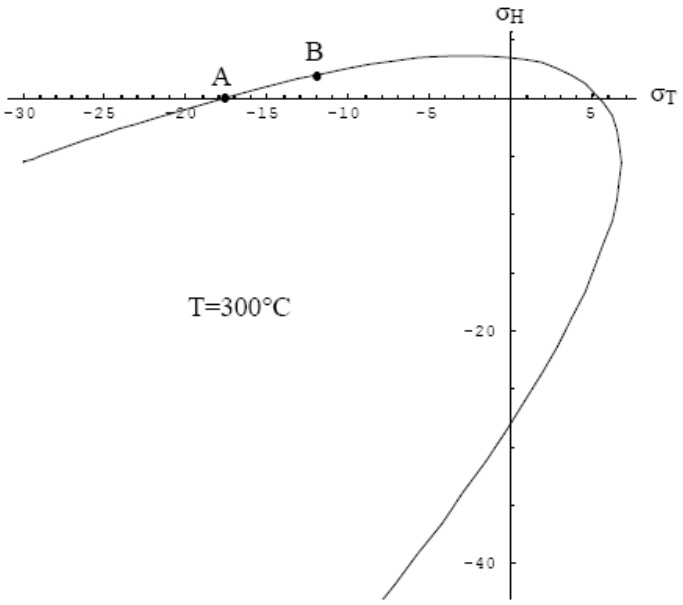

Fig. 16.3 Failure envelop for temperature-dependent surface: Point A-thermoplasticity and Point B-thermoporo plasticity at T=300°C.

The temperature-dependent envelop of the yield surface at temperature T=300°C is shown in Figure 16.3 where σ_T indicates the circumferential stress and σ_H are the axial and radial stress in the cylinder.

Case 1) Thermoplasty: assuming $\sigma_c = \sigma_T$ and $\sigma_r = \sigma_z = \sigma_H \approx 0$

Neglecting internal pore pressure results in thermoelastic or thermoplastic behavior which can be applicable to the dried specimen where no pore pressure is expected below T=350°C. Temperature near surface range in T=250~300°C when surface temperature reaches T=350°C. The temperature reaches T~300C at a location inside cylinder, and then the state of stress becomes approximately uniaxial state in compression. Analytical interpretation at this location where plausible spalling is initiated or observed is introduced using a concrete model.

Thermal stress, σ_T =-18.0 *MPa* can be calculated using the yield function, $F = 1$ when a circumferential stress $\sigma_c = \sigma_T$ and $\sigma_r = \sigma_z = \sigma_H = 0$ when concrete cylinder is subjected to a heating rate, 20C/min which corresponds to Point A in Figure 16.3. This indicates that material reaches yield surface and compressive failure occurs.

Case 2) Thermoporoplasty : assuming $\sigma_c = \sigma_T$ and $\sigma_r = \sigma_z = \sigma_H \approx 2.0$

Including internal pore pressure can be treated as thermoporoelastic or thermoporoplastic behavior which can be applicable to a partially or fully saturated specimen in open systems. At the same location the state of stresses becomes approximately uniaxial-circuferential compressive stress and biaxial tensile stresses in radial and axial directions when surface temperature reaches T=350C. Thermal stress, σ_T =-12.0 *MPa* can be calculated using, $F = 1$

when a circumferential stress is $\sigma_c = \sigma_T$ and estimated hygral stresses, $\sigma_r = \sigma_z = \sigma_H = 2.0\,MPa.$ More brittle failure is anticipated at Point B in Figure 16.3 as expected due to the combined stresses, compression-biaxial tension when compared to a failure in thermoplastic analysis at Point A.

From the above two analytical studies we can conclude that brittle or explosive failure of concrete cylinder subjected to high heating rate are susceptible to combined-thermal and hygral stresses and a level of initial moisture is very important factor to the explosive spalling.

17 Conclusions of Part III

• Explosive spalling is considered to be sensitive primarily to moisture contents, rapid heating rate and a build up of vapor pressures in concrete.

• Spalling as a result of stress induced by loading, restrained thermal expansion and geometry of structures is also significant but seldom explosive without moisture.

• There is limited test information on normal strength concrete spalling in response to the standard hydrocarbon fire when compares to high strength concrete. Note both responses to a fire are significantly different and the relevance of both resistances to spalling will have to be investigated respectively.

• Additional factors affecting spalling include section thickness, loading, reinforcement and the number of sides of the concrete section exposed to fire.

• There are a number of conclusions from literature reviews about the effect of individual variables. The complexities of mechanisms of the concrete spalling and the interactions associated with each variable have been conflicted as seen.

• In addition analytical and mathematical study has to be performed in parallel with experimental study to scrutinize underlying mechanisms of spalling. In this report the two mathematical models are presented: the three-field formulations for short term behavior and the four-field formulations for long term behavior in concrete.

18 References of Part III

Akhtaruzzuman, A.A., Sullivan, P.J.E. (1970), Explosive spalling of concrete exposed to high temperature, Concrete Structure and Research Report, Imperial College

Aldea, C.M., Franssen J.M., Dotreppe J.C., Fire Test on Normal and High-Strength Reinforced Concrete Columns, in: Proc. of Int. Workshop on Fire Performance of High-Strength Concrete, Gaitherburg, MD, USA, February 13–14, 1997.

Ali, F., Nadjai, A., Silcock, G., Abu-Tair, A. (2004), Outcomes of a major research on fire resistance of concrete columns, Fire Safety Journal, 39

Anderberg, Y. (1997), Spalling phenomena of HPC and OC, NIST Special Publication 919

Baroghel-Bouny,V., Mainguy, M., Lassabatere, T., Coussy, O. (1999). "Characterization and identification of equilibrium and transfer moisture properties for ordinary and high-performance cementitious materials." Cement and Concrete Research **29**(8): 1225-1238.

Z.P. Bazant, J. Planas, Fracture and Size Effect in Concrete and other Quasi-brittle Materials, CRC Press, New York, 1998.

Bazant, Z., Analysis of pore pressure, thermal stress and fracture in rapidly heated concrete, in: Proc. of Int. Workshop on Fire Performance of High-Strength Concrete, Gaitherburg, MD, USA, February 13–14, 1997.

Bažant, Z., and Kaplan, M.F. (1996). Concrete at high temperatures, material properties, and mathematical models, Longmon, Burnt Mill.

Bažant, Z., and Thonguthai W. (1979). "Pore pressure and drying of concrete at high temperature." Magazine of Concrete Research **31**(107): 67-75.

Both, R. (2000), The behaviour of unprotected loaded concrete tunnel linings subjected to RWS hydrocarbon fire, TNO report 2000-R01360

Breunese, A.J., Fellinger, J.H.H. (2004), Spalling of concrete and fire protection of concrete structures, TNO Report

BS 8110-2 (1985), BS 8110 Structural use of concrete, Part 2 Code of practice for special circumstances

Canisius, T.D.G., Waleed, N., Matthews, S.L. (2003), A preliminary study of the cardington concrete building under a compartment fire, Structure Faults and Repair

Castillo, C., Durrani, A.J. (1990), Effect of transient high temperature on high-strength concrete, ACI Materials Journal, 87-M7

Cheng, F.P., Kodur, V.K.R., Wang, T.C. (2004), Stress-strain curves for high strength concrete at elevated temperatures, Journal of Materials in Civil Engineering, V. 16, No.1, NRCC

CIRIA (1984), Spalling of concrete in fires, Technical Note 118

Clayton, N., Lennon T. (2000), Effect of polypropylene fibres on performance in fire of high grade concrete, BRE

Combescure, A., Reinforced concrete spalling, UPTUN project report, 2002.

Connolly, R.J. (1995), The spalling of concrete in fires, PhD thesis, University of Aston

Copier, W.J. (1977), The spalling of normal weight and lightweight concrete on exposure to fire Heron (Netherlands)

Coussy, O. (2004). Poro Mechanics, John Wiley & Sons.

Cruz, C.R., Gillen, M. (1980), Thermal expansion of Portland cement paste, mortar and concrete at high temperatures, Fire and Materials, Vol. 4, No. 2

de Boer, R. (1996). "Highlights in the historical development of the porous media theory: toward a consistent macroscopic theory." Appl. Mech. Rev. **49**(4), 201-62.

ENV 1992-1-1 (1992), Eurocode 2 Design of concrete structures, Part 1 General rules and rules for buildings

ENV 1992-1-2 (1996), Eurocode 2 Design of concrete structures, Part 1.2 General rules– Structural fire design

Gawin, D., Pesavento, F., and Schrefler, B. A. (2006). "Towards prediction of the thermal spalling risk through a multi-phase porous media model of concrete." comput. Methods. Appl. Mech. Engrg. **195**: 5707-5729.

Gawin, D., Pesavento, F., and Schrefler, B. A. (2002). "Modelling of hygro-thermal behavior and damage of concrete at temperature above the critical point of water." International Journal for Numerical and Analytical Methods in Geomechanics **26**: 537-562.

Gutaferro (1966), Fire resistance of prestressed concrete, Bauverlag GmBH, Berlin

Harmathy, T.Z. (1965), Effect of moisture on the fire endurance of building elements, American Society of Testing and Materials, Special Technical Publication 385

Harmathy, T.Z. (1970), Thermal properties of concrete at elevated temperatures, ASTM Journal of Materials

Hertz, K.D. (2003), Limits of spalling of fire-exposed concrete, Fire Safety Journal, 38

Huang, C.L.D., Ahmed, G.N., Fenton, D.L. (1991), Responses of concrete walls to fire, International Journal of Heat Mass Transfer, Vol. 34, No. 3

Kalifa, P., Francois-Dominique Menneteau and Daniel Quenard (2000). "Spalling and pore pressure in HPC at high tempeartures." Cement and Concrete Research **30**: 1915-1927.
Khoury, G.A. (2003), Passive fire protection in tunnels, Concrete

Khoury, G. A., Majorana, C. E., Pesavento, F. and Schrefler, B. A. (2002). "Modelling of heated concrete." Magazine of Concrete Research **54**(2): 77-101.

Khoury, G.A. (2000), Effect of fire on concrete and concrete structures, Progress. In Structural. Engineering and Materials, Issue 2, pp 429-447.

G.A. Khoury, Strain components of nuclear-reactor-type concretes during first heating cycle, Nucl. Engrg. Des. 156 (1995) 313–321.

Khoury, G.A., Grainger, B.N., Sullivan, P.J.E. (1985), Transient thermal strain of concrete: literature review, conditions within specimen and behaviour of individual constituents, Magazine of Concrete Research, 37 (132)

Khoury, G. A., Sullivan, P.J.E. and Grainger, B.N. (1984). "Radial temperature distributions within solid concrete cylinders under transient thermal states." Magazine of Concrete Research **36**: 146-156.

Khoylou, N. (1997), Modelling of moisture migration and spalling behaviour in non-uniformly heated concrete, Ph.D. thesis, Imperial College, London.

Kodur, V.K.R (1999), Fire performance of high-strength concrete structural members, Construction Technology Update No. 31, NRCC

Komonen, J., Vesa, P. (2003), Effects of high temperature on the pore structure and strength of plain and polypropylene fiber reinforced cement pastes, Fire Technology, 39

Lee, J. (2006). Experimental studies and theoretical modelling of concrete subjected to high temperatures, PhD thesis, University of Colorado at Boulder
Lee, J.S., Xi, Y., and Willam, K. (2008). " A Multiscale Model for Modulus of Elasticity of Concrete at High Temperatures." submitted to *Cement and Concrete Research*.

Lee, K. (2008). Evaluation of Concrete Behavior under High Temperature, PhD thesis, University of Colorado at Boulder
Lewis, R. W. and B. A. Schrefler (1998). The finite Element Method in the Static and Dynamic Deformation and Consolidation of Porous Media, John Wiley & Sons.

Lennon, T. (2000), Fire tests on tunnel lining segments containing polypropylene fibres, BRE

Lennon, T. (2004), Structural fire engineering design: materials behaviour – concrete, Digest 487, BRE

Marsh, B. (2002), Arup Internal Report

Meyer-Ottens, C. (1977), The behaviour of concrete structural elements in fires, Spalling of normal concrete elements under fire stress: causes and preventive measures, BRE Translation 2058

Msaad, Y. (2006). "Comparison between hydraulic and thermal spalling in heated concrete." Journal of Engineering Mechanics: 1-33.

Newman, J., Choo, B.S. (2003), Advanced concrete technology, Elsevier Ltd

Neville, A.M. (1995), Properties of concrete, Longman Group Limited

L.T. Phan, N.J. Carino, Effects of test conditions and mixture proportions on behavior of high-strength concrete exposed to high temperature, ACI Mater. J. 99 (1) (2002) 54–66.

Phan, L.T., Lawson, J. R., Davis, F. L. (2001). "Effect of elevated temperature exposure on heating characteristics, spalling, and residual properties of high performance concrete." Materials and Structures(RILEM) **34**: 83-91.

Phan, L.T., Lawson, J.R., Davis, F.L. (2000), Heating, spalling characteristics and residual properties of high performance concrete, NISTIR 6588

L.T. Phan, N.J. Carino, D. Duthinh, E. Garboczi (Eds.), Proc. Int. Workshop on Fire Performance of High-Strength Concrete, Gaitherburg, MD, USA, February 13–14, 1997, NIST Special Publication 919, NIST, 1997.

L.T. Phan, Fire performance of high-strength concrete: a report of the state-of-the-art, Res. Report NISTIR 5934, pp. 105, National Institute of Standards and Technology, Gaitherburg, 1996.

Saito, H. (1965), Explosive spalling of prestressed concrete in fire, Japanese Building Research Institute, Occasional Report 22, Ministry of Construction, Tokyo

Schneider, U. (1988), Concrete at high temperatures—a general review, Fire Safety J. The Netherlands 55–68.

Schneider, U. (1986), Properties of materials at high temperatures – concrete, RILEM

Schneider, U. (1982). "Verhalten von Beton bei hohen Temperaturen (Behavior of Concrete at High Temperatures." Deutscher Ausschuss Fur Stahlbeton.

Schneider, U. (1976), Behaviour of concrete under thermal steady state and non-steady state conditions, Fire and Materials, Vol. 1

G.W. Shorter, T.Z. Harmathy, Moisture clog spalling, Proc. Instit. Civil Engr. 20 (1965) 75–90.

Sertmehmetoglu, Y. (1977), On a mechanism of spalling of concrete under fire conditions, PhD thesis, King's College, London

Shuttleworth, P. (1997), Fire performance of concrete for tunnel linings, Channel Tunnel Rail Link Technical Report, Arup

SINTEF (1992), Fire testing of concrete element

Sullivan, P.J.E. Deterioration and spalling of high strength concrete under fire, Offshore Technology Report 2001/074, pp. 77, HSE Books, Sudbury, 2001.

P.J. Sullivan, A.A. Akhtaruzzaman, Explosive spalling of concrete exposed to high temperature, in: Proc. of First International on Structural Mechanics in Reactor Technology, Berlin, 1971.

Tenchev, R. T., Li, L. Y. and Purkiss, J. A. (2001). "Finite element analysis of coupled heat and moisture transfer in concrete subjected to fire." Numerical Heat Transfer, Part A **39**: 685-710.

Thomas, F.G., Webster, C.T, (1953), Investigations on building fires, Part VI – The fire resistance of reinforced concrete columns, National Building Studies Research Paper 18, HMSO, London

Yin, R., Lamont S., Lane B. (2005), Fire resistance of concrete enclosures, ArupFire Technical Report, Arup

Zeiml, M., Leithner, D., Lackner, R., Herbert A. Mang (2006). "How do polypropylene fibers improve the spalling behavior of in-situ concrete?" Cement and Concrete Research **36**: 929-942.

Zhukov, V., Explosive failure of concrete during a fire (in Russian). Translation No. DT 2124, Joint Fire Research Organization, Borehamwood, 1975.